Hierarchical Materials for Tissue Engineering and Regeneration

E. O. Fielder

Department of Materials, Imperial College of Science, Technology and Medicine
University of London
London
UK

2001

Ph.D. Thesis

Acknowledgements

I dedicate this book to my parents, and to the monoliths that didn't make it.

Thank you to Professor Hench for being my supervisor through the beginning years of the lab and his time at Imperial College.

Thank you also to EPSRC for funding this project and to my colleagues who helped out with various studies: Nik Royall, Graham Briers, Abil Aliev, Priya Pavan, Jason Maroothynaden, Yannis Xynos, Ian Thompson and Richard Cook.

Table of contents

	page
Abstract	**i**
List of Tables	**ii**
List of Figures	**iv**
Table of Abbreviations	**ix**
Chapter 1 Introduction	**1**
Chapter 2 Literature review	**4**
2.1 The general theory of sol-gel materials	5
2.2 The sol-gel process	6
2.3 Structure and properties of sol-gel bioactive glass-ceramics	9
2.3.1 Microphase separation	9
2.3.2 Homogeneity of multicomponent gels	10
2.3.3 Theory of bioactivity (Class A and Class B) bioactive materials	13
2.4 Applications of bioactive sol-gel materials	15
2.5 Research objectives and conclusions	17
2.5.1 Sol-gel derived bioactive glass powder	18
2.6 Variables and other process parameters that affect the sol-gel products	18
2.7 Thermal treatments and densification studies	20
2.8 Why are thermal treatments important?	21
2.8.1 Process parameters affecting densification kinetics	22
Chapter 3 The importance of composition for bioactive gel-glasses	**24**
3.1 The $CaO-P_2O_5-SiO_2$ system	24
3.2 The role of silica and other like compounds in nature	25
3.2.1 Soluble silica in nature	25
3.2.2 Silica in biology and the origin of life	26
3.2.2.1 Examples of silicate based organisms: algae and diatoms	27
3.3 The importance of phosphorous and its compounds	28
3.3.1 Phosphates in life processes	28
3.4 Phosphates, calcium and biomaterials	30
3.4.1 Calcium orthophosphates	30
3.4.2 Tricalcium phosphate	31
3.4.3 Apatites	31
3.4.4 Hydroxyapatite	31
3.5 Replicating bone and its properties	32
Chapter 4 Processing of the hierarchical materials	**35**
4.1 Processing of sol-gel monoliths	35
4.2 Comparison of the sol-gel product with melt-derived product	37
4.3 Structural evolution of the sol	39
4.3.1 Solvent quality effects in sol-gel processing	39
4.3.2 Pore size and texture modification	41
4.3.3 Drying	41
4.3.4 Stabilization	43
4.3.5 Densification	44

4.3.6 Choices of media for densification studies 46
4.4 The structure of the gel-glass 47
4.4.1 Role of interconnections in porous bioceramics 48
Chapter 5 Nitrogen adsorption on silicate surfaces 50
5.1 Particle size and packing, the nature of the silica surface and the hydroxylated surface 51
5.2 Surface area determination by gas adsorption 51
5.3 Examining the sol-gel product 53
5.3.1 Pore structure 53
5.4 Sample preparation and experimental procedure for nitrogen adsorption analysis 54
5.4.1 Degassing 54
5.4.2 Network theory 55
5.5 Instruments used 56
5.6 Nitrogen adsorption for surface area and porosity determination 57
5.6.1 Surface area – The BET Method 57
5.6.2 Porosity by gas adsorption 58
5.6.3 Adsorption isotherms 58
5.6.4 Pore size distribution 62
5.6.5 Nonporous materials 64
5.7 Nitrogen adsorption analysis of silica gels 64
5.7.1 Interpretation of results 65
5.8 Nitrogen adsorption analysis of Bioglass® compositions 65
5.8.1 Analysis of the mesoporous gels 65
5.8.2 Results of nitrogen adsorption of 68S Bioglass® 68
5.8.2.1 Analysis of mesoporous 68S Bioglass® 69
5.8.3 Results for 58S Bioglass® with various stabilization treatments and thermal histories 70
5.8.3.1 Analysis of isotherms of 58S stabilized at 400° (synthesized without HF catalyst). 70
5.8.3.2 Analysis of isotherms of 58S400 with thermal treatment in dry nitrogen atm. 72
5.8.3.3 Analysis of isotherms of 58S600 with thermal treatment in dry nitrogen atm. 76
5.8.3.4 Analysis of isotherms of 58S800 with thermal treatment in dry nitrogen atm. 78
5.9 Discussion of results obtained for 58S stabilized at 400, 600 and 800°C without thermal treatment 81
5.9.1 Analysis of isotherms obtained from 58S800 with thermal treatment in carbon dioxide atmosphere 82
5.9.2 Synthesis of 58S Bioglass® with HF catalyst [5%] 84
5.9.3 Discussion and conclusions 85
Chapter 6 Other analytical techniques employed to characterize 58S Bioglass® 90
6.1 Mercury porosimetry 90
6.1.1 Mercury porosimetry as a characterization tool 90
6.1.2 Hysteresis behaviour 92
6.1.3 Scanning versus stepwise data acquisition 92
6.1.4 Limitations of mercury porosimetry 93

6.1.5 Theoretical analysis of mercury intrusion porosimetry 94
6.1.6 Sample preparation 95
6.1.7 Results obtained using mercury porosimetry 95
6.1.8 Results obtained for 58S samples stabilized at different temperatures and those thermally treated in dry nitrogen 96
6.1.9 Density measurements for 58S800 thermally treated in carbon dioxide atmosphere 98
6.2 Helium pycnometry of 58S samples 100
6.3 Differential thermal analysis (DTA) 101
6.3.1 Results for DTA of unstabilized 58S and 58S stabilized at 400°C 102
6.3.2 Results of DTA for 68S Bioglass® 102
6.3.3 Results of DTA for 58S Bioglass® stabilized at 800°C 103
6.4 X-Ray powder diffraction (XRD) 104
6.4.1 Results of XRD analysis of 58S400 105
6.4.2 Results of XRD analysis of 58S800 105
6.4.3 Results of XRD analysis for 58S400 with thermal treatment 106
6.4.4 XRD analysis of 58S800 with thermal treatement up to 1200°C 106
6.4.5 Discussion of XRD results 108
6.5 Scanning electron microscopy (SEM) and energy dispersive X-ray analysis (EDAX) 110
6.5.1 Analysis of 58S Bioglass® using SEM and EDAX 111
6.5.2 SEM and EDAX analysis of 58S compositions versus those with HF addition 113
6.5.3 SEM EDAX analysis for a study employing different aging regimes for the synthesis of 58S800 versus US Biomaterials 58S powder 117
6.6 Transmission electron microscopy (TEM) 121
6.6.1 Sample preparation for TEM and results for 58S400 and 58S800 122
6.6.2 Discussion of TEM results 125
6.7 Nuclear magnetic resonance (NMR) 125
6.7.1 Results of NMR analysis of 45S5 and 58S Bioglass® powders 129
6.7.2 Discussion of results obatined by NMR analysis 129
6.8 Confocal microscopy and optical properties 135
6.8.1 Analysis of 58S by confocal microscopy 135
6.8.2 Refractive index results for transparent 58S400 138
Chapter 7 Dissolution studies and Fourier transformed infrared (FTIR) analysis of 58S samples **141**
7.1 Dissolution studies: theory 141
7.2 Dissolution studies: experimental 145
7.3 Results of dissolution studies for 58S stabilized at different temperatures after immersion in Tris buffer solution 146
7.3.1 ICP results for 58S stabilized in air at 400°C and thermally treated in dry nitrogen after immersion in tris buffer solution at 37°C 147

7.3.2 Results for 58S600 with thermal treatment after immersion in tris buffer solution at 37°C 148
7.3.3 Results for ICP analysis of solutions obtained from 58S800 with thermal treatments after immersion in tris buffer solution at 37°C 150
7.3.4 Discussion of data obtained from ICP analysis of solutions from 58S stabilized at different temperature and with thermal treatment after immersion in Tris buffer solution at 37°C 153
7.4 ICP results for 58S800 immersed in Simulated Body Fluid (SBF) at 37°C. 154
7.5 Fourier transformed infrared spectroscopy (FTIR) analysis of 58S samples 158
7.5.1 Experimental procedure for FTIR analysis 158
7.5.2 Results using FTIR pellets prepared from thermally treated 58S samples using method 1 160
7.5.3 Results obtained by method 1 FTIR from samples 58S800 after immersion in Tris buffer and SBF solutions 161
7.6 Results obtained from FTIR analysis of powder samples after immersion in SBF in an orbital shaker using Method 2. 162
7.7 Discussion of results from dissolution Studies and FTIR data obtained for 58S Bioglass® 167
Chapter 8 Cell culture studies **174**
8.1 Mimicking of bone materials 174
8.1.1 Microscopic organization of bone 174
8.1.2 Osteocytes 177
8.2 Sample preparation for cell culture studies and experimental procedure 177
8.3 Results of initial cell culture study for 58S400 179
8.4 Results of cell culture study using 58S with HF addition 180
8.5 Discussion 180
Chapter 9 Conclusions and future work **184**
9.1 Further work 189
List of references **193**
Appendix 1 **206**

ABSTRACT

Sol-Gel derived Bioglass® is a potential bone graft material, that has an ability to bond with tissue. It is possible to cultivate cells on this material (*in vitro*) following immersion in simulated body fluid (SBF). Under osteogenic conditions these materials demonstrate both osteoconductive and osteoproductive behaviour which leads to a rapid biological bond at the interface between the glass and the bony tissue. An important advantage of the bioactive sol-gel glasses is that their rate of resorption can be controlled during bone repair or tissue engineering by varying either their composition or their texture.

In this work a regime for producing reliable batches of monolithic bioactive gel-glass compositions of SiO_2 (58mol%), P_2O_5 (4mol%) and CaO (38mol%) in various geometries was established with unfractured monolithic yields of > 90% per batch.

The gel-glass samples were stabilized at 400°, 600°, and 800°C and also thermally treated in CO_2 and dry N_2 atmospheres to produce a wide range of textures.

Characterization of the bioactive gel glasses was done using the following techniques:- transmission electron microscopy (TEM), scanning electron microscopy (SEM), x-ray diffraction (XRD), differential thermal analysis (DTA), energy dispersive x-ray (EDAX), nuclear magnetic resonance (NMR), mercury porosimetry, helium pycnometry, nitrogen adsorption analysis and confocal microscopy.

Rates of resorption of the bioactive gel-glasses in Tris buffer solution and simulated body fluid (SBF) at 37°C were analyzed using induced coupled plasma spectroscopy (ICP) whilst pH changes were monitored. Initial bioactivity was assessed using Fourier transformed infrared spectroscopy (FTIR) analysis of the rates of formation of biologically active hydroxyapatite on the surface. Primary human osteoblast cell studies were performed to assess biocompatibility of the gel-glasses.

The most important findings of this study include comprehensive materials characterization of this sol-gel product, the positive results obtained when tested *in vitro* and limitations associated with final applications.

List of Tables

Table 2.1: Precursors used for the synthesis of 58S Bioglass® 6

Table 2.2: Typical Properties of Corning brand Vycor® Glass [19] vs. Typical properties of 58S800 Bioglass® synthesized at IC. 11

Table 2.3: Factors affecting pore size of the sol-gel product 19

Table 2.4: Factors affecting the homogeneity of the product 20

Table 3.1: Phases of silica 26

Table 3.2: Composition of compact bone [92]. 33

Table 4.1: Previous results [108] on the properties of porous silica (Type VI) gel-glasses 45

Table 5.1: The relative error associated with various C constants obtained from the Quantachrome manual for the AS-1 66

Table 5.2: Nitrogen adsorption data for 58S with and without HF additions 67

Table 5.3: Results of 68S samples stabilized at different temperatures. 68

Table 5.4: Results obtained for 58S samples unstabilized and stabilized at 400°C for 24 hours 71

Table 5.5: Results from the heat treatment study of 58S stabilized at 400°C and thermally treated in a dry nitrogen atmosphere 74

Table 5.6: Results obtained from nitrogen analysis of 58S stabilized at 600°C 76-77

Table 5.7: Results from 58S stabilized at 800°C with thermal treatment in dry nitrogen atmosphere 80-81

Table 5.8: Comparative results from thermal study outlining properties of 58S stabilized at different temperatures 82

Table 5.9: Results obtained from a study of 58S stabilized at 800°C and thermally treated in carbon dioxide at various times and temperatures 83

Table 5.9.1: Results from nitrogen adsorption of 58S made with HF [5%] catalyst 84

Table 5.9.2: Results from nitrogen adsorption data obtained in this work compared with previous studies 88

Table 6.1: Results for 58S stabilised at 400°C, 600°C, 800°C and also those thermally treated in dry nitrogen 97

Table 6.2: Results for data obtained from thermal treatment of 58S800 in carbon dioxide 98

Table 6.3: Results from data obtained by helium pcynometry of 58S800 samples with thermal treatment in dry nitrogen. 101

Table 6.4: Peak table for the XRD analysis of crystalline 58S400 after 75 minutes at 1050°C in air. 107

Table 6.5: Nitrogen adsorption data for the study of 58S800 made using different aging regimes. 119

Table 6.6: Results for NMR analysis of 58S and 45S5 129

Table 7.1:Reaction rates for 58S400 series after immersion in tris buffer solution at 37°C 148

Table 7.2:Reaction rates for 58S600 series after immersion in tris buffer solution at 37°C 150

Table 7.3:Reaction rates for 58S800 series after immersion in tris buffer solution at 37°C 152

Table 7.4: Mass in mg obtained for 45S5 powder after immersion in SBF [57]. 157

Table 8.1: Secretory products of osteoblasts 176-177

List of Figures

Figure 2.1: S_N2 - Si hydrolysis [8]. 7

Figure 2.2: Reaction stages of 45S5 Bioglass®. [33] 15

Figure 2.3: Ternary diagram for the bioactive gel-glasses. 16

Figure 4.1: Drying programme for 58S monolith batch preparation. 35

Figure 4.2a : 58S monoliths with HF addition, examples of cracked monoliths also shown. 38

Figure 4.2b: 58S monoliths made from cylindrical molds, examples of cracked monoliths also shown. 38

Figure 4.2c: Examples of transparent and opaque sections from cracked 58S monoliths cast from square molds with no HF addition. 38

Figure 4.2d: 58S Bioglass® monoliths showing both opaque and transparent natures. Some monoliths have surface cracks. 38

Figure 4.2e: 58S Bioglass® discs with HF addition – Inhomogeneity is clearly visible in top right hand side disc by blotchy appearance. 38

Figure 4.2f: 58S Bioglass® cylinders with HF addition and made with different aspect ratios. Total opacicity is observed. Cylinders are 0.5<cm<1cm in height and 0.5cm in diameter. 38

Figure 4.3: Cluster formation of gel ultrastructure with spherical groupings giving rise to pore families preferentially formed in acid catalysis of TEOS [97]. 40

Figure 5.1: The five types of isotherms as classified by Brunauer-Deming-Deming and Teller (Powers, [93]). 60

Figure 5.2: DeBoer's five types of hysteresis loops (Powers, [93]). 61

Figure 5.3: Typical BET isotherms for mesoporous 58S stabilized at 600 and 800°C. 66

Figure 5.4: Typical BET isotherms for mesoporous 68S stabilized at 350 and 400°C. 69

Figure 5.5: Typical BET isotherms obtained for 58S samples unstabilized and stabilized at 400°C for 24 hours. 71

Figure 5.6: Graph of total pore volume, pore diameter, and surface area for 58S400 with different thermal treatments. 75

Figure 5.7: Graph of pore diameter, surface area and total pore volume for thermally treated 58S stabilized at 600°C. 77
Figure 5.8: Graph of total pore volume, pore diameter and surface area for 58S stabilized at 800°C for different times in dry nitrogen. 79
Figure 5.9: Graph of AS-6 Results for 58S800 densified in CO_2 at different temperatures for 20 minutes. 84
Figure 6.1: Graph of different pore families obtained from mercury porosimetry of 58S800 samples treated in carbon dioxide atmosphere for 20minutes, and at different temperatures [28]. 99
Figure 6.2a: Pore data obtained by nitrogen analysis of 58S800 [28]. 99
Figure 6.2b: Pore data obtained using mercury porosimetry for 58S800. 100
Figure 6.3a: DTA of unstabilized 58S 103
Figure 6.3b: DTA of 58S stabilized at 400°C 103
Figure 6.3c: DTA of 68S stabilized at 400°C 104
Figure 6.3d: DTA of 58S stabilized at 800°C 104
Figure 6.4a: XRD of 58S400 110
Figure 6.4b: XRD of 58S800 110
Figure 6.4c: Crystalline XRD spectra obtained from 58S400 with Thermal treatment at 1050°C for 75 minutes in air. 110
Figure 6.4d: Combination XRD spectra at different temperatures for 58S800 treated up to 1200°C. 110
Figure 6.5a: Tweezer identation preserved in a rod of 58S400 without catastropic failure after stabilization. Mag. x 189. 114
Figure 6.5b: Side projection of 58S400 rod made from PTFE mold at a shorter programme. L = 1.5cm D = 1mm. Mag. x 17. 114
Figure 6.5c: End of 58S400 rod from 1 day shorter cycle. No evidence of surface porosity due to PTFE molding. D = 1mm. Mag. x 175. 114
Figure 6.5d: Internal porosity is exposed at the other end of the 58S400 rod from a brittle fracture. Mag. x 55. 114
Figure 6.6a: Graph of comparative study with 58S (normal recipe) against 58S with HF (5%) addition. 115

Figure 6.6b: Graph of compositional analysis by SEM EDAX for the compostion 58S samples synthesized. using different aging regimes versus US Biomaterial's 58S powder. 120
Figure 6.7a : Natural silica TEM scan (scale =10nm) *Phalaris Caneriensis.* 124
Figure 6.7b : TEM scan of 58S800. 124
Figure 6.7c : High resolution of surface of amorphous HA type growths on 58S. 124
Figure 6.7d : High resolution of amorphous HA type growths on 58S crystalline type growth on the surface of 58S. 124
Figure 6.8: Schematic diagram of types of disorder in a binary alkali disilicate glass [137]. 130
Figure 6.9a: Confocal microscopy image of mercury trapped within 58S glass pores, (0.1μm to 20μm). Field width 60μm. [x 63/ 1.25 na oil lens +1:8 sampling effective magnification = X 504]. 137
Figure 6.9b: Confocal image, showing preferential mercury (M) invasion tracks (L to R) into a 58S sol-gel specimen (G), accentuating a uniform advancing front, parallel to the exposed surface. Field width 250μm. [x40/0.85 na oil lens] 137
Figure 6.9c: Invasion of fluorescent labelled resin (from L), at [top] 24hrs and [bottom] 72 hrs. Resin / glass interface marked by brightest linear structure. Conforming to first order capillary uptake kinetics. [x40 /0.85 na oil lens] 137
Figure 7.1: Graph of dissolution product after immersion in tris buffer solution at 37C for 58S400 with heat treament in nitrogen at 850°C for 20mins. 147
Figure 7.2: Graph of dissolution products for 58S600 with heat treatment in nitrogen at 850°C for 20mins after immersion in tris buffer solution at 37°C. 149
Figure 7.3: Dissolution products for 58S800 after immersion in tris buffer solution at 37°C. 150
Figure 7.4: Graph of pH variation with respect to time for 58S samples stabilized at different temperatures and after immersion in tris buffer solution 153

Figure 7.5: Graph of ICP data for dissolution products of 58S800 after immersion in SBF at 37°C. 155
Figure 7.6: FTIR spectra obtained from untreated 58S800 using Method 1. 161
Figure 7.7: Spectra obtained by method 1 FTIR analysis of 58S800 after immersion in tris buffer solution at time periods of 2, 5, 7.5 and 12 hours. 162
Figure 7.8: FTIR spectra for 58S800 after immersion in SBF for 20 hours at 37°C. 163
Figure 7.9a: FTIR spectra of 58S800 with thermal treatments after immersion in SBF for 20 hours at 37°C. 163
Figure 7.9b: FTIR spectra for 58S800 treated at 1000°C for 20minutes in air after immersion in SBF for 20 hours at 37°C 164
Figure 7.9c: FTIR spectra for 58S800 and 58S800 with HF addition after immersion in SBF for 20 hours at 37°C 164
Figure 8.1: Diagram illustrating the formation of Haversian canals in compact bone [92]. 175
Figure 8.2a : Cell culture colony of primary human osteoblasts after 4 days on the surface of 58S400. Mag. x 320. 181
Figure 8.2b : Primary human osteoblast after 4 days on the surface of 58S400. Mag. x 2560. 181
Figure 8.2c: Closer examination of internal porosity of the 58S400 rod surface. Mag. x 1150. 181
Figure 8.2d: Hydrolyzed CaP growths on the surface of 58S400 after immersion in tap water for two days. Mag. x 2110. 181
Figure 8.3a: Primary human osteoblast on the surface of 58S800 with 1.5ml HF addition at 5%. Mag.x 600. 182
Figure 8.3b: CaF_2 crystals on the surface of 58S800 made with 1.5ml HF addition. Mag. x 800. 182
Figure 8.3c: Filopodia from primary human osteoblast penetrating voids which are large enough on the surface of 58S800 with HF addition. Mag. x 3000. 182

Figure 8.3d: Mineralisation of amorphous growths on the surface of 58S800 with HF addition, osteoblast filopodia are seen extending into growths. Mag. x 5000. 182

Figure 8.3e : General view of cell colony on the surface of 58S800 with 1.5ml HF addition. Mag.x 175. 182

Figure 8.3f : Other view of primary human osteoblast on the surface of 58S800 with 1.5ml HF addition. Mag.x 800. 182

Table of Abbreviations

TEOS	Tetraethyoxysilane
TEM	Transmission electron microscope
SEM	Scanning electron microscope
XRD	X-ray diffraction
DTA	Differential thermal analysis
EDAX	Energy Dispersive Atomic X-ray
NMR	Nuclear magnetic resonance
ICP	Induced coupled plasma
FTIR	Fourier transformed infrared
PE	Polyethylene
PTFE	Teflon
DCP	Dicalcium phosphate
TCP	Tricalcium phosphate
HAp/HA	Hydroxyapatite
SBF	Simulated body fluid
HCA	Hydroxyl carbonate apatite
PHA	Precipitated hydroxyapatite
DCP	Dicalcium phosphate
DCPD	Dicalcium phosphate
TTCP	Tricalcium phosphate
MCPM	Monocalcium phosphate
OCP	Octocalcium phosphate
DCCA	Drying control chemical additive
ACP	Amorphous calcium phosphate
FAp	Fluoroapatite
CAp	Chloroapatite
DHAp	Defective hydroxyapatite
IC	Imperial College

CHAPTER 1 INTRODUCTION

1 Introduction

Traditionally, glass has been considered as the passive element in the manufacture of containers and in the conveyance of light. This is contrasted by the active role played today by a whole new generation of glasses which are classified according to their roles in the fields of optics, electronics, chemistry, biology and medicine.

By hierarchical materials, we mean porous sol-gel materials which can be engineered for a broad range of textural qualities including: pore size (with pore ranges from 20-20,000Å), surface area, and total pore volume. Sol-gel technology has mostly been used in the optical and electronic industries where quality in small dimensions is of the utmost importance to the performance of the product. With sol-gel technology of glasses the separation of different phases and compositional features is orders of magnitudes smaller than in their melt-derived counterparts. In this work hierarchical bioactive materials for use in tissue engineering and regeneration have been processed using sol-gel technology and characterized. The CaO-P_2O_5-SiO_2 system studied is based on the 45S5 Bioglass® formula.

Bioglass® belongs to a biologically active group of glasses. When placed in contact with tissues it demonstrates an ability to bond with the tissue. It is possible to cultivate cells on these types of materials (*in vitro*) when immersed in simulated body fluid (SBF). Furthermore, in potentially osteogenic conditions these materials are both osteoconductive and osteoproductive, producing particularly good biological bonding at the interface between the glass and the bony tissues [1]. There is also evidence [2] of the up regulation of genes associated with bone synthesis when human osteoblasts are exposed to an extract of 45S5 Bioglass® *in vitro*.

Sol-gel processing has become a topic of great interest because there are many advantages to the final product arising from the control of ultrastructure - the structure that is beyond the scope of the scanning electron microscope, and on the nanometre scale. An important advantage of bioactive gel glasses is that their rate of resorption can be controlled during bone repair or tissue engineering by varying either composition or texture. In addition, benefits include cost reduction as the reactions occur at ambient pressure and temperature. The difference between the modern development of sol-gel derived materials, such as gel-silica optics, and the classical work of Ebelman [3] is that the drying of the monolithic silica optics can now be achieved in days rather than years.

Each year many people are affected by the loss of bone either through accident or the need for replacement. A range of materials is currently used for these purposes in surgery, one of which is Bioglass®. Bioglass® is a unique material as it elicits an osteoproductive affect when implanted. Other materials have also been used for these purposes but few of them elicit such a response and generally bond only mechanically at the biological interface.

This work focuses on the use of sol-gel bioactive glass for potential bone graft replacements and scaffolding for new bone ingrowth, based on the established bioactivity of Bioglass®. Professor Hench and colleagues [4] and subsequently US Biomaterials Corp. [5] produced a sol-gel recipe for 58S Bioglass® after the initial success with the melt-derived 45S5 system. Sol-gel materials for this application are of interest due to their high surface area and controlled level of porosity. Thus, they can be used to create resorbable scaffolds upon which new bone growth can develop after implantation. Bioactive glasses undergo surface dissolution in physiological environments, which gives rise to osteoproduction.

The main processing objective in this work was to produce 58S Bioglass® monoliths at >90% yield in the lab, followed by characterization and *in vitro* testing of the monoliths. This work adds to the experimental data of how this hierarchical material behaves and confirms that it is biocompatible. Much of the previous work done on bioactive glass systems has been done on melt-derived glass compositions [4,5]. However, modification was made by Hench et al. and US Biomaterials to produce a sol-gel recipe for 58S and 77S Bioglass® compositions. This work continues the process of

characterization of these new materials and their controlled ultrastructure, ultimately for use in bone repair.

Porous silicate glasses are made in two different ways. The first technique produces a phase separated glass with two continuous phases and then one or two of the phases are leached with an appropriate corrosive fluid. The second method, and primary objective of this work, focuses on producing gel-glasses that are monolithic via a moulding and a controlled gelation route. In the controlled gelation route, the hydrolysis and condensation of silicon alkoxide is used to form the glass. The regime formulated in this work produced monolithic samples after two weeks directly from the sol-gel process without the use of leaching of other phases, intricate drying procedures or drying control chemical additives (DCCA).

By using sol-gel processing techniques porous glasses are produced by low temperature methods, compared to their melt-derived counterparts, and can be tailored for textural features such as surface area (from 10^0-10^2 m^2/g), pore diameter (from 1.5nm-10^5nm) and total pore volume. Gels of different textures are explored in this work but common to all is enhanced bioactive behaviour due to rapid formation of apatite layers on the surface of 58S Bioglass® substrates.

In order to tailor glass compositions for particular applications a full understanding of the composition and the way it behaves in fluid media, as well as in the presence of osteoblasts is of utmost importance. In this work we look at the effects of different processing regimes on the dissolution kinetics and the mechanism by which the apatite layer is formed on the surface of sol-gel derived 58S Bioglass®. Batches of 68S Bioglass® and 58S Bioglass® with [5%] HF addition were also synthesized and characterized.

CHAPTER 2 LITERATURE REVIEW

The literature review in this chapter focuses on the sol-gel technology of bioactive gel-glasses implemented in this work. For general reviews of the field, the reader should consider Brinker and Scherer [3], Hench and West [6] or Hench [7].

2 Literature Review

The goal of sol-gel technology is to use low temperature chemical processes to produce net-shape, net-surface objects, films and fibres, particulates, or composites that can be used commercially after a minimum of additional processing steps. Traditional ceramic processing produces materials having microstructures typically in the range of 1-100 micrometres diameter. Sol-gel processing can provide control of microstructures in the nanometer size range, i.e. 1-100nm (0.001-0.1 μm), which approaches the molecular level.

Historical

Although the origins of chemical based ceramic processes may be dated to as early as 4000BC [8], the concept of control of shape and molecular structure of ceramics and glasses by use of sol-gel chemistry probably dates from Bergman's studies on water glasses in 1779, Ebelman's and Graham's studies on silica gels in 1847 and 1864, respectively, and a large body of work on the science of colloids in the mid-1800s [8].

From the late 1800s through to the 1920s, many noted chemists investigated the periodic precipitation phenomenon that leads to formation of Liesegang rings and the growth of crystals from gels [9]. In the early 1900s, sol-gel methods were used to produce highly porous silica gels that could be used for desiccants, adsorbents, and catalysts [3]. Some of the earliest (1930s) commercial sol-gel technology was the use of partially hydrolyzed alkoxysilane solutions for impregnation of porous stone, concrete, and brick; in dental cements; and for coating silica on the interior of light bulbs and vacuum tubes [3].

Numerous groups have studied the pure silica system [3,9] and we derive the main body of our theory of sol-gel processing from these studies. However, in a 3-component system one can expect thermal processes to occur at lower temperatures due to the network modifiers present.

In the 1940s, commercial applications of sol-gel-derived anti-reflective coatings on glass emerged [8], along with a growing industrial use of sol-gel derived catalysts. In the mid-1950s [10], the potential for achieving very high levels of chemical homogeneity in colloidal gels was recognized and the sol-gel method was used to synthesize many novel ceramic oxide compositions, involving Al, Si, Ti, and Zr. These could not be made using traditional ceramic powder methods.

During the 1980s, stimulated by several discoveries, interest in the sol-gel process increased greatly. Based on early work [6], very low-density silica monoliths, called aerogels, have been made by supercritical drying [11]. Supercritical drying of silica gels has been shown to yield large, fully dense silica glass monoliths [7]. Another important development was the preparation of large i.e. pieces of several mm, monolithic pieces of optically transparent alumina by sol-gel methods [12].

The seven main steps of the sol-gel process are mixing, casting, gelation, aging, drying, stabilization and densification. Authors such as Iler [3], Brinker and Scherer [9] have contributed much towards the understanding of this process on a chemical reaction level. General aspects of the chemistry of each of the seven sol-gel process steps are noted in this chapter. However, understanding of the molecular reaction mechanisms and the thermodynamics and kinetics of multi-component sol-gel systems is limited. Systematic studies on multicomponent gels are especially rare, thus, the results of this current work will add to knowledge of these complex systems.

2.1 The general theory of sol-gel materials

A brief description of the stages of the sol-gel process (from precursor sol to gel, to stablised monolith) follows. Detail on how specific factors and variables affect bioactive gel-glasess are described in Chapter 5.

2.2 The sol-gel process

a) Mixing

A liquid alkoxide precursor such as $Si(OR)_4$, where R is C_2H_5 (tetraethyloxysilane or TEOS), is hydrolyzed by mixing with water. As soon as any hydrolyzed species is present, condensation proceeds [8].

Table 2.1: Precursors used for the synthesis of 58S Bioglass®

Bioglass® SYSTEM	PRECURSORS
SiO_2	TEOS
CaO	$Ca(NO_3)_2.4H_2O$ or $Ca(O_2C_3H_7)_2$
P_2O_5	TEP $(C_2H_5O)_3P(O)$

The hydrated silica tetrahedra interact in a condensation reaction, forming (triple)=Si-O-Si bonds. Linkage of additional Si-OH tetrahedra occurs as a polycondensation reaction and eventually results in a SiO_2 network. The H_2O and alcohol expelled from the reaction remain in the pores of the network [8]. When sufficient interconnected colloidal (submicrometre) particles or sol is developed, the size of the sol particles and the cross-linking within the particles increases.

Acid-Catalyzed Hydrolysis

Under acidic conditions, it is likely that an alkoxide group is protonated in a rapid first step. Electron density is withdrawn from the silicon, making it more electrophilic and thus more susceptible to attack by water. Pohl and Osterholz [8] favour transition states of significant S_N2-type character. The water molecule attacks from its polar character to acquire a partial positive charge. The positive charge of the protonated alkoxide is correspondingly reduced, making alcohol a better leaving group. The transition state decays by displacement of alcohol accompanied by inversion of the silicon tetrahedra, see Figure 2.1.

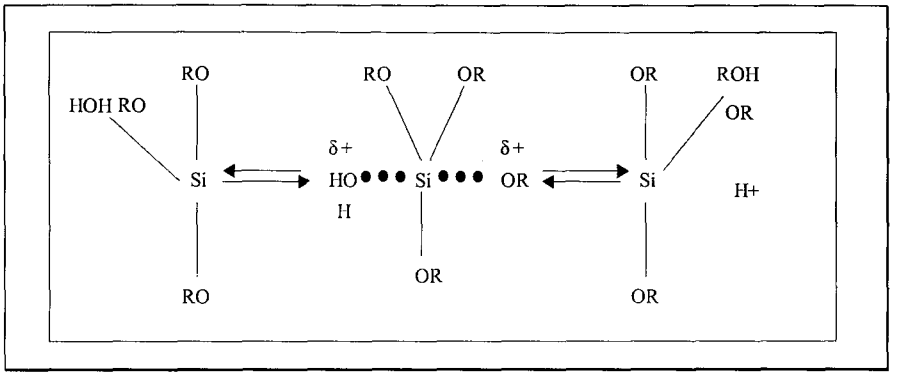


Figure 2.1: S_N2 - Si Hydrolysis [8]

b) Casting

Because the sol is a low viscosity liquid, it can be cast into a mould. The mould must be selected to avoid adhesion of the gel. The sol can also be applied as a coating on a substrate, drawn into fibres or emulsified. However, manipulation of the original formula to create linear chains rather than spherical structures (obtained with acid catalysis) must be observed.

c) Gelation

After some time the colloidal particles and condensed silica species link together to become a three dimensional network. The physical characteristics of the gel network depend greatly on the size of particles and extent of cross-linking prior to gelation. Using appropriate control of the time-dependant change of viscosity and choice of catalyst of the sol, fibres can be pulled or spun. Particles having controlled morphology and structure can be created during gelation.

d) Aging

The process that involves a continuous change in structure and properties of a completely immersed gel in liquid after the gel point is called aging. The shrinkage of the gel and the resulting expulsion of liquid from the pores during aging is called syneresis. During aging, polycondensation continues along with the localized solution and reprecipitation of the gel network, which increases the thickness of interparticle necks and decreases the porosity. The strength of the gel thereby increases with aging. An aged gel must develop sufficient strength to resist cracking during drying.

e) Drying

During drying, the liquid is removed from the interconnected pore network. Large capillary stresses can develop during drying when the pores are small (<20nm). These stresses can cause gels to crack catastrophically unless the drying process is controlled to produce a homogeneous structure, free from defects, by controlling the rates of hydrolysis and condensation.

f) Dehydration or Chemical Stabilization

The removal of surface silanol (Si-OH) bonds from the pore network results in a chemically stable ultraporous solid. To achieve dehydration it is necessary to recognize that water is present in two forms: free water within the ultraporous gel structure (i.e. physisorbed water) and hydroxyl groups associated with the gel surface (i.e. chemisorbed water). The amount of physisorbed water adsorbed onto the silica particles is directly related to the number of hydroxyl groups existing on the surface of silica.

g) Densification

Heating the porous gel at high temperatures causes densification to occur. The pores are eliminated and the density ultimately becomes equivalent to that of quartz or fused silica. The densification temperature depends on the dimensions of the pore network, the connectivity of the pores, and surface area. Alkoxide gels have been densified as low as 1000°C, whereas gels made by the commercial colloidal process require heating to 1500-1720°C. Colloidal silica gels that have carefully controlled dense packing can also be densified at temperatures as low as 850°C.

The major conclusion of several studies [8] is that despite the complex manner in which the gel evolves toward a glass, once the gel has been densified and heated above the glass transition temperature, its structure and properties become indistinguishable from those of a melt-derived glass. Mechanical properties are enhanced by the nanometre structure of the sol-gel product.

2.3 Structure and properties of sol-gel bioactive glass-ceramics

Glass-ceramics are materials that have been produced in a vitreous state by traditional or sol-gel methods and are given subsequent thermal nucleation and controlled crystallization treatment. The consequent development is a ceramic product with a high state of crystallinity composed of minute crystals set in a residual vitreous/glassy matrix left over from the crystallization process.

Glass is an unstable material, so there is no 'equilibrium glass' to use as a standard for comparison [9]. The properties of a glass depend on thermal history (e.g. cooling rate, annealing time) and can vary over a wide range, so the properties obtained by vapour deposition (for example) can generally be obtained from a melted glass following a suitable heat treatment. Thus, classical theories are employed when describing the structure, thermodynamics and kinetics of a glass.

2.3.1 Microphase separation

It is a common belief that sol-gel (or sintered-gel) glasses are more homogenous than a melt-quench glass [13]. In principle, the intimate mixing of the precursors should lead to homogeneity at molecular level. Roy [14] reported a gel route to prepare homogeneous glass by chemical mixing, and then melting the gel. He obtained greater homogeneity in such glasses than could be achieved after repeated melting of oxide powders. McCarthy et al. [15] extended this method to prepare other silicate glasses containing Na_2O, BaO, and K_2O. The conclusion of previous studies using electron microscopy, which confirmed XPS observations [13], was that phase separation is more easily achieved in heat-treated gels than in the corresponding melt-quench glass and in some cases the gel is phase separated well before it is transformed to a melt-quench glass-like structure. The phenomenon of phase separation in glasses, which since about 1950 has become an essential topic of modern glass research, was recognized as early as 70yrs ago [16].

Phase separation aspects also contribute to the crystallization kinetics of the glass. It is known that nucleation in the volume of the glass is less common than surface nucleation but volume nucleation is seen in some compositions, which employ nucleating agents [17]. In addition, limited hydroxyl content in the glass can

produce large increases in crystal nucleation and growth rates [17]. It is proposed in this work that in the 58S Bioglass® system (60mol%SiO_2, 3mol% CaO and 4%mol P_2O_5), that the 4 mol% phosphate addition could act as a nucleating agent and contributes to the temperature required to nucleate crystals in the gel-glass being lower than its melt-derived counterparts. However, it must be noted that phase separation can also affect the optical properties of a glass. Schott gives the following description: "My melting experiments revealed that SiO_2 and B_2O_3 were compatible, while P_2O_5 exhibits hostile behaviour." While SiO_2 + B_2O_3 as a glass-forming double acid accept bases in any proportions, the addition of P_2O_5 almost always causes milky opalescence, apparently because phosphates are "as insoluble in the melt as oil and water" [16]. Optical properties are an important factor when considering biosensor applications.

Vycor® type glasses can be made by taking advantage of the phase separation in the silica-borate-soda system [17]. A multicomponent glass is produced consisting of 65% silica, 27% B_2O_5, and 8% Na_2O which is cast in the desired shape. Upon cooling the glass phase separates in to two phases, a silica rich phase and a boron/sodium rich phase. It was also found that upon further heat treatment, the phases consolidate into two interconnected phases, the size and morphology of which increase with time and temperature [18]. Vycor® processing also involves leaching out the boron/sodium phase with hot dilute acid. In the preparation of 58S Bioglass® no such leaching was used but these two materials both share the same type of phase separation involving a silica rich phase interconnected with that of a network modifier phase (which is CaP rich in 58S Bioglass®). However, Vycor® remains the most similar model to the 58S Bioglass® synthesized in this work in terms of material properties rather than application use. Vycor is of composition 96.6wt% SiO_2, 2.95% B_2O_3, 4% Na_2O and <1% R_2O_3 + RO_2 [18]. Table 2.1 outlines the typical properties of Corning brand (7930) Vycor® glass.

2.3.2 Homogeneity of multicomponent gels

Work was done on the homogeneity of multicomponent bioactive gel-glasses by Pereira, Clark, and Hench [10]. They stated that high homogeneity can be achieved in a multicomponent gel-derived glass if the gel-to-glass conversion can be

accomplished without considerably changing the cation distribution achieved at the gel stage.

Table 2.2: Properties of Corning Brand Vycor® Glass [19] vs. Properties of 58S800 Bioglass® synthesized at Imperial College in this study.

Properties	Properties of Vycor®	Properties of 58S800 Bioglass® synthesized at IC
Appearance	Opalescent	Opalescent/Transparent
Refractive Index	1.33	1.33
Bulk Density (g/cm3)	1.5	1.5
Pore Volume (%)	28	33
Average Pore Diameter (Å)	50	61
Specific Surface Area (m2/g)	200	183

They also found that by using all alkoxide precursors, monolithic, transparent gel-glasses can be obtained in the $CaO\text{-}P_2O_5\text{-}SiO_2$ system with a heterogeneity level of about 1% (when using quantative evaluation through electron microprobe analysis). A slow hydrolysis rate using atmospheric water is necessary. In this work, we find that the phase separation of 58S is on the nanometre level and cannot be resolved by optical means or SEM EDAX. However, due to the composition of the bioactive gel-glass we must consider that phase separation may be present regardless of scale, as these characteristics will also govern how the glass reacts in a liquid medium.

Phase separation is the phenomenon whereby an amorphous homogeneous phase is divided into two immiscible phases of different composition, as discussed earlier. In glasses, this separation may occur spontaneously on cooling in air, or upon reheating. The resulting microstructure generally consists of finely dispersed droplets of glass or colloidal crystals in a matrix of the host glass. The dispersed phase can be amorphous or crystalline [20].

Glass-ceramics are polycrystalline materials, by definition, and are formed by the controlled crystallization in glasses of special composition. The polycrystalline environment also provides resistance to crack propagation. However, glass-ceramics are differentiated from solely phase separated glasses by their high crystallinity. Glass-ceramics are, by definition, $\geq$ 50% crystalline by volume and are generally > 90% crystalline. Upon ceraming, the glassy state of the host glass has phosphorus homogeneously in the structure, and promotes a very fine scale phase separation upon heating near annealing temperatures. The dispersed phase, typically metal or fluoride is structurally incompatible with the host glass and is normally highly unstable as a glass. However, near annealing temperatures the phosphate constituent will precipitate tiny crystals, these later serve as sites of nucleation for the primary crystalline phases. The resultant microstructure is highly uniform, consisting of fine grained randomly orientated crystals in the matrix ranging from < 0.1μm to > 10 μm.

During gel evolution at low pH i.e. < 3, with complete hydrolysis (4mol H_2O per mol TEOS) a highly branched fractal structure is produced with no discernable particles and very small pore size (<1nm). As the pH increases above 7, due to dissolution and condensation reactions, the structure of the gel may coarsen. Gel structures are composed of loosely bound, closely stacked spheres that produce small pores, shown in Figure 4.3, see page 43. In multicomponent gels, the more reactive species hydrolyze to form clusters before the less reactive alkoxide starts to polymerise. The regime for the synthesis of 58S Bioglass® adopted by US Biomaterials and used by previous authors [10,21] was further modified for the synthesis of monolithic 58S samples in this work. The chemical recipe for the sol was not changed but the drying regime was modified to accommodate the incremental temperature rises required for successful drying of monoliths. The US Biomaterials recipe was followed strictly during the synthesis of 58S Bioglass® at Imperial College as it is evident from previous studies [10,21] that the order of addition of the constituents in a sol, the TEOS to water ratio and the amount of time used for mixing the sol can affect the homogeneity of the gel and ultimately the correct composition of the 58S Bioglass®.

2.3.3 Theory of bioactivity (Class A and Class B bioactive materials)

The large differences in the rate of fibroblast proliferation and rate of bone bonding to bioactive implants indicates that different biochemical factors are occurring at the implant-tissue interface depending upon the glass or glass-ceramic composition [22]. This difference in rate of tissue proliferation is amplified when the bioactive materials are compared in the form of particulates [23]. Wilson and Low [24] compared 45S5 Bioglass® particulate with synthetic HA and other calcium phosphate granules in the treatment of surgically created periodontal defects in monkeys. Use of the highly bioactive powders (45S5 Bioglass®) led to a more rapid and complete repair of surgically created periodontal defects in Patus monkeys than was observed for the lower bioactivity HA or resorbable tricalcium phosphate (TCP) powders [24]. Bioactive glass powders with high bioactivity also resulted in the attachment of the periodontal ligament and little or no epithelial downgrowth.

The rate of development of the interfacial bond between the implant and bone can be referred to as "the level of bioactivity". Hench [25] introduced an index of bioactivity as a measure of this rate of bonding. The index is given the equation $I_B = (100/t_{0.5bb})$, where $t_{0.5bb}$ is the time for more than 50% of the surface to be bonded to bone. The highly bioactive glass powders (I_B = 12) show osteoconduction and osteoproduction of bone, whereas the powders with lower I_B values (I_B = 3 to 6) exhibit only osteoconduction [23].

Osteoproduction has been defined by Wilson [21,24,26] as "The process whereby a bioactive surface is colonized by osteogenic stem cells free in the defect environment as a result of surgical intervention". This differs from osteoconduction, where the implant simply provides a biocompatible interface along which the bone migrates. Recall that osetoinduction is considered to be the production of bone in an ectopic site [26,27], i.e., one in which bone is not normally found, such as muscle or skin. No alloplastic implant is osteoinductive regardless of level of bioactivity.

Class A bioactivity leads to osteproduction and Class B bioactivity leads to osteoconduction. Hench proposed a hypothesis to describe the difference in tissue

response [28] that "Class A, osteoproductive bioactivity, occurs when a material elicits both an intracellular and an extracellular response at its interface. Class B, osteoconductive bioactivity, occurs when a material elicits only an extracellular response at its interface", see Figure 2.2.

Class A bioactive glasses release soluble silicon in the form of silicic acid due to ion exchange with H^+ and H_3O^+ [29-31]. The release occurs immediately upon exposure of the glass to liquid medium or simulated body fluid [32-35]. Class A bioactive glasses release soluble silicon by both ion exchange and network dissolution. Class B bioactive materials have low or zero rates of ion exchange, low rates of network dissolution and therefore release small, or zero amounts of soluble silicon [23].

The subsequent reaction stages of 45S5 Bioglass® glass are summarized in Fig. 2.2 [33]. Following implantation or submersion into a simulated body fluid (SBF) under physiological conditions, calcium and phosphorous ions are leached out, along with partial dissolution of the silica network. This results in the formation of the microporous silica gel layer and release of soluble Si, in the form of silicic acid, $Si(OH)_4$. Within 1 to 3 hours an amorphous calcium-phosphate phase precipitates onto the gel layer, which crystallizes to form HCA. Throughout this process, adsorption of proteins and other biological molecules is occurring at the interface [33].

It is the highly hydrolysed, porous nature and high surface charge density of the silica surface that induces strong protein adsorption. Zhong et al. [36] have shown that acellular deposition and integration of collagen occurs on the silica gel and porous HCA layers of reacted melt-derived 45S5 Bioglass® *in-vitro*. Hench has theorized that two factors contribute to the distinctly different osteogenic behaviour of Class A and Class B bioactive materials [23]. First, the formation of a silica-rich gel layer due to ion exchange provides a suitable substrate for extracellular adsorption, particularly of hormones, growth factors, and attachment factors.

Retention of biological activity near the surface results in the proliferation and activation of bone cells around the implant. Second, experimental evidence

suggests that soluble silicon influences cellular metabolism, including bone cells [35-40]. Keeting et al. [41] show that the dissolution product of zeolite A, which includes soluble Si, increases the metabolic activity of cells.

Figure 2.2: Reaction stages of 45S5 Bioglass® [33]

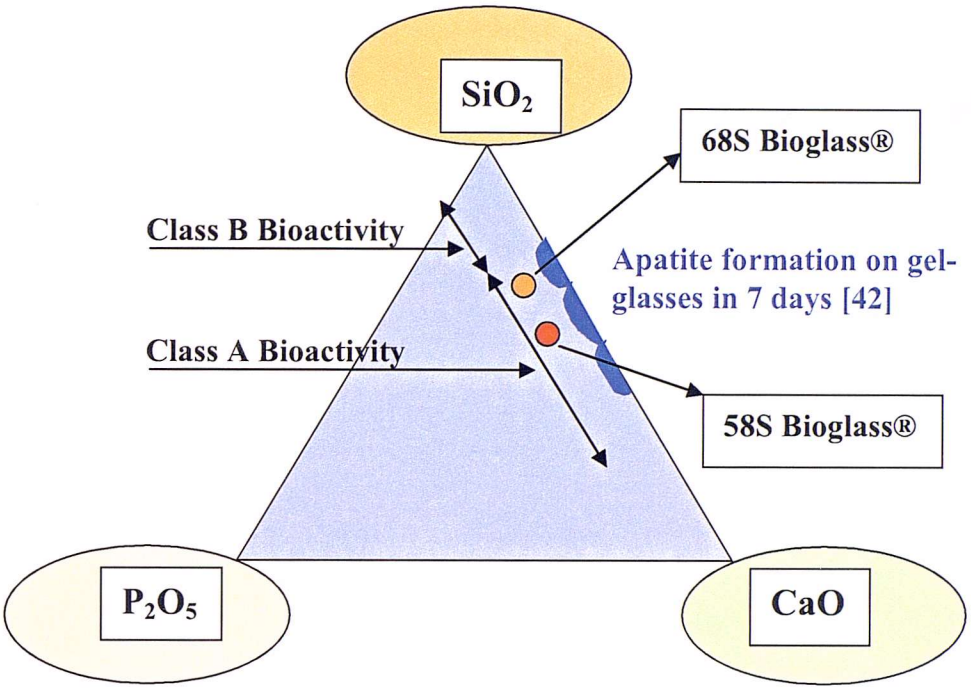
Stage	Surface Reaction Stages
1 & 2	Formation of SiOH bonds and release of $Si(OH)_4$ from glass surface to form a silica rich layer
3	Polycondensation of Si-OH + Si-OH ⟶ Si-O-Si
4	Adsorption of amorphous Ca^{2+} + PO_4^{3-} + CO_3^{2-} on surface
5	Crystallization of hydroxyl carbonate apatite (HCA)
6	Adsorption of biological moieties in HCA layer
7	Action of macrophages
8	Attachment of osteoblast stem cells
9	Differentiation of stem cells
10	Generation of matrix
11	Crystallization of matrix
12	Proliferation of bone

In vitro the sol-gel derived bioactive glass developed by Li et al. [42] remained bioactive with up to 90mol% SiO_2 (vs. 60mol% for melt-derived glass), and bioactivity was confirmed *in-vivo* at 80mol% SiO_2 for sol-gel glasses studied by Pereira et al., [43].

2.4 Applications of bioactive sol-gel materials

Bioceramics has evolved to become an integral and vital segment of our modern health-care delivery system [44]. In the years to come the composition, microstructure, and molecular surface chemistry of the various types of bioceramics will be tailored to match the specific biological and metabolical requirements of tissues or disease states. This 'molecular based pharmaceutical' approach to the design of bioceramics should couple with the growth of genetic engineering, sensor technology, and information processing, resulting in a range of products and applications not even imagined at present, but potentially beneficial to millions of people annually.

Figure 2.3: Ternary diagram for bioactive gel-glasses



Research and potential applications of sol-gel materials in biology and medicine can be divided into the following categories [6]:

1. Bioactive sol-gel coatings.
2. Bioactive sol-gel glasses.
3. Sol-gel matrices with enzymes and antibodies.
4. Doped sol-gel matrices as biological and chemical sensors.
5. Sol-gel matrices with entrapped living organisms.

As the focus in this work is on bioactive sol-gel glasses for potential use as bone replacement materials, attention is directed towards producing a material, e.g. one that has similar mechanical and structural qualities to bone as well as being bioactive and resorbable. Bone is a highly developed material with very different microstructures at different sites. In essence, it is collagen reinforced by hydroxyapatite. Aspects of interest to materials scientists include piezoelectric properties, its ability to absorb and reform to counteract the highest levels of

stress, the transitions from narrow dense shafts to broad porous heads to allow efficient transfer of the stress at articular joints, and directional porosity, which allows blood vessels to penetrate the structure without weakening it. This is a good example of how microstructure and design should be integrated throughout a component. It is suggested that for tissue repair of bone that a minimum pore diameter of 100-150μm [28] is required to allow ingrowth of blood vessels and therefore blood supply through the structure.

The reaction leading to a positive glass-bone bond has been well documented by Hench [23] and can be summed up with the reaction steps of Fig. 2.1. When placed in contact with a solution of blood plasma, Bioglass® undergoes a series of sequential surface chemical reactions. The outcome of the reactions is the development of a crystalline layer of calcium phosphate (HCA) set within the matrix of silica gel that allows a stable bond between the glass and bone tissue. Various authors have tackled the topics of producing sol-gel derived glasses with controlled surface reactivity [2] and others have studied the compositional limit [4,44] of these bioactive materials.

These studies show that increased silica content in the glass limits the bioactivity of the glass. Other studies show that binary systems excluding the phosphate constituent are not as 'bioactive' as those which do contain it [42]. 58S provides a good fundamental starting point with favourable bioactivity results and was synthesised rather than 100% pure SiO_2 gels or binary system (calcium and silica only) gels. In Chapter 3, the fundamental reasoning behind the choice of composition studied, a ternary system rather than the four-component system of the melt-derived 45S5 Bioglass® is discussed, as are the implications of this with regard to enhancing its function as an implantable and partially resorbable system for repair or replacement of bone.

2.5 Research objectives and conclusions

Other authors who have worked on the production of pure silica sol-gel products, [45] produced only discs and rods directly. Supercritical conditions of temperature and pressure are often used in sol-gel research to achieve rapid fracture-free drying. However, this process requires high-pressure autoclaves and is not

amenable to scale up for commercial processing. Most of the research conducted herein supports this finding. Initially, alkoxide gels were difficult to dry rapidly without fracture. The stresses were reduced by decreasing the drying rate and employing a humid environment. This had an undesirable effect of increasing the drying time. However, in this work every attempt has been made to keep the procedure economically viable and simple. No DCCA's were used or supercritical atmospheres for drying, and gels were densified later in dry nitrogen or carbon dioxide atmospheres.

It has been estimated that for an alkoxide gel with a typical strength of 0.1MPa, it would take 4 days to dry a 1 cm thick plate without cracking. Using the particulate gel synthesis route, much larger pores were produced and the drying rate was successfully increased [45]. Large monolithic particulate gels several centimeters thick were dried in a matter of a few days.

2.5.1 Sol-gel derived bioactive glass powder

Sol-gel derived powder is produced by the same route as monolithic shapes. However, because a monolith is not required from this process, remaining fragments after drying of cracked gels are ground further to obtain a powder (thus giving the particles an angular shape). Other methods have been employed since at US Biomaterials to obtain fine particle sizes for 45S5 Bioglass® (<20μm). Analysis of this powder is reviewed in Chapters 5 and 6.

2.6 Variables and process parameters that affect the sol-gel products

It is apparent that the amount of water present in the recipe for the gel is critical. It is suggested that a ratio of 5:1 or more (water to TEOS) should be observed. Otherwise, improper hydrolysis or incomplete esterification leading to insufficient development of the network may occur; in turn this may cause the gel to fracture before drying or on exposure to the atmosphere. Upon pouring the sol, a flat, non-vibrating surface is important where the sol may gel without disturbance, which may cause microcracking or defects in the newly formed structure. Areas that are free from dust should be used for pouring the sol. The temperature and time of gel aging is also important, and the amount of water used in which to dry them. Time,

temperature, and pH are variables that can effectively alter the aging process. Iler [46] recognized that once the gel has been formed, it can be further modified in the wet state by treatments to: (i) strengthen the structure without greatly affecting the pore structure (sometimes referred to as gel reinforcement), or (ii) enlarge the pore size and reduce the surface area by a process of dissolution and redeposition of silica thereby coarsening the gel texture.

In previous [5] work, large pore 58S Bioglass® was developed through the sol-gel route with drying at under near-equilibrium (liquid/gas) conditions. The water vapour in the near-equilibrium condition creates a pressure inside the pores of the drying gel. This counteracts the capillary pressure responsible for pore deformation which results in a larger pore network. The near-equilibrium drying method to achieve large pores is less expensive, safer and easier for production than supercritical drying without the difficulties in removing residual organics associated with surface modified gels. In addition, crack-free monolithic implants from sol-gel derived Bioglass® can also be fabricated by drying under near-equilibrium conditions.

Factors that affect the pore size of the eventual monolithic sample are summarized in Table 2.3.

Table 2.3: Factors affecting pore size of the sol-gel product

Pore size may be increased by any of several approaches [47]:

1) The formation of large particles (pore size scales with particle size)
2) Particle aggregation
3) Supercritical drying
4) Stiffening of the network by increased condensation rates or aging, causing less shrinkage upon drying
5) Double-dispersion procedures that produce hierarchical microstructures

Factors that affect homogeneity of the monoliths are listed in Table 2.4.

Table 2.4: Factors affecting the homogeneity of the product

The degree of homogeneity of a multicomponent gel is strongly influenced by various processing parameters [10]:

(1) Nature, structure, and chemical reactivities of reactants

(2) Nature of solvents and solubility of reactants in solvents.

(3) Concentration of water and sequence of addition

(4) pH of the reaction medium

(5) Time and temperature of reactants

2.7 Thermal treatments and densification studies

There are at least four mechanisms responsible for the shrinkage and densification of gels [48]:

1) Capillary contraction;

2) Condensation;

3) Structural relaxation;

4) Viscous sintering.

Models indicate that the temperature for the beginning of the third stage of densification is in the range 1000-1150°C for acid-catalyzed alkoxide 100% silica gels. Densification is the last treatment process for the gels; i.e., it converts the gel to a glass. Controlling the gel-glass transition is essential to retain the initial shape of the starting material. It is necessary to eliminate volatile species prior to pore closure and to eliminate density gradients due to nonuniform thermal or atmospheric gradients. The amount of water or hydroxyls in the gel is a major factor in the gel sintering because the viscosity of silica is strongly affected by the concentration of water, which in turn determines the temperature of the beginning of densification. Gels have higher free energy than glasses mainly because of their very high specific surface area and unsatisfied bonds on the surface.

During sintering, the driving force is a reduction in surface area of the gel. There is an important topological consequence of this process of densification; i.e., the pore network remains interconnected up to nearly full density, as shown by Vasconcelos [8]. In his work, the two types of gels used contain a very large number (10^{19}) of interconnecting branches per cc of material. However, a small

pore, acid catalysed gel has nearly an order of magnitude more branches than a base catalysed gel. The topological differences of the gel networks affect their densification behaviour. However, the interconnectivity of the pore network of the gel with larger pores remains stable to much higher temperatures. This large difference is related to the character of the porosity, the 12Å pores are 'ink bottle' shaped whereas the larger pores are cylindrical. Therefore, the cross-section of the cylindrical pores uniformly decrease as densification occurs, gradually decreasing the mean pore radii without 'cutting off' the branches.

2.8 Why are thermal treatments important?

Stabilisation

Surface hydroxyl groups are sites where physical adsorption of water (and other polar molecules) occurs. On a completely hydroxylated surface of silica (4.9 OH/mm^2) H_2O will cover the first accessible OH sites forming a multiple hydrogen bonded layer. In general, OH groups are gradually lost with increasing temperature, but at 800°C where the extent of viscous sintering (pure silica system) may be substantial, the OH coverage is still about 1 OH/nm^2. The sequence of surface dehydration is the initial removal of physically adsorbed water at low temperatures followed by the progressive removal of weakly hydrogen bonded hydroxyls, strongly bonded hydroxyls, and finally isolated hydroxyls. For multicomponent systems, heat treatment procedures are more difficult due to lower sintering temperatures and thus rapid sintering can start at 500°C, (for a multicomponent borosilicate xerogel (wt%: - 83 SiO_2, 15 B_2O_3, 1.2 Na_2O, 0.8 Al_2O_3) system studied by Gallo et al. [49]).

Altering the surface character with respect to physisorption, condensation reactions take place that involve neighbouring surface OH groups to produce a distribution of cyclic species (rings) on the dehydroxylated surface. Thus, both physical and chemical adsorption processes are affected by the extent of surface dehydroxylation. In small pore gels, it is hard to remove excess H_2O and residual organics before pore closure. Hydroxyls are usually removed in a two-step process and thermal processing removes molecular H_2O and most of the silanol groups.
The final OH must be chemically reacted with chlorine (or fluorine) at elevated temperatures. Chlorine is the most commonly used reactant. It requires

temperatures greater than 800°C, and preferably greater than 1000°C for faster reactions. Otherwise the sintering at T > 1000°C will cause the structure to collapse and trap the H_2O and chlorine (or Cl^-), either in the pores or in the matrix. Both species could reboil at higher temperatures. Ultimately it is cleanest to use a vacuum furnace, and for larger items, DCCA's can be introduced to maintain an interconnected pore network and avoid failure during drying and stabilization [7].

Densification and Sintering

Densification is important because the mechanical properties are enhanced to the point where the glass-ceramic can be machined. The skeletal density of the structure is increased as well as the geometric density [47]. Sintering is a process of densification driven by interfacial energy. Material transport occurs in viscous flow or diffusion in such ways as to eliminate porosity and thereby reduce the solid-vapour interfacial area. In gels, the interfacial area is enormous, so the driving force is great enough to produce sintering at exceptionally low temperatures, whereas the transport processes are relatively slow due to the interconnective pore network in these materials [47]. The kinetics of densification of gels are complicated by the concurrent processes of dehydroxylation and structural relaxation. This leads to the result that faster heating permits complete densification at a lower temperature. Different theories describing the kinetics of sintering have been studied by various authors [50]. However, each compositional system must be optimized by trial and error since the theories contain too many adjustable parameters to predict sintering behaviour [50].

2.8.1 Process parameters affecting densification kinetics

The onset of crystallisation and nucleation of new crystallites within a densfiying gel structure is governed by a characteristic activation energy. The Arrhenius equation describes this activated process. Without a critical minimum value of activation energy, theoretically no crystallisation occurs in the material during crystallization.

However, if a porous gel is held at a temperature for a long period of time crystallization may occur. Enhanced vapour pressures present in humid atmospheres accelerate the densification process by interaction of water molecules

with metastable surface states (see Hench, [47] for details). Thus, better results are obtained in less time than using a dry atmosphere.

The main problems with this area lie in the quantification of the densification atmosphere used in a non-equilibrium temperature range and with the accurate measurement of humidity in the densification atmosphere in this temperature range. There are very few humidity sensors that will operate above 111°C [51]. Where possible it is desirable to reduce the temperature to a range between 22°C and 67°C. The current state of the art in humidity measurements (particularly in industrial applications) dictates that measurements in relative humidity can rarely be made to an accuracy greater than ± 3%, and measurement of the dew point temperature can seldom be made more accurate than ± 1°C [52]. These accuracy limitations apply to clean environments. Contamination levels in the environment, such as occur during stabilization of gel-glasses reduce these accuracy levels to something more like ± 5% in terms of relative humidity and ± 2°C in terms of dew point.

Densification kinetics may be affected by the type of gas in the atmosphere; i.e., pure CO, CO_2, mixtures of gases. The use of CO_2 could be adequate to test the theory of two oxygen atoms being present in the densification process; i.e., similar to the use of water as an example of enhanced vapour pressure. Being easily measurable and with a known behaviour in non-equilibrium conditions i.e.> 400°C, CO_2 was chosen to compare to densification in a dry nitrogen atmosphere. It was found in previous studies that fully dense translucent carbonate apatite could be formed only in wet carbon dioxide atmospheres [53]. Also, the authors reported that 93% dense carbonate apatite was formed after 4 hours sintering at temperatures as low as 700°C [53] when sintering carbonate apatite, which had been precipitated from solution and then dried into gels. It is also noted that few hydroxyapatites are free from carbonate since carbon dioxide is often present in physiological solutions unless precautions are taken to remove it.

CHAPTER 3 THE IMPORTANCE OF COMPOSITION FOR BIOACTIVE GEL-GLASSES

In this chapter, we discuss the importance of composition on the behaviour of bioactive (Class A) gel-glasses. In addition, the effect of soluble silica on biological systems is reviewed. The chemistry of the calcium phosphate family, its relation to hydroxyapatite and a brief review on the compositional aspects of bone is also included in this chapter.

3.1 The $CaO-P_2O_5-SiO_2$ system

The focus of this work is on the bioactive ternary system of 58S Bioglass®, e.g. $CaO-P_2O_5-SiO_2$. These bioactive gel-glasses are surface reactive glasses, and glass-ceramics that attach directly by chemical bonding to the bone [21,54,55,56] (termed bioactive fixation). Other studies have shown bioactivity in binary compositions that do not contain a phosphate [44,57-62] and compositions with additives as well as a phosphate [63,64]. However the study of soluble silica and its importance on osteoblastic activity is well known [23,24,31,38,39,40,41,65]. It is also noted that other authors have used phosphates as the focus for their investigations [66]. The following sections discuss these theories and introduce the calcium phosphate family chemistry, which is also fundamental to bioactive gel-glasses of this composition when studying possible reactions/dissolution products occurring in liquid mediums, see Chapter 7. Others authors have noted accelerated HCA layer growth with pohsphate addotions in comparison to other compositions [67-71]. With other work focusing on layer formation on compostions conatinaing other compounds such as MgO and anitbacterial drugs [72-75].

Composition remains a point of great interest when considering the synthesis of materials for biomedical bone void filling applications. The following sections deal with the importance of the constituents of the sol-gel Bioglass® recipe. In addition, current work [2] outlines the significance of the up shifting of DNA markers associated with bone growth by incorporating osteoblasts in an extract solution of 45S5 Bioglass® without any material (substrate) being present and by the presence of certain concentrations of ions in solution. In addition, the interaction of macrophages and moncytes with 45S5 and 58S Bioglass® has also been studied *in vitro* [76].

3.2 The role of silica and other like compounds in nature

3.2.1 Soluble silica in nature

Silica is constantly dissolving and precipitating over every part of the earth's surface. The sedimentary cycles have been described in complex detail by Siever [77]. Soluble silica is mainly derived from the weathering of minerals, which, in some cases results in amorphous silica residues that then dissolve. Very little soluble silica comes from sands or quartz, which is soluble to only a few parts per million; furthermore, the rate of dissolution is extremely slow. River waters range from 5 to 35ppm SiO_2, a few up to 75ppm, and by the time they reach the sea the silica concentration may range from 5 to 15ppm. Seawater varies widely, but the silica content is generally in the range from 2 to 14ppm [77]. *However, Lisitsyn and Bagdanov [78] report that the surface waters in the Pacific Ocean contain only 0.0001-0.3ppm SiO_2. Plankton converts 6 x 10^9 tons SiO_2 from soluble to suspended form each year, but this is only 0.16% of the available silica.

In addition to the silica carried into the sea by fresh water, additional soluble silica comes from the suspended colloidal silicates; clay will dissolve in seawater sufficiently to give a silica concentration of 10ppm [79]. Soluble silica is found in all plants and animals, e.g. human blood contains 1ppm. Ingested monosilicic acid as an undersaturated solution rapidly penetrates all tissues and body fluids and is excreted in the urine apparently without any effect [80]. Plants, especially grasses, including grains and rice, take up silica and deposit it in the tissues as characteristic microscopic amorphous opaline particles. The widespread occurrence and possible role of silica in living systems is more fully discussed in Section 3.2.2.

Our knowledge of life forms of the remote past is based on examination of specimens preserved as silica psuedomorphs. Best known of these is petrified wood, but of even greater importance are the fossilized microorganisms discovered by Barghoorn [81]and Schopf [82], which are as much as three billion years old. The latter were apparently coated with, then later impregnated with and enveloped in, amorphous silica, which later was converted to a very fine-grained black chert (sub microscopic quartz), which preserved the form of the filamentous algae and bacteria-like organisms. Small amounts of organic matter are still present. The most perfect replication of organic forms is by silica, which is the one mineral that is transported in solution in water and deposited in

amorphous form. All other minerals are deposited as crystals, which in most cases are larger than the detailed structure of the organism. Even after amorphous silica has crystallized into chert, the crystals are so small that even sub microscopic structures are retained, visible only by electron microscopic techniques. Table 3.1 summarises the various phases of silica found in nature.

Table 3.1: Phases of silica [83]

1. Crystalline SiO_2 (α-quartz).
2. Hydrated crystalline $SiO_2.xH_2O$.
3. Anhydrous silica of microporous anisotropic form such as fibres or sheets.
4. Anhydrous and hydrous amorphous silica of colloidally subdivided or microporous isotropic form such as sol gels, and fine powders.
5. Massive dense amorphous silica glass.

3.2.2 Silica in biology and the origin of life

Even though silicon is one of the most abundant elements, it has been considered to be nonessential in most living organisms, whereas carbon, which is far less plentiful, is the primary element upon which all life depends. However, it has been suggested that compounds of silicon originally may have played an important, perhaps necessary, part in the origin of life. As pointed out by Gamow [84], the transition between non-living and living matter may have been very gradual. Oparin [85] has postulated that life began through the association of simple, naturally occurring carbon compounds with inorganic colloids. Bernal [86] has speculated on the possible role that colloidal silicates played in catalysing the formation of complex organic molecules from simple ones. He presumes that the original atmosphere prior to the appearance of life must have consisted of simple compounds such as methane, ammonia, hydrogen sulphide, and water vapour. As shown by Miller [87], amino acids can be formed from methane, nitrogen, and water vapour under the influence of electrical discharges, so that a wide variety of organic compounds may have been present in the ancient seas. Bernal [86] suggests that a concentration of simple organic molecules might have been brought about by adsorption on colloidal clays, which have enormous surface area and an affinity for organic matter. He also points out that small molecules attached to the surface of the clay are not held at random, but are in definite positions relative not only

to the clay but to each other, and are thus held in a position so that they can interact to form more complex compounds, especially if energy is supplied in the form of light [88]. The formation of asymmetric molecules which are characteristic of compounds occurring in living organisms might have first occurred, according to Bernal, through the preferential adsorption of a pair of asymmetric molecules on the surface of quartz, which is the only common mineral possessing an asymmetric structure.

3.2.2.1 Examples of silicate based organisms: algae and diatoms

Out of thousands of types of algae, one group, the diatoms, constitute the class *Diatomaceae* or *Bacillariophyceae*, which absorb soluble silica from water even at extremely low concentrations and deposit it as an external skeleton. According to Calvert [89], there are more than 10,000 varieties of diatoms, some living in fresh water, some in salt water. Nearly all varieties are alike, in that their walls are impregnated with silica. These plants are single-celled organisms consisting of two parts with the edge of one part fitting inside the other like the two halves of a pillbox. In addition to secreting the siliceous skeleton, each cell accumulates a droplet of oil, and it is suspected that this oil, together with other hydrocarbons formed by the decomposition of the organic matter of the diatom, might have been the reason for the formation of a great part of our petroleum resources. Deposits of diatomaceous mud as large as 400 miles long and 100 miles wide have been found off the coast of Africa. The organic shales from which petroleum is obtained are believed to have been from the dead bodies of these organisms, which were deposited on the bottom of ancient oceans.

Seawater contains only 2-14ppm of SiO_2 and is far below saturation with respect to amorphous silica and part of this is suspended fragments of siliceous organisms. A certain minimum concentration of silica in solution is essential to the growth of each kind of diatom. Increasing the silica content from 3.5 to 8.3ppm doubles the rate of growth of one type of diatom of which the dry weight of the cells is 4-22% SiO_2. However, some species that contain only 0.4% SiO_2 can obtain enough silica for growth from ordinary glassware. When silicon becomes depleted, cells become coated with a gelatinous capsule of polyuronide of glucuronic residues.

3.3 The importance of phosphorous and its compounds

In the phosphate minerals, there are at least 17 series of crystalline solid solutions in which a considerable composition range is covered, and there are a large number of additional cases in which limited substitution is found. All of the known phosphate minerals are orthophosphates [90].

Because of its complicated crystallographic structure [unit cell: $Ca_{10}(PO_4)_6(F,Cl,OH)_2$], the apatites can serve as a host for a number of minor substitutions. In francolite, as well as in other apatites, VO_4, AsO_4, SiO_4, and SO_4 can replace equivalent small amounts of PO_4. Likewise, minor amounts of Mg, Mn, Sr, Pb, Na, V, Ce, Y, and other elements are found to substitute for calcium in the crystal structure. Naturally, the electrical charge of the over-all crystal will be kept neutral by the balancing of electron losses or gains due to cationic substitution by opposite gains or losses due to anionic substitution. The effect enhances the number of ionic substitutions that can occur. The large number of minor elements found in apatite deposits plays an important role in supplying trace elements to soils treated with mineral fertilizers.

The most likely process of apatite formation in this scenario appears to be the phosphatisation of aragonite pellets. Such pellets of calcium carbonate constantly build up by accretion as they are rolled along the ocean floor by currents. Upon growing to a size where the current would no longer move them, the pellets became stationary and undergo a relatively slow phosphatisation due to the action of the apatite-saturated water coming from the depths below which plant life cannot exist. The aragonite form of calcium carbonate is much more easily phosphatised than is the calcite form.

3.3.1 Phosphates in life processes

Phosphorous, a universal constituent of protoplasm, is required for growth, health, and reproduction in all forms of plants and animals. Other less important chemical actions of the phosphates in biology are pH buffering, formation of soluble complexes with cations, and precipitation of orthophosphate ions with calcium to give a highly insoluble hydroxylapatite, which forms the basis of bones. The physical role of the phosphates is exemplified in the "lock and key" concept of biology where the phosphate groupings afford negatively charged sites on complicated molecular structures. Moreover, the

polyphosphates give a highly localised concentration of negative charge thereby greatly increasing the ionic strength within a volume of molecular dimensions. Related to these two ideas is the strong interaction between positively charged substances of high molecular weight and/or high charge (e.g. the proteins) with the polyphosphate anions.

Following Liebeg's work, which introduced a period in which emphasis was put on the need for phosphorous in plant and animal nutrition [90], Pasteur and his followers [91] focused attention to the relationship between yeast multiplication and fermentation, processes which subsequently have been shown to involve phosphates. With vertebrates, the concentration of phosphorous is about 100 times higher in the skeleton and teeth than in soft tissues; whereas the concentration in soft tissues varies no more than two or threefold amongst the different organs. An important factor underlying the dominant role of the phosphates in controlling biochemical reactions is the extremely slow scission of P-O-P linkages in the absence of enzymes, as compared to a rapid rate in their presence [90].

Evidence of alkaline deficient hydroxyapatite (ADHAp) in humans is found in mineralised tissues. Mineralised tissue is found in animal life from the basic protozoans to the highly developed vertebrates. In the lower forms of animals the mineral phase is usually calcium carbonate in the form of calcite and/or aragonite. However, there are cases of phosphatic mineral tissue in lower animals. Even in the predominantly carbonaceous mineral tissue there is often, if not always, a trace of calcium phosphate. Similarly, phosphatic mineral tissue always contains a trace of calcium carbonate. The exact crystal-chemical nature of the carbonate in a predominantly phosphatic mineral matrix is not completely understood. Whether the carbonate is substituted for the phosphate, forming a so-called carbonate apatite, or just admixed physically as a separate phase is not known at this stage.

In the development of bone, collagen is laid down before the mineral matter. The exact chemical or physical relationship between the mineral and the collagen is not yet fully understood. The collagen fibres act as a latticework which is filled in by the bone mineral, the ground substance and the reticulin fibres. In addition, there is the interstitial fluid, which connects the solid substance in the bone with the blood system in the animal.

3.4 Phosphates, calcium and biomaterials

The inorganic fraction is predominant in the tooth (dentin 75% and enamel 96%). The main constituents, Ca and PO_4 for apatite phases in which are contained various amounts of CO_3, Na, Mg and citrate and contents of K, Cl, and F. From the literature [90] a great portion of Ca^{2+} and PO_4^{3-} ions could form defective hydroxyapatite (DHAp) with $Ca_{10-x}(HPO_4)_x(PO_4)_{6-x}(OH)_{2-x}$ or interlayer of octocalciumphosphate $Ca_8(HPO_4)_2(PO_4)4.5H_2O$ (OCP) and hydroxyapatite (HAp). In all the hard tissues the impurity ions have strong preference for incorporation in different calcium phosphates. Na and CO_3 have preference for apatite structures having compositions:

$$Ca_{8.5}Na_{1.5}(PO_4)_{4.5}(CO_3)_{2.5}$$

In addition, citrate occurs in the OCP phase with following:.

$$Ca_{7.5(citrate)}(PO_4)_{4.5}H_2O$$

The various analytical data for the constituent content found in literature [90] show the possible HAp formation. In tooth enamel, the excess of carbonate ions not contained in the sodium-carboxyapatite with a small amount of Cl and F can induce the new apatite compound:

$$Ca_{10}(PO_4)_6(OH)_{1.59}(CO_3)_{0.1}(F)_{0.01}$$

Similarly, in the bone and dentin mineral a part of CO_3 not accounted for the same Na-CO_3 apatite can form the compound:

$$Ca_9(PO_4)_{4.5}(CO_3)_{1.5}(OH)_{1.5}$$

3.4.1 Calcium orthophosphates

Well known calcium orthophosphates, other than apatite, are ($CaHPO_4$) (DCP), $CaHPO_4.2H_2O$ (DCPD), $Ca_3(PO_4)_2$ (TCP) with three polymorphic forms, $Ca_8H_2(PO_4)_6.5H_2O$ (OCP) and $Ca_3(PO_4)_2.3\text{-}4.5H_2O$ so-called amorphous calcium

phosphate (ACP). The last two compounds are interesting as biological precursors during the course of HAp formation *in vitro* [90]. ACP formed is unstable in aqueous media and crystallises gradually to other orthophosphates or apatites.

3.4.2 Tricalcium phosphate

Various allotropic forms of $Ca_3(PO_4)_2$, can be obtained by the following processes:-

$\beta TCP > 950°C$ (4Gpa) = γTCP

$\beta TCP > 1120\text{-}1180°C = \alpha TCP > 1430\text{-}1470°C = \alpha'TCP$

A stoichiometric mixture of DCP or DCPD or $Ca_2P_2O_7$ with $CaCO_3$ or CaO, heated for 0.5-1 hours, allows the β form preparation, whereas a similar preparation at higher temperatures yields the α form. Octocalcium phosphate (OCP) or $Ca_8(HPO_4)_2(PO_4)_4.5H_2O$ lies as an intermediate between the apatitic and brushite structures. Thermodynamically the metastable phase of OCP is fairly stable in aqueous media and more stable in air. It precipitates when solutions of $Ca(NO_3)_2$ and Na_2HPO_4 are added to the CH_3COONa solution around neutral pH.

3.4.3 Apatites

Typical apatites are $Ca_{10}(PO_4)_6(OH)_2$ (HAp) and $Ca_{10}(PO_4)_6F_2$ (FAp). HAp easily forms solid solutions via chemical reactions with various metal oxides, halide or carbonate ions. Ca^{2+} and OH^- ions can be replaced with various cations and by halide or carbonate ions respectively. Moreover, HAp typically exhibits nonstoichiometric compositions with calcium or OH^- deficiency. HAp and FAp crystallise in the hexagonal space group P63/m. The incorporation of Cl^- ions induces the formation of chloroapatite (CAp) with the monoclinic symmetry space group P21/b.

3.4.4 Hydroxyapatite

Producing hydroxyapatite by wet methods involves precipitation from mixed aqueous solution or hydrolysis of calcium phosphate [90]. During the hydrolysis chemical synthesis with water reacts with the starting calcium phosphates such as DCPD or α-TCP. HAp powders possess a Ca/P ratio that depends on the pH, time, temperature

reaction, the nature and concentration of the starting compounds. Non stoichiometric HAp (Ca^{2+} deficiency Ca/P < 1.67) formation is mainly due to the fact that ACP is a precursor precipitate.

The following formula is mainly used for the explanation of the non-stoichiometry:

$$Ca_{10-x}(HPO_4)_x(PO_4)_{6-x}(OH)_{2-x}nH_2O$$

With $0 < x < 1$ and $0 < n < 2.5$

This compound at x = 1 is called defective hydroxyapatite (DHAp)
Numerous works have demonstrated that the combination Na^+ - CO_3^{2-} ions interfere with calcium phosphate. Na^+ and CO_3 ions are incorporated in the apatite structure from the solid state reaction with the composition formula:

$$Ca_{10-x}Na_x(PO_4)_{6-x}(CO_3)_{1+x}$$

Where $0 < \text{or} = x < \text{or} = 1.5$
For x +1.5, 40% of carbonate ions are in the OH positions.

3.5 Replicating bone and its' properties

Bone has at least six functions in the body: 1) support, (2) locomotion, (3) protection of various organs, (4) storage of chemicals, (5) nourishment, and (6) sound transmission (in the middle ear and cranium) and in some animals bone is also involved in reproduction [92]. The support function of the bone is most obvious in the skeleton. The body's muscles are attached to the bones through tendons and ligaments and the system of bones plus muscles supports the body.

Bone acts as a chemical "bank" for storing elements for future use by the body. The body can withdraw these chemicals as needed. For example a minimum level of calcium is needed in the blood; if the level falls too low, a "calcium sensor" causes the parathyroid glands to release more parathormone into the blood, and this causes the bones to release the needed calcium [92]. A good blood supply is essential for the cells, which make up 2% of the volume of bone. By observing the living model we realise

that implant materials will have limited use unless they can be vascularised and implanted with access to bone mineral, proteins and cells, so that the correct stimulus for healing to occur.

Since bone is a living tissue it undergoes changes throughout life. A continuous process of destroying old bone and building new bone, called bone remodelling, is done by specialized bone cells. Osteoclasts destroy the bone, and osteoblasts build it. Primary human osteoblasts are used for the cell culture studies in this work, (see Chapter 8). Compared to many body processes, bone remodelling is slow work. We have the equivalent of a new skeleton about every seven years: each day the osteoclasts destroy bone containing about 0.5g of calcium (the bones have about 1000g of calcium), and the osteoblasts build new bone using about the same amount of calcium [92]. While the body is young and growing the osteoblasts do more than the osteoclasts, but after the age of 35-40 the activity of the osteoclasts is greater than that of the osteoblasts, resulting in the gradual decrease in bone mass that continues until death. As in other aspects of life, destruction is easier than construction. One osteoclast can destroy bone 100 times faster than one osteoblast can build it. This decrease is faster for women due to hormone-related osteoporosis and can result in spontaneous fractures, especially of the spine and the hips. Mass decreases slowly, 1 to 2% per year. Table 3.2 summarises the composition of compact bone.

Table 3.2: Composition of Compact Bone [92]

Element	Compact bone, femur (%)
H	3.4
C	15.5
N	4.0
O	44.0
Mg	0.2
P	10.2
S	0.3
Ca	22.2
Misc.	0.2

Bone mineral is made up of calcium hydroxyapatite – $Ca_{10}(PO_4)_6(OH)_2$. As discussed previously, similar crystals exist in nature: fluoroapatite, a common rock, differs from calcium hydroxyapatite in that fluorine takes the place of the OH. Fluorine in drinking water prevents caries in teeth, by turning microscopic areas of the teeth into fluoroapatite, which is more stable than bone and tooth mineral. Studies using X-ray scattering have shown that the bone mineral crystals are rod shaped with diameters of 20-70Å and lengths from 50-100Å. Because of the small size of the crystals, bone mineral has a very large surface area. Around each crystal is a layer of water containing in solution many essential chemicals. The large surface area exposed by the bone mineral crystal permits bone to interact rapidly with chemicals in the blood and other body fluids.

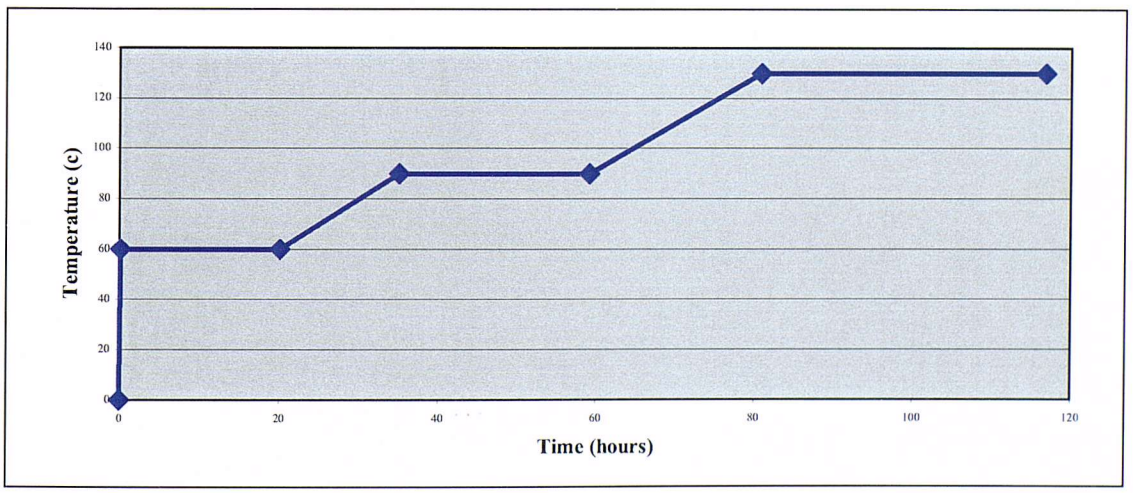
CHAPTER 4 PROCESSING OF THE HIERARCHICAL MATERIALS

In this chapter we discuss the main issues surrounding the development of a porous sol-gel Bioglass® for use, primarily, as resorbable scaffolds for tissue engineering of bone and hard tissues. Comparisons between the sol-gel derived product and the melt-derived product are made. Other processing anomalies, factors and observations are noted.

4.1 Processing of Sol-gel Monoliths

The US Biomaterials recipe obatined was used for batch production of 58S Bioglass®. This involved the mixing of the main ingredients in a glass beaker at room temperature. Firstly HCl was combined with water and then TEOS was added, after which the other ingredients of TEP and $CaNO_3$ were then added. A magnetic stirrer was placed in the beaker throughout to maintain adequate mixing in the solution. Polyethylene (PE) jars were initially proposed for moulding of the 58S gels. However, it was found that Teflon (PTFE) pots yielded the best monoliths and these pots could also withstand the temperatures required for the drying process. After many different methods of drying were tried (as the regime received from US Biomaterials had proven unsuccessful for producing monoliths) over a period of several months (various techniques including microwave/pressure cooking and various humid atmospheres were tried) the first stabilized monoliths were produced by the following method. Figure 4.1 summarises the drying programme developed in this study. As described below this schedule yields a large percentage of dried 58S monoliths.

Figure 4.1: Drying programme for 58S monolith batch preparation



A drying regime was developed which employed more incremental temperature rises over long periods using the same temperature profile as given by US Biomaterials and incorporated 250ml of D.I. H_2O during drying.

Evolution of gels and their physical / optical properties is explained more extensively in the work of Kevin Powers [93] along with further detail on the inorganic chemical reactions taking place during the sol-gel process involved when synthesizing monolithic gels for optical applications. There are also data on other compositions such as Vycor®. Pressure-cooking the samples was tried but produced transparent monoliths, which were not fully dried and tended to fracture during the stabilization process. Quantifying the amount of water released over time was also difficult with a standard domestic pressure cooker so was not further used.

Once monolith production had been achieved, stabilization was initially performed at 400°C for 24hrs and then raised to 800°C. Dissolution results (see Chapter 5) proved that these samples gave the most controlled dissolution profiles. Samples were partially densified after stabilization at 800°C for 24hrs. A shrinkage rate of 50%, by volume, was observed for all samples. This must be taken in to account when tailoring monoliths for a specific purpose. Large discs of average diameter 3.93cm and height of 3.83mm were produced by drying within the PE pots. The gels were then transferred to a watch glass, on top of a glass cylinder, within a large screw top PTFE jar containing 250ml of deionised H_2O. All PTFE drying jars had a pin hole in the top of the lid to release excess vapour pressure in a controlled manner, as vapour pressure released too quickly was responsible for gels cracking prematurely.

After the first cell culture study it was found that samples dried on the watch glass produced two different surface topologies. Cell morphology was different on these two surfaces, one which was face down on the watch glass and the other which had been exposed to the atmosphere. At this point a drying rack made of pure silica glass (to avoid contamination of species such as Na^+ ions, activated at elevated temperatures) was made to produce evenly dried monoliths and in greater numbers per time. After this, up to 52 discs could be produced in two large PTFE jars (25 monoliths per rack). However, it was also observed that gels would stick to the bottom of the PTFE jars after several uses and recovering these gels then induced cracking before drying. Care was taken after

this to seal the jars with film after pouring so that pore liquor would remain in the pots making liberation of the gels easier after the gelation and aging cycles had finished.

From initial results of thermal treatment experiments with powders it was found that nitrate liberation created colour changes in the samples at different temperatures if the powder was exposed for only 10 minutes. The sample powder would go through a transition of yellow to a slightly brown appearance in colour in the temperature range of 300-500°C (when the nitrates in the structure evolved during heating). After stabilization, monoliths would return to their transparent or opaque nature. For this system there seems to be a critical value for thickness of the sample which dictates its transparency or opacity. However, no difference in phase or crystallinity has been found between the two states. The opaque nature of the monoliths can also be explained by Rayleigh light scattering affects, when light is scattered within the structure by small pores and other anomalies in the material. This phenomenon is discussed in more detail in section 6.8.2. 58S discs which were produced as monoliths with a diameter of 1.5cm and a thickness/height of 2mm remained transparent as did small rods 1cm x 2mmOD. Figures 4.2a–f show the various products made in the lab along with cracked monoliths. Batches of 58S were also made using HF additions in order to decrease gelation rates and also to observe whether this recipe could produce a more biocompatible product in comparison to the original recipe. Optical properties are further discussed in Chapter 6.

4.2 Comparison of the sol-gel product with melt-derived product

With the recognition that the silica gel layer plays a major role in hydroxycarbonate apatite (HCA) formation on the bioactive glasses, sol-gel bioactivity has been studied extensively *in-vitro* [54]. Due to the porous structure and high surface area, the rate of HCA formation on the gel glasses with respect to time has been shown to be more rapid than in melt-derived glasses.

For the compositions studied [56], the calcium concentration in Tris buffer solutions reaches a value approximately 6 times higher than for the corresponding melt-derived compositions. Also, the texture produced by sol-gel processing results in a porous gel structure even with reduced ion exchange and dissolution rates as the SiO_2 content increases.

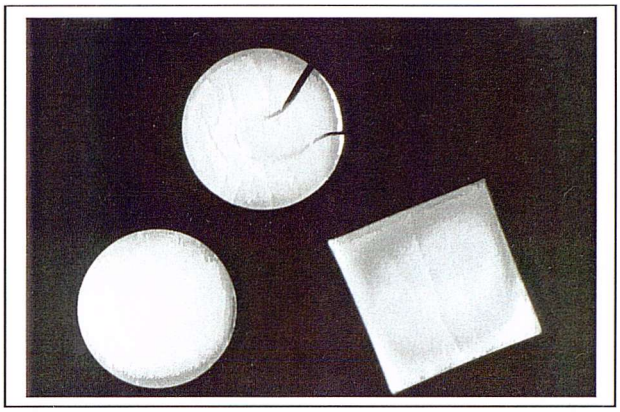


Figure 4.2a : 58S monoliths with HF addition, examples of cracked monoliths also shown.

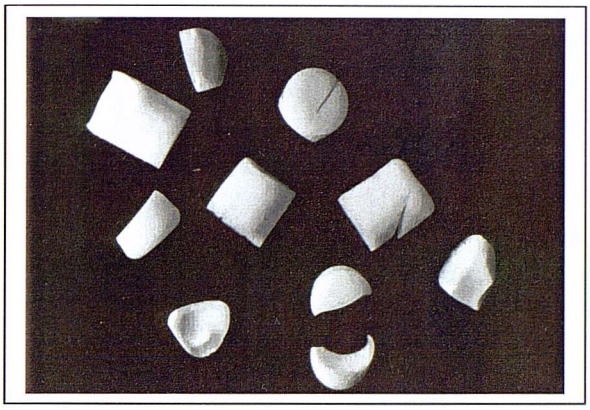


Figure 4.2b: 58S monoliths made from cylindrical molds, examples of cracked monoliths also shown.

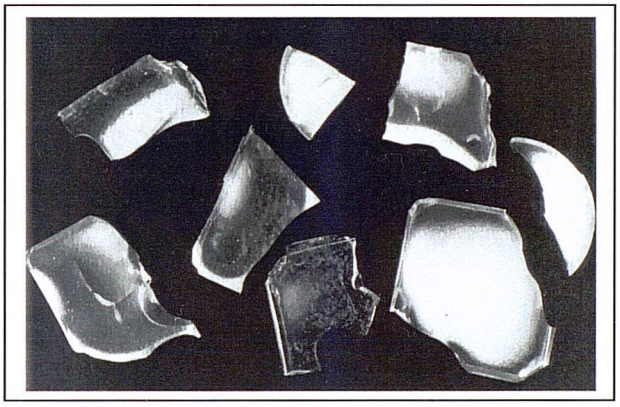


Figure 4.2c: Examples of transparent and opaque sections from cracked 58S monoliths cast from square molds with no HF addition.

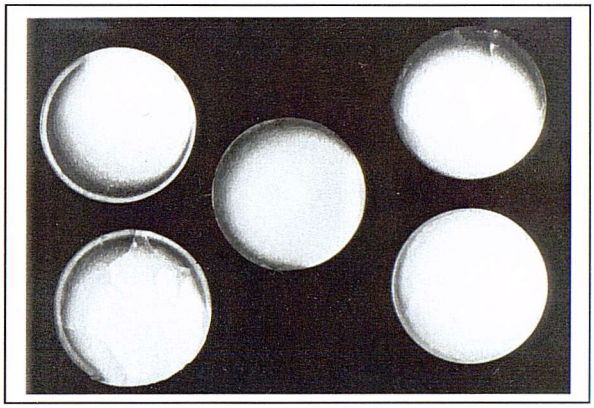


Figure 4.2d: 58S Bioglass® monoliths showing both opaque and transparent natures. Some monoliths have surface cracks. Discs are 1.5cmD and 0.5cmH.

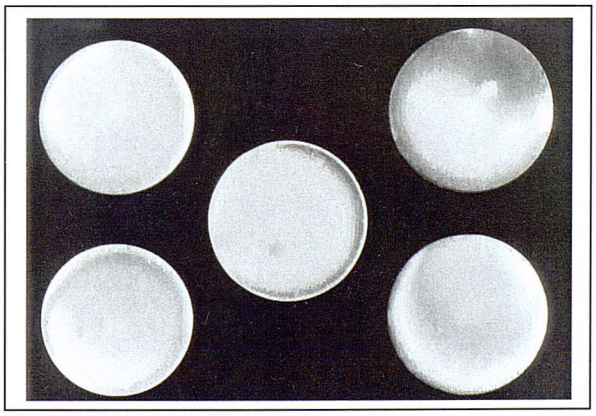


Figure 4.2e: 58S Bioglass® discs with HF addition – Inhomogeneity is clearly visible in top right hand side disc by blotchy appearance.

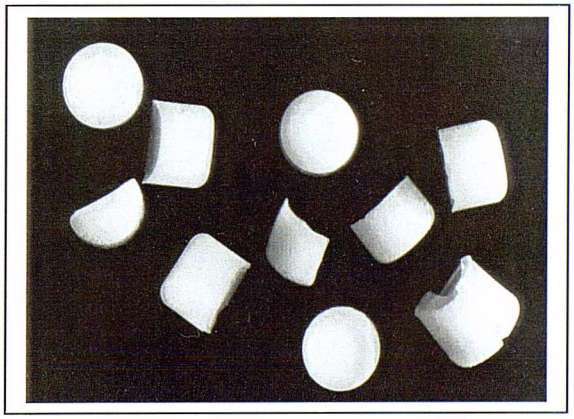


Figure 4.2f: 58S Bioglass® cylinders with HF addition and made with different aspect ratios. Total opacicity is observed. Cylinders are 0.5<cm<1cm in height and 0.5cm in diameter.

These two factors are responsible for the high rate of HCA formation and for the extension of the compositional bioactivity range in the sol-gel derived bioactive glasses.

4.3 Structural evolution of the sol

As discussed previously, the gel texture is created in the first three steps of the process (1) mixing, (2) casting and (3) gelation. However, it is postulated that pore size could be altered in the drying and heat treatments afterwards. A feature attributed to sol-gel processing of multicomponent materials is the high degree of homogeneity on a molecular scale. When precursors are alkoxides, homogeneity can be reached only if hydrolysis and polycondensation reactions occur in a synchronized manner.

In this work, inhomogeneity was avoided by pre-hydrolysing the TEOS well before adding other ingredients to make the sol. In previous studies, synthesis of phosphate containing glasses by sol-gel processing yielded phosphorous losses during drying and sintering in excess of 50% of the nominal content [94]. The basic initial structure is said to follow an agglomerative pattern like balls sticking together to make chains and circles rather than lines (due to acid catalytic effects – agglomeration is preferential to linear structures).

Another process, called 'coarsening' or 'Ostwald ripening', is due to selective dissolution and precipitation with the gel network. As shown earlier by Iler [95], convex surfaces are more soluble than concave surfaces. Thus, if a gel is immersed in a liquid in which it is soluble, dissolved material will tend to precipitate in regions of negative curvature. Necks between particles will grow and small pores may be filled, resulting in an increase in the average pore size of the gel and decrease in specific surface area.

4.3.1 Solvent quality effects in sol-gel processing

Previous authors [96] concluded that a usual result is that the polymer molecular weight is found to be higher in good solvents than in poor solvents. The solvent quality affected the properties of thin films and bulk gels. For the films, the influence of solvent quality could not be decoupled from the influence of molecular weight, whereas for bulk gels, the correlation between solvent quality and gel properties corresponds with the idea that a good solvent expanded, giving interpenetrating aggregation and thus dense films and

microporous gels. A poor solvent collapsed and had non-interpenetrating aggregation, giving porous films and macroporous gels.

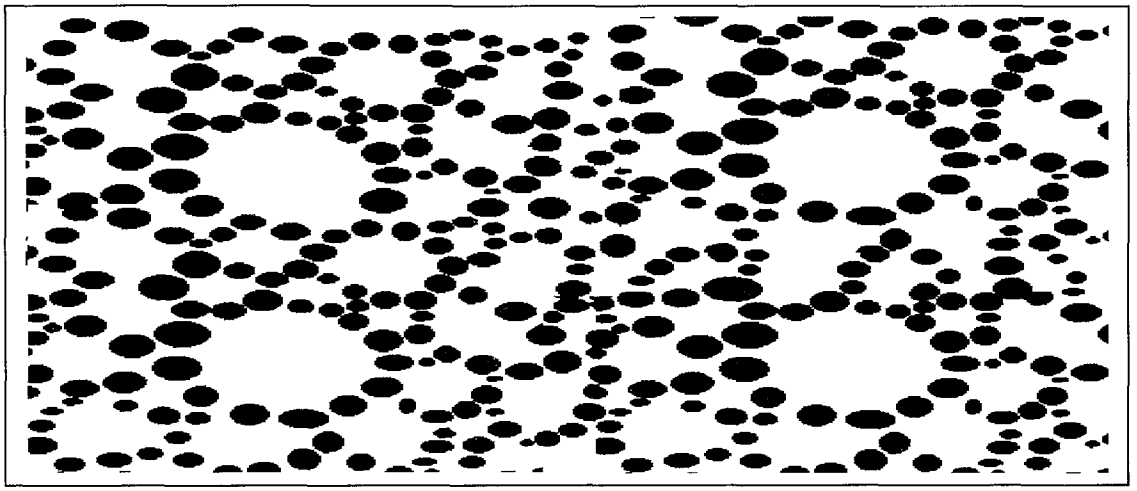


Figure 4.3: Cluster formation of gel ultrastructure with spherical groupings giving rise to pore families preferentially formed in acid catalysis of TEOS [97].

No attempt was made to modify reagents in this work. However, it is noted that solvent quality is another way in which the sol-gel chemist can tailor material properties. In the initial stages of the mixing water to TEOS ratio (R ratio) is of critical importance to the stability of the monolith. Authors who studied the initial stages of hydrolysis of TEOS report that [98] the amount of water added to the solution determines not only the extent of the hydrolysis reactions, but also the combination of oligomeric species, which form in solution. They observed different hydrolysis/condensation behaviours depending upon the amount of water added to the solutions, with the higher water to TEOS ratios leading to enhanced concentrations of a compound whose Raman spectrum is similar to that of cyclotrisiloxanes. Changes in catalyst concentration and solution temperature changed the rate of the reactions, but did not seem to alter the reaction products. It was not clear from these results what the effect of the rate of addition of water fraction has on the reaction. In this work ingredients were titrated into the sol mixture and the water ratio was fixed by the recipe received from US Biomaterials which is as follows: (for 120ml batch) 44.93ml D.I. H_2O, 7.47ml HCL (2N), 61.35ml TEOS (mix for 30 minutes), 6.26ml TEP (mix for 20 minutes), 38.99g $CaNO_3$ (mix for 60 minutes) at room temperature.

4.3.2 Pore size and texture modification

The change in pore morphology, size and surface texture for two different porous silica xerogels as a function of silylation has been examined [99]. The pore size distribution could be considerably narrowed and the mean pore size typically reduced by a dimension comparable to the R group diameter (4-6Å). They also concluded that silylation appears selectively to modify the large pores in the size distribution. This is possibly a result of less steric hindrance to silylation reactions in larger pores. Silylation also smoothes the surface of the pores and may be used as a probe of the surface fractal dimension.

In this work two batches of 58S were made including an HF catalyst for the purpose of decreasing gelation time and modifying pore diameter. It was found that this addition altered the surface charge (seen in the results of C coefficients obtained during nitrogen analysis) and this recipe was also used to compare with the originial recipe with respect to being able to create a more bioactive surface for later studies. Results of these batches are included in Chapter 5, 6 and 7. In addition, a study involving different aging programmes was also used to understand whether this could modify pore diameters or composition of the gel-glasses. Results for this study are included in Chapter 6.

4.3.3 Drying

Both particulate and alkoxide derived silica gels have been studied in depth, and both types have their respective advantages and disadvantages for the production of high quality glass. A considerable amount of research in the field of sol-gel science has been devoted to the drying and sintering of large silica monoliths [45] and many additives have been tested in the process.

However, during this project, care was taken to avoid the use of expensive additives to limit the potential for contamination of the eventual biomaterial, as well as for economic reasons. This increased the difficulty of producing crack-free monoliths. Indeed, most of the research reviewed here seems to support the fact that alkoxide gels are difficult to dry rapidly without fracture. However, after much patience monoliths were obtained in various geometries, see Figures 4.2a-f.

Wang et al. [48] showed that drying started not from the gel surface but in the bulk through the formation of drying pockets. It appears that initiation (or nucleation) of drying from the inside prevented the stresses from extending through the entire characteristic gel thickness. Contrary to the conventional wisdom, the small pore size gels (<40Å) were easier to dry than the larger pore size gels. These experimental results were subsequently explained by a theory of cavitation [48]. Also precaution was taken to keep ingredients in the sol mixture simple as the gels may crack during the removal of organic residues at 200-500°C, due to heat generation and/or vapour expansion if pore size is small (<40Å). In this study use of an acid catalyst (HCl) remained unchanged from the parent recipe. In addition, results were obtained from 58S gel-glass monoliths using an HF catalyst addition, previously not studied for its bioactive properties. Chapter 8 describes the results.

Hydroxyl groups as well as excess nitrates can effectively be removed only above 500°C. At such temperatures, appreciable shrinkage and pore closure may occur, trapping impurities in the glass. Monoliths produced in this work were stable enough after drying that the temperature gradient did not need to be quite so carefully controlled. By comparison, removal of impurities from the large pore size particulate gels did not prove difficult in this work. However, the large pores also cause their consolidation temperature to be higher than 1400°C. Crystallization, warping and/or sagging of the sintered glass are often encountered at such temperatures. The rate of drying through the opaque stage was the critical kinetics factor in preventing crack initiation. After the opaque stage, caused by optical scattering of a diffuse drying front of free water, the rate of removal of the remaining bound water layer can be rapid and will not lead to fracture. Combining the drying analysis of Wilson [100] and the pore analysis of Wallace [101] yields a schematic of the changes in gel surface due to drying. Fully dried gels from the 58S system studied in this work were both transparent and opaque after stabilization depending on their thermal history.

The surface area of the wet gel is initially largely free water separated by a relatively small areal fraction of silica gel network with a transition zone of bound water. As the free water evaporates, the solid network is drawn together by the capillary stresses, which decreases the areal fraction of free water and increases the areal fraction of solid.

Shortly after entering the second stage [102], the silica gel monoliths turn opaque starting at the edges and progresses linearly toward the centre. Shaw [103] suggests that this type of drying phenomenon is caused by light scattering from isolated pores (or groups of pores) in the process of emptying of such a dimension that they are able to scatter light.

Gels in this work regained transparency after liberation of water that was adsorbed when samples were left undessicated for periods. This study shows a connection between critical thicknesses, position on monolith drying rack and water content due to exposure to the atmosphere with respect to the samples' transparent nature. It was found that samples left out in air were so hydrophilic that they turned opaque with time of exposure. The opaque nature of the samples is likely to be due to Rayleigh light scattering from the pores.

If a gel cracks before entering the drying process it was not properly hydrolysed after aging. Either complete hydrolysis must be achieved to combat this or prolonged aging must be employed otherwise gels will fail to stabilize and end up as the initial large granules of powder products. We found that most gels failed in drying due to uncontrolled rises of temperature at the critical points where organic species in the gel evolved (in particular nitrates evolving from the $CaNO_3$ addition to the sol as the calcium component in the glass).

Bubbles, precipitates and dirt particles are defects that can be introduced during gel processing and magnify local strain concentrations [104]. Bubbles generated from the mixing step can be retained within the gel. During drying, the bubbles serve to concentrate drying stresses and induce a strong stress field, which can nucleate one or more cracks. We did not try to eliminate all bubbles by vacuum treatment in this work.

4.3.4 Stabilization

A critical step in the processing of sol-gel material Type V (full theoretical density) or Type VI (porous) gel-silica components is the stabilization of the porous silica network. Both thermal and chemical stabilization is necessary for the material to be used as a Type VI porous matrix in an ambient environment or used for impregnation with an

optically active (or living organisms in the biomaterial case) as an active second phase [105]. Only chemical stabilization is necessary prior to heating the gel to produce a full density glass (Type V gel-silica). The reason for the stabilisation treatment is the very large concentration of silanols on the surface of the pores of these large surface area (>200m^2/g) materials and presence of strained trisiloxane and disiloxane rings to the gel surface.

The mechanisms of thermal and chemical stabilization are interrelated because of the extreme effects that the surface silanols and chemisorbed water have on structural changes. Full densification of the silica gels, i.e. transforming them to glass, is nearly impossible without the dehydration of the surface prior to pore closure. Dehydration is completely reversible up to about 400°C. Above 400°C, the dehydration process is irreversible because of the loss of surface silanols and shrinkage, and sintering occurs. Thus, the amount of hydroxyl groups on the surface is an inverse function of the temperature of densification. Viscosity is controlled by the water present, which is directly related to the pore size and surface of the gel. Viscous flow occurs above 850°C with the exact temperature depending on the pore size of a specific gel. The isolated hydroxyl groups on the gel surface react with each other bringing particles together, thereby eliminating voids within the gel. If surface water is unable to be desorbed prior to pore closure, it is trapped inside the densified gel.

4.3.5 Densification

Densification is the last treatment process for the gels, converting the gel to a glass. Controlling the gel-glass transition is essential to retain the initial shape of the starting material. It is necessary to eliminate volatile species prior to closure and to eliminate density gradients due to nonuniform thermal or atmospheric gradient [106].

.

For alkoxide-derived silica, with control of the kinetics and ultrastructure, optically transparent pure Type VI silica can be produced with a large fraction of porosity [107]. For densification temperatures greater than 800°C, porous gel silica has an interconnected porosity of 15-35%. The small mean pore radius of 1-10nm leads to only a low degree of Rayleigh light scatter, giving the gels an opalescent appearance. During densification, the number of interconnected pores decreases as the temperature is

increased but the mean diameter of the interconnected pores does not change significantly. Over the range of 600-900°C in previous work [107] porous silica gel samples showed property changes over the ranges summarised in Table 4.1.

Table 4.1: Previous results [108] on the properties of porous silica (Type VI) gel-glasses

Total pore volume	from 0.4 to 0.2 cm^3/g
Specific surface area	from 620 to 290 m^2/g
Bulk density	from 1.3 to 1.5 g/cm^3

The above bulk density and total pore volume results are similar to those obtained from 58S, (see Chapters 5 and 6) and in King's work [108] it was also found that the glass showed several forms of light scatter from different scale ranges of inhomogeneity. There was evidence also for ultrastructure on the nanometer, micrometer and millimetre scale, but it was probable that there was a continuous distribution of structural scales leading to a multiple set of scattering and optical loss mechanisms.

The amount of water or hydroxyls in the gel is a major factor in the gel sintering because the viscosity of silica is strongly affected by the concentration of water, which in turn determines the temperature of the beginning of densification. A gel prepared in acidic conditions has a higher surface area and water content than a gel prepared in basic conditions and starts to densify about 200°C sooner than a base catalysed gel, as shown by Nogami and Moriya [109].

The presence of water or hydroxyls in the gel or in the sintering atmosphere acts to accelerate the elimination of surface area by hydrolysis of the silica (3-membered ring). Studies by Wang [110], showed the effect of ambient atmosphere on the densification of TMOS derived silica gel monoliths. In ambient air, the silica gels with 12Å pores densified to nearly 2.2 g/cc, the same as fused silica, at only 860°C. In contrast, samples densified in the CCl_4 environment required 1150°C sintering temperature. This difference shows that hydroxyl groups significantly decrease the sintering temperature by one or more mechanisms.

Araujo, et al. [107] also used dilatometry to show that densification of silica gels with large pore radii (30Å) requires a higher temperature of 1050°C to reach full density in

ambient air, as compared with 860°C for Wang's 12Å gels [111]. Heating the 30Å gels in a dry atmosphere of He or O_2 increased the sintering temperature required for full density to approximatey1200°C. Thus, the effect of water on densification is greater for smaller pore gels because of the larger concentration of silanols, strained surface defects, and larger surface area for the chemically enhanced depolymerization reactions. The initial sintering, modelled by constant heating rate experiments, was found to occur with an apparent activation energy of approximately 65kcal/mol associated with viscous flow and dehydroxylation [107].

There is an important topological consequence of this process of densification; i.e., the pore network remains interconnected up to nearly full density, as shown by Vasconcelos [105]. Both types of gels contain very large number (10^{19}) of interconnecting branches per cc of material, however, the small pore, acid catalysed gel has nearly an order of magnitude more branches than the base catalysed gel. As mentioned earlier, the topological difference of the gel networks affects their densification behaviour. However, the interconnectivity of the pore network of the gel with larger pores remains stable to much higher temperatures. This large difference is related to the character of the porosity, the 12Å pores are inkbottle shaped whereas the larger pores are cylindrical. Therefore, the cross-section of the cylindrical pores uniformly decrease as densification occurs, gradually decreasing the mean pore radii without 'cutting off' the branches.

4.3.6 Choices of media for densification studies

CO_2 gas was chosen in preference to water for the high temperature densification studies for the 58S Bioglass® sol-gel monoliths. This was primarily because water is not in equilibrium for this set of experiments and therefore the effects of amounts of water in the system could not accurately be quantified.

4.4 The structure of the gel-glass

The final sol-gel 58S Bioglass® product is a glass with a uniform distribution of the silica rich network and the modifying orthophosphate phase.

During the heat treatment of the gel to form a glass it may be converted to a microcrystalline structure. Crystallisation involves nucleation and crystal growth and these determine the final microstructure and therefore the mechanical properties of the glass-ceramic [112]. Crystal nuclei are formed by nucleation and this is then followed by the growth of the crystal nuclei and growth of one or more crystalline phases on the nuclei. Nuclei are uniformly distributed through the bulk glass to give a fine microstructure. Crystallites were identified using confocal microscopy, (see Chapter 6), in the 58S800 glass along with bubbles in the structure (about 2 microns in diameter). Crystallisation may be initiated, by either of two nucleation processes, homogeneous and heterogeneous nucleation. The former occurs evenly throughout a homogeneous phase. The nuclei are of the same constitution as the crystals that grow upon them. In contrast, heterogeneous nucleation involves the formation of the nuclei of a new phase on preferred pre-existing sites. Theses sites may be free surfaces, second phase particles and other discontinuities. The nuclei can be chemically different from the deposited crystals. Heterogeneous nucleation is the more commonly observed mechanism and occurs during the crystallization of Apoceram® [112].

In general, the parent glass must usually contain suitable nucleating agents in order to initiate crystallization either by homogeneous nucleation or by initiation of crystallization on heterogeneous sites. TiO_2, ZrO_2, P_2O_5 and fluorides are typical examples of effective nucleating agents. In the case of Apoceram® an appropriate phosphate is used, as $(PO_4)^{3-}$ ions are also constituent of the desired apatite crystal phase. The literature reports wide ranges of glass compositions in which P_2O_5 is between 0.5 and 3 weight percent [112].

If nucleation occurs at a phase boundary, between the glass and the air or the surface of the vessel then crystals grow from that surface into the bulk, this is termed surface crystallisation. In bulk crystallisation once stable homogeneous nuclei have formed in the parent glass then crystallisation proceeds by the growth of the new phase. Crystal growth is dependant on 1) The rate at which the irregular glass structure can be re-arranged into the periodic lattice of the growing crystal; 2) The rate at which energy is

released in the process of phase transformation can be removed, i.e. the rate of heat flow away from the crystal-glass interface [112].

4.4.1 Role of interconnections in porous bioceramics

The interconnections in a porous biomaterial are the pathways between the pores; they favour bone ingrowth inside the gel-glass network. Pore interconnectivity is demonstrated in the 58S monoliths produced in this work by means of oil intrusion in combination with confocal microscopy, (see Chapter 6). Results of Lu et al., [113] showed that human osteoblasts can penetrate interconnections over 20μm in size, and colonise and proliferate inside macropores, but the most favourable size is over 40μm.

By use of mercury porosimetry and morphometry, White and Shores [114] show that there is a relation between pore size and the tissue elements that favour good bone ingrowth: a pore size of 10μm allows ingrowth of cells, while 15-50μm pore size assures fibrous tissue formation, and a pore size greater than 150μm favours new bone formation. However, the pore size for new bone formation is variously reported. Eggli et al., [113] in a comparative study of β-TCP and HA found that osteogenesis in the cortico-medullar site of the tibia in 50-100μm pore material is greater than in 200-400μm size pores. On the other hand, Uchida et al., [115] have noticed that osteogenesis in HA, β-TCP and calcium aluminate (CA) was greater in 210-300μm pores than in 150-210μm pores. The osteoblasts were seen only in the ring of ceramics (1.2 ± 0.2mm), and never in the centre. However, these studies have neglected the effects of interconnections that influence directly the biological fluids, especially cells and blood vessels that favour tissue nutrition and new bone formation [116].

In β-TCP, the rates of calcification and new bone formation increase significantly with time. At the same time, the size and density of interconnections in β-TCP increase with time. A correlation is observed between new bone formation and interconnection size and pore density after 12 weeks in β-TCP. Nevertheless, their results indicated that pore sizes over 50 μm allow mineralised bone formation inside the macropores of the material. Indeed, Uchina et al.[115], measured the diameter of Volkman canals inside the ceramic microradiographically, these varied between 10 and 20 μm. Vascular penetration was deeper in β-TCP than in HA because of the *in vivo* degradation of β-

TCP which increases the pore size. Interconnections act only as pathways for nutritional elements, vascularisation and cells, although pores are sites for bone tissue growth. They concluded that pore size must be larger than interconnection size. Before and after the cell culture, they noticed that not only the sizes of the interconnections but also their density are important to favour cellular penetration inside porous ceramics.

Their *in vitro* and *in vivo* investigations allowed them to say that in resorbable materials, pore and interconnection densities play a more important role than size of pores, because sizes are modified by degradation. Uchina et al. [115], demonstrated that *in vitro*, human osteoblasts can cross through interconnections, spread and proliferate inside macropores. The minimal necessary interconnection size is 20μm, but the most favourable size for cell penetration was over 40μm. In addition, it was found that *in vivo*, pore sizes of over 20μm permits only chondroid tissue formation inside macropores, and that pore sizes of over 50μm can assure mineralised bone formation.

CHAPTER 5 NITROGEN ADSORPTION OF SILICATE SURFACES

As adsorption is one of the widest used methods for analysing the surface and pore character of a material and is reasonably simple. It is based on the investigation of capillary condensation of vapours and gases. Analysis of adsorption and desorption isotherms i.e., of the dependence of the volume of adsorbed vapour on pressure allows one to obtain data on atomic characteristics of porous material structures: pore sizes; total pore volume and specific surfaces. This method is described in detail by Kiselev and Dreving [117]. Its advantageous use for investigations of porous glass is illustrated in a series of papers by Zhdanov and others [117]. A hysteresis loop in the capillary condensation region is a distinctive feature of adsorption isotherms obtained from porous bodies. The width of this loop and the shape of its desorption branch convey information on features of the adsorbent porous structure, i.e. on pore shapes, radii, non-uniform sizes, etc. One can use this method in investigating pores with effective diameters from 20 Å to 200 Å. Isotherms have been generalised into six types, however, there are no specific mathematical models to relate exact pore geometries and topology with unique features of isotherms obtained using nitrogen adsorption techniques. For other techniques used to characterize porous 58S monoliths produced in this study see Chapter 6.

In this chapter the theory of the technique, results, difficulties and limitations of nitrogen adsorption analysis are discussed. This was one of the main tools used to analyze the sol-gel product before experimental work was done by any other methods. The analyses were made using Quantachrome AS-1 and AS-6 instruments. Mercury porosimetry was used as a complementary method to analyse the porosity which exceeds the limits attainable from nitrogen adsorption data.

Because adsorption characteristics change with pore size, it is convenient to classify porosity by the terms submicro-, micro-, meso- (intermediate), and macropores. This terminology was proposed and later modified by Dubinin [93] who defined the terms as follows:

	Diameter (Å)
Micropores	10-12 to 26-28
Mesopores	30-32 to 2000-4000
Macropores	2000-4000

5.1 Particle size and packing, the nature of the silica surface and the hydroxylated surface

Since the silicon atoms on the surface of amorphous silica are not in an exactly regular geometric arrangement, it is obvious that the hydroxyl groups attached to these silicon atoms will not be exactly equidistant from each other. They are therefore not all equivalent either in their behaviour in gas adsorption or in chemical reactions. Also, in aqueous solution, monosilicic acid molecules may condense on the surface to give silicon atoms with two or even three attached hydroxyl groups. The number of hydroxyl groups per unit surface area has been a matter of much research and discussion. It was observed by Belyakova et al. [93] that the number of silanols was about the same on different types of silica. On the other hand, Dubnin, Bering, and Serpinskii reported quite diverse results [93] in the surface of different samples of amorphous silica made in different ways.

5.2 Surface area determination by gas adsorption

When a solid is exposed to a gas, the gas molecules impinging on the surface may not be elastically deflected, but may remain for a finite time. This is designated as adsorption as opposed to absorption, which refers to penetration into the solid body. The graph of the amount adsorbed (V), at constant temperature, against the adsorption pressure (P), is called the adsorption isotherm. For a gas at a pressure lower than the critical pressure, i.e. a vapor, the relative pressure $x = P/P_0$, where P_0 is the saturation vapor pressure, is preferred [118]. The amount of gas adsorbed depends upon the nature of the solid (adsorbent), and the pressure at which adsorption takes place. The amount of gas (adsorbate) adsorbed can be found by determining the increase in weight of the solid (gravimetric method) or determining the amount of gas removed from the system due to the adsorption by application of the gas laws (volumetric method).

A commonly used method of determining the specific surface of a solid is to deduce the monolayer capacity (V_m) from the isotherm. This is defined as the quantity of the adsorbate required to cover the adsorbent with a monolayer of molecules. Usually a second layer may be forming before the monolayer is complete, but V_m is deduced from the isotherm equation irrespective of this. Adsorption processes may be classified as physical or chemical, depending on the nature of the forces involved. Molecular

interaction forces cause physical adsorption, also termed Van der Waals adsorption; the formation of a physically adsorbed layer may be likened to the condensation of a vapor to form a liquid. This type of adsorption is only of importance at temperatures below the critical temperature for the gas [118]. Not only is the heat of physical adsorption of the same order of magnitude as that of liquification, but also physically adsorbed layers behave in many respects like two-dimensional liquids.

Chemical adsorption (or chemisorption) involves some degree of specific chemical interaction between adsorbate and the adsorbent. The energies of adsorption may be quite large and comparable with those of chemical bond formation. Since chemisorption involves chemical bonding, it can occur at temperatures greater than the critical temperature. This implies that chemisorption is restricted to, at most, a single surface layer. With chemisorption, adsorption is limited to specific sites, and the adsorbent molecules have limited ability to migrate around the surface. Thus, chemisorption can be used to determine the number of active sites on the surface. It is postulated in Chapter 9 that this method could also be used to define silanol sites on the surface of the material produced.

Since physical adsorption is the result of a relatively weak interaction between solids and gases, almost all the gas adsorbed can be removed by evacuation at the same temperature at which it was adsorbed. The quantity of physically adsorbed gas at a given pressure increases with decreasing temperature; consequently most adsorption measurements, for the purpose of determining surface area, are carried out at low temperatures. Chemisorbed gas may be difficult to remove merely by reducing the pressure and, when chemisorption does occur, it may be accompanied by chemical changes. Mathematical theories to describe the adsorption process must, of necessity, be based on simplified models since the shapes of the isotherms depend not only on the specific surface of the powder but also upon the pore structure.

Various boundary conditions limit each of the theories, hence a range of equations have been developed to cover the various phenomena. The equation developed by Brunauer, Emmett and Teller commonly known as the BET equation, is for multilayer adsorption, but it is based upon the Langmuir equation where adsorption is restricted to a monolayer, as the application of the Langmuir equation to gas adsorption is restricted to adsorption of micropores, where adsorption is limited to a monolayer due to pore

geometry. Langmuir adsorption isotherms are common in adsorption of solute from solution [118].

From initial experiments, the family /type of isotherm for our material (58S sol-gel Bioglass®) was defined as being a Type 4 Isotherm. A characteristic feature of Type 4 isotherms is the hysteresis loop. The desorption branch of the isotherm follows a different path to the adsorption branch, although the curve closes as the relative pressure approaches 0.4. This hysteresis is attributed to capillary cracks from which the adsorbate molecules do not desorb as readily as they adsorb, due to the vapor lowering over the concave meniscus formed by the condensed liquid in the pores. This type of isotherm is found with many mesoporous adsorbents.

5.3 Examining the sol-gel product

5.3.1 Pore Structure

Pores are invisible to the naked eye in the majority of porous media. The porous nature of a material is usually established by performing any one of a number of experiments on a sample and observing its behaviour, because porous materials behave differently from nonporous ones in a number of respects [119].

Porosity

Porosity (also called "voidage") is the fraction of the bulk volume of the porous sample that is occupied by pore or void space. Sometimes, this word is used inaccurately with a different meaning, for example in the expression "graded porosity" of a filter consisting of different layers of different grain sizes, "porosity" is not a measure of the void fraction but rather of the void size.

Types of void space

It is important to distinguish between two kinds of pore and void space, one that forms a continuous phase within the porous medium, called "interconnected" or "effective" pore space, and the other that consists of "isolated" or "non-interconnected" pores or voids dispersed over the medium. Non-interconnected void or pore space cannot contribute to

transport of matter across the porous medium, only the interconnected or effective pore space can. "Dead-end" or "blind" pores are connected only from one side. Even though these can often be penetrated, they usually contribute negligibly to transport.

5.4 Sample preparation and experimental procedure for nitrogen adsorption analysis

5.4.1 Degassing

A most important preliminary to the accurate measurement of an adsorption isotherm is the preparation of the adsorbent surface. In their usual state, all surfaces are covered with a physically adsorbed film, which must be removed or degassed before quantitative measurements can be made. As the binding energy in physical adsorption is weak van der Waal's forces, this film can be readily removed if the solid is maintained at a high temperature while under vacuum. The degree of degassing attained is dependent on three variables, pressure, temperature and time. In test and control work, the degassing conditions may be chosen empirically and maintained identically since only reproducibility is required. However, obtaining the 'cleanest' surface possible before the experimental run can improve accuracy of results. Factors such as 'statistical thickness' are implemented in the Quantachrome software governing results (along with BET and Langmuir analysis parameters) to outline a thickness in the wall of a pore that may be taken up by frozen water trapped beforehand in the pore due to insufficient degassing during sample preparation. Recommended temperatures and times for degassing vary considerably in the literature [118] and it is difficult to establish any single acceptable degassing condition for all solids.

However, Orr and Dallevalle give an empirical relationship, which they suggest is acceptable as a safe limit for ordinary degassing at pressures lower than 5×10^{-6}mm Hg.

$$T = 14.4 \times 10^{4} t^{-1.77}$$

Where t is in hours and T is in °C (applicable between 100°C and 400°C). This can only be taken as a general safe limit since others have found the necessary time to be much shorter. Holmes et al., [118] determined the surface area of zirconium oxide using

argon, nitrogen and water vapor as adsorbates. They found that the surface properties depend upon the amount of irreversibly adsorbed water, which was in excess of a monolayer. Degassing at 500°C resulted in a 20% decrease in area.

Most solid adsorbents are capable of adsorbing water vapour from the atmosphere and should therefore be dried. This is usually done by heating for 2 to 3h at a temperature between 120°C and 130°C. Some workers [118] claim that this temperature rise is sometimes not high enough to drive away vapours previously adsorbed on to the solids. If higher temperature is used, care has to be taken that the surface of the solid is not altered in any way i.e. that sintering or surface texture are not changed. However, because the 58S porous gel-glass samples had already had a stabilization history of 400 to 800°C, the optimum temperature for degassing was found to be 3 hrs at 150°C and was used for all studies. This was found by comparing previous results of various experiments involving 10 adsorption and 10 desorption points with those of a 40 adsorption/desorption and 80 adsorption/desorption points run in order to identify differences in results obtained form various degassing regimes at the beginning of the project.

Adsorbate gas used for the analysis throughout the thesis was usually nitrogen. Nitrogen and argon are the most commonly used adsorbates but any non-corrosive gas can be used without specific calibration: He, H_2, O_2, CO_2, CO, or by using a special krypton unit. Krypton analysis was attempted unsuccessfully due to gas fitting problems but is noted as another option in Chapter 9. The standard technique is the adsorption of nitrogen at liquid nitrogen temperature, evaluation being by the BET equation in the approximate relative pressure range $0.05 < x < 0.35$.

5.4.2 Network theory

There is a growing consensus of scientists [118] who consider the present approach to pore size determination to be unreliable and prefer a different approach. They consider that pore size determination from the desorption branch of the isotherm gives misleading data particularly if the hysteresis loop is broad. Network theory describes isotherms in terms of pore connectivity and pore size distribution. At the end of the adsorption, when a high relative pressure has been reached and the adsorption isotherm has formed a plateau, all the accessible pores have been filled. On reducing the

pressure, liquid will evaporate from the larger open pores but will be prevented from evaporating from equally large pores that are connected to the surface via narrower channels. Desorption more closely reflects the distribution of channels rather than the distribution of pores.

Network theory defines the resulting hysteresis between the adsorption and desorption branches of the isotherm in terms of pore connectivity. As the pressure is reduced, a liquid filled cavity cannot convert the liquid to the gas phase until the liquid in at least one of the channels to the outside has evaporated [118]. If the radii of all the channels are less than the equivalent radius of the cavity, the largest channel radius, rather than the cavity radius, which will take place at a reduced pressure, governs the emptying. Once the liquid in the channel evaporates, the liquid in the cavity can also evaporate and the cavity empties. This is what causes hysteresis; adsorbate in the small channel must evaporate before the adsorbate in the cavity can evaporate. As a result the geometry of the network determines the shape of the desorption branch of the isotherm. Adsorption provides more accurate pore size information since adsorption takes place through the porous network. This means that even though small cavities fill first they do not block off what is happening in the internal big cavities. Adsorption is a continuous process where the adsorbate molecules continue to be transferred to the interior with no resistance.

5.5 Instruments used

Quantachrome Monosorb (AS-1)

This is a fully automated, single point instrument operating in the surface area range 0.1 to 250m^2 with the measurement time of around 6 minutes and reproducibility better than 0.5%. Its autocalibrate feature eliminates the need for calibrating each sample. Degassing is carried out in an in-built degassing station. The AS-1 also has micropore analysis capabilities.

Quantachrome Quantasorb (AS-6) multiport

A variety of gases can be used as adsorbates in this manual multipoint instrument. For rapid operation, pre-mixed gases can be used. If many data points are required a linear

mass flow meter is available to dial in the flow rates of the adsorbate and the carrier gas. The area under the desorption peak is determined automatically using a built-in digital integrator.

5.6 Nitrogen Adsorption for Surface Area and Porosity Determination

The BET method is used to find a value for the surface area of our materials as follows.

5.6.1 Surface area – The BET method [93]

This is the most widely used procedure for the determination of surface areas of a solid. It is based on the equation: -

$$\frac{1}{W[(P_o/P)-1]} = \frac{1}{W_m C} + \frac{C-1}{W_m C}(P/P_o) \qquad (5.1)$$

Where W is the weight of gas adsorbed at a relative pressure of $\frac{P}{P_0}$ and W_m is the weight of the adsorbate constituting a monolayer pf adsorbed gas. C is called the BET constant and is related to the attractive forces between the surface and the gas.

For most solids plotting $s = \frac{C-1}{W_m C}$ vs. $\frac{P}{P_0}$ usually results in a straight line in the region from $0.05 < \frac{P}{P_0} < 0.35$. The slope(s) and the intercept (i) of this line can be used to calculate W_m, the weight of the monolayer of the adsorbate.

Given the weight of the monolayer of adsorbate, the surface area of the sample can be calculated using the equation:

$$S_t = W_m N A_{cs} / M \qquad (5.2)$$

Where N is Avagadro's number, A_{CS} is the cross sectional area of the adsorbate molecule, and M is the molecular weight of the adsorbate. Nitrogen, the most widely

used adsorbate, has a cross sectional area A_{CS} = 16.2A^2 in a hexagonal close packed arrangement at 77K. Surface area for solids is usually reported as the specific surface areas, that is, the surface area per gram of sample.

$$S.A. = \frac{S_t}{w\ (\text{grams})} \tag{5.3}$$

The C constant in the BET equation is related to the interaction between the solid and the adsorbate.

$$C = (S/_i) + 1 \tag{5.4}$$

Its magnitude can be an indicator of the reliability of the BET data. Low values for C (<50 in the case of silica) indicate lower attraction between adsorbate and the surface. This can lead to multilayer formation before the monolayer is complete and consequently inaccurate surface area approximations. The C constant can be calculated from the slope and intercept of the BET curve [93].

5.6.2 Porosity by Gas Adsorption

When analysing porous materials by gas adsorption pores are generally classified by their diameters. Pores with diameters in excess of 500μm are called "macropores". Those with diameters between 20μm and 500μm are termed "mesopores" and pores with diameters less than 20μm are "micropores"(Classification of pore sizes by The International Union of Pure and Applied Chemistry (IUPAC)). The porosity and pore size distribution of a porous solid are analysed by adsorbing nitrogen over a range of relative pressures up to the limiting P/P_0 ratio of 1.0. The total adsorption of nitrogen at a P/P_0 approaching unity represents the total pore volume of the porous solid.

5.6.3 Adsorption Isotherms

Much information regarding the porosity and surface area of a solid can be obtained by inspecting the adsorption isotherm. The isotherm is so named because it represents the volume of gas adsorbed at constant temperature over a range of relative pressure, P/P_0. In the case of nitrogen, the solid is placed in a glass tube and immersed in a bath of

liquid nitrogen to control the temperature at 77.4K. Adding or removing gaseous nitrogen then regulates the pressure above the solid and until the desired equilibrium pressure is reached. Plotting the quantity of adsorbed gas versus the equilibrium pressure yields the characteristic isotherm for the solid. All isotherms tend to fall into five general types as characterized by Brunauer-Deming-Deming and Teller in 1940 [93]. The isotherms observed for the 58S gel-glasses in this work were primarily Type IV Isotherms (see Figure 5.1) – representing a mesoporous material. Description of other isotherms shown in Figure 5.1 are as follows: -

The Type I isotherm, or Langmuir isotherm, is concave to the P/P_0 axis over its entire span and approaches its limiting value as P/P_0 approaches1.0. Type I isotherms are characteristic of microporous solids having a relatively small external surface. Examples of solids giving type I isotherms include activated carbons, molecular sieves, zeolites and some types of silica gels.

Type II isotherms are exhibited by non-porous or macroporous solids. This type of isotherm represents unrestricted surface adsorption beginning with a monolayer and progressing to multilayers at higher P/P_0. Characteristic of the type II isotherm is an inflection at point "B" marking the start of a linear central section of the isotherm. This point usually marks the relative pressure at which the monolayer is complete and multilayer adsorption begins.

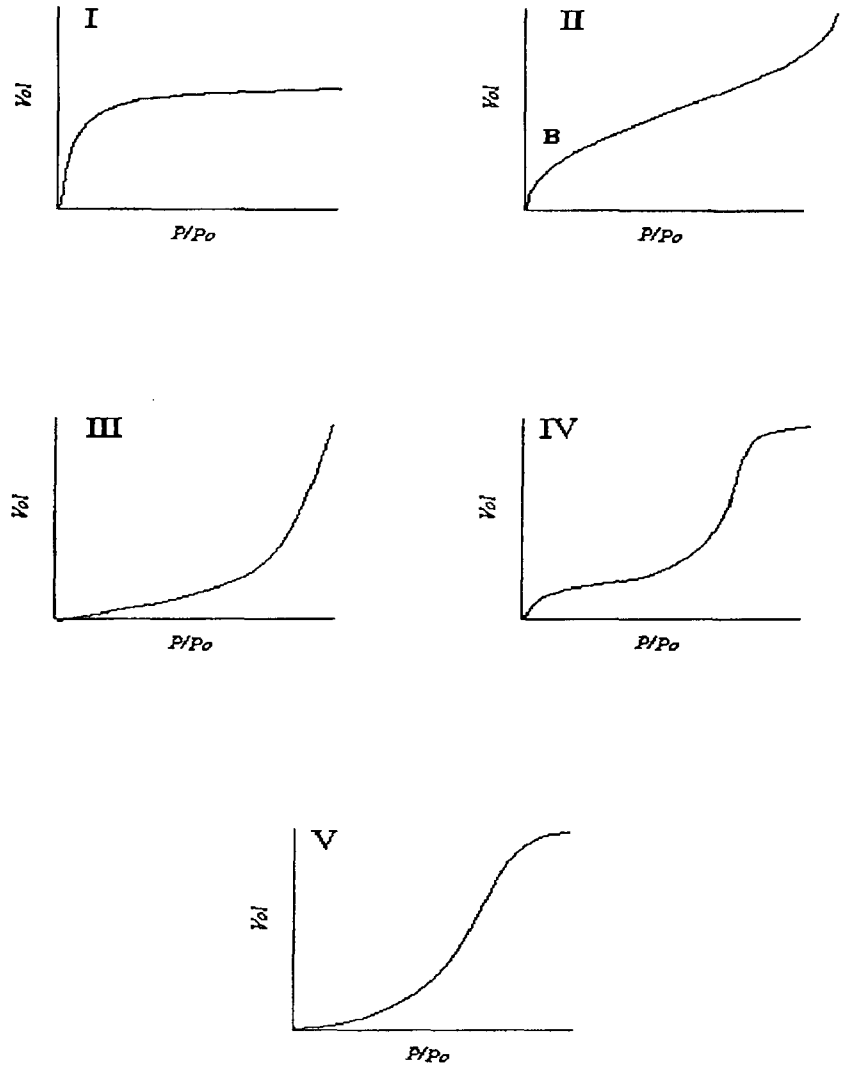
The Type III isotherm is convex to the P/P_0 axis and has no distinct point B as in type II. This is representative of a material where the solid-adsorbate interactions are weaker than the adsorbate-adsorbate interactions. This type of isotherm is rare but one example is the adsorption of water vapour to a nonporous hydrophobic carbon.

Type IV isotherms are indicative of mesoporous materials. The steep slope at higher relative pressures is associated with capillary condensation in the pores.

Type V isotherms are similar to Type III but also have mesopores. They are also relatively uncommon.

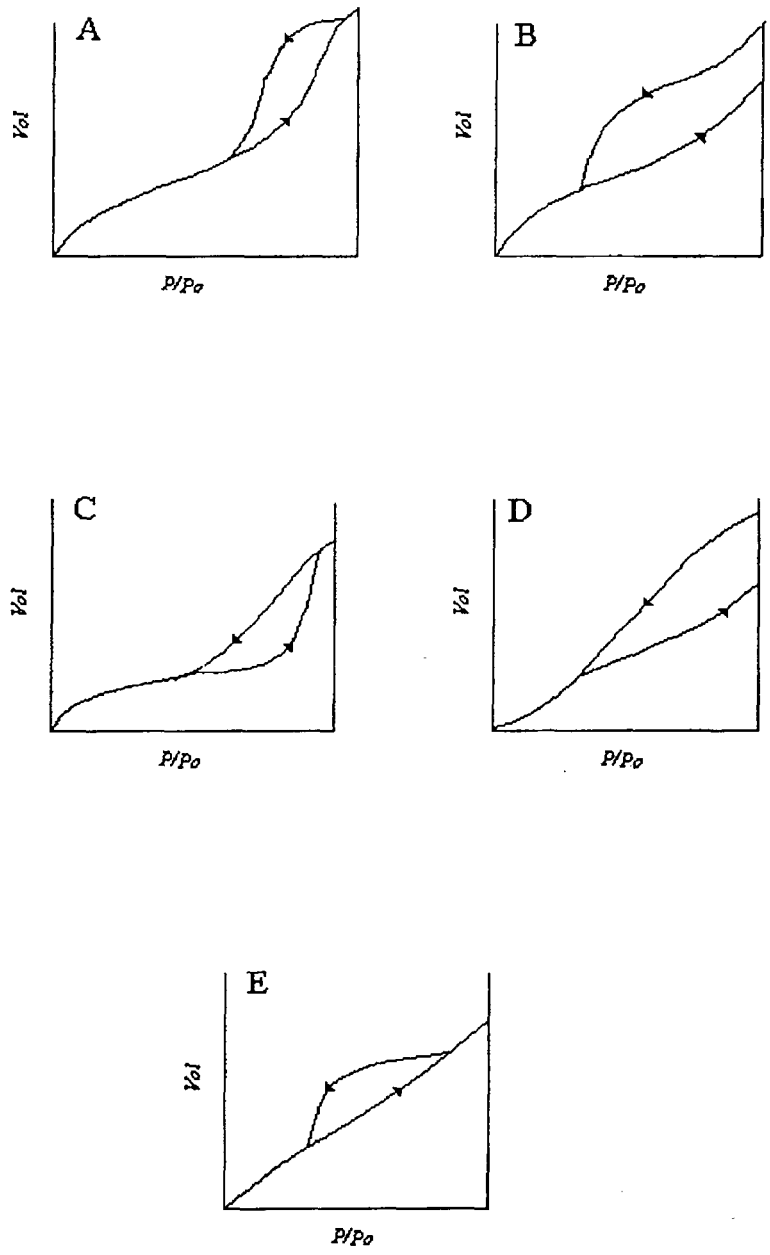
The desorption isotherms for types I, III, IV are reversible, that is; they follow a similar path as the adsorption isotherm.

Figure 5.1: The five types of isotherms as classified by Brunauer-Deming-Deming and Teller. (Powers, [93])



Types II and V however are associated with mesoporosity and exhibit hysteresis between adsorption and desorption curves. The hysteresis is associated with the filling and emptying of mesopores in the material. DeBoer [93] has identified five characteristic types of hysteresis and associated them with pore shape Figure 5.2 shows examples of DeBoer's classification. Typically the hysteresis loops for all isotherms close at or above a relative pressure of P/P_0=0.30.

Figure 5.2: DeBoer's five types of hysteresis loops. A – cylindrical pores, B- Slit shaped pores, C – wedge shaped pores with open ends, D – wedge shaped pores with narrow necks at one or both ends, E – inkbottle shaped pores. (Powers, [93])



5.6.4 Pore size distribution

The distribution of pore sizes in a porous material is determined using the Kelvin equation, which relates the radius of curvature of a pore to the capillary of a pore to the capillary condensation of liquid nitrogen. The Kelvin equation can be written as:

$$r_K = \frac{-2\gamma V_m}{RT \ln(P/P_o)} \qquad (5.5)$$

Where γ=surface tension of nitrogen at 77K (8.85 ergs/cm^2)

V_m= the molar volume of liquid nitrogen (34.7cm^3/mol)

R=the gas constant (8.314 x 10^7 ergs/deg-mol)

T= boiling point of nitrogen (77.4K)

The Kelvin radius, r_K, is the radius of the pore in which condensation occurs at a relative pressure of P/P_0. In actuality by the time the relative pressure is high enough to promote capillary condensation, some multilayer adsorption has already occurred on the pore walls. This adsorption reduces the nominal radius of the pore by the thickness of the adsorbed layer, for a monolayer of nitrogen this thickness is 3.54Å.

Thus, the actual pore radius is the Kelvin radius adjusted by the thickness of the preexisting multiplayer on the pore wall:

$$r_P = r_K + t \qquad (5.6)$$

Where, t is the statistical thickness for the adsorbed layer.

Barrett, Joyner and Halenda [93] developed a method for calculating the pore radius distribution taking into consideration the statistical thickness at the given desorption equilibrium pressure. The BJH method is the most common method in use for calculating pore size distributions. The desorption isotherm is normally used for pore size determinations since desorption from mesopores generally occurs at lower relative pressures. It is theorized that the desorption isotherm is closer to thermodynamic equilibrium but as we shall see this is not a simple assumption.

Upon desorption of condensate from a particular pore of Kelvin constant radius r_K, the volume of desorbed gas consists of the amount emptied from the pore plus the amount of condensate evaporated from the surface of all the pores that have already been emptied. Thus to quantify the pore volume emptied during any incremental decrease in relative pressure, the total area already emptied must be calculated and multiplied by the decrease in statistical thickness over that pressure drop. The BJH method makes use of the following equation to calculate the volume of the emptied pore.

$$V_{pn} = \left(\frac{r_{pavg}}{r_{Kavg}}\right)^2 V_n - \Delta t_n \sum_{j=1}^{n-1} A_j \qquad (5.7)$$

The subscript n in this equation represents the desorption increment to be calculated.

V_{pn} = the volume of the current pore increment being emptied

V_n = the total volume of gas desorbed over increment n.

r_{pavg} = average radius of pore being emptied.

r_{Kavg} = average Kelvin radius of the pore being emptied.

Δt_n = change in the statistical thickness of the adsorbed multiplayer.

A_j = the core area j emptied prior to the current increment. $A_j = 2V_j / r_{Kavg}(j)$

Assuming cylindrical pore geometry.

The incremental volume (D_v) of each desorption step can be plotted against the average pore radius of the interval to yield a graphical representation of the pore size distribution. Since the Kelvin radius is inversely related to the log of the relative pressure, the largest changes in pore radius are measured at higher relative pressures. For example, a relative pressure of $P/P_0 = 0.5$ corresponds to a Kelvin radius of 14Å, a P/P_0 of 0.80 to 42Å, and a P/P_0 of 0.90 to 90Å. Since the volume of the pore scales as the radius cubed, D_v/r or D_v log r is often used to give a more realistic depiction of the proportion of pores of any given radius.

In a purely mesoporous material, the average pore radius can be calculated by assuming cylindrical pore shape and using the hydraulic pore radius given by the equation:

$$r_{avg} = \frac{2 \cdot V_p}{S.A.} \qquad (5.8)$$

This equation is not very satisfying since few materials have idea cylindrical pore shapes but is nonetheless useful for making comparisons between materials of similar composition. According to DeBoer's classification of pore shape, a sharp square-shaped hysteresis loop is attributed to cylindrical pores. It should be kept in mind however, that at high relative pressures the adsorbed multilayer would tend to modify the core pore shape into a cylindrical shape as surface asperities are smoothed out. Therefore, as irregular pores get larger they tend toward a type A (cylindrical) hysteresis (Figure 5.2A) regardless of their actual shape. To date nitrogen adsorption, in combination with optical microscopy and mercury porosimetry remain the best methods of quantifying the textural features of a porous material.

5.6.5 Nonporous Materials

Comparisons between materials with similar morphologies can help elucidate surface chemistry and thermodynamic properties even when the shape is not known. Various samples were examined in the lab that exhibited non-regular isotherms due to their dense surfaces. Many times this was a product of the way in which these materials had been processed or the temperatures to which they had been subjected prior to analysis.

In this case krypton analysis is advised. As the isotherm showed definite signs that the adsorbate gas was not attracted to the surface, this was clarified when the C coefficient was taken into account and was apparently low, i.e.<10, or a negative number. However, more details about these materials are beyond the scope of this current work and the only sample of real relevance here as a comparative model is 45S5 melt-derived Bioglass® powder, which is a non-porous glass.

5.7 Nitrogen Adsorption Analysis of Silica Gels

Due to its wide variation in surface area and porosity, silica gel has been one of the most thoroughly investigated materials by use of nitrogen adsorption. It is stable and has a well-characterized surface, which gives it predictable interactions with nitrogen and other adsorbates. Thus, it is a good material for describing the nitrogen adsorption process.

5.7.1 Interpretation of results

Care must be exercised in the interpretation of the results of nitrogen adsorption analyses. Modern instruments are sophisticated and can automatically measure not only the adsorption data but also the density of the sample. For surface area determinations only a few points in the region of $P/P_0 = 0.0 - 0.3$ are required. For similar materials a single adsorption point taken at $P/P_0 = 0.3$ is often sufficient, especially if the C constant is known. The C constant is important data. For silicas, a C-constant of 50-250 is normal. Abnormally low C-constants indicate low adsorbate-adsorbent interaction energy (as for dense materials), which can lead to incomplete monolayer formation. This invalidates the BET equation, which assumes that the monolayer is complete before multilayers form. In particular, surface area analyses with C values that lie below a value of 20 should be regarded as questionable. An abnormally high C-constant can be indicative of microporosity in which cooperative adsorption takes place in small pore openings. It may also indicate selective adsorption on particular lattice sites or planes. (i.e. the surface is heterogeneous with respect to the adsorbate). However, interpretation of the results from N_2 adsorption is, in general, often a simple matter for powders and porous materials which have good adsorbate gas attraction.

Special attention should be given to the overall shape of the isotherm as well as to the C constant. An unexpectedly high or low C constant indicates a deviation from the standard isotherm and can invalidate the results of the analysis (see Table 5.1). The BET plot can be nonlinear over the normal range for these materials and the BET range may have to be redefined. Generally, the more points taken in the region of interest, the better. The importance of the C constant with respect to relative error is shown in Table 5.1.

5.8 Nitrogen adsorption analysis of Bioglass® compositions

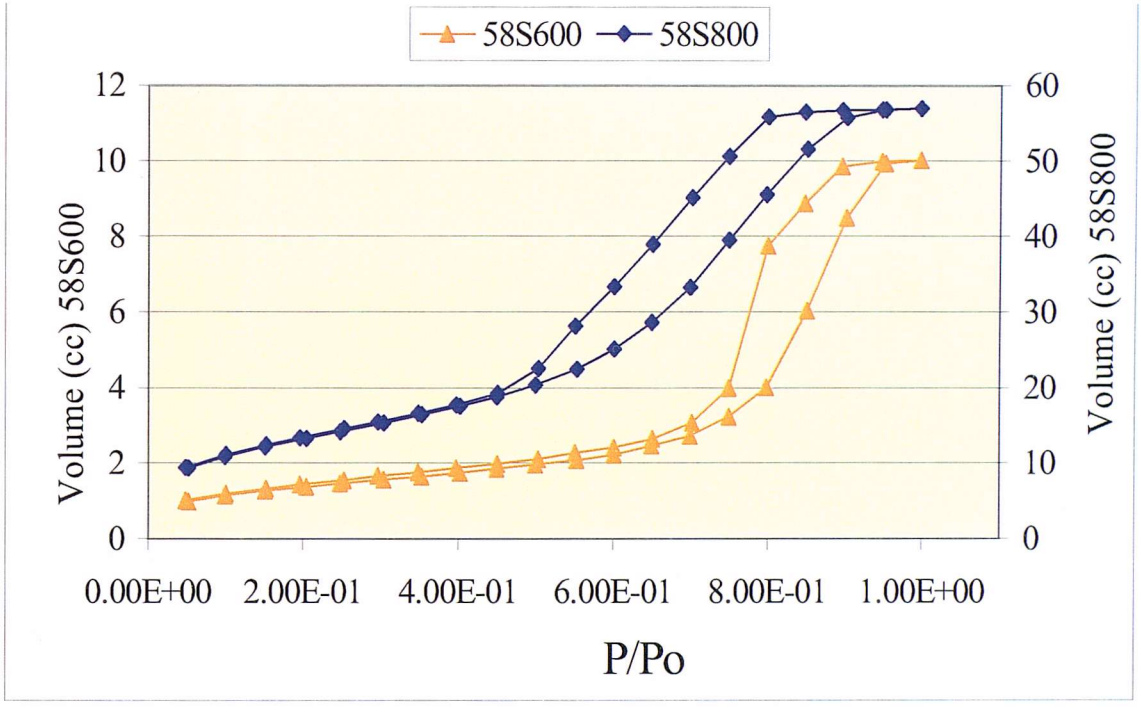
5.8.1 Analysis of the mesoporous gels

Nitrogen adsorption analysis of the 58S and 68S gel-glasses prepared as described in chapter 4 yielded mostly type IV isotherms, with the inflection point occurring at low relative pressure, as shown in Figure 5.3.

Table 5.1: The relative error associated with various C constants obtained from the Quantachrome manual for the AS-1.

C constant	Relative Error
1	0.7
10	0.19
50	0.04
100	0.02
1000	0.002
Infinity	0

Figure 5.3: Typical BET isotherms for mesoporous 58S stabilized at 600 and 800°C.



Increasing the temperature of stabilization from 600 to 800 shifted the isotherms but the shape of a Type IV hysteresis was maintained.

Table 5.2 is a summary of N_2 adsorption data for a series of 58S porous gel-glass samples made with and without HF additions to modify texture. Modification of the gel process, as discussed in chapter 4, has a marked effect on the surface area and pore volume but little effect on the pore size.

Table 5.2: Nitrogen Adsorption Data for 58S with and without HF additions.

Sample Description	S.A. (m2/g)	Pore Width (Å)	Total Pore Vol. (cc/g)	C intercept	M.Point BET Coeff
58S stab at 800C, No HF	199	61	0.32	68	0.999951
58S stab at 800C, No HF	166	61	0.30	80	0.999833
58S 1.5HF@5%, PTFE pot	95	60	0.26	110	0.999725
58S 1.5HF@5%, PTFE pot	88	60	0.24	151	0.999754
58S 3mlHF@5%, PTFE pot	114	61	0.26	93	0.999775
58S 3mlHF@5%, PTFE pot	57	61	0.17	113	0.999702

The stabilized product showed a very defined pore diameter of 55<Å<65 in most cases and typical C coefficients remained high i.e. >90, with the shape of the isotherm indictating a mixture between ink-bottle and cylindrical shaped pores. The mean pore size was always highly localized and defined about 61Å±2Å.

From Table 5.2 it is evident that the samples synthesized without HF addition had the highest surface area values but small additions of HF decreased the surface area giving lower values and finally with 3ml HF addition lowest values of surface area were seen taking in to account that all samples in the study were stabilized at 800°C. The high value (114) seen for the sample with 3ml HF addition can be explained by the fact that it was smaller in size to the final sample data reported in the table. This error is noted in the work as contributing to less accurate results. However, the pore diameter is consistent throughout all studies as lying within the range of 61Å±2Å, as noted above. Total pore volume values decrease with in creasing HF addition, which is shown in Table 5.2. The C intercept indicates that samples data was more accurate when HF addition was used, indicating a different charge on the sample surface with relation to 'attractiveness' to the adsorbate gas (nitrogen in this study). Multi point BET coefficients show that all runs achieved an acceptable level of accuracy to be used as data throughout the study.

5.8.2 Results of nitrogen adsorption of 68S sol-gel Bioglass® samples

Synthesis of 68S monoliths was according to standard procedure with a stabilization regime of 350°C for 24 hours for some samples and 24hours at 400°C for the others. The gel was synthesized without using HF catalysis according to the procedures discussed in Chapter 4. The gel was aged for one week at room temperature and for 3 days at 60°C, followed by the standard drying regime created for monoliths (see Figure 5.4). The gels were stabilized at 350°C and 400°C for 24hrs. Drying was carried out in the same Teflon container set-up shown in Chapter 4. A small (0.1mm) pinhole is placed in the septum to allow water vapour to escape while maintaining 100% relative humidity in the drying container. 300ml of deionized water was added to the container to provide a humid atmosphere and to reinforce the gel by Ostwald ripening during the drying process. These monoliths were retrieved after drying in both large discs sizes obtained from drying in large PE pots 3cm (D) by 5mm(H) as well as smaller 1.5cm(D) by 5mm (H) sizes.

Table 5.3: Results of 68S samples stabilized at different temperatures.

Sample	Stabilisation	Surface Area (m^2/g)	Total Pore Volume (cc/g)	Pore Size (Å)
68S	350°C – 24 H	271.6	0.07732	72.17
68S	400°C – 24 H	240.0	0.2708	57.78

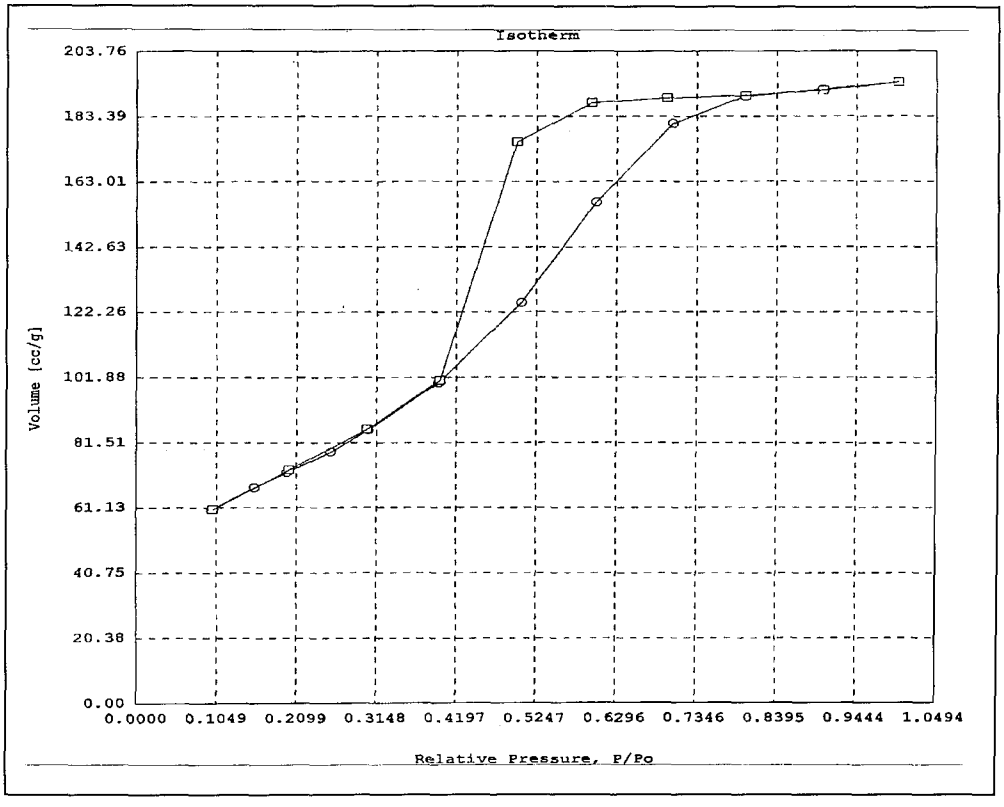
Results are obtained by an average of 5 similar samples. From table 5.3 we see that the lower stabilization temperature produces a material with higher surface area. Total pore volume results for 68S350 are uncertain due to weight of the sample being low. However, pore size measurements remained unaffected. All attempts were made to keep the samples weight approximately equivalent (even though one would consider them small in comparison to later studies once all techniques and batch making had been perfected). The average weight of the samples used in the 68S stabilized at 350°C study was 0.0764g. For the study of 68S stabilized at 400°C the average weight of sample was 0.0368g. This was due to two main reasons: 1) Initial batch preparation only allowed for small amounts of monoliths to be prepared at one time, 2) Because the initial tubes purchased for the Autosorb machine had an inside diameter of 5mm, monolithic samples could not be analyzed whole. These problems were corrected in later studies. Drying apparatus was upgraded to include a drying rack (to overcome the problem of

limited amounts of sample produced per time and effects due to 'uneven' drying) and wider bore tubes for analysis were purchased so that monoliths could be analyzed without the need for excessive cutting or small sample weights. More voluminous samples create less "dead space" and give more accurate results.

5.8.2.1 Analysis of mesoporous 68S Bioglass®

This sample was prepared and analysed according to standard procedures. A 40-point analysis was made with 20 desorption points. The maximum P/P_0 point was used for both branches of the isotherm. Most of the points were selected in the P/P_0 range of 0.9-0.999 since this is where the majority of the capillary condensation occurs for pores greater than 100Å in radius. Equilibrium time allowed between doses of adsorbate was 3 minutes. The total analysis time was 7 hours and 15 minutes. The resulting isotherm is shown in Figure 5.4. At a relative pressure of 0.992, the pores are filled and the isotherm levels off until the maximum is reached at a relative pressure of 0.997. The BET analysis indicates a specific surface area of approximately 255.9m^2/g. The total micro pore volume is 0.1253 cc/g. Using instrument software an average pore diameter of 57.14Å is derived.

Figure 5.4: Typical BET isotherm for mesoporous 68S stabilized at 350°C.



Several interesting characteristics of the analysis are worth noting. The average pore radius is similar to that of the 58S400 previously prepared. The bulk of the nitrogen is adsorbed very near the upper limits of the instrument. The hysteresis loop can be clearly recognized as a Type A, indicating cylindrical shaped pores. The steep vertical rise and fall of the isotherm suggests a narrow pore size distribution.

5.8.3 Results for 58S Bioglass® with various stabilization treatments and thermal histories

The section below covers results obtained from 58S studies using different stabilization temperatures as well as studies employing thermal treatments in dry nitrogen and carbon dioxide atmospheres after stabilization.

5.8.3.1 Analysis of isotherms of 58S stabilized at 400°C (synthesized without HF catalyst)

After initial synthesis, 58S Bioglass® samples were then stabilized at different thermal temperatures to create gels of different textures. Efforts were also made to shorten the total processing schedule. Initially this involved reducing the aging at 60°C by one day. This worked for samples of relatively small dimensions (rods of diameter 1mm and length 1cm). It proved unsuccessful for monoliths of larger dimensions that failed during drying. Results for the unstabilised / undried product of 58S gel as a comparison is included in Table 5.4. For all thermal treatments, pieces of monoliths were studied because the total batch yield produced at one time gave 52 monoliths per batch (100% yield) and took more than two weeks to make. However, care was taken to take enough data so that averages could be taken but in general, deviations were less than 0.05% from any previous result taken from the same material from the same batch. The surface was not cut after thermal treatment to avoid creation of a new surface for experiments after this analysis. Samples success stood at >90% yield for most batches.

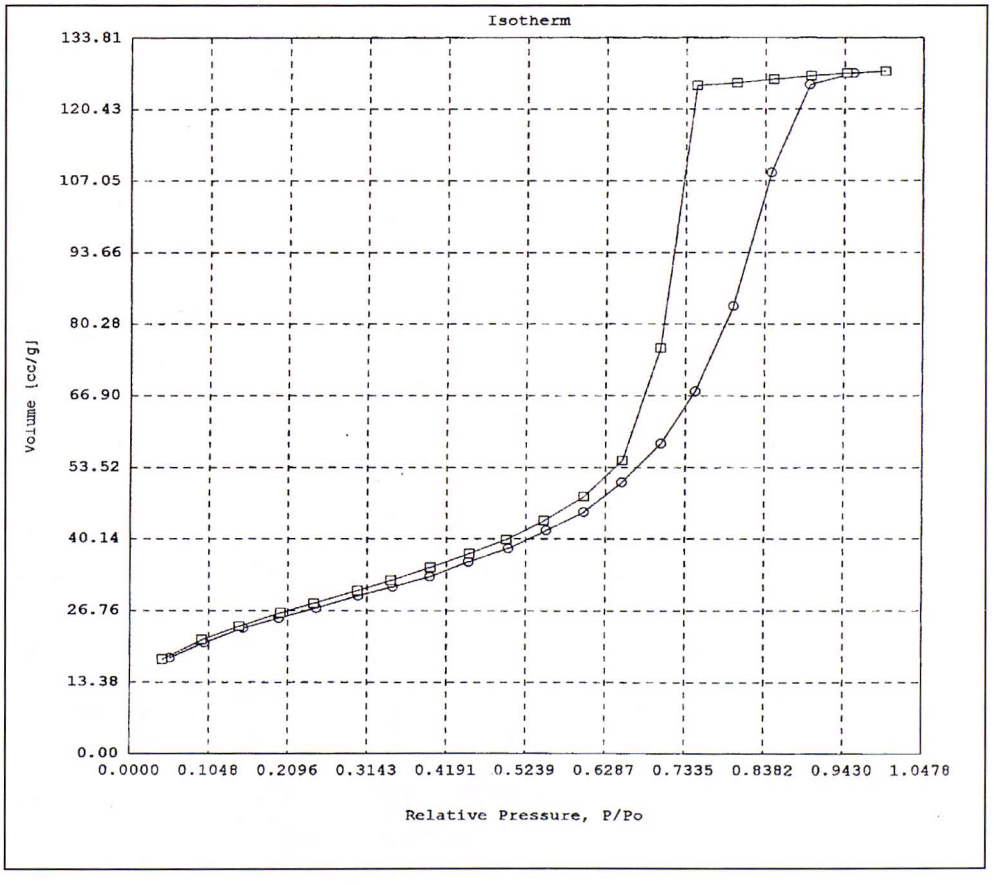
Stabilizing the 58S at 400°C created a stable gel (stable to rehydration in water without explosion), which had the highest dissolution rate, (see Chapter 7). However, XRD analysis showed no apparent difference between gels stabilized at 400 and 800°C. DTA analysis of unstabilized 58S showed that nitrates were no longer liberated from the gel-glass once it passed the NO decomposition temperature of 550°C. Thus, for cell culture

studies 800°C was considered be the optimum stabilization temperature because this stabilization regime produced a gel with the most controlled dissolution profile. In addition, at 800°C one could be assured that all nitrates had been fully liberated and chlorides had reacted fully. This is of great importance for use as a tissue engineering scaffold. Nitrogen adsorption analysis of the 58S gel-glass samples produced the results presented in Table 5.4. Typical isotherms are shown in Figure 5.5.

Table 5.4: Results obtained for 58S samples unstabilised and stabilised at 400°C for 24 hours.

Sample	Stabilisation	Surface area (m^2/g)	Total pore Volume (cc/g)	Pore Diameter (Å)
58S	Unstabilised	99.64	0.1857	61.6
58S	1 day less in aging / 400°C for 24 H	104.1	0.5369	57.9
58S	400°C for 24 H	252.3	0.3615	53.4

Figure 5.5: Typical BET isotherm obtained for unstabilized 58S.



From the results shown in Table 5.4 the unstabilized 58S has the lowest surface area value recorded, this sample still contained nitrates and various other surface groups which could be bound and be non-representative of a 'clean' surface which had been stabilized (involving decomposition of the nitrate groups and liberation of surface bound water). The sample used for analysis of the 1-day shorter programme is a rod produced (dimension 1mmD x 1cm in length) indicating that results were affected by inaccuracies due to weight of sample being too low and too much dead space in the tube. The sample, which had been stabilized at 400°C, shows the highest surface area value. Total pore volume was highest for the sample which had been processed with the 1-day shorter programme, (see Figure 6.6d). This is due to the internal porosity of the rod being exposed at one end where fracture had occurred. In this respect, (substrate geometry) the unstabilized and stabilized at 400°C for 24H were similar and results were generated from similar substrates (monolithic discs). Total pore volume values differed between the similar substrates (unstabilized to stabilized 58S) due to the surface and internal chemistry described previously to explain the differences in surface area values. However, the pore size diameter remained unaffected by these variables and was consistent at 58Å±3Å. After processing had been perfected, a compositional aging study was done with the help of Priya Pavan from the team at Imperial College. In this study, samples were synthesized with the same 58S sol batch but were given different aging regimes to see whether this would affect pore size diameters or compositional content when analyzed with SEM EDAX, (see Chapter 6).

5.8.3.2 Analysis of isotherms of 58S400 with thermal treatment in dry nitrogen atmosphere

58S was synthesized according to standard procedures. The control group was stabilized at 400°C for 24hours and then samples were thermally treated in dry nitrogen atmosphere in a tube furnace for various times and at various temperatures. The flow rate used for all experiments was 60mm/min, used to ensure there no compromising effects due to "flow back" into the furnace. Nitrogen adsorption analysis was then performed.

The results of nitrogen isotherm analyses of the samples are listed in Table 5.5. The 58S400 control for this study had a surface area of 252.3 m^2/g, with a pore diameter of

58Å and a total pore volume of 0.3615 cc/g. The C coefficient for these results was 93.3 giving an error of ≈ 0.02% on these data.

For each result stated in table 5.5, three samples was used to obtain the average value shown. C coefficients obtained during analysis gave a range of values, the maximum C coefficient value of 115.1 and a minimum of –52.27 was recorded showing that accuracy levels varied on results obtained. Results became less accurate with prolonged thermal treatment for the 58S gel-glass samples, giving negative C coefficients (thus affecting the accuracy of surface area values obtained). However, pore diameters remained relatively unchanged throughout the analysis at 71Å± 20Å.

However, it was found that after thermal treatment (see Figure 5.6), the densified surface was less attractive to the adsorbate gas and results tended to get more unreliable, even though the average pore diameters remained realively unchanged. Pore diameters were then accepted as being fixed from the initial structure of the stabilized product in all cases and this in turn meant that the silicate structure was not changing even though different pore families may be evolving with increased thermal treatments. This behaviour could also be related to phase changes which were also evident in XRD work (see Chapter 6).

However, it was also apparent that the more thermal treatment a sample was subjected to, the more chalky white its appearance was, and calcification was seen. To the extent that no transparent samples were seen at treatments involving temperature in excess of 950°C for longer times i.e. > 40 minutes. Crystallinity however, is not seen as a total detriment in the case of effects on bioactivity as it has been shown that bioactivity is unchanged in samples of 100% crystallinity for 45S5 Bioglass® [120]. Care was taken to identify the onset crystallization point by means of XRD analysis so that these samples were not included in the density analysis studies.

Table 5.5: Results from the heat treatment study of 58S stabilized at 400°C and thermally treated in a dry nitrogen atmosphere.

Sample	Temperature of tube furnace (°C)	Time of exposure to dry nitrogen (mins)	Surface area (m^2/g)	Total pore Volume (cc/g)	Pore Diameter (Å)
58S400	Control	Control	252	0.36	58
"	850	10	194	0.32	60
"	850	20	341	0.39	64
"	850	30	305	0.37	62
"	850	40	268	0.35	62
"	850	60	166	0.29	62
"	900	10	153	0.27	62
"	900	20	149	0.25	61
"	900	30	201	0.29	62
"	900	40	139	0.26	63
"	900	60	129	0.20	64
"	950	10	79	0.21	63
"	950	20	91	0.20	62
"	950	30	70	0.15	64
"	950	40	52	0.12	63
"	950	60	54	0.13	64
"	1000	10	13	0.03	90
"	1000	20	42	0.12	62
"	1000	30	18	0.05	66
"	1000	40	12	0.08	71
"	1000	60	41	0.12	60
"	1050	10	10	0.06	64
"	1050	20	33	0.07	75
"	1050	30	11	0.07	76
"	1050	40	7	0.05	52
"	1050	60	9	0.08	70
"	1100	10	17	0.04	69
"	1100	20	3	0.02	82
"	1100	30	9	0.04	83
"	1100	40	5	0.02	81
"	1100	60	5	0.03	78

Figure 5.6: Graph of total pore volume, pore diameter, and surface area for 58S400 with different thermal treatments.

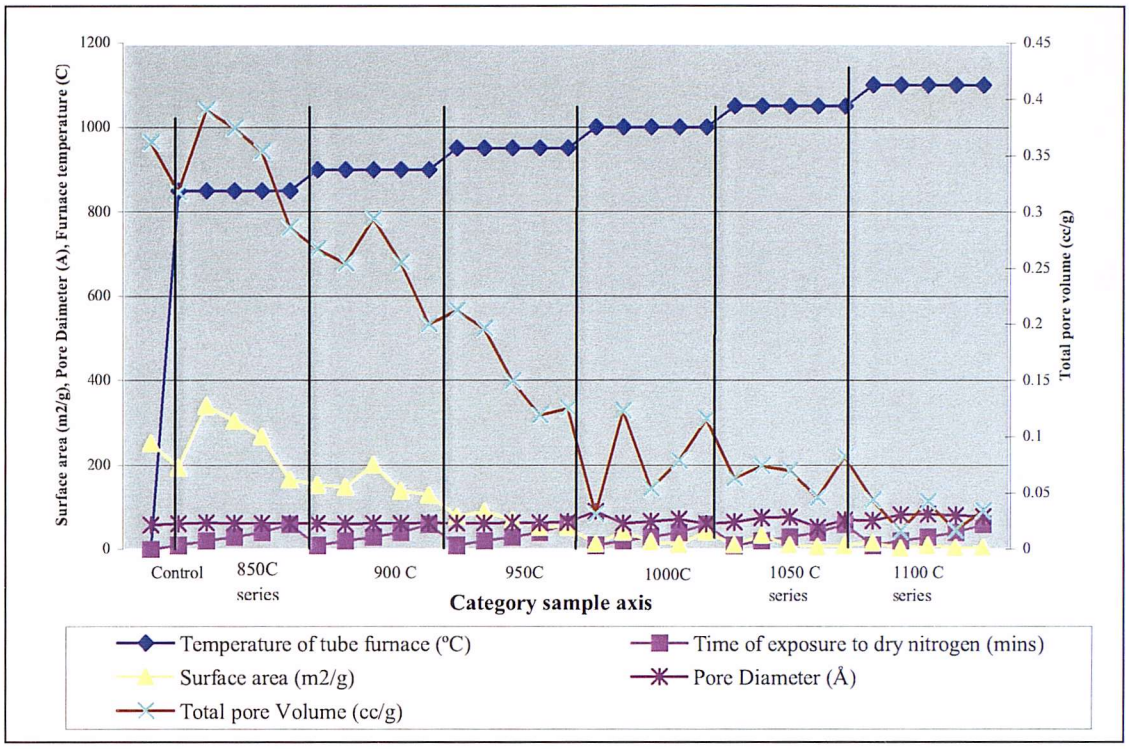


Figure 5.6 indicates that the pore diameter remains unaffected by thermal treatments whereas the surface area and total pore volume both decrease with increased thermal treatments at prolonged times. However, the fact that the pore size remains unchanged dictates that the silicate structure remains stable and there may be sintering occurring at increased temperature. Clearly, the data shows that surface area decrease with respect to increased thermal treatment regimes. This is also apparent for the values of total pore volume shown in Figure 5.6. It is proposed that at higher temperatures, pores are closing but leaving others open, explaining the decrease in total pore volume but no significant change in pore diameter measurements. Thus, confirming the previous proposal that the silica network is stable and that pore sized is fixed at the end of the aging cycle. In Chapter 4, it is confirmed that both bulk and skeletal density values increased with respect to time. However, changes in the skeletal density are also a factor of the overall changes involved in density experiments, the structure becomes more consolidated from previous stabilization regime, which has impact on the dissolution profiles of the thermally treated 58S samples, see Chapter 7.

5.8.3.3 Analysis of isotherms of 58S600 with thermal treatment in dry nitrogen atmosphere

58S was synthesized according to the normal procedures and stabilized at 600°C for 24 hours. The results obtained by this temperature regime are fundamentally different from the other stabilization temperatures in this study. The specific temperature for this system (600°C) produces a material that behaves differently from those from the other stabilisation regimes. From later results, differential thermal analysis (DTA, Chapter 4) we may deduce that this is due to the specific CaP phase formed during thermal treatment at 600°C. Results are shown in Table 5.6.

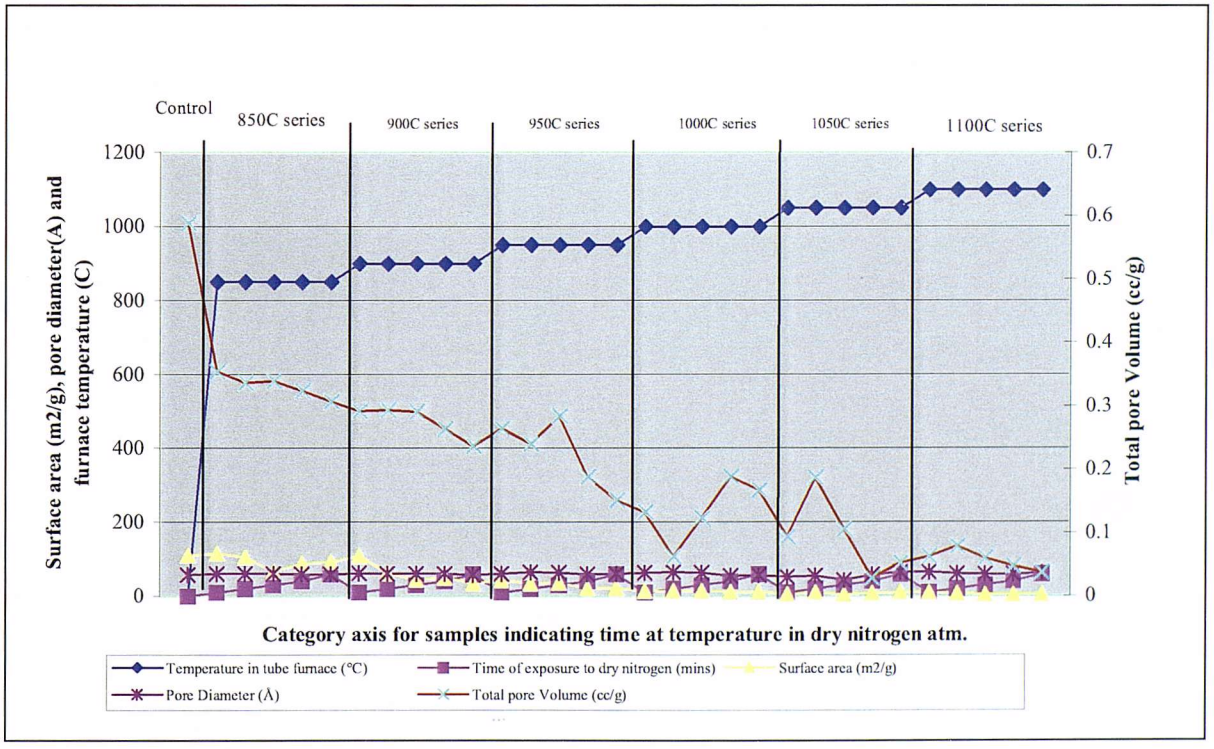
Table 5.6: Results obtained from nitrogen analysis of 58S stabilized at 600°C.

Sample	Temperature in tube furnace (°C)	Time of exposure to dry nitrogen (mins)	Surface area (m^2/g)	Total pore Volume (cc/g)	Pore Diameter (Å)
58S600	Control	Control	110	0.59	58
"	850	10	116	0.35	60
"	850	20	105	0.34	60
"	850	30	67	0.34	60
"	850	40	88	0.32	60
"	850	60	93	0.31	60
"	900	10	109	0.29	62
"	900	20	63	0.29	60
"	900	30	45	0.29	61
"	900	40	51	0.26	60
"	900	60	35	0.24	59
"	950	10	44	0.26	61
"	950	20	35	0.24	65
"	950	30	36	0.28	63
"	950	40	22	0.19	60
"	950	60	22	0.15	62
"	1000	10	14	0.13	64
"	1000	20	14	0.06	66
"	1000	30	14	0.12	64

Sample	Temperature in tube furnace (°C)	Time of exposure to dry nitrogen (mins)	Surface area (m^2/g)	Total pore Volume (cc/g)	Pore Diameter (Å)
58S	1000	40	12	0.19	55
"	1050	10	5	0.09	52
"	1050	20	10	0.19	55
"	1050	30	4	0.11	44
"	1050	40	8	0.03	58
"	1050	60	11	0.05	66
"	1100	10	9	0.06	65
"	1100	20	7	0.08	61
"	1100	30	5	0.06	59
"	1100	40	4	0.05	60
"	1100	60	4	0.04	62

Table 5.6 con't: Results obtained from Nitrogen analysis of 58S stabilized at 600°C.

Figure 5.7: Graph of pore diameter, surface area and total pore volume for thermally treated 58S stabilised at 600°C.

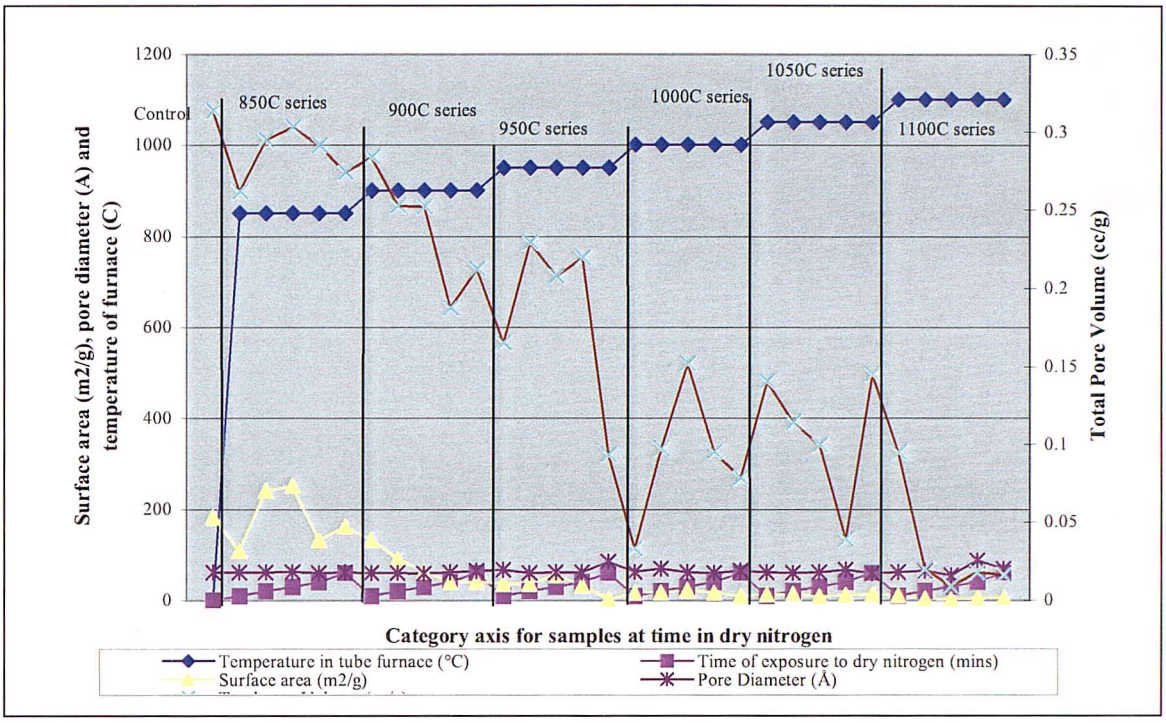


From the graphical representation of the data, we see that the general trends of surface area and total pore volume decreasing with increased thermal treatment in the tube furnace was confirmed. Yet again it is evident that the pore diameter remains stable and is unaffected by these parameters. From pore distribution graphs created after analysis, a defined distribution of pore families turned into a trimodal distribution after 30 minutes at 950°C. This is not unusual for 58S and is seen in the 58S samples stabilized at 800°C and could also be due to 'noise' from the analysis. The average C coefficient during this data set was 109, corresponding to an error of ≈ 0.02%. At high temperatures C values became spurious, the minimum value of –143.5 and a maximum value of 295.2 for this data set, giving a large range for this value.

5.8.3.4 Analysis of isotherms of 58S800 with thermal treatment in dry nitrogen atmosphere

58S was synthesized by the standard procedure and then densified in a dry nitrogen atmosphere at a flow rate of 60mm/min in a tube furnace. The table following outlines data obtained. Throughout most of the data sets, C coefficients remained high for the initial samples and then decreased as surface area decreases with added heat treatments. Again, the same trends are seen as in the other samples stabilized at different temperatures in the densification experiments run in dry nitrogen atmosphere. The surface area decreases from an order of $10^2 m^2/g$, down to $10^0 m^2/g$ and total pore volume decreases whilst pore size remains unaffected. It is realized that the pore structure is created in the original gel and cannot be much modified by thermal treatment in dry nitrogen. Pore sizes remain the same even where we would expect to see sintering behaviour in the gel-glasses, lower total pore volumes are shown. The fact that total pore volumes decreases however, does indicate that void closure is occurring combined with an increase in skeletal density values of the material. Different phases could be evolving with time at different temperatures. However, this cannot be determined by pore size, surface area data or density results alone, as the new phase may be less dense than the original parent phase.

Figure 5.8: Graph of total pore volume, pore diameter and surface area for 58S stabilised at 800°C for different times in dry nitrogen.



From Figure 5.8, it is evident that the general trend is of surface area decreasing with time in increased thermal treatments, along with total pore volume being rapidly decreased. The pore diameter does not change at all regardless of thermal history. In the samples treated at 850°C, surface area is increased between increments of 20 and 40 minutes. After this, the surface area steadily drops to values of order 10^0. Total pore volume decreases with increased thermal treatment, and in samples with more than 30 minutes exposure and thereafter the trend is a decline in values until reaching values for those samples treated at 1000°C, mirroring the behaviour of surface area but not like the unchanged pore diameter readings in the data. From this we can confirm that the pore structure is created at an early stage in the gel and after stabilization, remains unchanged within ± 10Å. Apparent peaks seen in total pore volume values in the middle of time periods can be explained by different pore families evolving with respect to time and also other pore closures during this period.

However, with the test results from other methods we see that the product stabilized at 800°C is by far the most stable regime of the study. It has more controlled behaviour when placed in liquid medium and displays a fine grained structure of multi-phase components, which we later find to be biocompatible and successful in cell culture

studies when HF additions are made to the recipe, (see Chapters 7 and 8). The monoliths proved mechanically stable to rehydration stresses induced when subjected to liquid medium, sometimes the catastrophic failure of monoliths is due to incomplete stabilization which can create spallation problems in studies involving liquid mediums, where constant surface substrate conditions are essential. Investigations that are more thorough proceeded with the 58S800 system afterwards.

Table 5.7: Results from 58S stabilized at 800°C with thermal treatment in dry nitrogen atmosphere.

Sample	Temperature of tube furnace (°C)	Time of exposure to dry nitrogen (mins)	Surface area (m^2/g)	Total pore Volume (cc/g)	Pore Diameter (Å)
58S800	Control	Control	183	0.31	61
"	850	10	109	0.26	61
"	850	20	241	0.29	62
"	850	30	251	0.30	62
"	850	40	132	0.29	60
"	850	60	162	0.27	61
"	900	10	134	0.28	60
"	900	20	91	0.25	60
"	900	30	64	0.25	59
"	900	40	40	0.19	62
"	900	60	41	0.21	65
"	950	10	37	0.17	68
"	950	20	37	0.23	61
"	950	30	55	0.21	61
"	950	40	34	0.22	61
"	950	60	25	0.09	86
"	1000	10	17	0.03	63
"	1000	20	17	0.10	70
"	1000	30	23	0.15	61
"	1000	40	17	0.10	60
'	1000	60	10	0.08	65
"	1050	10	13	0.14	61

Sample	Temperature of tube furnace (°C)	Time of exposure to dry nitrogen (mins)	Surface area (m^2/g)	Total pore Volume (cc/g)	Pore Diameter (Å)
58S800	1050	20	15	0.11	60
"	1050	30	9	0.10	62
"	1050	40	12	0.04	67
"	1050	60	13	0.14	59
"	1100	10	11	0.09	61
"	1100	20	3	0.02	65
"	1100	30	3	0.01	55
"	1100	40	5	0.02	87
"	1100	60	6	0.02	69

Table 5.7 con't: Results from 58S stabilized at 800°C with thermal treatment in dry nitrogen atmosphere

5.9 Discussion of results obtained for 58S stabilized at 400, 600 and 800°C without thermal treatment

As stated previously, using 800°C as the stabilization temperature yielded the most stable monoliths. Stabilization at 400°C created a product which was biocompatible, but still contained nitrates that could in the long term be harmful. The product stabilized at 600°C gave unusual dissolution results and even though it had the largest pore volume, it did not have the largest pore diameter.

58S stabilized at 800°C provided a reproducible and high yield combination over all other regimes applied and was also biocompatible with better density than the control product, and had the most controlled dissolution results. With a higher stabilization temperature, it was possible to eliminate hazards from any nitrates still contained in the final product. Stabilization temperatures near to the nitrate evaporation temperature of 550°C, may leave residuals. Chlorine entities are reacted at temperatures of 800°C and above, 58S800 provided a more readily understood ultrastructure than the sometimes erratic behaviour of the 58S stabilized at 600°C. Table 5.8 shows comparative data for 58S stabilized at different temperatures.

Table 5.8: Comparative results from thermal study outlining properties of 58S stabilized at different temperatures.

Sample	Surface area (m^2/g)	Total pore Volume (cc/g)	Pore Diameter (Å)
58S400 control	252	0.36	58
58S600 control	110	0.59	58
58S800 control	183	0.31	61

It was also observed that the isotherm changed shape with temperature treatments and that the distance between the adsorption and desorption curves increased, this was apparent for 58S800 after 40mins at 1000°C. The isotherm was then seen to shrink in these dimensions and become increasingly jagged after 20mins at 1100°C. Again this behaviour is due to changes on the surface of the material with the C coefficient also being affected and the pore family becoming bi- or trimodal rather than the defined distribution of the control product. This effect could be due to noise, but is unlikely and the behaviour also indicated calcination of the surface and low surface areas values which created low C coefficients during nitrogen adsorption analysis.

5.9.1 Analysis of isotherms obtained from 58S800 with thermal treatment in carbon dioxide atmosphere

58S was synthesized using the normal procedure and then exposed to a carbon dioxide atmosphere at a flow of 6mm/min at various temperatures. This set of experiments was used to provide a comparative model to the dry nitrogen atmosphere previously tried with 58S stabilized at different temperatures. Carbon dioxide was used in place of water because of its quantifiable nature at high temperatures, unlike that of water at temperatures above 400°C which exhibits behaviour in a 'non-equilibrium' zone. From previous studies it was seen that there was little difference in results obtained after thermal treatment at 850°C and 900°C. Therefore 850°C was not used, the minimum temperature for thermal treatment was 900°C. A short time of 20 minutes in the atmosphere was chosen as optimal and used in all proceeding results, keeping the costs of the process down by minimising the heat treatment. Table 5.9 summarises the data obtained for 58S thermally treated in carbon dioxide.

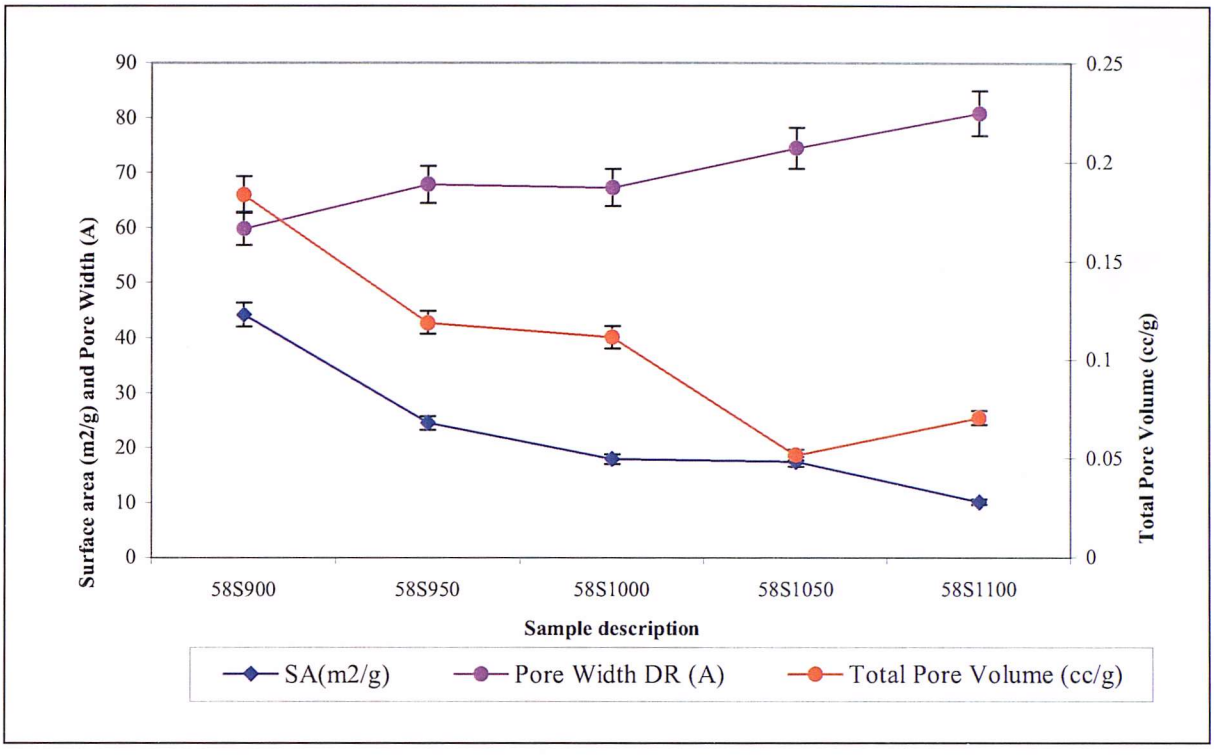
Table 5.9: Results obtained from a study of 58S stabilized at 800°C and thermally treated in carbon dioxide at various times and temperatures

Sample temperature (°C)	Surface Area (m2/g)	Pore Diameter (Å)	Total Pore Volume (cc/g)
900	44	60	0.18
950	24	68	0.12
1000	18	67	0.11
1050	17	75	0.05
1100	10	81	0.07

Again, we see that surface area and total pore volume decrease with increased temperature. Pore diameter however, is seen to increase at the higher temperatures of 1050°C and 1100°C, whereas it remains unchanged at the lower temperatures of 900-1000°C. The carbon dioxide atmosphere produced better densities after thermal treatment. Carbon dioxide is safe to use and is adsorbed on the materials' surface without contamination during processing.

The C coefficients for these experiments were positive and the average was 55.66 correlating to an error of ≈ 0.04% for results with the minimum value being 4.2 and the maximum being 135. The sample surface was more attarctive for the absorbate gas rather than the 58S which had been denisifed in nitrogen gas. Thermal treatment in carbon dioxide had created a more attractive surface for the adhesion of nitrogen molecules with which to form a uniform monolayer for the adsorption analysis. In each case three samples were used to give an average value with a (SD = 12.5) for surface area measurements, 33.63 for pore size measurements and 0.06 for total pore volume measurement. The high value of the pore size measurement was produced by a small sample in the group that gave an unusually large value for the pore diameter.

Figure 5.9: Graph of AS-6 Results for 58S800 densified in CO_2 at different temperatures for 20 minutes



5.9.2 Synthesis of 58S Bioglass® with 5% HF catalyst

Synthesis of these gels followed the normal regime for 58S Bioglass® with a final addition to the sol mixture of HF before pouring. In one sol mixture of 58S, 3ml of 5% HF was added. A second sol mixture using 1.5ml of 5% HF was also made. Samples were then dried and stabilized at 800°C in air for 24 hours. No thermal treatment was applied to these samples but a cell culture study was done to find out whether the different surface charge created by the HF along with any effects from CaF_2 crystals found on the surface after stabilization at 800°C, had affected the biocompatibility of the material.

Table 5.9.1: Results from nitrogen adsorption of 58S made with HF [5%] catalyst.

Sample description	Surface area (m^2/g)	Pore diameter (Å)	Total Pore Volume (cc/g)
58S800 + 1.5ml HF (5%)	77	61	0.21
58S800 + 3ml HF (5%)	86	61	0.44

From the data, it is evident that the addition of 3ml HF (5%) creates a product with the highest total pore volume of any batch previously made from the 58S original recipe. In comparison, a normal batch of 58S800 made earlier without HF gave the following results: Surface area was measured at 182.55 m^2/g, pore diameter was 61.04 Å and total pore volume was 0.3135 cc/g. The product without HF catalysis has a higher surface area than those with it and a total pore volume in between the values given for 58S800 with 1.5ml and 3ml addition of HF. However, the pore size diameter remains unaffected by this treatment, consistent with all other batches. The average C coefficient for the HF catalyzed batches was 111.7 ≈ to an error of 0.02%, with the maximum value being 150.7 and the minimum being 92.48. From these data is also evident that the HF catalysis produces an attractive surface for nitrogen adsorption. However, thermal treatment was not done on these samples. Isotherms were similar in comparison to previous batches with a defined pore distribution (mode shown in table above).

5.9.3 Discussion and conclusions

The stoichiometry and conditions of gelation are known to have a dramatic effect on the texture and porosity of silica gel monoliths [93]. For most applications, it is desirable to have a good understanding of the specific surface area, pore volume, pore shape, and pore size distribution. Nitrogen adsorption analysis is an excellent technique for elucidating this information. Accurate and highly reproducible results can be obtained for silica gels and a variety of other porous silaceous materials. Silicate materials have often been the subject of such studies over the years and their interactions with nitrogen are well characterized [93]. Dense powders and mesoporous silicas can be quite reliably analyzed by this method. Microporosity is somewhat more difficult to analyse due the nature of cooperative forces in the micropores and requires special analytical techniques. Likewise, one must turn to other techniques such as mercury porosimetry for the characterization of large macropores. It is clear however, that understanding the nature of the adsorption process and the information it provides is essential to the correct interpretation of the data. Although the surface area and pore volumes of materials are easily and accurately determined, the exact nature of the porosity can be somewhat more ambiguous and nitrogen adsorption data must be carefully analysed to give the proper clues for overall pore characterization.

The trend seen in the samples tested from all series (stabilized at 400, 600, and 800°C) is that the surface area decreases and the pore size is stable with increasing temperature treatments. The total pore volume also decreases with heat treatment.

A simple indicator of the changes is seen when looking at the multipoint BET data. The BET constant (C) is the 'attractive' quality that the adsorbent gas has for the adsorbate surface. C is seen to change throughout the readings taken for various samples and is known to have a typical value of 50-250 for silica materials [93]. Abnormally low C-constants indicate low adsorbate-adsorbent interaction energy, which can lead to incomplete monolayer formation, this was seen in those samples which had been thermally treated at higher temperatures or for longer times. However, in the study using carbon dioxide gas and the HF catalysed materials it is apparent that these variables produced a more attractive surface for nitrogen adsorption which in turn gave high C coefficients and more accurate data.

This effect can either be due to the morphology of the sample surface changing due to heat treatment or due to the change in crystal arrangement on the surface itself. To further investigate this it is possible to look at fractal dimensions. This series of calculations refers to the 'roughness' of the surface. Thus, by analyzing plots of the BET constant (C) vs. the surface area (m^2/g) it is possible to determine if the surface morphology/roughness is changing.

In various isotherms studied, it has been noticed that the pore size distribution may change from a highly defined distribution about the average into a bi or trimodal distribution with increased temperature treatments. This may indicate a change in phase, leading to the liberation of further pore sizes that were not accessed by previous heat treatment. XRD can be used to analyze the various phases formed at certain temperatures throughout the material; this may also change the attractive potential of the surface for the gas.

As the pore diameter is apparently unchanged (maximum deviation = 10Å) we assume that the network structure of the glass-ceramic is staying intact. Pore distribution may change throughout the material but the mode will always lie fairly close to original measurements of untreated samples. Dissolution results indicate that 58S800 is a more skeletally dense material, which has controlled dissolution kinetics, slower than 58S

stabilized at lower temperatures. This trend correlated with decreasing values in total pore volume. Density measurements and other methods are discussed in more detail in Chapter 6. Dissolution data are shown in Chapter 7.

Changes in phase in the material through temperature treatments also explain the difference in pore size and results for the batch of 58S stabilized at 600°C. In this set if data we see a pattern that doesn't quite fit the trend between 400 and 800°C, this could be due to a TCP phase formed when the sample is left at 600°C for time. It is also noted that the temperature in question is that nearest the nitrate evolution temperature. However, because resorption of the material must also be kept in mind, this can be critical when the material is placed *in vivo* where evolution of extra ions or nitrates would be toxic. A higher temperature of stabilization stopped erratic dissolution and produced a biocompatible material with enhanced density which resorbs more slowly than samples produced at the other two stabilization temperatures. This has been seen in the dissolution studies performed in both Tris buffer and SBF (see Chapter 7).

Analysis to obtain micropore information about 58S800 initially failed as the dewar repeatedly fell empty before adequate points could be taken, as a high vacuum was set for enhanced accuracy during the analysis (10^{E-6} Torr). However, upon doing a 40 X 40 adsorption with 11 point BET analysis for surface area the results were quite different from those from larger pieces. Overall, pore size average was in the order of 100Å and the surface area was substantially lower than previously recorded. This can be explained by the sample being chipped off a bigger piece and, in the process other bigger pores had been opened. With the surface area being low, this is consistent with the area of the pores being 'smoothed over', a natural process with this material as was seen in confocal microscopy. The sol-gel glasses studied tended to heal over rugged and rough surfaces when exposed for a time in the atmosphere, due to the hydrophilic nature of the surface. If the sample had not been freshly fractured then the surface area would decrease with time in the atmosphere alone. It is also proof of the rapid reactivity of the material when in contact with hydrated species and explains the XRD plots giving slight peaks in HCA areas before the glass has been treated with any cultures or fluids to produce this effect. Through nitrogen analysis we also see that mercury porosimetry can be used as a complementary method to provide information on families of pores that are larger and in the nanometer and micron range.

Overall, nitrogen adsorption provides a safe method of generating accurate and comparative data. The results obtained are compared with those of previous studies on the same systems in Table 5.9.2 below; refer to list of references for authors.

Table 5.9.2: Results from nitrogen adsorption data compared with previous studies on 58S systems.

Material and source	Surface Area (m2/g)	Total Pore Volume (cc/g)	Pore Size (Å)
58S400 (IC)	252	0.36	58
58S **[121]**	289	0.49	34
58S **[56]**	286	0.44	60
58S **[122]**	207	0.41	43
58S600 (IC)	110	0.59	58
58S600 **[123]**	289	0.49	34
58S800 (IC)	183	0.31	61
58S800 **[123]**	223	0.34	30
58S850 (IC/N_2/40min)	132	0.29	60
58S850 **[123]**	128	0.18	26
58S900 (IC/N_2/20min)	91	0.26	60
58S900(IC/CO_2/20min)	44	0.18	60
58S900 **[123]**	92	0.15	-
68S400 (IC)	240	0.27	58
68S **[121]**	326	0.41	25

For 58S, the surface area measurements are closest to those of the 58S400 synthesized in this work. Total pore volume and surface area measurements are comparable for this group but a slightly larger pore size is observed in the product synthesized at Imperial College (IC). The 58S600 product that gave sporadic results has less than half the surface area reported previously by other authors, similar total pore volume and a slightly larger pore size. In the 58S800, group results are consistent with previous work but again a product with a larger pore size (double the size of that previously reported) distinguishes the IC product from that of earlier work. In the 58S850, series the most similar product to the values obtained by previous work were found to coincide with 58S850 that had been treated for 40 minutes in dry nitrogen atmosphere. The other products from the IC study showed values much similar to that of 58S800 with higher

surface areas. Again, the fundamental difference between the two products is the larger pore size of the 58S850 IC product, which is double the value previously reported [123]. There is no obvious explanation for this

The final group of the thermally treated 58S is 58S900. From this work 58S was thermally treated in two different atmospheres at 900°C for 20 minutes, the results show that the CO_2 atmosphere produces a material with lower surface area and total pore volume. However, the pore size remains unchanged when comparing the two different atmospheres. The 58S900 reported from the literature was sintered in air (as were the other samples derived from this study [123]) and is most similar to the IC product which had been treated in a dry nitrogen atmosphere, however, there were no pore size data obtained in this study [123].

In the 68S group, only one batch was made of this material for analysis and stabilized at different temperatures. The IC product, which had been stabilized at 400°C, had a lower surface area and total pore volume than the product reported in previous work. It is observed that the pore size obtained for the IC product is double that of that reported previously [124]. In general, the products are very similar and the only assumption we can make to explain the pore size discrepancy is that the value for pore size radius has been quoted rather than that for pore width.

CHAPTER 6 OTHER ANALYTICAL TECHNIQUES EMPLOYED TO CHARACTERISE 58S BIOGLASS®

A brief description of the various analytical techniques used to examine this material is described; TEM was used to identify the structure of the material as having nanophase separation, SEM was used for surface analysis of the stabilized material, the surface after immersion in solution and after cell culture, XRD outlined the phase evolution in the material after various heat treatments, DTA described the nature of bound water in the material and a crystallization temperature, EDAX confirmed the accuracy of composition of the material produced according to the recipe received from US Biomaterials, NMR provided data on the predominant type of Q species in the structure of the glass, Mercury porosimetry was use to determine the bulk density and helium pycnometry was used to obtain values for the skeletal density. Nitrogen adsorption analysis was used for values of total pore volume, mean pore diameter, pore size distribution, and surface area (covered in Chapter 3). Confocal microscopy was used to identify an interconnecting pore network bound by a glassy surface phase of the monolithic samples. Fourier transformed infrared analysis and dissolution kinetics are covered in Chapter 7.

6.1 Mercury Porosimetry

Mercury porosimetry was used as a complementary analysis to nitrogen adsorption of the sol-gel bioactive glasses to look at pore size distribution. This was also the main method for obtaining bulk density values for the material, in conjunction with helium pycnometry that was used to find data on the skeletal density of the material. Another advantage was that the intruded samples could be viewed by confocal microscopy to outline pore interconnectivity, another vital characteristic of these bioactive gel-glasses.

6.1.1 Mercury porosimetry as a characterisation tool

Mercury porosimetry is by far the most popular method employed for the characterization of relatively large pores, in particular macropores and has been suggested as a recommended tool for the characterization of porous solids by

IUPAC [125]. Compared to alternative pore size characterization methods (e.g. gas sorption) mercury porosimetry is based on a simpler principle (the Washburn equation), is much faster, (producing full pore size distributions in minutes compared to hours in gas sorption tests) and perhaps more importantly, is unique in that it covers a very wide range of pore sizes, including large pores (0.5microns) that are difficult or impossible to probe reliably by other techniques. Yet much like other techniques, mercury porosimetry analysis yield cumulative raw data from which differential pore size distributions are numerically derived. The Washburn equation clearly provides a simple and convenient relationship between applied pressure and pore size. Pore size distributions are therefore generated by monitoring the amount of non-wetting mercury intruded into the pores as a function of increasing applied pressure [125].

The choice of cylindrical pore geometry was one of mathematical convenience in order to avoid the complexities of having to deal with mean radii and contact angles in pores of irregular cross sections.

$$\mathbf{Pr = -2\gamma\cos\theta} \qquad (6.1)$$

Where P is the intrusion pressure of mercury, r is the radius of the pore throat and θ is the contact angle (for silica this is 140°).

For this reason mercury porosimetry has traditionally treated solids as porous materials containing a bundle of capillaries of various sizes. Little error is introduced by the presence in solids of interconnected channels, provided that all the pores are equally accessible to the exterior mercury reservoir; that is access to pores of a given size D must always be possible through pores of size >- D. If the pores have only smaller entrances, they can only be filled upon reaching a pressure higher than that required by their actual (inner) dimensions. Once the pressure to fill the largest entrance is reached, the filling of the entire pore would ensue. In such case, the calculated pore size distribution would be biased towards smaller than actual (inner) pore sizes. The converse would be true upon mercury extrusion, and could presumably lead to entrapment and hysteresis in so-called inkbottle pores [125]. The total content of ink-bottle pores, when estimated from the end point of the depressurisation curve, has been reported to vary widely from

a negligible fraction of total pore volume in a silica-alumina gel to >80% in an activated carbon [125].

6.1.2 Hysteresis behaviour

Many explanations have been offered to account for the experimental observation that mercury extrusion curves do not overlap intrusion curves [125]. Currently, three explanations appear to be favored by different groups: (i) the ink-bottle pore assumption (ii) network effects, i.e. an extension of the ink-bottle concept which is substantiated by complex computer simulations (as discussed in Chapter 5); and (iii) a pore potential theory whereby mercury is not subjected to pore wall interactions during its initial intrusion but is partly held in the pores upon extrusion as a function of the wall interaction. According to the latter mechanism, the work done to expand the mercury surface area upon initial intrusion consists of two parts: (i) the irreversible work of intrusion, associated with mercury entrapment in potential wells or ink-bottle pores; and (ii) the reversible work of intrusion, which is greater than (iii) the reversible work of extrusion.

The latter is quite feasible thermodynamically and is ascribed to the extrusion of mercury being facilitated by a decrease in the tensile extrusion contact angle θ_E relative to the compressive intrusion contact angle θ_I. In this context, good qualitative agreement has been reported [125] upon comparing the results of pore potential predictions with contact angles changes. Moreover, it is an experimental fact that hysteresis gaps can in many cases be eliminated completely (within about 1%) by modifying the extrusion contact angle until the extrusion curve and the second intrusion curve overlap.

6.1.3 Scanning versus stepwise data acquisition

Early porosimeters operated exclusively in a stepwise fashion, i.e. raising or lowering the applied pressure in steps. This approach had several drawbacks, including: (a) an inability to hold the pressure constant at any given step; (b) the need for long analysis times; (c) the poor resolution obtained as a result of collecting relatively few data points in order to construct pore size distribution curves; and (d) the possibility of skipping important information in pressure

ranges corresponding to filling a narrow or multimodal pore sizes. All these drawbacks were eliminated by the production of the scanning technique pioneered by Quantachrome [125]. In addition, Quantachrome porosimeters were designed to balance mercury compression under pressure and its expansion due to the compressive heating of the hydraulic oil.

6.1.4 Limitations of mercury porosimetry

Pores are not usually circular in shape and so the results can only be comparative. When considering the presence of ink-bottle pores or other shapes with constricted necks opening into large void volumes, all the volume will be assigned to the neck diameter so that the capillaries will be classified at too small a radius. This also leads to hysteresis and mercury retention in the pores [126]. The assumption here is a constant value for the surface tension for mercury. The largest source of error in calculating pore diameter is the assumption of a constant value for the angle of contact of mercury. The receding angle of contact may well differ from the advancing angle, i.e. the angle of contact between the mercury and the wall as it advances into the pores under increasing pressure may differ from the contact angle as it recedes under reducing pressure. The contact angle θ also be affected by surface roughness.

The effect of compressibility of mercury, sample container, sample and residual air with increasing pressure. Breakdown of the porous structure during examination is possible due to the high mercury pressure used during intrusion. This effect was also noted in the work of Powers [93]. In this work, a maximum limit of 30Kpsi was set for all samples. However, it was also noted that not enough mercury was intruded on low pressure runs using the Quantachrome Poremaster 33 and, most results were created using high pressure runs that went up to 30Kpsi. Time effects were not a problem due to the dynamic Quantachrome Porosimeter 33 used, in which the pressure changes continuously, generating data on different pore size distributions quicker than static porosimeters, where the pressure increases in steps, with time for the system to come to equilibrium between steps. 36Å is the limiting size of pore that can be measured by this method.

6.1.5 Theoretical analysis of mercury intrusion porosimetry

Drainage capillary pressure curves obtained by mercury intrusion porosimetry are customarily interpreted in terms of the bundle of capillary tubes model. The so-called pore size distribution of the model can be derived from the capillary pressure curve [119] by assigning the volume dV to the pores having entry diameters between D_e and $D_e + dD_e$:

$$dV = \alpha(D_e)dD_e \qquad (6.2.1)$$

Here $\alpha(D_e)$ is a (volume based) density function of pore diameter distribution, assuming $\varnothing = 0$ and letting $R = D_e/2$, in the case of constant and uniform values of the contact angle and the interfacial tension, one obtains by differentiation

$$P_c dD_e + D_e dP_c = 0 \qquad (6.2.2)$$

It is generally understood that these equations assign the volume of pores to the diameter D_e of the entry pores (necks) through which they are accessible. Drainage capillary pressure curves normally do not give any information on the pore size of the pores that are accessible through the entry pores.

An example of the distortion in the pore size distributions calculated from the drainage capillary pressure curves is where the mercury intrusion porosity pore size distribution curve for sandstone is compared with the pore size distribution obtained by optical means [119]. It is apparent that mercury porosimetry does not detect the presence of larger pores and assigns their volume to the pore entry necks. Despite this inadequacy of mercury porosimetry for even approximate characterization of the distribution of pore volume by the approximate pore dimensions, owing to its simplicity the method is used widely.

In spite of the distortion arising from not giving any information on a wide range of pore sizes and assigning the wrong volumes to the pore diameters that they have detected, the information contained in the drainage capillary pressure curves is very important. This is because the resistance offered by the pore structure to

various transport phenomena is controlled by the pore necks, and the sizes of the entry pore necks are deduced from the drainage capillary pressure curves.

In summary, the pore size distributions calculated from the drainage capillary pressure curves should be used with discretion and, preferably, in combination with pore size distributions obtained by optical means. This approach has been emphasized by Dullien and Dhawan [119] and has resulted in reasonably successful prediction of various transport phenomena.

Meyer [119] worked out a computational procedure, based on probability considerations, to correct mercury porosimetry curves. His procedure, however, has not been used widely. No probability consideration is able to determine the unknown sizes of those larger pores entered by the mercury through narrower necks for density results obtained using the Quantachrome Poremaster 33. The theory was governed by the Archimedes principle using the volume of displaced mercury in the empty and full cell, compared to a cell filled with mercury and with a test sample. This is a costly and good method as high pressure runs can retrieve a lot of information about pore families in the structure of the sample.

6.1.6 Sample preparation

Samples were left in the oven at 60°C overnight to combat the usual degassing problems incurred by these highly hydrophilic gel-glasses. Degassing of the samples was also attempted, but were time consuming to achieve results relatively equal to those obtained by drying overnight. Some procedure to liberate surface bound water is highly recommended otherwise full penetration of the sample will not occur. Problems can be incorporated whilst analysing solids with fine pore structure, where the existence of an adsorbed layer reduces both the effective pore diameter and the pore radius [120].

6.1.7 Results obtained using mercury porosimetry

Data sets were obtained for samples that had been densified in dry nitrogen atmosphere and a short study of 58S800 that had been densified in carbon

dioxide. This is a destructive technique, which requires a fair amount of sample to achieve accurate results. Earlier trials with small amounts of sample proved unfruitful. On average, the sample weight used for each run was ≈ 0.4g. Care was taken to keep weights similar throughout studies, so that this would not affect results.

6.1.8 Results obtained for 58S samples stabilized at different temperatures and those thermally treated in dry nitrogen

Software included in the Quantachrome Poremaster 33 programme, provided values for the skeletal density of the samples. This was calculated using the density of helium in combination with the amount of mercury displaced in a high pressure run. Low pressure runs proved unfruitful for the samples as only a small amount of mercury (0.1cc) penetrated the structure and was not enough for accurate calculation of the bulk density (requiring in the order of 0.4cc). This was only possible using high pressure runs with this material, care being taken not to use too much pressure i.e.>33Kpsi to avoid structural collapse during the run. Care was also taken to observe the temperature at which each run was made due to the variability in the density of mercury for even a 1°C rise in temperature. However, even though it is a highly costly and potentially hazardous method, mercury porosimetry was proved fast and effective in obtaining bulk density results. Thermally treated samples were chosen from the 58S800 series to obtain further results after a comparative study was run on the different stabilization products from the 58S formula and 58S800 proved the most stable of all regimes tested.

Standard deviation for the calculation of 58S800 without thermal treatment was 0.7584 for the bulk density measurement and 0.2000 for the skeletal density measurement, thus showing that the method for calculating these parameters was accurate for different samples. These results are gained from the extrusion curve of the run because intrusion results are rarely used to calculate useful data with this technique. A total porosity for the 58S800 sample was also measured as 36.75%. With the pore range being measured from 10.6 – 0.006μm. Tortuosity was also measured for this sample, with a value of 1.9776 and a throat/pore ratio of 0.2258 was obtained. This confirms that the pores are mainly cylindrical and

ink-bottle shaped, as a value of 2 for the tortuosity correlates to cylindrical pores. Table 6.1 summarises results for 58S stabilised at 400°C, 600°C, 800°C and samples thermally treated in dry nitrogen.

Table 6.1: Results for 58S stabilized at 400°C, 600°C, 800°C and samples thermally treated in dry nitrogen.

Sample	Weight (g)	Bulk density (g/cc)	Volume (cc)	Apparent (skeletal) density (g/c)
58S400	0.39	1.0	0.28	1.41
58S600	0.41	1.2	0.33	1.35
58S800	0.40	1.5	0.22	2.08
58S800/20mins dry$N_{2(g)}$at 900°C	0.40	1.5	0.26	1.55
58S800/20mins dry$N_{2(g)}$at 950°C	0.38	1.7	0.22	1.73
58S800/20mins dry$N_{2(g)}$at 1000°C	0.39	1.55	0.25	1.58
58S800/20mins dry$N_{2(g)}$at 1050°C	0.23	1.63	0.13	1.75
58S800/20mins dry$N_{2(g)}$at 1100°C	0.23	1.78	0.13	1.80

From the results, we see a trend of bulk density increase with increasing temperature, which also correlate to an increase in skeletal density with increasing temperature. The time of exposure for all samples was 20 minutes. Samples which had been treated at 1100°C for 20 minutes were analysed and deemed the thermal treatment limit before the glass-ceramic was fully crystalline.

6.1.9 Density measurements for 58S800 thermally treated in carbon dioxide atmosphere

A short study involving a select group of samples which were thermally treated in a carbon dioxide atmosphere at 60mm/min (consistent with the nitrogen study) in a tube furnace was completed as a comparison to the dry nitrogen model. This was to test the theory that a more condensed atmosphere with a molecule containing two oxygen atoms could produce a denser product at similar time intervals to those of the nitrogen study. Table 6.2 summarises the data for 58S800 treated in carbon dioxide.

Table 6.2: Results for data obtained from thermal treatment of 58S800 in carbon dioxide.

Sample	Weight (g)	Bulk density (g/cc)	Volume(cc)	Apparent (skeletal) density(g/cc)
58S800 Control	0.40	1.54	0.26	1.59
58S800/20mins at 900°C	0.43	1.58	0.27	1.68
58S800/20mins at 950°C	0.43	1.69	0.26	1.86
58S800/20mins at 1000°C	0.41	1.72	0.24	1.82
58S800/20mins at 1050°C	0.41	1.74	0.24	1.85
58S800/20mins at 1100°C	0.42	1.75	0.24	1.91

It is evident from the results that a carbon dioxide atmosphere produces a more highly densified product than does a dry nitrogen atmosphere under the same conditions. This is explained by the increased vapour pressure created by a gas molecule containing two oxygen atoms and its action on the material. Carbon dioxide provides a quantifiable alternative to testing the theory of whether enhanced densification could be produced by treatment using a more condensed atmosphere in comparison to dry nitrogen, as applying a water atmosphere at such temperatures above 400°C lies outside equilibrium conditions producing a system which can only be quantified by simple means (i.e. volume water in compared to

volume of water out). A graphical representation of the pore families obtained from the above study follows, showing that there are different sets of families in existence at different treatment temperatures and that a defined pore family is only present in the control material. This is also in accord with the nitrogen adsorption results and cannot be considered as noise.

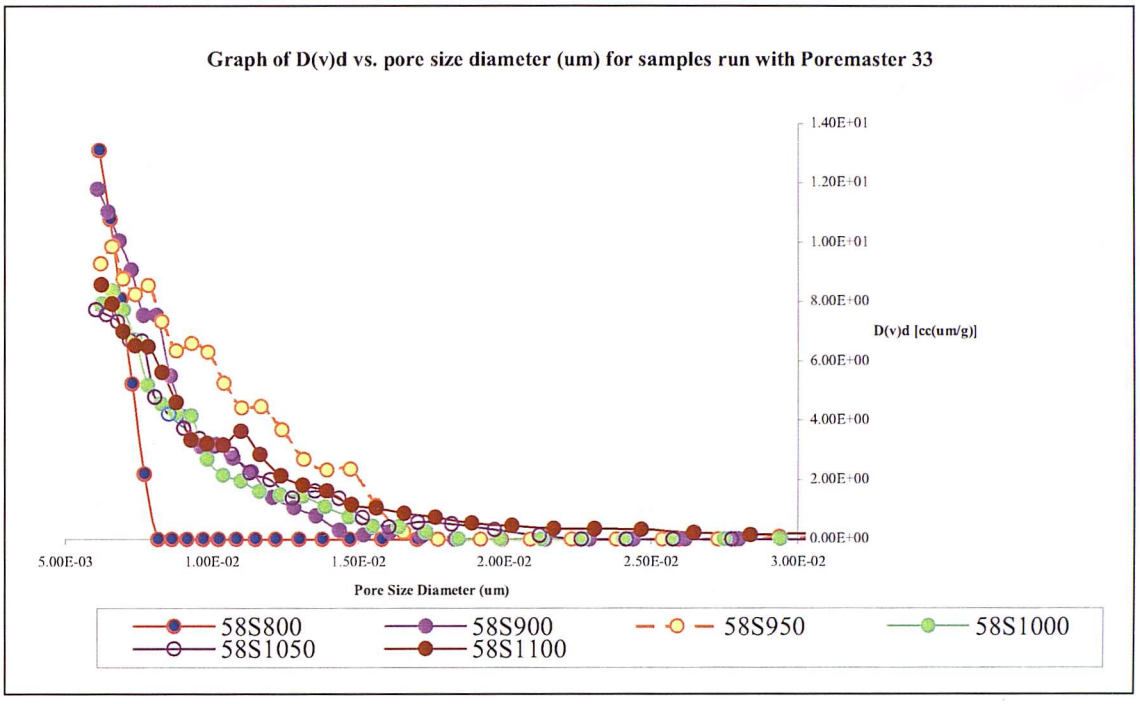


Figure 6.1: Graph of different pore families obtained from mercury porosimetry of 58S800 samples treated in carbon dioxide atmosphere for 20minutes, and at different temperatures.

A comparative graph of the pore size distributions generated from both nitrogen adsorption and mercury porosimetry is shown in Figures 6.2a and 6.2b outlining the complementary analysis available by both methods.

Figure 6.2a: Pore data obtained by nitrogen analysis of 58S800 [28].

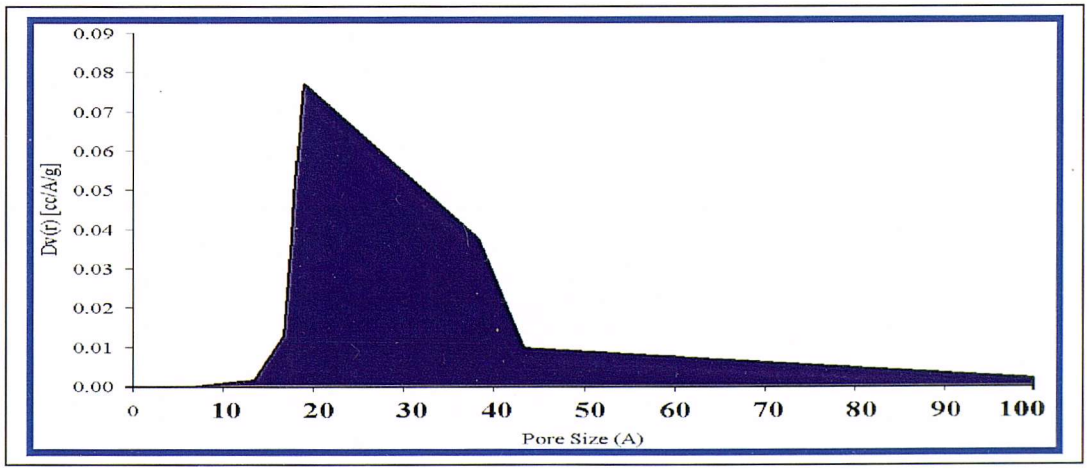
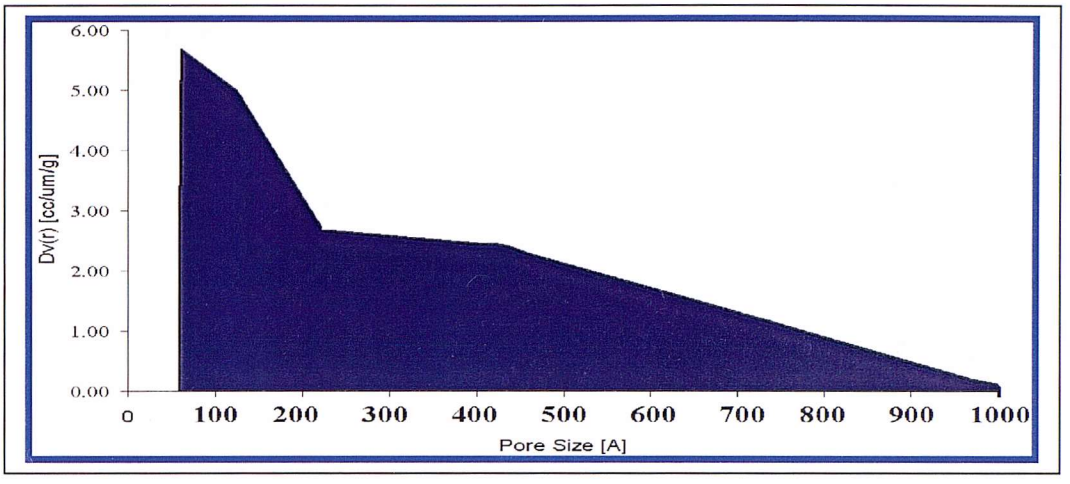


Figure 6.2b: Pore data obtained using mercury porosimetry for 58S800 [28].



6.2 Helium pycnometry of 58S samples

A Quantachrome helium ultrapycnometer was used to obtain data on the skeletal density of samples using partial pressures of helium gas. Analysis of an empty cell is first done to calibrate the instrument with an object of known volume, mass and density introduced afterwards. It was found that the apparatus would work most accurately whilst attached to a water bath (which kept the temperature of the apparatus constant) throughout the run. A level of tolerance, P = 0.05% was set for each run to assure the accuracy of the data. Since 20 or 30 runs could be collected on one sample in a matter of minutes. Since this technique was non-destructive many samples could be used for each experiment. Degassing the samples beforehand also was observed, samples were left in the oven at 60°C overnight. Followed by degassing conducted at 150°C for 3 hours just before analysis. Results are shown in the Table 6.3. A successful attempt was made to use this data to compare with the skeletal values obtained with mercury porosimetry.

An average weight of 0.4g was found for all samples tested in the study, this was found to be the weight giving the least 'dead volume' in the microcell used. However, it is evident from the above table that skeletal density is maximum for 58S800 (the product stabilised at 800°C for 24 hours) without further thermal treatment. This could be due to a lighter phase evolving during thermal treatment. In comparison to the skeletal density results obtained from mercury porosimetry for 58S the results are higher by a factor of 45% on average than those obtained by helium pycnometry for the same sample.

Table 6.3: Results from data obtained by helium pycnometry of 58S800 samples with thermal treatment in dry nitrogen.

Sample	Weight (g)	Average Volume (cc)	Average skeletal density (g/cc)	STD (g/cc)	Deviation (± %) 0.05%requested
58S400	0.38	0.30	1.29	0.014	0.35
58S600	0.38	0.29	1.31	0.017	0.50
58S800	0.38	0.28	1.40	0.037	0.97
58S800/20mins at 900°C	0.39	0.31	1.27	0.010	0.28
58S800/20mins at 950°C	0.38	0.34	1.10	0.022	0.79
58S800/20mins at 1000°C	0.38	0.34	1.12	0.022	0.69

Mercury porosimetry can be used to provide a value for the skeletal density but helium pycnometry is considered as most accurate for this data due to the way analysis is carried out. The helium molecule is small in comparison to mercury atoms trying to move throughout the structure (which has a limitation of pores which can be detected i.e. > 36Å when using mercury porosimetry). From nitrogen analysis, we see that the average pore size for 58S is around 60Å. This is too small for accurate penetration via mercury intrusion. In this work, ultrapycnometry was used to generate accurate skeletal density measurements and mercury porosimetry was used for the bulk density measurements of the materials. Skeletal density measurements obtained by mercury porosimetry in this work are for comparison only. It was noticed however, that temperature fluctuations and rough/undegassed surface hindered the accuracy of this method. But allowing for this it proved a quick and clean way of obtaining accurate results with known errors in a short amount of time.

6.3 Differential Thermal Analysis (DTA)

The sample and an inert reference material (Al_2O_3) were heated under identical temperature regimes (at controlled rate) and the difference in temperature recorded as a function of the sample temperature. All samples were scanned at a rate of 10°C/minute and with a final temperature of 1200°C using an STA-780 series Thermal analyser by Stanton Redcroft.

6.3.1 Results for DTA of unstabilised 58S and 58S stabilized at 400°C

DTA run on the unstabilized product of 58S, showed that there was a substantial weight loss of 10% due to physisorbed water at just over 100°C followed by a further 23% weight loss and a small event at 450°C followed by a larger event at 500°C, these features are attributed to nitrate evolution and decomposition in the material. At 580°C there is a glass transition event in the spectrum. No further weight loss is observed after 550°C. A crystallization (endothermic) peak was noticed at 930°C.

A subsequent DTA run on 58S stabilized at 400°C for 24 hours showed a similar weight loss of 10% at just over 100°C with an event occurring at 457°C followed by another event (creating a doublet) at 510°C. These features involved a further weight loss of 12%. These features are consistent with the amorphous calcium phosphate phase changing into β-$Ca(PO_3)_2$ [121]. At 580°C, the glass transition point occurs. After this, low weight loss (2%) was observed as the sample was then heated to 1200°C. Crystallisation occurred at 930°C and shown clearly in the spectrum as an endothermic peak. The resultant spectra were similar to work done by previous authors on the 58S system [123] and the $CaO-P_2O_5-SiO_2$ system [53]. Figures 6.3a and 6.3b show the DTA traces for the above experiments.

6.3.2 Results of DTA for 68S Bioglass®

68S Bioglass® was synthesized by the normal method and stabilized at 400°C. From the data obtained a weight loss of (8% was initially observed at just over 100°C. A further weight loss of (2%) was observed, coinciding with an event at 520°C, followed by an endothermic event occurring at 550°C. This was followed by the same gradual weight loss (7.5%) upon further heating to 1200°C and a small endothermic event at 1030°C, indicating a crystallisation event in the material, see Fig. 6.3c.

6.3.3 Results of DTA for 58S Bioglass® stabilized at 800°C

58S Bioglass® was synthesized in the normal procedure and stabilized at 800°C for 24 hours. The DTA showed a relatively 'flat' line, indicating that the material did not undergo any significant changes whilst being heated up to 1200°C. A similar weight loss at around 100°C was not observed. The material used for this run however, was highly desiccated after processing (as it had become evident that previous material processed was very hydrophilic). A small and broad peak was observed from 400°C to 650°C, which indicated the formation of β-$Ca_2P_2O_7$ (event 550°-575°C) [127], ending with a glass transition event at 580°C. A small event is seen at 1207°C, indicating the crystallisation temperature. However, due to the consistently 'flat line appearance' of the trace it could be hypothesized that a certain amount of crystallisation has already occurred in the product due to the higher stabilization temperature. But upon XRD analysis of the same material an amorphous halo is apparent, see section 6.4. An explanation for this 'flatter' trace is the fact that the material is already partially crystalline and that few, if any changes are occurring between the temperature range of 100-1200°C. Gradual weight loss is exhibited throughout the run (total 2.9%). This feature is also observed in the DTA spectra of 58S400 and 68S400. Figure 6.3d shows the DTA spectra for 58S800.

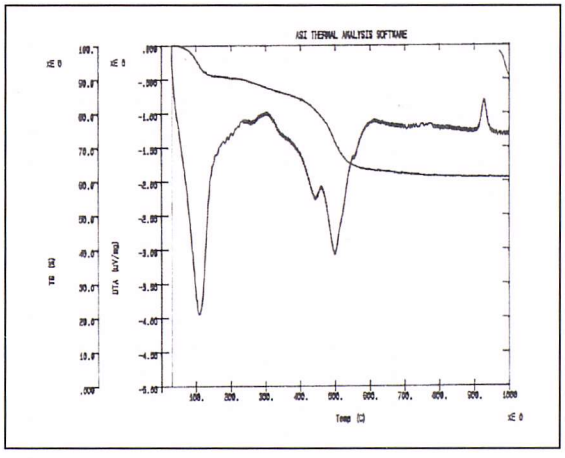


Figure 6.3a: DTA of unstabilised 58S.

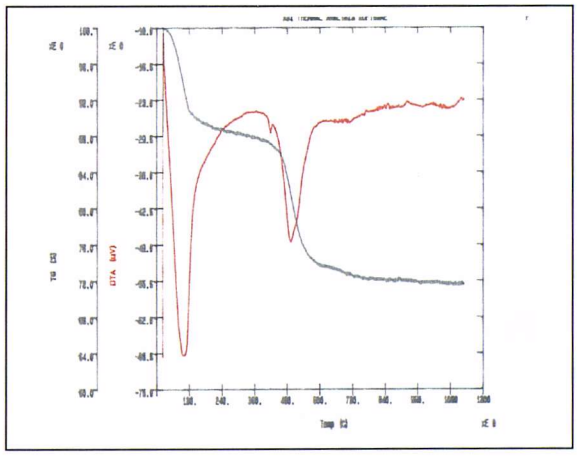


Figure 6.3b: DTA of 58S stabilized at 400°C.

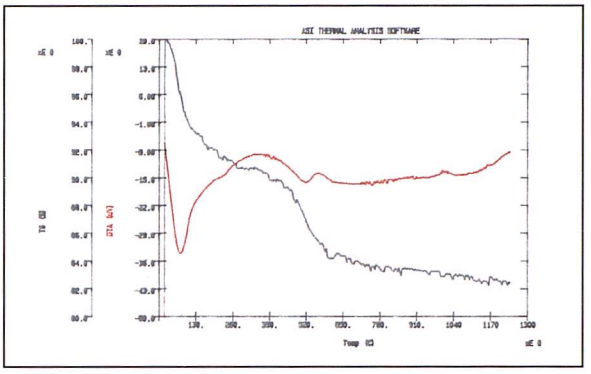


Figure 6.3c : DTA of 68S stabilized at 400°C.

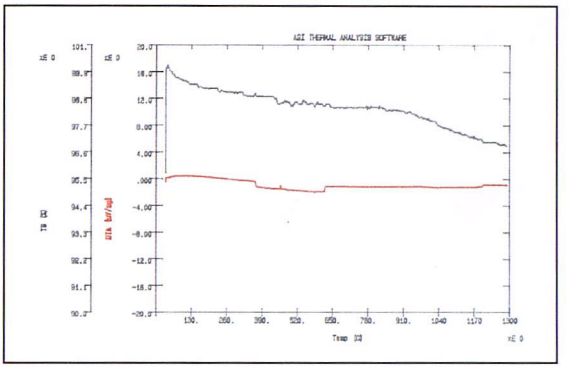


Figure 6.3d: DTA of 58S stabilized at 800°C.

6.4 X-Ray Powder diffraction (XRD)

The principal physical process involved in X-ray diffraction is the diffraction of X-Rays by planes of atoms. When an X-ray photon is incident on an atom, the electrons in the atom will experience the alternating electromagnetic field of the X-ray photon and will be made to oscillate. Charged particles such as electrons give out radiation when they are accelerated and thus, while they are oscillating in the electromagnetic field of the X-ray beam, the electrons of the target atom will emit radiation. The emitted radiation has the same wavelength as the incident X-rays emitted in all directions.

The Bragg equation for diffraction is:

$$n\lambda = 2\,d \sin\theta$$

where n is the order of diffraction, λ is the wavelength of the X-rays, d is the spacing between planes of atoms, and θ is the incident angle.

If a known monochromatic source of x-rays is used, such as Cu Kα radiation, the first order diffractive peaks due to constructive interference from diffractive rays will occur at a diffraction angle dependent on the spacing of the diffraction centres. If the intensity of diffracted X-rays is measured as function of increasing diffraction angle 2θ, then the spacing of diffraction centres can be calculated from

the angles of the diffraction peaks. A specific crystal structure will act as a diffraction grating in an X-ray diffractometer to produce a unique pattern from an unknown sample.

XRD Experimental

Powder (10mg) made from grinding 58S monoliths was used for the analysis and was investigated using a diffractometer with Cu Kα. radiation. Spectra were obtained from a starting angle (°2θ) of 5 and ending with an angle of 70. The same scan time and step level were used for all following experiments. The resultant patterns of initial products confirmed that the glasses were not crystalline. XRD was also used to look for other phases in the structure apparent after heat treatments. A Philips PW 1729 X-ray generator was used for all the experimental data apart from the data collected involving spectra recorded at different temperatures over time, these data were collected using a Philips Xpert X-ray generator, using the same scan rate as in all previous experiments.

6.4.1 Results of XRD analysis of 58S400

58S was synthesized in the lab using the normal procedure (see Chapter 4). The monoliths were then stabilized at 400°C for 24 hours. The run was timed at 1 second per step. This incurred noise on the trace but the amorphous halo produced showed that the product was not crystalline. The amorphous halo observed is centred around 22.5 (°2θ) representing the presence of a silica rich network-forming phase. Figure 6.4a shows the spectra obtained from this experiment.

6.4.2 Results of XRD analysis of 58S800

58S was made according to the normal regime and stabilized at 800°C for 24 hours. Again, an amorphous halo was obtained. However, a secondary 'hump' was also apparent. At this point, it was postulated that the material exhibited phase separation and this second feature was due to the secondary phase in the bulk material. It is not uncommon for these types of features to arise in amorphous phase separated glasses, sometimes even with a third 'hump' being visible in some cases, outlining the different phase constituents in the glass [128]. The second

'hump' occurring at an angle of 31.8° represents that reported by other authors concerning apatite ($Ca_{10}(PO_4)_6(OH)_2$) and β-$Ca_2P_2O_7$ formation, [127,129].
A third event is evident at 39.3° which indicates that calcite is also present in the material and also represents another peak in the spectrum reported for hydroxyapatite [129], see Figure 6.4b.

6.4.3 Results of XRD analysis for 58S400 with thermal treatment

58S was synthesised by the normal regime and stabilized at 400°C for 24 hours. Heat treatment was then applied for 75mins at 1050°C in air to obtain a more crystalline product. Many peaks are evident for the spectrum however, the remnants of an amorphous halo (non-flat base line) indicate that the material is still only partially crystalline. Table 6.4 outlines the major peaks within the range of 5-40 for the angle (°2θ). From the spectrum the previous two main phases seen in the amorphous products is still also part of the more crystalline spectra. This indicates that the parent glass is a reflection of the crystallised glass. At 22.9°2θ, the peak for the silica-rich glass forming phase [57] has been diminished and is covered by the other peaks, which represent crystalline phases of a CaP modifying agent in the glass. It is apparent from this that surface crystallization has occurred and that still within the bulk there is a volume of the residual glass phase as the baseline of the spectra are not entirely flat. Table 6.4 shows possible phases identified from XRD spectrum of thermally reacted 58S400.

6.4.4 XRD analysis of 58S800 with thermal treatment up to 1200°C

A Philips analytical XRD used to perform x-ray diffraction analysis from the surface of a 58S800 monolith that was placed upon a piece of platinum. XRD data were taken at three different temperatures (36, 600 and 1200°C respectively) followed by XRD of the final product that had been exposed to 1200°C. For the data taken at 35°C a clear double amorphous halo is observed with the first major halo centred about 22.5°2θ, indicating a silica-rich [53] or cristobalite-like network forming phase and the second halo is centred about 32°2θ, indicating the presence of an apatite phase. It is assumed that 58S800 is an amorphous combination of these two phases. However, it could also be the effect of randomly distributed crystallites or phase agglomerations in the material, which are too small to be

resolved by XRD. Table 6.4 summarises peak data obatined for 58S400 after thermal treatment in air.

Table 6.4: Peak table for the XRD analysis of crystalline 58S400 after 75 minutes at 1050°C in air.

Possible phase	Angle(°2θ)	Relative Intensity(%)
Apatite precursor	20.830	19.2
β-$Ca(PO_3)_2$	25.455	2.9
β-$Ca_2P_2O_7$	26.615	100.0
β-$Ca(PO_3)_2$	28.910	1.7
β-$Ca(PO_3)_2$	29.950	7.5
β-$Ca_2P_2O_7$	31.435	1.9
β-$Ca_2P_2O_7$	31.930	2.2
β-$Ca_2P_2O_7$	32.640	1.0
$Ca_{10}(PO_4)_6(OH)_2$	33.860	0.7
CaO	36.485	6.6
CaO	39.455	6.5

At 600°C there is the evolution of a peak which is further developed by 1200°C at 39°2θ. This is due to the transformation of precursor phases to crystalline β-tricalcium phosphate. Therefore, when a spectrum was taken of the surface of the monolith (giving a reading applicable for surface crystallisation only) these three peaks are still visible in amongst the noise of the amorphous halo, Figure 6.4d shows the spectrum obtained.

There is no doubt that this phase separated material contains a definite mixture of the above mentioned phases. There are certain known temperatures at which certain phases dominate but previous data accumulated for the Bioglass® system in particular has been mainly concentrated on melt-derived glasses and therefore a derived description is assumed for the situation occuring in the sol-gel derived glass. It may even be the case that the crystallites are distributed homogeneously throughout the gel-glass with similar diffraction spacings to the parent phases found in melt-derived glasses at the same temperature but are of a smaller size entirely due to the nanoscale features of this material. In this case, results may need further examination with techniques such as NMR that do not require the presence of long range atomic ordering. The spectra are also noisy and a more

lengthy analysis should be made to identify all peaks fully. The phase evolution of this material is of importance when considering its dissolution properties in a liquid medium, as some calcium phosphate phases are more soluble than others. This is discussed in Chapter 7.

6.4.5 Discussion of XRD results

In previous work done on melt-derived glasses most studies of phase evolution have been on binary systems, giving α-wollastonite on crystallisation. The main peaks for XRD are at 30, 27, 25.4, 23.2, and 28.9. The consensus given by this previous XRD work in combination with MAS-NMR analysis seems to be that P_2O_5 is present in an orthophosphate environment in the glass [130] with the presence of peaks correlating to the presence of hydroxyapatite also visible [53,129]. There remains no evidence that P_2O_5 takes part in the glass network for concentrations below about 8mol% and there is no evidence of pyrophosphate groups at that concentration either. Charge balance is achieved in glasses by removing calcium from its network modifying role to give calcium orthophosphate. However, one cannot eliminate effects due to phase separation in 58S perhaps involving other phases with different forms of phosphate behaviour. Due to the nanophase separation clearly visible from TEM analysis of 58S this is still unresolved: however, one of these phases visible could be calcium orthophosphate. Resolution down to the 2Å level would be required for this type of analysis and was beyond the scope of current work.

Previous work done on the formation of apatites *in vitro* [57] showed that glass-ceramics which employed biocompatible β-$Ca_2P_2O_7$ (β-DCP) have more soluble Ca-containing phases in the microstructure. XRD spectra from this study also confirm the presence of β-$Ca_2P_2O_7$ giving a peak at 32°2θ and the other predominant phase produced would be that of the bulk polymerized silica network phase, cristobalite (peak at 22.9 - 23°2θ). Due to the processing regime of the sol-gel monolith it is quite possible that the Q^4 network is set up (this being that the network constitutes four bridging oxygen bonds present in the glass structure) in the early stages of the gel evolution and then the connected units are 'frozen' in a randomly orientated state of chain-linkage. Cooling of the samples was not ramped and samples were contained in desiccant whilst still 'warm' to prevent surface reactions. Even though the gel-glasses are not quenched at any time the rapid drop from 800°C down to room temperature

without ramping is enough to burn off nucleated crystallite phases on the surface. This result in turn explains the NMR results shown later on in this chapter, which found evidence of a pyrophosphate environment, in combination with an orthophosphate phase and with the structure of the 58S sol-gel materials being predominantly Q^4 in nature. The main amorphous network forming phase is a common feature in all the XRD spectra for the amorphous product 58S, regardless of stabilization temperature. In the product stabilized at 800°C we can see that the double hump and presence of β-$Ca_2P_2O_7$ (β-DCP). From other XRD spectra shown before we see that the amorphous phase halo centred around 22.5°2θ, is the predominant phase of the glass structure with far more intensity, in all cases, than the secondary hump. In conclusion, the results indicate a primary silica-rich cristobalite phase with microphase separated regions of β-DCP homogeneously distributed throughout the material.

The structural chemistry of phosphates has much in common with that of silicates (based on the SiO_4 tetrahedron). SiO_2 tetrahedra link together in various ways to form Si_2O_7 ions, ring and chain ions of composition $(SiO_3)_n$ in metasilicates, layers and infinite 3D complexes, so PO_4 tetrahedra can link up to form pyro – or metaphosphate ions and $P_3O_{10}5$- ions. In these ions only one or two corners of the PO_4 are shared with others [131]. Any arrangement in which every PO_4 groups shares 3 of its O atoms with other PO_4 groups is necessarily electrically neutral and has the composition P_2O_5. Layer structures comparable with those of silicates is therefore not possible, but only complex groupings in which some of the PO_4 tetrahedra share < 3 corners. Orthophosphates can exhibit base exchange and reversible hydration like zeolites.

Some authors have identified the importance of calcium phosphate ceramics and have outlined that the stability of hydroxyapatite (HA) and β-tricalcium phosphate (β-TCP) ceramics depends on the temperature of preparation and the partial pressure of water in the reaction atmosphere [132]. This is of importance to this work when considering the solubility of the 58S Bioglass®. It is shown from these authors that the regions of decomposition in the β-TCP crystal show the presence of CaO as one if the major phases [132]. This is also conclusive with the decomposition of 58S Bioglass® in this work, found by XRD analysis.

Relatively soluble materials such as α- or β-TCP are resorbable, whereas stoichiometric and highly crystalline apatites (HA) are considered nonbioresorbable [132].

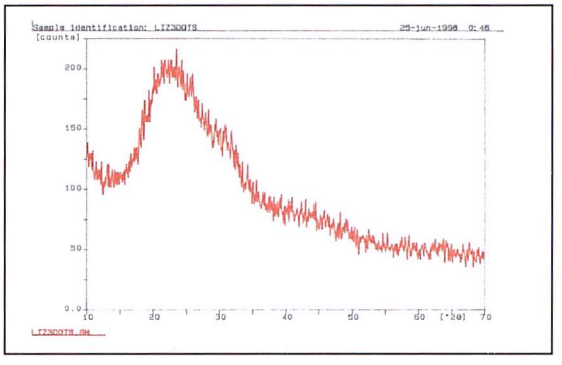


Figure 6.4a: XRD of 58S400.

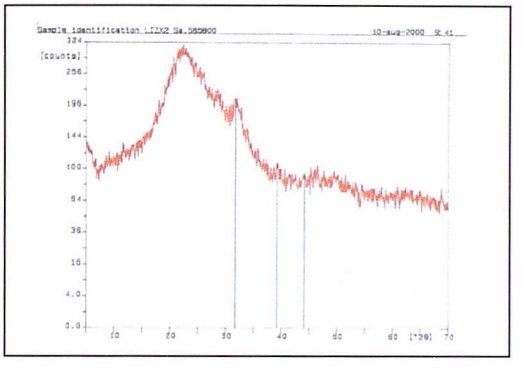


Figure 6.4b: XRD of 58S800.

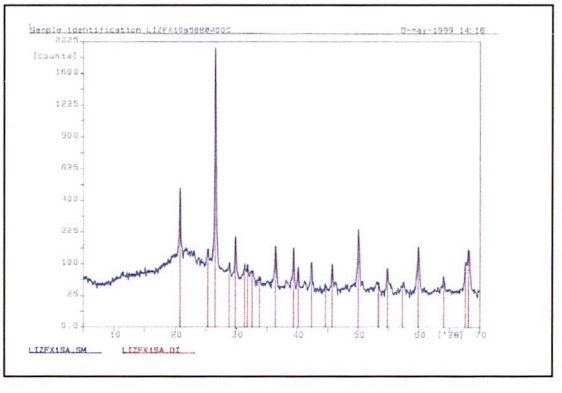


Figure 6.4c: Crystalline XRD spectrum obtained from 58S400 with thermal treatment at 1050°C for 75 minutes in air.

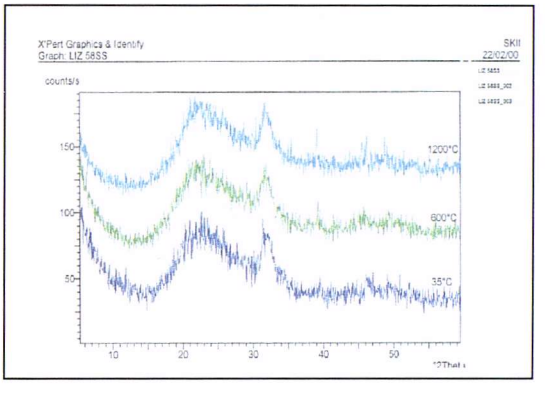


Figure 6.4d: Combination XRD spectra at different temperatures for 58S800 treated up to 1200°C.

6.5 Scanning electron microscopy (SEM) and Energy dispersive X-ray analysis (EDAX)

In scanning electron microscopy a beam of electrons approximately 10nm wide is scanned across the surface of the sample. Secondary electrons are generated from the surface of a sample where the electron beam is incident. The intensity of secondary electrons detected is related to the topography of the sample. High magnification images of the surface topography of a sample can be generated with a good depth of focus.

The intensity of back scattered electrons generated from deeper in the sample is influenced by the atomic number of the region examined. Therefore, back scattered

images can highlight compositional changes within the sample. EDAX is used in the SEM. The principle of EDAX is that incident electrons cause the ionisation of core electrons in the sample. When these core electrons return to their original state they emit X-rays with wavelengths characteristic of the type of atom. By analysing the X-ray energies produced in a SEM, quantitative chemical analysis of the region can be achieved. The resolution of such an analysis is of importance in the case of a sol-gel nanophase separated material due to the fact that analysis results taken from a region, being 10nm, it can be considered a result for the bulk composition only in the case of 58S Bioglass® and not for individual phases seen in the TEM micrograph (due a higher beam resolution of about 2Å being required to outline individual phases).

Experimental

Quantative EDAX was used for 58S Bioglass® rod samples and 68S Bioglass® pellets with a glassy phase. A comparative study was also carried on the affect of different aging regimes on the 58S formula, also in comparison to powder 58S obtained from US Biomaterials. SEM was used for 58S pellets dried by the 'watch glass' method and having been exposed to different mediums e.g. after immersion in water or with adhered cells. SEM was used to examine the surface of the 58S batch made with HF addition. This technique was also used to look at 68S pellets. In general samples are prepared by adherence with Araldite® glue to a 10mm diameter aluminium stub. In general, gold coating was used to insure conductance and thus a better result for pictures of the glass-ceramic, as these materials are non-conducting. Carbon coating was used where necessary to reduce charging effects for SEM EDAX analysis only. TEM analysis was also carried out on 58S to identify the ultrastructure of the material and was used to identify nanophase separation in the gel-glass.

6.5.1 Analysis of 58S Bioglass® using SEM and EDAX

Samples were not easily degassed, however vacuum effects were only applicable to distortion of results when considering the cell culture studies (when cells and the surface were freezed dried before analysis, see Chapter 8). It was found that cell arms were broken and cells became highly dehydrated due to this step in sample preparation. SEM EDAX analysis was performed directly after production of each batch. SEM analysis was performed both before and after immersion in deionised water. It was

found that the original surface was rough with growths of calcium rich deposits on the surface after limited exposure to atmospheric water. It was virtually impossible to perform analysis on an atmospherically sterile product. Exposure to the atmosphere during the processing procedure was inevitable, since samples were transferred from one oven to another between the drying and stabilization regimes of the monolith. It was also apparent that the material produced was highly reactive and hydrophilic in nature after CaP growths were repeatedly found on the surface of unreacted 58S.

When the sample had been immersed in water for 2 hours the growths became more bulbous and characteristic of an amorphous calcium phosphate rich phase. These types of growths had been regularly seen in studies involving liquid mediums with the bioactive gel-glasses. The rod produced from the day shortened cycle for 58S, was smooth on the surface down to the microscopic level due to moulding in Teflon (PTFE), (see Figure 6.5b). However, from the identification of a tweezer indentation on the surface of this rod it was also apparent that any feature imprinted in an undried gel could be successfully replicated on the surface of a stabilized monolith without catastrophic fracture created by cracks in the undried gel.

Pieces were later cut and dried to form monolithic shapes successfully as long as the gel was normally aged. Gels failed by brittle fracture whilst being cut at times of prolonged aging. It was also seen from the rod that most of the void fraction occurred below the surface and essentially the monoliths dried in such a way similar to that of a cake baked in the oven. With a porous interior and glassy like/smooth exterior, with a crisp edge which, in some samples, produced a transparent glass-like phase. Micrographs of the samples are shown in Figs.6.4a to 6.4f (in which the rod shown is transparent). For micrographs of the HF addition batch see Figs. 4.2a to 4.2f.

From the SEM analysis of the HF addition batch, it is clearly seen that CaF_2 is formed on the surface of the material with primary human osteoblasts (see Chapter 8). These are characteristically square in shape due to halide crystal geometry. In the case of the HF addition batch, the square crystallites on the surface indicate the presence of CaF_2 crystallites. In the normal recipe for 58S800, these phases evaporate due to the high temperature involved during stabilisation. This was followed by cooling inside the oven, which was neither graduated nor ramped.

This may explain the presence of the modifying phase in the glass developing into different CaP forms throughout the regime, nucleated from CaP-rich clusters formed during processing. The presence of the CaF_2 crystallites on the surface of the 58S800 batches with HF addition creates a more highly charged surface making analysis of this product easier and also creating a material that had the same biocompatible benefits of the original formula 58S800, (see Chapter 8).

For the SEM EDAX compositional study, 58S was prepared in the lab by the normal method but given different aging regimes. It is evident from the results that this variable does not drastically affect composition and that composition remains constant to levels of 1% homogeneity previously reported [10] when studying the bulk composition. However, from TEM analysis (see Figure 6.7b) it was not possible to perform EDAX on the nanosized phases occurring in the material due to the size of beam used. Any EDAX taken would encompass an area of 10nm, making all EDAX measurements representative of a bulk value. During analysis of the US Biomaterials (710-90μm) particles a flocculated phase was observed which had a slightly different composition to that of the bulk. This is thought to have occurred during the processing reime used in order to obtain a finer particle size rather than the traditional method of ball-mill grinding.

6.5.2 SEM and EDAX analysis of 58S compositions versus those with HF addition compositions synthesized in the lab

The processing procedure for these materials is already stated in Chapter 2. SEM was used to look at the surface of these materials, where growths were found even on unreacted specimens. EDAX was used to identify the composition of these areas as well as the matrix/bulk of the material. In Figure 6.6a, it is observed that the composition is varied from the growths on the surface to the bulk center of the material where silica is dominant and consistent with values expected from the compositional recipe of this material.

More frequently it is observed that the HF addition batches have regions of reaction product seen as a compositional feature, which are higher in calcium than the bulk of the sample which is seen in the data obtained from the original 58S formula (containing SiO_2 (58mol%), P_2O_5 (4mol%) and CaO (38mol%)).

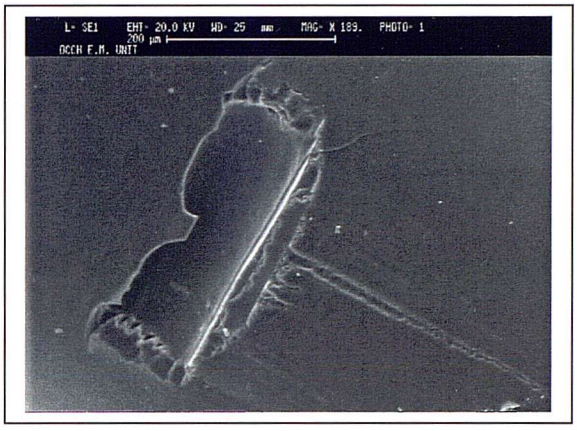


Figure 6.5a: Tweezer identation preserved in a rod of 58S400 without catastropic failure after stabilization. Fieldwidth, 635 µm.

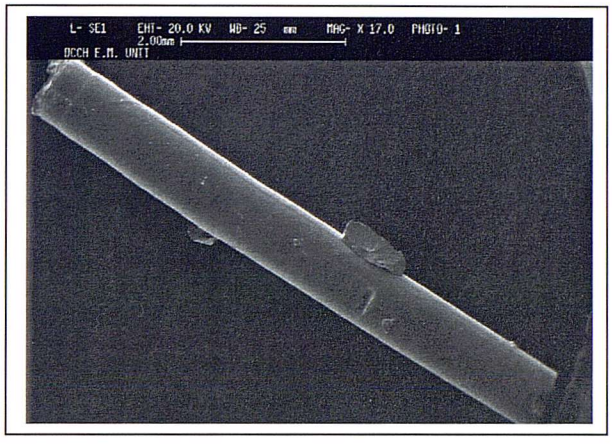


Figure 6.5b: Side projection of 58S400 rod made from PTFE mold at a shorter programme. L = 1.5cm D = 1mm. Fieldwidth, 6.8 mm.

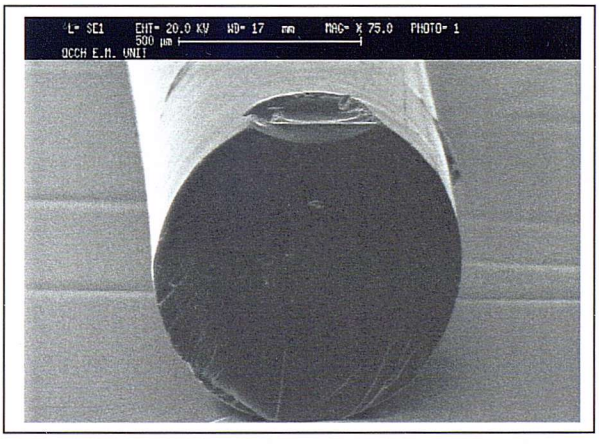


Figure 6.5c: End of 58S400 rod from 1 day shorter cycle. No evidence of surface porosity due to PTFE moulding. Fieldwidth, 2.4 mm

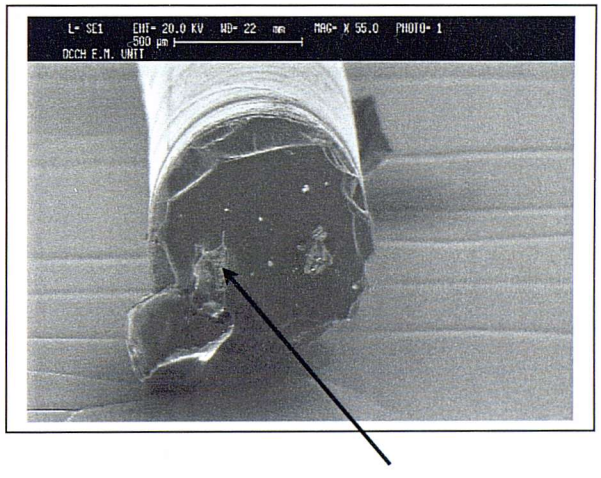
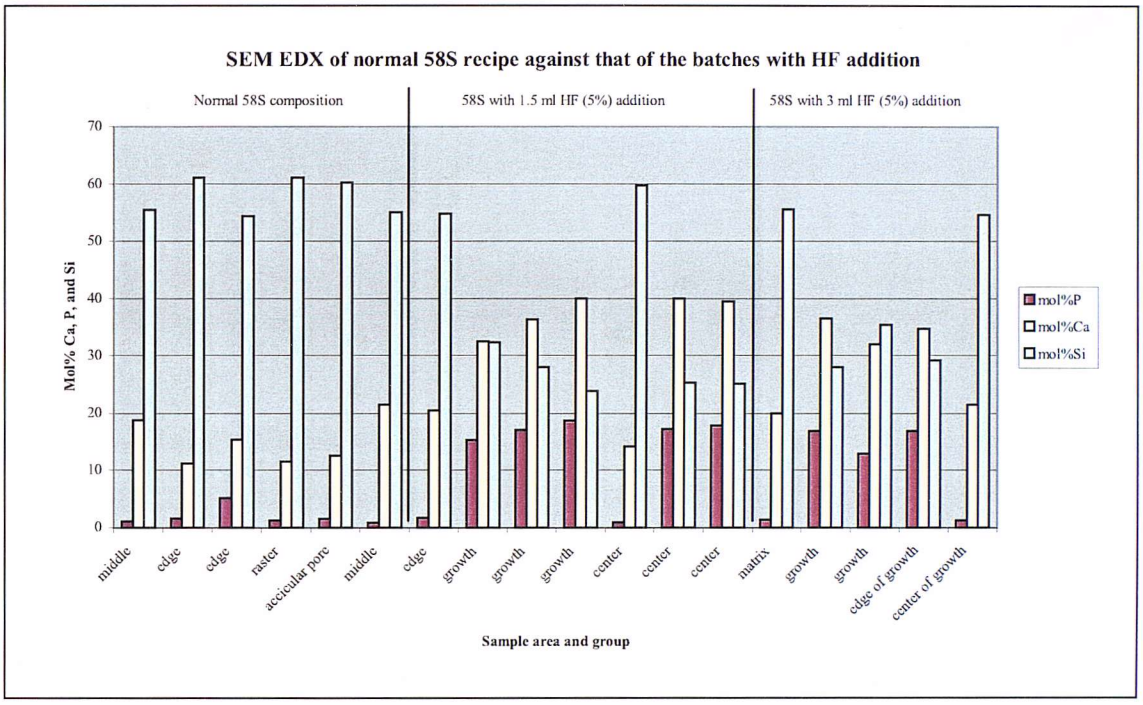


Figure 6.5d: Internal porosity is exposed at the other end of the 58S400 rod from a brittle fracture. Fieldwidth, 2.1 mm.

This was anticipated after precise synthesis using the US Biomaterials recipe and confirmed that the composition of US Biomaterials' product was the same as that made in the lab at Imperial College.

Figure 6.6a: Graph of comparative study with 58S (normal recipe) against 58S with HF (5%) addition.



All samples in the above study have undergone stabilization at 800°C and had the same processing regime. This indicates the difficulties arising when trying to replicate products in the lab using alkoxide sols, which are highly sensitive to a range of variables throughout the processing regimes. In addition, some compositions have proven difficult to produce to batch level in the lab due to factors such as the relative humidity in the room in which the gel is left to age and the temperature at which aging occurs. More phosphate content is also seen on the surface of the HF addition batches and silica content is lower in the areas where there are growths on the surface but remains at around the 60mol% level for the matrix and bulk of the material. This indicates that the HF batches are more reactive than the original 58S formula.

However, it is also seen that in the centre of the 1.5ml HF (5%) batch there is also a phase of high calcium and phosphate constituent. These types of surface topologies are thought to be hydrated calcium phosphate rich growths, the nucleus of the secondary growth of an amorphous calcium phosphate phase, but not fully crystalline in nature.

However, the surface of these calcium and phosphate rich growths have rough textures showing ordered and repeated topological features displayed by a bulbous and spherical type nucleus which increases in size with time and becomes more ordered, unlike the crystallite square geometry of the CaF_2 crystallites viewed on the surface of 58S with HF addition. However, these features can be considered as precursors to hydroxyapatite by compositional results which have Ca : P ratios ranging from 1.26-1.52 indicating an alkaline-poor hydroxyapatite formation. There are certain conditions of preparation where octocalcium phosphate cannot participate as a precursor in the formation of HA, high temperature, high pH, presence of fluoride ions, and very low levels of supersaturation. In all these cases, the resultant apatite tends not to have the stoichiometric Ca/P ratio. On the other hand, most conditions of the synthesis of HA tend to have low Ca/P ratios [133].

The Ca/P ratios of many synthetic and biological calcium phosphate precipitates are in the range 1.4 to 1.67; and since interlayered mixtures of OCP and HA have clearly been shown to exist by single crystal and by powder X-Ray diffraction studies [133] it is logical to expect that a low Ca/P ratios are related in part to the interlayering. However, the situation is probably more complex than simple combinations of layers of idealized OCP and HA. The hydrolysis of OCP to HA is an irreversible, topochemical process and almost certainly does not produce a defect-free HA. It is evident from the range of ratios calculated for the comparative study that the material has already reacted with the atmosphere on the surface and therefore, HA-like ratios are achieved. The flocculated phase found on the surface of the US Biomaterials' powders, which was high in silica and calcium could be formed due to the high reactivity on the surface of the fine particles. It could be considered that HA has already formed on the surface after initial exposure to the atmosphere during preparation for the experiment.

However, these phases cannot be openly identified from XRD spectra alone, which indicates a secondary apatite-like phase in the material which is present. It may also be the case that the crystallites formed are very small and beyond the resolution of a fast XRD scan with an amorphous halo of the bulk covering the identifying peaks. However, the Ca : P ratio indicates a phase not unlike hydroxyapatite. This phase is discussed further in Chapter 7 where FTIR analysis is used to try to identify the bonding nature of species in the grown layer on the surface of the samples. Many substitutional elements can be involved in the apatite structure and all growth formations on the surface of

bioactive materials may not strictly belong to the group of hydroxyapatites, but may not be adequately developed to give a Ca:P ratio of 1:1.67. The fact that crystalline spectra were only achieved using thermal treatment and not fluid reaction also indicates that the primary phase formed is not crystalline or that the crystallites are indeed beyond the resolution of XRD, or that a random homogeneous distribution of these crystallites may exist.

6.5.3 SEM EDAX analysis for a study employing different aging regimes for the synthesis of 58S800 versus US Biomaterials 58S powder

For this study, we prepared several batches of original formula 58S for use in different aging cycles to see whether this had an effect on the bulk composition of the product. US Biomaterial 58S powder was also analysed for comparison with the powder (710-90um) as received. Table 6.5 shows the sample description and nitrogen adsorption data on the 58S compositional study. The average sample weight for this study was 0.02g so that samples fit all tubes (without further cutting which would produce a newer surface) and avoiding small sample volumes which proved less accurate for comparative studies. Again the trend is of pore size remaining unaffected, in agreement with previous results describing the affects on phosphate glass pore size, which changes with increased temperature treatment [94].

Results shown in Table 6.5 shows that pore size values are consistently regular at 57Å ± 2Å in all batches made and stabilized at 800° and compared to other samples tested using the normal regime that yielded batch monoliths of 58S. Pore size still remained independent of any difference in aging cycles, along with total pore volume. The gel texture is developed within four days of aging (regardless of temperature) in the 58S system. Surface area changes throughout the different samples but does not show the expected general trend i.e. that a longer aging cycle will produce a material with lower surface area. However, it is generally seen throughout the batches made that the final product and gel evolution is very sensitive to both room temperature and relative humidity throughout the aging cycle.

We can say that those samples which have spent more time at room temperature (25°C), have lower surface areas, indicating that by increasing the temperature of aging a more solid shell on the outside of the monolith is formed more rapidly (due to surface

evaporation) once the material is exposed to higher temperatures of aging i.e. 60°C. The gel structure is formed quickly, perhaps within the first few days of gel aging and once the gel becomes solid (normally within 2 days at room temperature) the surface area ceases to change before syneresis occurs, squeezing out the pore liquor from the gel monolith. These effects are also shown in data obtained from nitrogen analysis of unstabilised 58S which gave similar pore diameter results as the stabilised product. However, due to its wet state, density measurements could not be performed on this sample as the structure would not with stand a low pressure run (13KPsi).

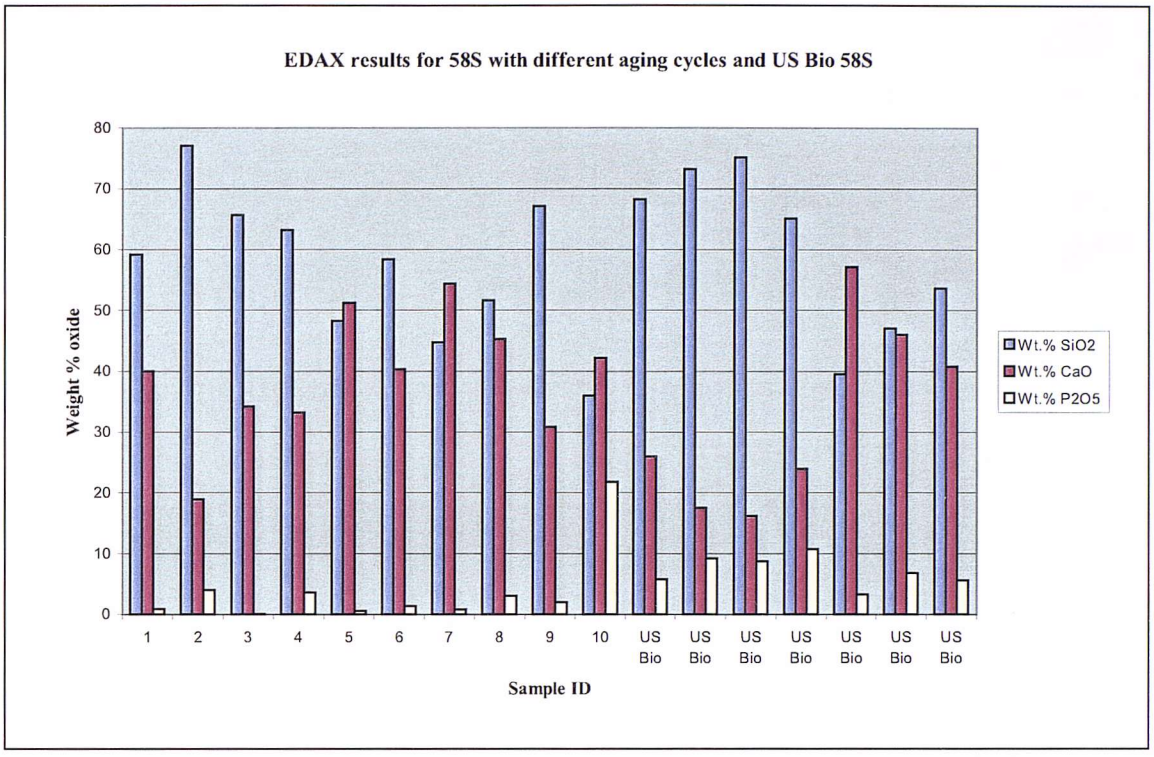
The corrosive nature of the undried gel also presented problems with other forms of analysis i.e. XRD, Hg porosimetry and helium pycnometry which could have provided important information on the gel evolution. Other authors have tackled this type of research using different recipes with which to make to initial sol [10]. A graph showing the results of the compositional analysis by SEM EDAX for 58S samples synthesised using different aging regimes versus US Biomaterials 58S is shown on the following page (see Fig. 6.6b). However, composition is seen to vary over the surface of the sample. This shows that the 58S material is highly reactive but can vary in composition by the 'location' of production. It is apparent (from processing many batches in this work) that room temperature and humidity are also critical factors which can produce differences from batch to batch and also outline the sensitivity of this process to basic variables, allowing the 58S Bioglass® product (which has been processed in a different place but by using the same recipe and a slightly longer drying programme in this case) to have finite differences in their compositional make-up when analyzed later using SEM EDAX. However, from this work it is seen that nitrogen adsorption analysis shows that there is no fundamental change in pore diameter due to change in aging processes (see Table 6.5). But that surface area of the product may vary, due to less time in aging producing a product material with a larger surface area. The changes in composition seen (when comparing the US Biomaterials product and the 58S made at Imperial College) can only be explained by the sensitivity of the sol-gel process to variables mentioned above or by the age of the sample i.e. older samples would have a higher Ca/P ratio on the surface due to longer exposure to atmospheric water and growth of HA on the surface. This higher Ca/P ratio is shown for the US Biomaterials 58S product, see Figure 6.6b.

Table 6.5: Nitrogen adsorption data for the study of 58S800 made using different aging regimes.

Sample ID: 58S Stabilized at 800°C	Sample Weight (g)	S.A (m^2/g)	Pore Diameter (Å)	Total Pore Vol. (cc/g)
Cycle 1 (2d - 25°C + 2d - 60°C)	0.022	111	55	0.48
2 (4d - 60°C)	0.027	109	56	0.43
3 (2d - 25°C, + 2d - 60°C)	0.019	64	56	0.45
4 (5d - 60°C)	0.018	83	57	0.42
5 (2d - 25°C + 4d - 60°C)	0.020	94	57	0.47
6 (6d - 60°C)	0.022	104	58	0.42
7 (2d - 25°C + 5d - 60°C)	0.022	71	59	0.43
8 (7d - 60°C)	0.026	71	59	0.44
9 (7d - 20°C + 3d - 60°C + 38d - 20°C)	0.024	99	58	0.50

Total pore values are stable with an average of 0.46 +/-4 cc/g. Pore diameters are also stable across the different aging regimes. However, when looking at the SEM EDAX results a different story emerges about the stability of the composition across the various aging regimes. We find that compostion does vary somewhat given the different processes and that some sample seem to be calcium predominant at the surface and others have maintained bulk composition much more like that of 58S.

Figure 6.6b: Graph of compositional analysis by SEM EDAX for 58S samples synthesised using different aging regimes versus US Biomaterial's 58S powder.



Sample ID 1-9 correlate with those given in Table 6.5 for the compositional study in which 58S gels underwent different aging regimes. EDAX analysis was performed in the matrix/center of all samples to obtain a value for the bulk of the product. However, the edge of the 58S powder sample supplied by US Biomaterials was also analysed (represented in the last 3 Sample IDs on the right hand side of the graph) shows a definite difference in composition which is high in silicate and calcium concentration.

This may be the flocculated phase induced when the powder was processed. It is also evident that in samples numbers 5-10 there is a replication of this phase, which is high in silica and calcium, unlike the usual high ratio of Ca to P present in apatitic type materials. Sample number 10 shows the EDAX results of a growth on the surface of sample number 9 and yet again indicates the high reactivity of this material in the atmosphere alone creating instantaneous CaP rich growth formation on the surface incorporating the more mobile modifying agents in the glass. These ions have greater mobility to move within the silica-rich network structure of the parent glass. The high mobility of such entities to the surface, explains the high reactivity of the sol-gel derived gel-glass.

Calcium is usually the first ion present at the surface, with silica forming the matrix of the material and phosphates being involved in a hydroxyapatite like complex (which appears as a bulbous type amorphous growth) on the surface of the material. In samples 5-10, we subjected the normal 58S sol to longer aging cycles than samples 1-4, perhaps allowing enough time for the calcium to become mobilized and reach the surface. This rapid movement of calcium to the sol surface after exposure to atmospheric water is indicative of a reactive surface with a high surface area of a sol-gel product. The sol-gel product can liberate more ions in liquid mediums and in shorter times than that its melt-derived counterparts, which show behaviour likened to that of a non-porous glass with low surface area.

The composition produced in the lab displayed correct composition values consistent with those obtained from US Biomaterials. However, it is clear that a material with such small phase separated regions can only be quantified accurately on the angstrom level. From TEM images seen in the next section we conclude that there are three different phases within 20nm from any given point on the surface. It is therefore a question of how the phosphate and calcium modifiers may exist in these regions and how this could affect the rates of evolution of ions from the bulk glass, knowing that one of the regions is defined as the random network of silica rich chains in the glass.

6.6 Transmission electron microscopy (TEM)

The Transmission electron microscope (TEM) is analogous to an optical microscope, and uses lenses to form an image, to look at the internal structure of the material. However, operation and interpretation of results is difficult, depending on the wave-like character of electrons. The interaction/scattering of electrons by matter is very strong therefore, one needs a high vacuum in a microscope column and very thin specimens i.e. <100nm.

In the TEM analysis of amorphous materials, phase contrast shows the two main phases that are present in the area observed from the surface of a thin section cut from a thin shard of 58S monolithic fragment. Diffraction patterns are observed resulting from the local fluctuations in atomic distribution; local atomic spacing information is also contained in the image if a crystalline phase is present. The principal use is in mass-thickness contrast. Amorphous halos were seen in all other experiments performed and

one diffraction pattern was obtained from the edge of a particle which represented the reacted HA product after exposure and reaction with –OH groups. These groups are present in ethanol (involved in sample preparation for adherence to the copper grid). However, results obtained from the thin sectioning rather than particles proved very revealing about the scale of the phase separation in this amorphous material.

From the dispersion of the different phase regions (given by grey-scale appearance) in the 58S material it is evident that there are several phase changes within the space of 50nm, this is similar to the scale of a natural grass depicted in Figure 6.7a. These nanoscaled phases formed in the sol-gel 58S where not visible using other optical techniques.

Electrons are scattered by the atoms in the specimen. Therefore, the thicker the specimen or the higher the atomic number the more electrons will be scattered as the electron beam passes through the specimen. The objective aperture, positioned in the back focal plane of the objective lens stops all electrons scattered by an angle greater than α. As thick regions or regions of higher atomic number scatter more electrons these will appear darker. With such analysis, it is of fundamental importance to try to create as thin a specimen as possible for analysis as there can be interference between two layers making the phase change picture less clear. This type of superimposed layer was seen in thicker specimens examined by TEM scan prior to the thinnest specimen being analysed.

6.6.1 Sample preparation for TEM and results for 58S400 and 58S800

The main requirement is for the sample to be thin for analysis. It is often not possible to satisfy completely all these requirements and thus the first TEM sample was made with 58S400 powder adhered to a copper grid. Particles were immersed in ethanol, as water was known to react quickly with the powder surface. An ultrasonic bath was then used to ensure random distribution of the particles in the solution that the copper grid was then dipped into. When the dispersion of particles was analyzed, it was apparent that even ethanol supplied -OH groups had reacted with the surface of the particle but not with the bulk. A diffraction pattern was obtained from this crystalline region on the edge of the particle after reaction and was found to be similar to that of hydroxyapatite.

However, a direct match could not be made with pure hydroxyapatite. From data using other analytical techniques this reaction product could be either a precursor to fully crystalline hydroxyapatite of a calcium deficient type, as the number of diffraction distances available from this method were not directly matching to those given for fully crystalline HA, sourced from XRD reference cards.

Another reason for the mismatch in identifying the d-spacings from the pattern obtained from the edge of the particle could be that the type of hydroxyapatite formed has a different orientation from those spacings recorded for pure hydroxyapatite in the literature. It could also be the case that the crystals do have the exact same d-spacing of that of regular hydroxyapatite due to their size. Crystallites formed on the surface of the sol-gel glass would be small in size. However, within the bulk of this same sample, only an amorphous halo could be obtained. From this is it thought that the reaction product found on the edge of the particle was not present in the bulk. This remains the only diffraction pattern available from this technique.

A second attempt was made to see some type of structure within the glass and this time slivers obtained from fractured 58S800 monoliths were cut into thin slices with a diamond saw in the presence of ethanol. This method proved to give the best results for structures, which were found to be on the nanometer scale. However, because no cold field TEM analysis was available one can see that the specimen was destroyed during the analysis by the 'melted' appearance seen in the top right hand corner of some micrographs.

The phase change within the sample is so small that EDAX analysis could not be done on each specific phase. However, it is known that certain TEM microscopes in Oxford can find EDAX resolution to that of 2Å, (see Chapter 9). By using this image, one can calculate a volume (by grey scale) of each phase in the image and also some shape of the phases, which exist there. Other methods such as chemical thinning were not used but TEM would prove a powerful tool for further analysis of the microstructure of this sol-gel produced glass-ceramic.

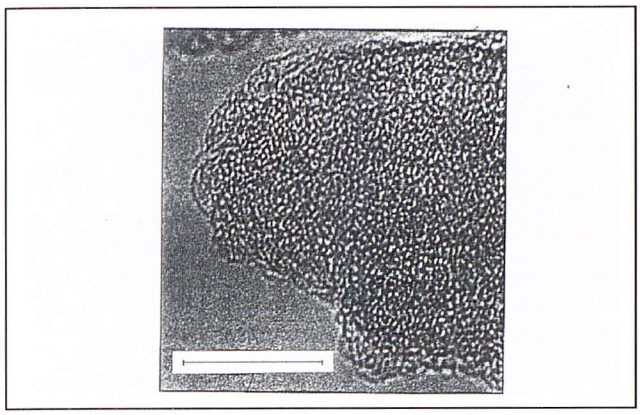


Figure 6.7a: Natural silica TEM scan. Fieldwidth, 24.5nm *Phalaris caneriensis.* [134]

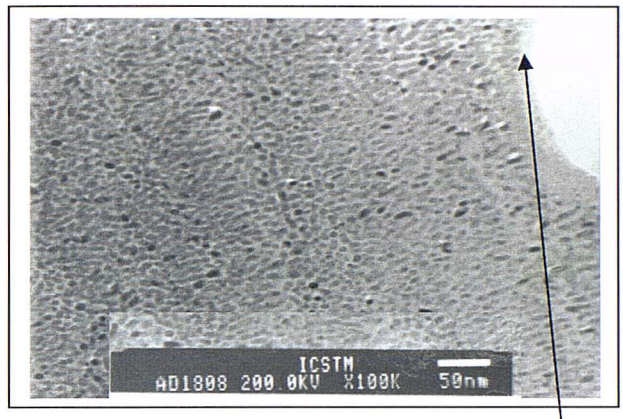


Figure 6.7b: TEM scan of 58S800 Fieldwidth, 506nm.

Melted area

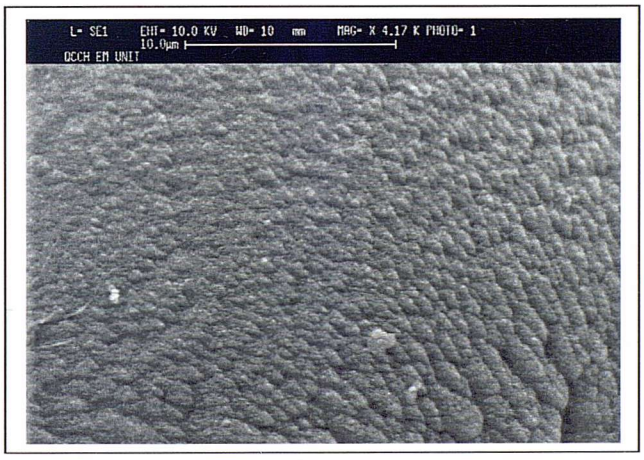


Figure 6.7c: High resolution of surface of amorphous HA growth on the surface of 58S. Fieldwidth, 28.2 ìm.



Figure 6.7d: High resolution of crystalline type growth on the surface of 58S. Fieldwidth, 11.6 ìm.

6.6.2 Discussion of TEM results

In this work a structure similar to that seen by Bailey et al. [135], who were looking at the development of silica sol-gel glasses is observed. It is also possible to compare the structure of this sol-gel derived material to that of zeolites. Zhang et al. [136] state that this type of structure can be hard to interpret because indications of 10-15nm grains in the samples make it hard to differentiate between surface and bulk crystallinity using microscopical techniques. Others who have dealt with the synthesis of zeolites and like materials for analysis by this method report that the silicon environment in synthetic silica is the same type as that found in biological systems, e.g. in the choanoflagellate, *Stephanoeca diplocostata*, and in various grasses [134]. These authors also report that the very high resolution electron microscope study of rods of *Stephanoeca diplocostata* shows that the silica present was amorphous down to the highest level of resolution. Upon examining the nature of the silica in the grass *Phalaris canariensis*, the image produced looks similar to that of the micrograph obtained from the TEM of 58S. The opaline bodies have no order down to the level of 10Å. These materials can also contain various amounts of tightly held water. It is evident from the TEM micrograph of 58S that the phase changes 10 times within the space of 50nm. The difference in grayscale colours defines the heavier and lighter phases within the material, in combination with the structural analysis of the densified product it is possible to say that there is an amorphous silicate matrix in the bulk with a CaP interstitial compositions dispersed amongst the network forming silica rich phase.

6.7 Nuclear magnetic resonance (NMR)

NMR has long been used to obtain structural information about glasses. The information given by these studies has, in the main, been concentrated on quadripolar nuclei, for example the use of ^{11}B to determine the relative amounts of 3 and 43 fold co-ordinated boron in glasses. Other main themes have been concerned with using dipolar broadened line shapes to test for the probability of particular local configurations [137].

The basic concepts of oxide glass structure are that certain oxides can form strong ionic-covalent bonds in a 3D network; this presents a kinetic barrier to bond rearrangement and crystallisation. Other modifier oxides can react with the network to break these

bonds producing mobile ions and increasing the degrees of freedom of the network such that rearrangement becomes easier and the glasses less kinetically stable. The usual example of this involves the soda-silica binary. In pure silica, four strong Si-O-Si links exist between $[SiO_4]$m units and the rigid network results. Addition of modifier oxide Na_2O produces $Si\text{-}O^- Na^+$ units which reduce the rigidity of the network since Na^+ are mobile and the Si-O- make more than 9 degrees of freedom available to the network than Si-O-Si. At a Na_2O content of 33.3mol% there is enough added oxygen to give an average of one non-bridging oxygen [nbo] per silicon and three bridging oxygen [bo] remaining . At 50mol% Na_2O the average is 2 [nbo] per silicon, which now have only two strong links to the other silicons, i.e. the 3D network has degenerated into chains. Any further disruption of the linkages results in a rapid decrease in stability and glasses can only be formed with considerable difficulty. So far, we have referred to an average number of [bo] and [nbo] per silicon. The properties of the glass will in fact depend quite critically on the exact way in which the different bond types are distributed, i.e. quantities of different Q^n species present.

There are several possible arrangements [137]:

1. Statistical distribution (unconstrained random) – the distribution of [nbo] is determined only by composition and statistics;
2. Binary distribution (constrained random) – [nbo] repel each other leading to maximum dilution which in turn gives successive formation of lower Q^n types and homogeneous distribution of no more than 2Q types results;
3. Clustered – [nbo] cluster, eventually leading to phase separation.

Although octahedral silicon was not observed in this binary glass, it has been observed in $Na_2O\text{-}SiO_2\text{-}P_2O_5$ glasses [137]. Others have realised the importance of understanding the structural nature of bioactive glasses [138]. Most of the glasses are based on systems which present a concentration of calcium higher than 30mol%. The behaviour of this group has been mainly related to their chemical composition, but a careful understanding of their structure is also necessary to understand their properties. It is proposed by Galliano et al. [138] that SiO_4 and PO_4 tetrahedra are the basic structural units in most of the studied glasses. But their arrangement is strongly dependant on composition, which determines the degree of polymerisation and the distribution of the P- and Si- containing structural units.

In particular, phosphorus tetrahedra can be linked together in chains and/or rings in phosphate glasses. However, phosphorus in alkaline earth silicate glasses with low phosphate contents was reported to be in isolated $(PO_4)^{3-}$ tetrahedra which do not share oxygens with other phosphorus or silicon groups, with respect to the silicate glass structure. Phosphorus was found to exist in an orthophosphate environment if the amount is lower. The results also indicated that the nature and amount of the alkaline earth cations have little effect on the environment of phosphorus in the range of compositions used in the study [138].

The introduction of P_2O_5 into the binary alkali silicate glasses has a profound effect on their structure, particularly at high concentrations. Dupree et al. [137] have studied the $R_2O : 2SiO_2$-P_2O_5 system over a wide concentration range of P_2O_5; small amounts of P^{5+} act as a 'scavenger' for alkali ions giving $P\text{-}O^-R^+$ units in preference to SiO^-R^+. This removal of R from the silicate network allows it to repolymerise i.e. the number of [nbo] is reduced and Q^n units of higher n are formed. In the case of the disilicate glasses, Q^4 silicons are formed from Q^3 when P_2O_5 is added. The ^{31}P environment depends on the P_2O_5 concentration and the type of alkali metal oxide. At very low concentration and low atomic weight, alkali metal is the predominant species with the chemical shift of 10-15ppm closely resembling that in alkali orthophosphates.

A 'nucleating agent' may be broadly defined as an addition that either causes volume crystallisation (after suitable heat treatment) of a composition which would not otherwise show it, or, if the composition already exhibits low volume nucleation, increases it. In spite of their importance, the roles of non-metallic nucleating agents are often obscure. In addition, their action is specific to certain systems.

Detailed studies of the role of P_2O_5 in various systems have been reviewed by McMillan and James [137]. One system in which P_2O_5 is particularly effective as a nucleating agent is Li_2O-SiO_2. In a previous study by James [137] nucleation rates of lithium disilicate in a $33.3Li_2O.65.7SiO_2,1P_2O_5$ (mol%) glass were compared directly with a $Li_2O.2SiO_2$ base glass. The nucleation rates in the P_2O_5-containing glass were much greater than in the base glass at higher temperatures (1000 times greater at 500°C), but the effect became less with decreasing temperature and below 450°C the nucleation rate converged. Amorphous phase separation was also observed in the P_2O_5 glass. Another particularly effective 'nucleating agent' is 'water', which is present in most glasses in

small amounts as either hydroxyl groups or molecular water. The effects of water content are also highly relevant to crystallisation studies of glasses prepared by the sol-gel process, as discussed by Zarzycki [137]. These glasses often contain higher hydroxyl levels than glasses prepared by conventional melting.

Phase separation in glass has been examined by many authors; one of the earliest studies being by Greig [137]. Since then it has been the subject of many investigations and there is a whole area of glass science devoted to this phenomenon as it affects microporous glass applications. There are essentially two types of phase separation, stable and metastable immiscibility. Stable immiscibility occurs when the glass separates into two or more distinct phases at temperatures greater than the liquidus temperature of the glass. On cooling, the resulting glass shows distinct regions of differing composition. These manifest themselves as layers of milkiness in the glass. Metastable immiscibility occurs at temperatures below the liquidus temperature. An example of a system that exhibits stable immiscibility is the $CaO\text{-}SiO_2$ system between about 2 and 27 wt% CaO. Above the liquidus temperature of 1705°C the melt separates into the liquid phases.

The data gathered for Vycor® glass [139], which has similar physical properties to those of Bioglass® 58S, showed that subsequent removal of the soluble alkali-borate phase by acid leaching resulted in a high siliceous (>95%) skeleton with a mutually interconnected pore structure. The tendency for borosilicate glasses to phase separate was controlled by the addition of other elements to the glass. Small quantities of P_2O_5, V_2O_5, MoO_3 and WO_3 shift the immiscibility region with the result that the more soluble high-borate phase contains less silica and this enhanced the leaching properties glasses made in the work of Tomozawa and Takamore [137].

Thermal heat-treatment of Vycor® glasses has a very strong influence on the phase separation process and hence the pore size distribution and morphology of the leached glass network. The liquidus temperature of the insoluble silica phase is around 1000°C with the onset of phase separation at 750°C [93]. Heat-treatment between 750°C and 1000°C results in both phase separation and devitrification although the resulting structure is one of droplets of the soluble phase in a continuous silica-rich matrix. To develop a fully interconnected structure heat-treatments for a few hours to several days at temperatures between 500-600°C are required and there is evidence that prolonged

heat-treatment above 600°C results in coarsening of a finely interconnected system to that of droplets by diffusion controlled agglomeration of the soluble phase. In many cases, the phase-separated glasses exhibit opalescence and techniques commonly used to this end are electron microscopy and differential thermal analysis (DTA). Synthesis of Vycor glass and its properties is noted in the work of Powers [93].

6.7.1 Results of NMR analysis of 45S5 and 58S Bioglass® powder

NMR analysis was performed by Abil Aliev of the Department of Chemistry, UCL, London. Both single-pulse excitation (with 45 degree of pulse and 10s recycle time) and CPMAS (contact time 5ms) 29Si spectra were recorded. Of the samples analysed 45S5 (melt-derived) Bioglass® was compared with sol-gel derived 58S produced by US Biomaterials and that produced in the lab at Imperial College (58S800). CPMAS shows that sample 1 (45S5) is different from Samples 2 and 3 (58S). In sample 1, SiO_4 tetrahedra are low Q species and in samples 2 and 3 are mainly $Q_2 - Q_4$. . Based on these and Gaussian deconvolution results, contents of Q-species estimated are shown in Table 6.6.

Table 6.6: Results of NMR analysis of 58S and 45S5

Sample No.	Type of Bioglass	Powder Size	mol% SiO_2	mol% P_2O_5	mol% CaO	mol% Na_2O	$\%Q^2$	$\%Q^3$	$\%Q^4$
1	Melt-Derived 45S5	<20μm	46.1	2.6	26.9	24.4	100	0	0
2	US Bio. SG 58S	<20μm	60	4	36	0	16	11	70
3	IC SG 58S	<25μm	60	4	36	0	4	19	77

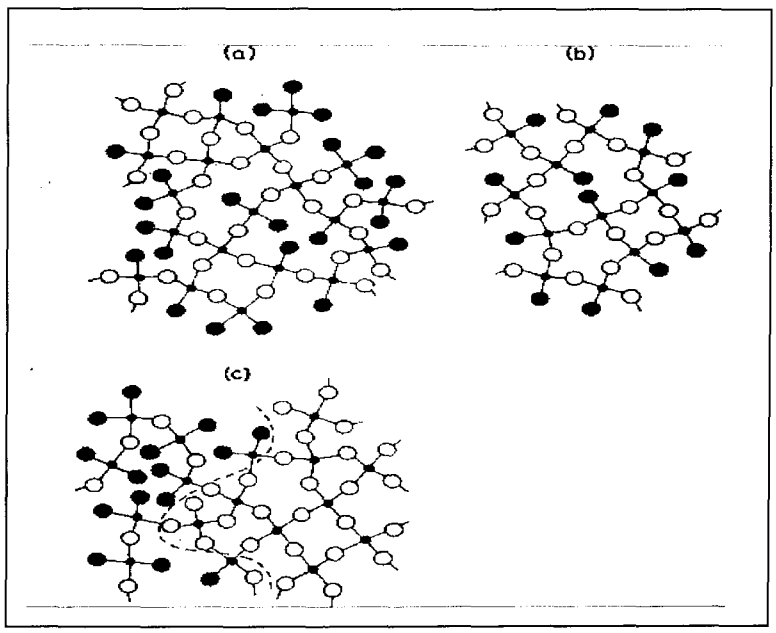
6.7.2 Discussion of results obtained by NMR analysis

An attempt has been made below to resolve the results obtained with the use of previously reported materials. However, due to that fact that superimposition could interfere with the accuracy of results for a ternary system glass, they should be treated with caution. Fig. 6.8 is a schematic diagram of types of disorder in a binary alkali disilicate glass (a) Random distribution of Q types; (b) all Q_3; (c) phase separated in to

Q_4 and Q_2. The basic unit is a silicon atom (small circle) surrounded by four oxygens (large circles). Bridging oxygens are open circles and non-bridging oxygens filled circles [137]. This technique gives us information on the network structure. When regarding the dissolution kinetics, when the IC product dissolves less quickly than the US Biomaterials' product, this can be explained by a higher percentage of Q_4 than Q_3 species in the IC product. In previous experiments [54], it is founnd that resorption may be controlled and ion release is far higher in the sol-gel derived product, when compared to the melt-derived product.

From the ^{29}Si MAS NMR it is evident that melt-derived 45S5 glass is different from both of the 58S sol-gel derived products. The results obtained for the melt-derived 45S5 Bioglass® were in accordance with previously published results [138] and from the spectra obtained Q^2 species were seen to predominate in the glass structure. This had been reported in other work done on some amorphous and crystalline systems containing both SiO_2 and P_2O_5, where strong dependence of the local structure of the Si with RO content was not observed in relation to the structure in this study [138].

Figure 6.8: Schematic diagram of types of disorder in a binary alkali disilicate glass [137].
a) random distribution of Q types; (b) all Q_3; phase separated into Q_4 and Q_2.



The phosphorus was present in monomeric (Q^0) units in all the samples tested. A heterogeneous distribution of alkaline earth cations resulted, since the RO content surrounding the P-containing structural units is higher than the corresponding values associated with each Si tetrahedron. However, the results suggested the existence of microheterogeneities in the glass structure, due to the presence of: a) P- and R-rich zones, and b) Si-rich zones with a relatively lower R content. Results from earlier EDAX investigations suggested compositional changes within a very small area in the glass, due to the spontaneous growth of an apatitic phase on the surface when 58S is exposed to moisture in the atmosphere. We suggest that these CaP rich sites present in the bioactive glasses studied are the nucleating agents for further growth of hydroxyapatite on the surface, which gives these materials enhanced bioactivity. Others concluded [138] that bioactive glasses which contained microheterogeneities (glasses with Si/P molar ratios of 2.46) showed phosphate–rich zones surrounded by a silicate matrix. In agreement with this interpretation, nucleation of apatite (a calcium orthophosphate with the same P-containing structural unit in glasses) takes place homogeneously at temperatures slightly above Tg [138]. The US Biomaterials processing regime was modified for monolithic production in this work for the synthesis of 58S. However, the recipe and procedure used for the sol mixture in both 58S compositions is the same.

When placed in liquid medium, the open gel structure permits rapid migration of Ca^{2+} and PO_4^{3-} to the interface region which subsequently produces a CaO-P_2O5- rich film on the gel layer which develops into a thicker and denser amorphous layer via the arrival of more ions from the bulk glass and adsorption of calcium and phosphate ions from the physiological solutions. The final stage involves crystallisation of the amorphous calcium phosphate into a mixed hydroxyl, carbonate and fluoro-apatite layer, the necessary OH-, CO_3^{2-} and F^- anions again being derived from host tissue.

Work on the same nominal composition by Lockyer et al. [137] was reported to show only 80% of the Ca^{2+} behaving as network modifiers, the remainder actually forming linkages within the network. However, the ^{29}Si MAS-NMR recorded by Dupree et al. [137] showed that all the modifier ions produced non-bridging oxygens and that their distribution was close to that predicted for a binary system. However, care must be taken in interpreting results from other authors as most previous work has been done on melt-derived glasses. From this experiment it is evident that the melt-derived 45S5

Bioglass® glass contains much higher levels of Q_2 species that the sol-gel derived 58S Bioglass® compositions which have higher levels of Q_4 species predominant in the structure. This result is confirmed by other authors who investigated on apatite formation on binary CaO and SiO_2 compositions. They report of a starting structure mainly composed of Q_2 species in the glass followed by the conversion to Q_3 by means of condensation with silanol groups after soaking in physiological solutions [55].

^{31}P MAS analysis revealed an apatitic environment in both sol-gel derived glasses at 2.3ppm ± 0.3ppm; the Imperial College lab produced 58S also showed evidence of an orthophosphate environment, confirming the hypothesis that hydroxyapatite was instantaneously formed on the surface of these glasses when exposed to the atmosphere. Orthophosphate is replaced by pyrophosphate, which in turn is replaced by metaphosphate (chemical shift ~ -15 to –20ppm). Brown et al. distinguished between calcium apatites and other calcium phosphates with simliar ^{31}P MAS spectra, which indicated the presence of hydroxyapatite [140]. The phosphate constituent also affects the repolymerisation of the glass and increases the effect of amounts of Q_4 and Q_3 species. Because the compositions examined involved three or more components, we expected the peaks given for these compositions would overlap and give an unclear picture of events. The melt-derived 45S5 from US Biomaterials revealed an orthophosphate environment whereas the US Biomaterials 58S showed apatite and no evidence of an orthophosphate environment. The Imperial College 58S showed the presence of apatite formation as well as an indication of an orthophosphate environment.

However, caution must be exercised when considering these results because of overlapping peaks in these multi-component bioactive glasses. In these samples, indications from the ^{31}P MAS-NMR spectrum contain two separate resonances originating from an orthophosphate and an apatitic environment in the glass. It is possible that shifting will occur in these lines due to the calcium cations responsible for charge neutralization. The width of the lines in all samples indicates that the phosphorus is not crystalline in nature.

The Imperial College 58S has had a higher stabilization temperature than the US Biomaterials' 58S which was stabilized at 700°C. The regime developed in this work was for the production of monoliths and was approximately twice the time of the US

Biomaterials regime. Time increased during initial aging to obtain stable monoliths. At the stabilisation stage time was decreased by a factor of 2.5 as heat ramping was not used. One must take this into account when comparing two samples of similar composition, such as the two 58S samples in this NMR study, as different processing regimes can change the structure and specific phases created, in the drying and stabilisation stage. Lengthy heat treatments or high temperatures can encourage phase changes and crystallite growth and nucleation of other phases from the randomly amorphous product obtained after stabilization.

EDAX analysis of the two products shows that they are similar in composition (± 5wt% oxide). Ramped and non-ramped heat treatments can also control nucleation and crystallization of a separate phase. However, square voids were also noticed on the surface of the Imperial College lab produced 58S due to the evaporation of a halide phase from the surface after stabilization and unramped cooling. This phase probably required ramped insulative methods to persist after samples had been stabilised, unless it was an artefact of a previously 'burnt-out' phase. But the increase in surface voidage and the fact that no instability had been identified as a result of the evaporation of this compound allowed us to disregard this. We considered that halide calcium phases had reacted and been 'burnt-out' during stabilization.

Due to porosity and surface area differences in the melt-derived and sol-gel derived bioactive glasses, combined with more rapid dissolution kinetics in the sol-gel derived product, it could be hypothesized that the sol-gel derived product has enhanced bioactive features with a rapid evolution of ions into solution. Due to the high proportion of Q_4 species present in the sol-gel derived product, the silica rich matrix of the gel-glasses would stay intact giving more controlled network dissolution after initial rapid interaction on the surface (as proposed by Hench [4]) to eventually form a hydroxyapatite layer.

Upon examining the results obtained for the 45S5 melt-derived glass we see the presence of mainly Q_2 species, which does not agree with studies on soda-lime-silica systems [137]. Dupree and Holland found that only Q_2 species were present in a glass at 50mol% Na_2O, whereas the compositional percentage for 45S5 is 24.4mol% which should correlate, in this case, with a mixture of Q_3 and Q_2 species. However, from this work it is also determined that there is no direct correlation between percentage content

of Na_2O and Q_3 and Q_2 species being present in the glass [137]. However, the observation that only Q_2 species are present in a glass of composition 50mol%Na_2O is in agreement with Dupree and co-workers results [137]. The result obtained from the experiment indicates that the 45S5 has a metasilicate composition, where every SiO_4 tetrahedron would have 2[bo] and 2[nbo].

It should be noted that NMR is a "bulk' technique unlike XPS and that the distribution of the Q types may be random or clustered to form separate phases. Detailed distribution of these [nbo] groups is still unknown. We can say that the other two modifying constituents in this glass have a charge balance effect equivalent to that of a soda-lime-silicate glass of 50mol% with CaO and P_2O_5 acting in accordance to give an overall distribution of only Q_2 species. In total the mol% of entities other than SiO_4 in 45S5 ($CaO + P_2O_5 + Na_2O$) is equal to 53.9mol%, If we consider the subtotal of the CaO and Na_2O constituent we have a total of 51.3mol% which could be close to that of the 50mol% scenario. However, with the sol-gel network, the scale of interconnectivity in the bridging oxygen network is greater than in the melt-derived product. This creates the structure of phase separated regions intermingled with the silica-rich network forming phase on a nanometre scale.

On analysis of the sol-gel derived glasses, we see a definite majority of Q_4 and Q_3 species respectively which is akin to that of synthetic silica gel, biological silica from *Phalaris canariensis* (see Figure 6.7a) and dealuminated zeolites [134]. In this material, a substantial number of silicon atoms have OH groups attached. These groups may not be present simply as 'surface' hydroxyl-groups. From the width of the adsorptions (5-15ppm) observed this may reflect the non-crystalline nature of these materials. These sol-gel derived materials also fit the nature of silica in biological materials, which Mann et al. have written as $[Si(OSi\equiv)_n(OH)_{4-n}]$ [134] allowing for some $Si(OSi\equiv)_3(OH)$ units and many $Si(OSi\equiv)_4$ species. This formula readily accounts for the following properties of these silicas: (a) amorphous nature, (b) the mobility and the ever ready dissolution of silica in certain biological products, (c) the ready formation of compounds with divalent metal ions owing to the acidic nature of the Si-OH unit.

6.8 Confocal Microscopy and Optical Properties

6.8.1 Analysis of 58S Bioglass® by confocal microscopy

Confocal microscopy involves the use of an aperture in the conjugate focal plane of an objective lens in both the illumination and imaging pathways of a microscope [142] : The area surrounding the aperture rejects stray light returning from the areas not in the focal plane. Watson [142] goes on to describe that for a useful image to be made, some form of scanning optical microscope device is required. Expressed simply, this type of scanning optical microscope enables high-resolution images to be made of samples, often below the surfaces of translucent materials, with minimum requirements for specimen preparation. In this work mercury intrusion (done firstly to find the bulk density of the sample) and oil immersion were used as a marker fluid to outline the interconnective pathways of the pore network in 58S Bioglass® made at Imperial College. See Figs for images of these experiments.

High resolution confocal microscopic images may be made of either the surface of a sample or beneath the surface [142]. Watson [142] also says that these images can be likened to optical tomograms, giving thin (>0.35 μm) slices up to 200 μm below the surface of a transparent tissue: With microscopes running under normal conditions, the optical section thickness will be >1 μm and the effective penetration into enamel and dentin a maximum of 100 μm. High quality numerical apertures should be used for highest resolution. Refractive index matching of lens immersion media and substrate will avoid distortions of images in the optical axis [142]. Errors could occur when imaging at considerable distance i.e. >40 μm into a cell containing water with an oil immersion objective above the cover slip.

Experimental

58S monoliths were synthesized using the normal procedure and then stabilized at 800°C for 24 hours. The monoliths were then penetrated with mercury using a Poremaster 33 by Quantachrome Ltd. (High pressure run (30KPsi)) and then examined with confocal microscopy. These samples had previously been analysed using nitrogen adsorption (Chapter 5), helium ultrapycnometry (Chapter 6.2) and bulk density (Chapter 6.1).

Samples were examined by confocal microscopy by Richard Cook at Guy's Hospital Dental Materials Unit [28]. The mercury clearly outlined the pathways of diffusion of liquid into the sol-gel bioactive gel-glasses hence outlined pore interconnectivity as a function of the material. Interconnectivity had never been proven visually before this. An order rate of diffusion could be realized for these materials if they were doped with rhodamine B using luminosity to test this. However, after the samples were fully doped i.e. with rhodamine B or oil, microscopically they appeared completely homogeneous and thus the usual optical methods were not appropriate. Only air bubbles of 2 micron diameter could be resolved as features in the material. This technique proved useful after mercury intrusion to understand the interconnecting pore network of the glass. This outlined pore connection features which previously had not been seen using optical methods.

Confocal reflected light microscopy identified measurable pools of pore contained mercury, ranging from the optical resolution limit (0.1μm in X&Y &0.35 μm in Z) up to 20μm. The glass appeared blackened, due to the myriad mirror surfaces of the entrapped metal. Confocal microscopy of a partially intruded sample showed a uniform advancing mercury front, parallel to the glass surface, with localised areas of preferential invasion, indicating the presence of lower resistance paths within the network, indicating that the pathways within the material into which a liquid could infiltrate, where not all of the same size. Small samples were easily intruded without added vacuum within 2 hours (0.5cmD x 2mmH).

58S monoliths were individually immersed in rhodamine B-labelled dentine bonding monomers (2HEMA, Bis-methacrylate) for 24, 48 and 72 hours respectively in light-proof reservoirs, see Fig. 6.9. Subsequent command polymerisation (blue light), suspended the resin's movement through the pore network. The specimens were sectioned through the middle and underwent confocal sub-surface fluorescence imaging. The more viscous and slower moving labelled resin penetration patterns clearly showed an interconnecting network.

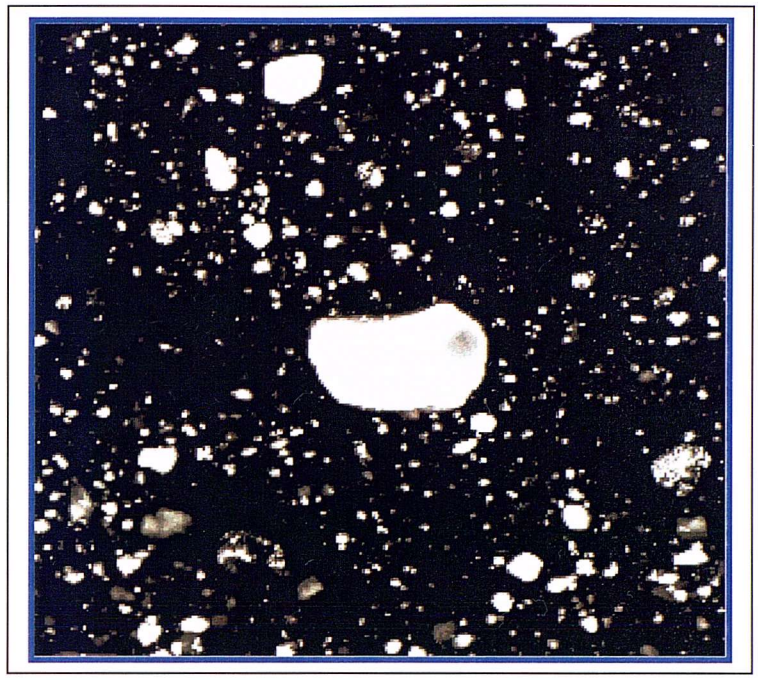


Figure 6.9a: Confocal image of mercury trapped within 58S glass pores, (0.1µm to 20µm). Fieldwidth, 60µm. [Mag. x 63/ 1.25 na oil lens +1:8 sampling, effective mag. x 504].

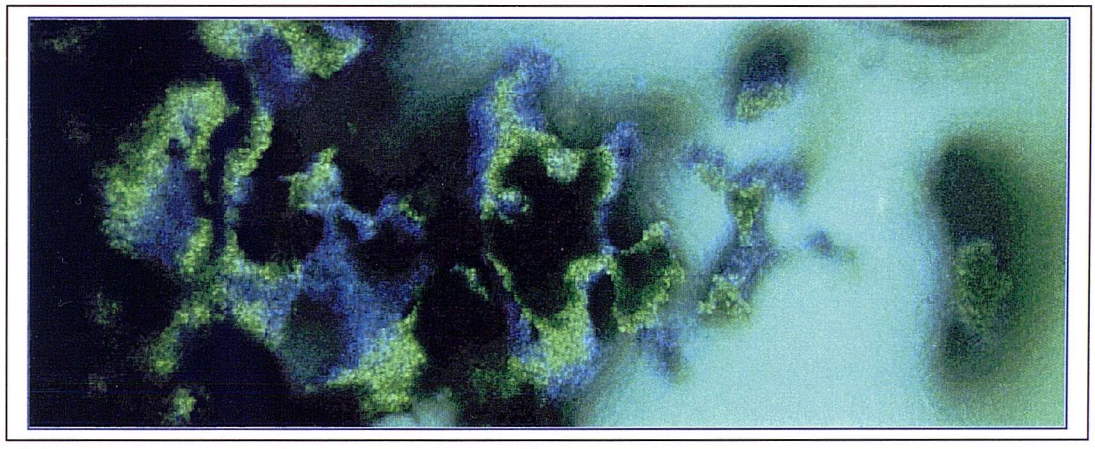


Figure 6.9b: Confocal image, showing preferential mercury (M) invasion tracks (L to R) into a 58S sol-gel specimen (G), accentuating an advancing front with different rates, parallel to the exposed surface. Outlinging 'A' and 'B' road type diffusion. Fieldwidth, 250µm. [Mag. x 40 /0.85 na oil lens]

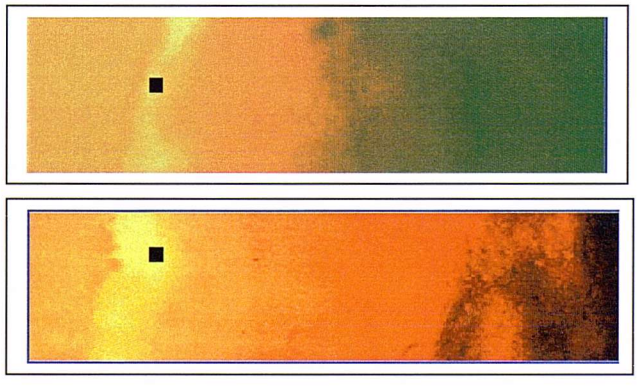


Figure 6.9c: Invasion of fluorescent labelled resin (from L), at [Top] 24hrs, [Bottom] 72 hrs. Resin / glass interface marked by brightest linear structure. [Mag. x 40 /0.85 na oil lens]

The leading front of resin penetration was always parallel to the glass surface [143] (Fig. 6.9c, top), conforming to all the external surface contours (Fig. 6.9c, bottom). Confirmation of infilling of secondary networks, after lower resistance paths had been filled, was indicated by apparent strengthening of the fluorescent signal behind the advancing front, proving the ease with which the sol-gel 58S could be doped [28], an important factor when considering the use of a bioactive material is used for drug delivery.

A uniformly distributed, isotropic, interconnecting pore network (5Å to 20μm diameter), was demonstrated in monolithic 58S bioactive glass. The pore network appeared contiguous with the solid silicate matrix. Mercury intrusion in combination with fluorochrome capillary uptake patterns, confirmed the absence of pressure induced artefacts in the glass, see Figures 6.9a to 6.9c [28]. Glass and Green [143] describe the permeability of truly open pore networks in a solid as being directly proportional to the square root of time. They also go on to match diffusion kinetics with the Washburn equation. The implication is that the advancing front rate declines over time as expected, but the intruded front on average will stay parallel with the outer surface as a whole the network is isotropically intruded. A simple analogy can be drawn by referring to these pathways as 'A' and 'B' roads, 'A' roads being wider in diameter than 'B' roads.

6.8.2 Refractive index results for transparent 58S400 Bioglass®

58S monolithic transparent discs (1.5cmD x 1mmH) prepared by the normal regime with stabilization for 24 hours at 400°C were tested at the Physics department at Imperial College for their refractive indices. A simple set-up using real and 'apparent' depth of a slab material and taking the ratio, using a travellling optical microscopes with a vernier. A value of 1.33 for the refractive index was obtained for these samples. It was noticed that this value was very close to that of water. Optical properties were tested in a basic experiment, using a simple depth of field set-up. Experiments were performed with the help of Gilbert Sattherwaite and Prof. Jon Maxwell, Department of Physics at Imperial College.

Slinner and Appleman noted a relationship between density and refractive index. The anhydrous crystalline phases were arranged in order of increasing density and

refractive index, and found to have a linear relationship [46]. Stishovite falls on the same line [grad=1/2] and it has been noted that the line for silica polymorphs has been extrapolated to meet that of certain forms of water. The analogous structures of SiO_2 and H_2O have been compared by Kamb [46], who points out that the ratios of the densities of the various phases or polymorphs of SiO_2 and water to those of the corresponding forms of ice and cristobalite are very similar, and for each type of silica there is an ice counterpart with the same type of crystal structure.

The opalescence and sometimes transparent appearance of the monoliths can be explained by the diffraction of light waves in the continuous pore network of the glass. For the basic experiment that obtained values for the refractive index of 58S, measurements were only obtained for transparent samples of 58S. However, when using mercury porosimetry to outline the network, the sample did not have to be transparent, which is an added advantage. Mercury porosimetry can prove that a network is continuous throughout the gel-glass with no apparent changes between glassy transparent regions of the glass and opaque regions with regard to liquid transport pathways.

When light is scattered amongst the subsurface regions of the glass monolith we can use the phenomenon of Rayleigh light scattering to explain the apparent opacity of the gel-glass, which contained various amounts of micropores throughout the specimen which could contain significant amounts of bound water. The presence of water is confirmed by spectra obtained using Fourier transformed infrared spectroscopy (FTIR). Liquid water has several strong adsorption bands in the infrared region of the spectrum. Light scattering occurs when a layer of pure water is irradiated with a beam of monochromatic visible light. Most of the light is either transmitted through the layer or reflected from the surfaces of the layer, but a fraction is scattered in other directions.

The conventional measure of the light scattered in a direction that forms an angle θ with the incident beam is the Rayleigh ratio, R_u (θ), given by:

$$R_u(\theta) = I_\theta d^2 / I_O$$

Where I_θ is the intensity of light scattered by a unit volume of the sample at the angle θ, I_O is the intensity of the incident beam passing though the sample, and d is the distance between the sample and the point at which I_θ is measured. The subscript u signifies that the incident light is unpolarized. Rayleigh scattering assumes that the scattered light has the same frequency as the incident beam, and that the scattering of light by liquids arises from two distinct effects. The first of which we are interested in because it explains the scattering of light when samples appear more opalescent or opaque in nature. This is seen when the incident beam induces oscillating dipole moments in the molecules, and the oscillating dipoles act as sources for secondary light waves. These scattered light waves have the same frequency as the incident beam. If the molecules are regularly arranged, as in a crystal, the scattered waves from different molecules interfere destructively with one another, and scattered light is visible only at a few angles of observation. Smoluchowski and Einstein considered the effect of these inhomogeneities on light scattering and found that they contributed a factor to the Rayleigh ratio [141].

The presence of micropores in these sol-gel materials studied creates this light scattering effect in most monoliths. After days of exposure to the atmosphere the samples had attracted water and became more opaque (becoming transparent again if dried overnight). However, samples that had been considerably heat-treated and were chalky and white in appearance after densification never regained their transparent nature. A critical aspect ratio governed the transparent nature of the samples made in this work and all monolithic shapes made with low critical aspect ratios (thin/small samples) remained transparent throughout the drying and stabilisation regimes. In this work, no compositional or structural differences were found between the opaque and transparent forms of 58S synthesized in the lab.

CHAPTER 7 DISSOLUTION STUDIES AND FOURIER TRANSFORMED INFRARED (FTIR) ANALYSIS OF 58S SAMPLES

In this chapter, experiments investigating the dissolution properties of 58S stabilised at different temperatures and with different thermal treatments are discussed, with an account of results achieved using FTIR analysis of 58S samples.

7.1 Dissolution studies: Theory

The dissolution and deposition of silica in water involves hydration and dehydration reactions catalysed by OH^- ions [46]:

$$(SiO_2)_X + 2H_2O \rightleftharpoons (SiO_2)_{X-1} + Si(OH)_4$$

Although $Si(OH)_4$ is nonvolatile at ordinary temperatures and polymerises quickly when heated, nevertheless at elevated temperature and pressure in water its solubility is greatly increased and it can exist at equilibrium as the vapour phase in the steam, as shown by Kennedy [46]. Reported solubility values for the amorphous silicas range from 70 to more than 150ppm at 25°C [46].

According to Baumann [46], when amorphous silica powder (Aerosil) is placed in water at 25°C, the approach to equilibrium is different at high and low pH. Below pH 7, the concentration of soluble silica increases for several days and approaches the final solubility value asymptotically. Above pH 7, the silica concentration rises rapidly in the first day to form a supersaturated solution containing, for instance, 155ppm at pH 9. Then the concentration drops over a period of 3-4 days to the solubility characteristic of the pH and type of silica, such as 125ppm. Thermal treatment effects were studied for silica gels made from sodium silicate and $SiCl_4$ respectively [46]. Samples, which had been dried and heated to different temperatures up to 900°C, all showed the same solubility in water, according to Morachevsky and Piryutko [46]. For the effects on living tissues according to Foucault and Collette [46], finely divided silica dissolves more rapidly in the peritoneal cavity of a rat than it does at 37°C in a buffer solution at pH 7.4.

The reason for this is unknown by the authors, but they point towards the action of compounds present which have catetchol-like structure as being responsible. We propose that it may be due to the action of macrophages.

The hydroxyl ion is the unique catalyst in alkaline solutions and hydrofluoric acid in acid solutions. The structure of amorphous silica is an even more open arrangement than that of cristobalite, to which it is closely related. On the surface, there are spaces between oxygen ions sufficiently large to accommodate hydroxyl ions. Such a surface then bears an ionic charge and silica is constantly being exchanged in equilibrium between solution and surface. The first step is the adsorption of OH^- ion, after which a silicon atom goes into solution as a silicon ion. If the pH is much below 11, the silicate ion hydrolyses to soluble silica, $Si(OH)_4$ and OH ions and the process is repeated.

A buffer solution is a solution that has the ability to maintain a stable composition when various components are added or removed and they are solutions that resist change in pH on the addition of strong acid, H+, or strong base, OH-. The pH of about 95% of the naturally occurring waters is within the range of 6 to 9 [144]. Carbonate ions participate in heterogeneous equilibria with solids containing carbonate, notably calcium carbonate. The formation of $CaCO_3$ precipitates is one of the bases of the precipitation process for water softening. Carbonates and bicarbonates form complexes and ion pairs with metals such as Ca^{2+} and Mg^{2+}.

Equilibrium calculations and log concentration diagrams of systems involving heterogeneous equilibria may only provide us with the boundary conditions of the system rather than the situation that truly exists [46]:

1. Some heterogeneous equilibria are slowly established.
2. The thermodynamically predicted stable solid phase for a given set of conditions may not indeed be the phase that is formed.
3. Solubility depends both on the degree of crystallinity and the particle size of the solids (which may vary).
4. Supersaturation may exist; that is, solution concentrations in excess of those predicted by equilibrium calculations may prevail.
5. The ions produced by the dissolution of solids may undergo further reaction in solution.

For the development of a hydroxyapatite layer on the surface of a bioactive material both dissolution and precipitation kinetics are involved. However, we saw that the formation of an HCA layer is instantaneous on the highly reactive surface of 58S Bioglass® upon exposure to moisture in the atmosphere. After immersion in liquid medium the HCA growths on the surface become more apparent.

The initial solid formed by precipitation may not be the most stable solid (the thermodynamically stable phase) for the reaction conditions. If this is the situation, then over a period of time the crystal structure of the precipitate may change to that of the stable phase [144]. This change may be accompanied by additional precipitation and, consequently, a reduced solution concentration because the more stable phase usually has a lower solubility than the initially formed phase. The changes in crystal structure that take place over time is called aging. A phenomenon called ripening may also take place whereby the crystal size of the precipitate increases. Since very small particles have a higher surface energy than the larger particles, the solution concentration in equilibrium with small particles is higher than that in equilibrium with larger particles. Consequently, in a mixture of particle sizes, the large particles will continue to grow because the solution is supersaturated with respect to them [144]. Conversion of small particles into larger particles is also enhanced by the agglomeration of particles to form larger particles on the surface.

When carbonate and hydroxyapatite precipitates form because of those dissolution products in solution, which are also common to the solution itself (i.e. Ca^{2+} in solution may originate from the solid in solution and also from the solution itself). This situation results in the 'common ion effect' [145], in which the presence of a common ion modifies the solubility of the solid. It may be further complicated by the production of the presence of solutes that react further with solution constituents. Examples are $CaF_2(s)$ dissolving in water containing Ca^{2+} ion and $CaCO_{3(s)}$ dissolving in a solution containing CO_3^{2-} ion. In general, solubility increases with increasing temperature with a few notable exceptions such as $CaCO_{3(s)}$, $Ca_3(PO_4)_2$, $CaSO_4$ and $FePO_4$, which are of importance in water chemistry. When a solution contains an ion that is the same as one of the ions, which result from the dissolution of the solid, the solubility of the solid will be less than when the solid dissolves in pure water. The modification of solubility is called the 'common ion effect'.

The 'common ion effect' is applicable to the studies performed with simulated body fluids and Tris-buffer solutions when we consider that there are species such as Ca^{2+}, phosphates, chlorides and carbonates already in these solutions and are also present as dissolution products of materials such as 58S. Calcium ions form weak soluble complexes with carbonates, such as $CaCO_3^-$ and $CaHCO_3^+$, and with hydroxides, such as $CaOH^+$ as well as forming the sparingly soluble, $CaCO_{3(s)}$. Pure calcium carbonate exists in two distinct crystalline forms. These are the trigonal solid calcite, which in its pure form, has a solubility product K_{so} of $10^{-8.34}$ and the orthorhombic solid, aragonite, which in its pure state has $K_{so} = 10^{-8.22}$, both at 25°C.

Ferguson et al. [46] showed that if a crystal seed of precipitated calcium phosphate was added to a solution supersaturated with respect to hydroxyapatite, previously formed precipitates acted as nuclei for further precipitation. Following nucleation the formation of an amorphous precipitate occurred. An amorphous solid is one that does not have a well organised crystal structure and which is usually more soluble than the corresponding crystalline solid. The amorphous nature of calcium phosphate precipitates may indeed be an important reason why phosphate solution concentrations are present in natural waters at higher levels than those predicted by equilibrium with the crystalline solid. In the case of calcium phosphate precipitate given, it is evident that precipitation not only results in an amorphous solid but also a precipitate whose solubility is greater than the thermodynamically stable phase [144].

Such a solid is not stable and will transform, albeit slowly, to the stable solid phase. However, the first formed solid may be stable enough to control solution phosphate concentrations in a pseudo-equilibrium or steady-state situation. This is important when considering the analysis of the layer produced on the surface of a biomaterial after immersion in SBF or Tris-buffer solution. It also known that the growth of a perfectly stoichiometric HA layer takes considerable time [66].

Perez-Pariente et al. [63], have investigated the influence of composition and surface characteristics on the *in vitro* degradability and bioactivity of SiO_2-CaO-P_2O_5-MgO sol-gel glasses. In these experiments synthesis of silica glasses with composition $_{60\text{-}80}$ (mol%) SiO_2, and 4mol% of P_2O_5 were used, whilst keeping the molar ratio in all cases of CaO:MgO = 4. The layer formed on the surface was found to be composed of apatite

and whitlockite. Greenspan et al. [56] obtained glasses in the system SiO_2-CaO-P_2O_5 by the sol-gel method with a high surface area and porosity and stated that HCA layer formation rate was higher than for melt-derived glasses. However, the surface area was decreased by the thermal treatment of the glasses that simultaneously produced a decrease of both pore volume and average pore size. Pereira et al., [54] showed that the textural effects (pore size and pore volume) on the *in vitro* formation of the HCA on gel-silica surface could be understood if pores as nucleation sites were assumed and stated that when the pore size and volume decrease the HCA induction time increase. However, no substantial influence of pore radii above ~ 2nm on the *in vitro* bioactivity was found by Perez-Pariente et al. [63]. Also, in this study the SBF solution was renewed every 60 hours and samples remained in polyethylene containers for up to 14 days, a different regime from that which we used.

They concluded that a higher CaO content in the glasses implied higher porosity, facilitating the apatite nucleation on its surface from the early stages of the assay, whereas a higher SiO_2 content increased the surface area and the growth rate of a calcium phosphate rich layer on the surface of the gel-glass. Other work was done on binary systems [56,63,129,146] of SiO_2 and CaO glasses. It was found that these binary glasses did form an apatite layer on the surface after immersion in SBF, but that the rate of formation was increased by the addition of Na_2O and P_2O_5 while it decreased with the addition of MgO, B_2O_3, CaF_2 and Fe_2O_3. It was postulated that when the P_2O_5 is added, the $P^{(V)}$ ion will dissolve, increasing the degree of supersaturation of the surrounding fluid with respect to the apatite, and hence accelerate apatite formation.

7.2 Dissolution studies: experimental

Rates of resorption in Tris-buffer solution, and SBF at 37°C were analysed using induced coupled plasma spectroscopy (ICP). Rates of resorption vary with thermal history, as does the texture of the gel glass samples. Results are compared with prior *in vitro* rates of resorption of bioactive gel glasses. Initial bioactivity was assessed by immersion in SBF and later analysis with FTIR to identify calcium phosphate activity on the surface of the material.

The same samples prepared for the density studies and those used in previous nitrogen adsorption experiments were used in this dissolution study to identify the

stabilisation temperature, which would produce the most controlled dissolution rates. SBF and Tris-buffer Solution were prepared according to standard protocol and samples were kept at 37°C throughout the experiment in a water bath at 37°C. A constant ratio of weight to volume equal to 0.012 ± 0.002g/cm^3 was used, consistent as done by Pereira et al. [54]. This ensured that there was adequate liquid to mass ratio for each sample, as the liquid medium in each case was not replenished.

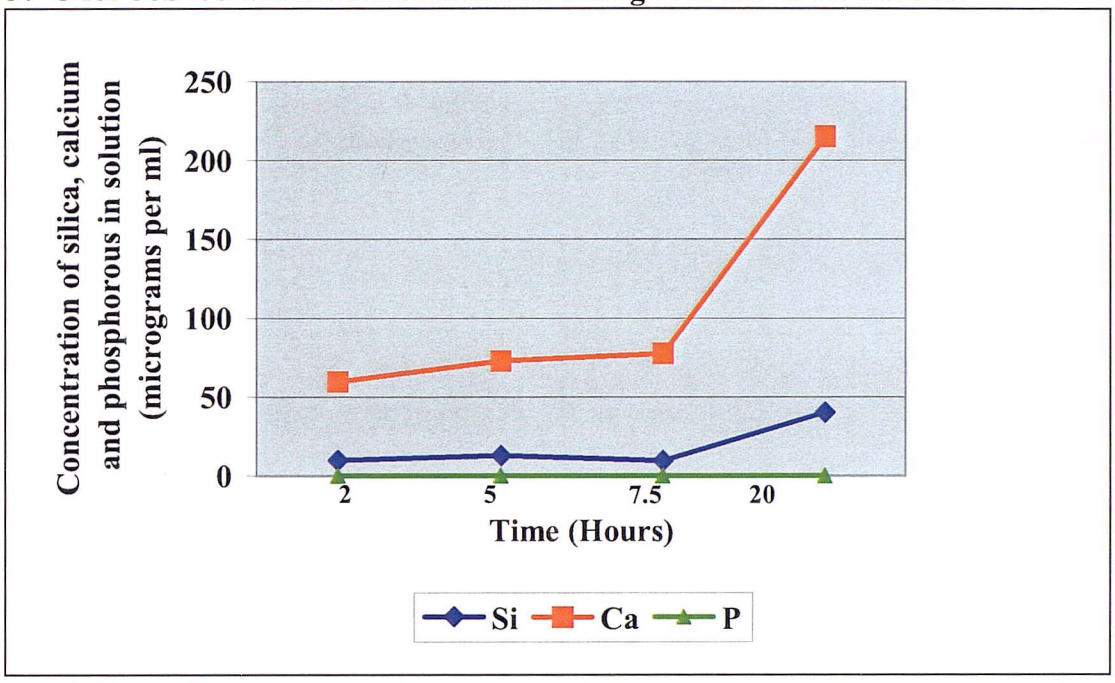
Times for extraction of the samples were 2hours, 5hours, 7.5hours, 1day, 2days, 6days, 12days, 15days, 21days up to a maximum of 30 days in solution. After extraction, samples were washed in acetone and dried in the oven overnight at 60°C, to stop any further reaction [147]. pH measurements were also taken at the various time intervals.

7.3 Results of dissolution studies for 58S stabilised at different temperatures after immersion in Tris buffer solution

58S was synthesized by the normal regime and then stabilised in air for 24 hours at 400°, 600° and 800°C respectively. The samples were then thermally treated in dry nitrogen at a flow rate of 6mm/min at 850°, 950°, 1050° and 1100°C for 20 minutes. A short study was done, immersing the samples in Tris buffer Solution at 37°C for various time intervals (2 hours, 5hours, 7.5 hours and 20hours) and observing a weight to volume ratio of 0.012g/cm^3, as before. After removal from solution, samples were washed with acetone and dried overnight in the oven at 60°C. Solutions were then analysed using induced coupled plasma (ICP) spectroscopy, giving concentrations (parts per million) of elemental species in solution. A Fison/ARL 3580B ICP was used for all experiments using standard operating conditions; data was compiled by Barry Coles at Imperial College, Department of Geology. Graphs were created to identify rates of dissolution and concentrations [micrograms per ml] of Si, Ca and P in solution, (see Figures 7.1 to 7.3). For all other graphs showing dissolution profiles for 58S with different thermal treatments see Appendix 1.

7.3.1 ICP results for 58S stabilised in air at 400°C and thermally treated in dry nitrogen after immersion in Tris buffer solution at 37°C

Figure 7.1: Graph of dissolution product after immersion in Tris buffer solution at 37°C for 58S400 with heat treatment in nitrogen at 850°C for 20mins.



In the above graph the elemental concentration in solution is not represented as a log scale due to phosphorus values remaining low throughout the 58S400 series, i.e. 0-0.4ppm or including negative values and reaction rates for this phosphorus in solution could not be accurately measured. For calcium and silica we observe high concentration values, which are characteristic of the sol-gel derived product given its high surface area. Using the relationship of $[Si] = kt^{1/2}$ and $[Ca] = kt^{1/2}$, reaction rates calculated for silica and calcium are included in Table 5.1 for the 58S400 series. For results of surface area and other variables for 58S400, see Chapter 5. In Figure 7.1 we see that dissolution rates were high for calcium and silica and also observe a controlled release of ions into solution by the 58S stabilized at 400°C. Log graphs were plotted for all silica and calcium rates with respect to concentration, (see Appendix 1). For the first set of results, (produced at 850°C in dry nitrogen for 20 minutes) we see the lowest values of phosphorus in solution for all of the samples. However, silica and calcium release remain equivalent with time with a slight decrease at 7.5 hours for Si and at 5 hours is equivalent to that of calcium, this is followed by an increase at 20 hours. Rate k in each case is calculated in micrograms per second.

For the second set of data representing 58S400 samples thermally treated at 950°C for 20 minutes (see Appendix 1) we see an active release of phosphorus into the solution between the minimum and maximum times of 2 and 20 hours. With Si and Ca concentration exhibiting similar profiles to those in the first set of data but with overall lower values, as from the effect of thermal treatment. The third set of data representing samples treated at 1050°C for 20 minutes in dry nitrogen (see Appendix 1), we see a similar trend for concentration of Ca and Si in solution, also following the falling trend of values with increasing thermal treatment. However, P liberation increases steadily from 7.5 hours until the end of the experiment at 20 hours. In the final data set of 58S400 with thermal treatment of 1100°C for 20 minutes in dry nitrogen (see Appendix 1), it is observed that Ca and Si concentration follow a similar pattern with less concentration at the final time interval. Phosphorus is liberated steadily from 5 hours to the end of the experiment at 20 hours, giving the highest overall value (0.5ppm) for all samples in the 58S400 data set. Rates of evolution into solution are seen to decrease with increased temperature treatments. Table 7.2 shows the reaction rates for 58S400 series after immersion in Tris buffer solution at 37°C.

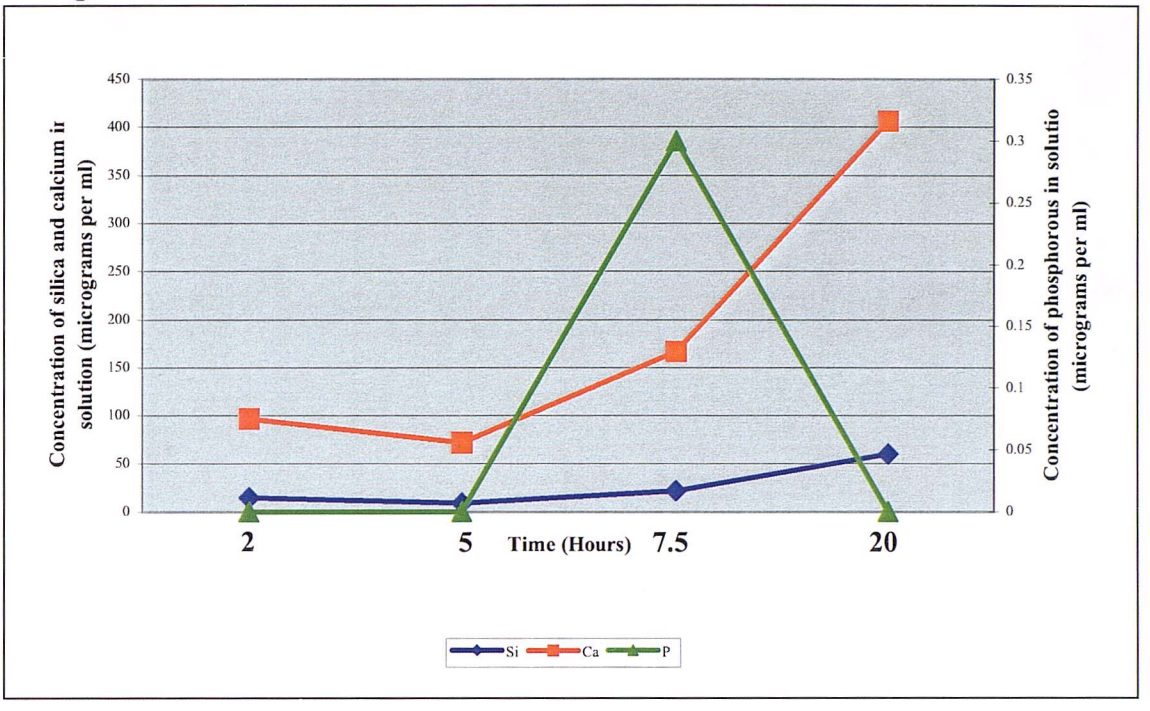
Table 7.1: Reaction rates for 58S400 series after immersion in Tris buffer solution at 37°C.

Sample	Species	Rate (k) 0-2Hrs	Rate (k) 2-5Hrs	Rate (k) 5-7.5Hrs	Rate (k) at 7.5-20Hrs
58S400/850	Si	1.37E-03	2.87E-04	-3.66E-04	6.80E-04
58S400/950	Si	4.76E-04	5.69E-04	3.56E-04	3.67E-04
58S400/1050	Si	2.24E-04	2.77E-04	5.00E-05	3.72E-04
58S400/1100	Si	2.03E-04	2.00E-04	2.00E-04	2.60E-04
58S400/850	Ca	8.29E-03	1.23E-03	5.33E-04	3.05E-03
58S400/950	Ca	3.44E-03	1.51E-03	2.14E-03	7.20E-04
58S400/1050	Ca	8.43E-04	6.39E-04	2.22E-05	5.62E-04
58S400/1100	Ca	8.22E-04	4.86E-04	2.33E-04	3.07E-04

7.3.2 Results for 58S600 with thermal treatment after immersion in Tris buffer solution at 37°C

As previously stated, results were obtained for similar thermal treatments as the 58S400 set recorded previously giving nitrogen adsorption data. Figure 5.2 shows the graphical representation of results from ICP analysis of dissolution products for 588S600.

Figure 7.2: Graph of dissolution products for 58S600 with heat treatment in nitrogen at 850°C for 20mins after immersion in Tris buffer solution at 37°C.



In the first data set representing those samples with thermal treatment at 850°C for 20 minutes, calcium and silica concentrations rose initially and then fell by 5 hours followed by a steady rise again until the final time of 20 hours. However, the phosphorus concentration is more variable with a high level of concentration in solution seen at 7.5 hours, then dropping back to zero. In the second data set for samples treated at 950°C for 20 minutes (for graph see Appendix 1) we see a consistent zero value for phosphorus in solution whereas the calcium and silica concentration are virtually parallel in behaviour. For the second two data sets representing sample thermally treated at 1050°C and 1100°C respectively for 20 minutes, we see very similar patterns regarding the calcium and silica concentrations in solution and both species remain almost equivalent with an increase in concentration in solution with time. However, when observing the phosphorus concentration in solution we see that there is an incubation period from zero time and delayed release, which is progressive after 7.5 hours until the end of the experiment at 20 hours. The final value of the phosphorus concentration being higher in the 1100°C sample than the 1050°C sample. For log graphs and other graphs for thermally treated 58S600, see Appendix 1. Rates of evolution of Si and Ca in to solution again fell with increasing thermal history. Table 7.3 summarises the reaction rates for 58S600 series after immersion in Tris buffer solution at 37°C.

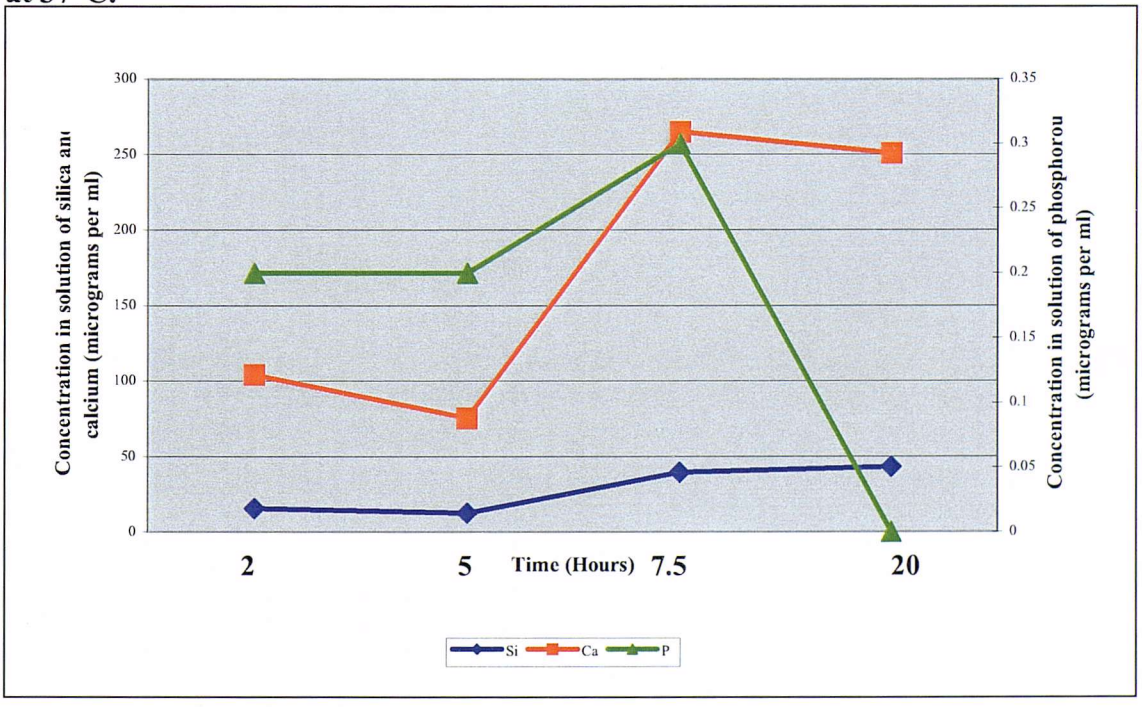
Table 7.2: Reaction rates (micrograms per sec) for 58S600 series after immersion in Tris buffer solution at 37°C.

Sample	Species	Rate (k) 0-2Hrs	Rate (k) 2-5Hrs	Rate (k) 5-7.5Hrs	Rate (k) 7.5-20Hrs
58S600/850	Si	2.05E-03	-5.37E-04	1.44E-03	8.47E-04
58S600/950	Si	7.85E-04	1.53E-03	1.56E-04	3.91E-04
58S600/1050	Si	4.04E-04	7.41E-05	3.52E-04	3.71E-04
58S600/1100	Si	4.63E-04	4.26E-04	7.39E-04	2.56E-04
58S600/850	Ca	1.35E-02	-2.29E-03	1.05E-02	5.31E-03
58S600/950	Ca	5.25E-03	2.86E-03	6.82E-03	1.73E-03
58S600/1050	Ca	1.70E-03	3.33E-04	2.56E-04	1.06E-03
58S600/1100	Ca	1.63E-03	1.28E-03	2.73E-03	4.10E-04

7.3.3 Results of ICP analysis of 58S800 with thermal treatments after immersion in Tris buffer solution at 37°C.

Figure 5.1 shows the results obtained from ICP analysis of solutions obtained from the above experiment. Control 58S800 without thermal treatment is also included as the first data set. There was not enough sample from the other groups stabilised at 600°C and 400°C to test. In the 58S800 series, from the first data set, (Control 58S800) we observe a dip in calcium and silica concentration values at 5 hours with a general rise and stabilization towards the end of the experiment at 20 hours.

Figure 7.3: Dissolution products for 58S800 after immersion in Tris buffer solution at 37°C.



Phosphorus concentration values remain stable initially, then reach a maximum at 7.5 hours, followed by a fall to zero at 20 hours. For other data set graphs see Appendix 1. In the second data set (representing 58S800 with thermal treatment of 850°C for 20 minutes in dry nitrogen) we see that the phosphorus concentration reaches its maximum value at 7.5 hours, after maintaining zero values at all other time intervals.

Calcium and silica concentrations gradually increase until the final time interval of 20 hours but remain slightly lower than those from the control group, as expected. The third data set, showing the results of solution obtained from 58S800 thermally treated at 950°C for 20 minutes, show the same characteristic maximum phosphorus concentration value at 7.5 hours. However, there is a steady rise from the start of the experiment and then a decrease in values after 7.5 hours up to 20 hours. Calcium and silica concentrations remain parallel, gradually increasing until the end of the experiment but values remain lower than those of the control and the sample treated at 850°C for 20 minutes.

For the fourth data set, of 58S800 treated at 1050°C, (see Appendix 1), we also see the parallel pattern of calcium and silica concentration, which rise initially, followed by a drop at 7.5 hours and then a rise again at 20 hours. Phosphorus concentration reaches a maximum at 5 hours, unlike the preceding data sets, and then values drop again up to the 20 hour termination time. For the final data set, we also see a gradual and parallel rise in the concentration values for silica and calcium species in solution. Phosphorus however, is more variable with an initial drop at 5 hours followed by a steady rise until the end of the experiment, giving the highest values of 0.5 for all data sets regarding phosphorus concentration in solution. See Appendix 1 for graphs representing reaction rate trends with respect to time for all series 58S. Table for 7.4 summarises the reaction rates 58S800 after immersion in Tris buffer solution at 37°C.

Table 7.3: Reaction rates for 58S800 series after immersion in Tris buffer solution at 37°C.

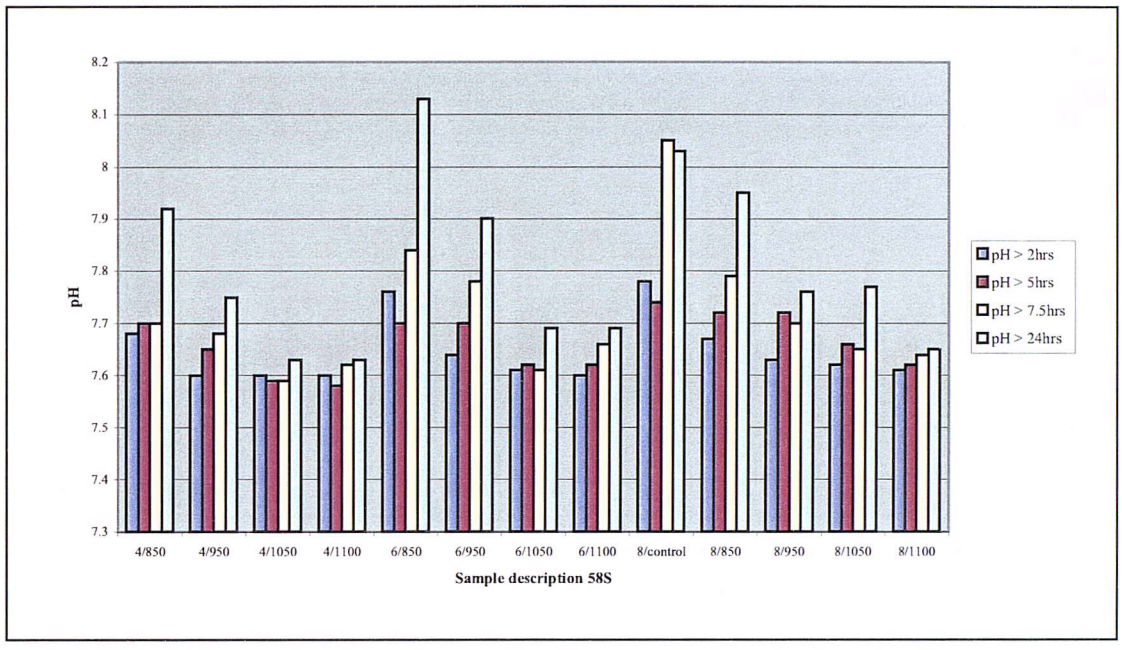
Sample	Species	Rate (k) 0-2Hrs	Rate (k) 2-5Hrs	Rate (k) 5-7.5Hrs	Rate (k) 7.5-20Hrs
58S800	Si	2.16E-03	-2.69E-04	3.00E-03	8.44E-05
58S800/850	Si	8.40E-04	3.27E-04	5.22E-04	4.51E-04
58S800/950	Si	4.74E-04	4.14E-04	3.78E-04	3.11E-04
58S800/1050	Si	3.76E-04	2.24E-04	-4.68E-04	5.79E-04
58S800/1100	Si	1.61E-04	1.87E-04	4.16E-04	2.21E-04
58S800	Ca	1.45E-02	-2.63E-03	2.10E-02	-3.11E-04
58S800/850	Ca	6.18E-03	2.26E-03	3.18E-03	2.44E-03
58S800/950	Ca	2.68E-03	3.14E-03	3.33E-05	8.76E-04
58S800/1050	Ca	1.69E-03	8.24E-04	-1.64E-03	1.76E-03
58S800/1100	Ca	6.41E-04	4.21E-04	7.89E-04	4.02E-04

The pH variation throughout the Tris-buffer experiment shows a general increase to highest values except for the 58S800 control group, where the pH measured is at the highest value after 7.5 hours. However, we see that the Tris-buffer solution maintains constant values averaging 7.69 at 2hrs, 7.66 at 5hrs, 7.2 at 7.5hrs and 7.1. at 24hours across all samples groups. The highest value measured (8.13) was at 24 hours for the 58S stabilized at 600°C after thermal treatment at 850°C for 20 minutes. However, it has been noted that stabilization at 600°C yielded variable results for both pore, density and dissolution data, unlike those obtained from 58S stabilized at 400°C and 800°C. Taking into account that stabilising at 600°C could develop a secondary, but unknown phase in the material which could involve a different orthophosphate environment to that in the calcined material. This material could liberate further phosphate entities into solution more rapidly.

However, it has been noted that these types of glasses are hard to produce by melt-derived techniques due to the high temperatures required. Phase changes are evident in the material from DTA and XRD spectra of thermally treated samples of 58S. The sol-gel derived glasses studied in this work have lower crystallisation temperatures and favorable crystallisation environments. By using this process to synthesize 58S it is also noted that the product has a defined silica-rich network containing small clusters of CaP agglomerations. With the previous recognition of phase separation in this gel-glass, the secondary phase could be that of a mixture of β-$Ca_2P_2O_7$ and other phases i.e. β-$Ca_3(PO_4)_2$ (β-TCP), as seen from XRD analysis. The phase could be that of another CaP phase with a slightly different Ca:P ratio. As the Ca:P ratio for pure β-$Ca_2P_2O_7$ is 1, which does not correspond to any readings taken from EDAX analysis even when

allowing that beam width dictated the area scanned, we must assume a hydroxyapatite (on the surface) and an orthophosphate environment in the bulk of the gel-glass.

Figure 7.4: Graph of pH variation with respect to time for 58S samples stabilized at different temperatures and after immersion in Tris buffer solution.



In the case of 58S, EDAX readings could only be interpreted as a bulk quantity due to the very small size at which phase separation occurs, as shown by TEM. Similar Ca:P ratios for hydroxyapatite are shown from SEM/EDAX readings taken from the large visible features on the surface of the materials after immersion in liquid medium. If β-$Ca_2P_2O_7$ phase was in the material it would in turn be evident by the grayscale colour in the TEM analysis (which for β-$Ca_2P_2O_7$ would be lighter than the other phases) but this is not the case. It is also evident that β-TCP inhibits apatite growth and no layer formation is seen on this material after several weeks in SBF. This could explain regions of the surface without apatitic, amorphous CaP bulbous growths created.

7.3.4 Discussion of data obtained from ICP analysis of solutions from 58S stabilized at different temperature and with thermal treatment after immersion in Tris buffer solution at 37°C

From the data sets obtained from these experiments there is a general trend that liberations of Ca and Si species in solution fall with increased thermal treatments. This is to be expected, given that the heat treated sample in each case has lower surface area

and total pore volume values. However, a marked pattern is seen in the first data sets i.e. (those with low thermal treatment temperature) at 850°C or the control in the case of 58S800 where initial levels of calcium and silica concentrations undergo a drop and then rise again towards the final time period at 20 hours. This pattern is also observed in the samples that have undergone heat treatments at temperatures of 1050°C and 1100°C. We also observe that heat treatments at 1100°C gives a product which, after some time delay gives the highest release of phosphorus species into solution at a maximum value of 0.5 (0.4 in the 58S600 series).

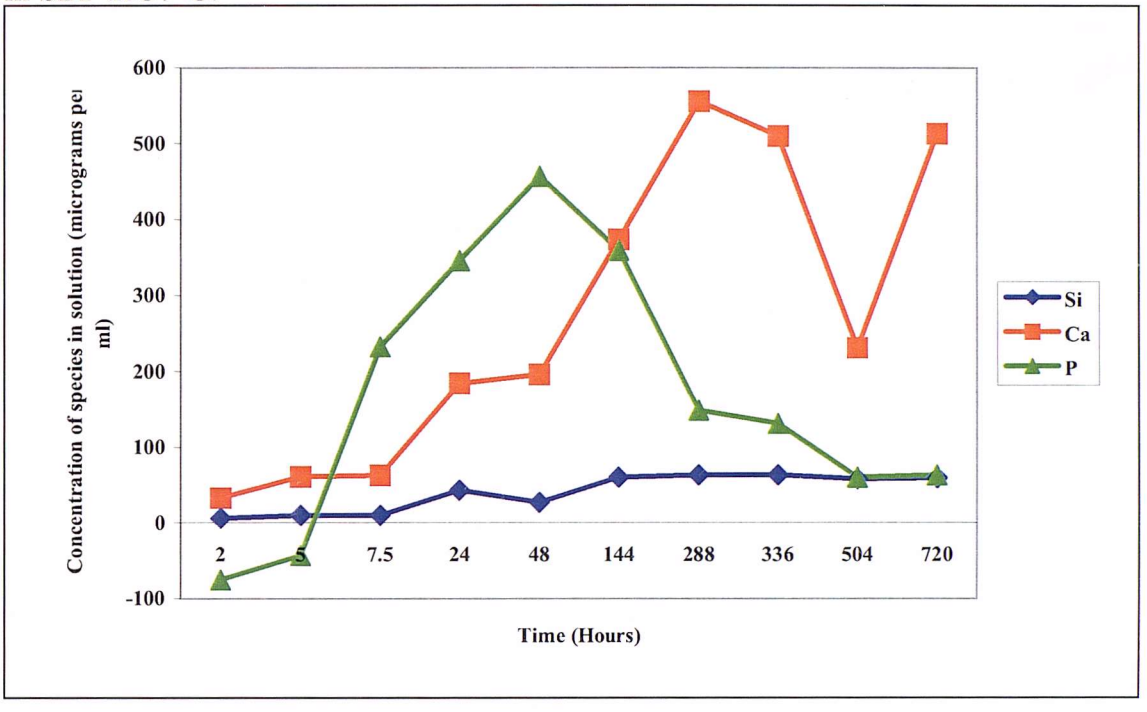
These features can be explained by the structural changes undergone by the material at certain temperatures. We see that the product has a more controlled release when subjected to heat treatments of 1100°C whereas at 1050°C calcium and silica liberation initially drops from the initial recorded level and then rises again in a 'second wave'. This suggests that the 58S has undergone an initial attack from the liquid medium followed by a period of time where liberation is halted and then recommences when the glass network breaks down. These trends are important because the concentrations of calcium, silica and phosphorus could prove harmful in a biological medium. Pre-soaking of the monolith may be done before exposure to cells or any biological implantation, see Chapter 8. Fortunately, this sol-gel derived composition does not contain sodium as it has been previously noted that a concentration of sodium can prove toxic when placed in a biological medium [148].

7.4 ICP results for 58S800 immersed in Simulated Body Fluid (SBF) at 37°C.

Again time release experiments were done using ICP to analyse solutions obtained after various time intervals, after soaking the monolithic fragment in SBF using the normal regime of synthesis and weight to volume ratio of $0.012 g/cm^3$ [54]. By this stage in the work, 800°C had been chosen as the optimum stabilisation temperature producing the most controlled dissolution results. It was also a processing temperature at which others had noted the disappearance of nitrate species in the material, which had been detected by DTA in other composition which had not been calcined at 700°C [53]. Care was also taken to avoid higher temperatures for thermal treatments as it had been suggested that a more crystalline material was apparent after treating samples at 1050°C for 75 minutes in air [53]. For this study a maximum temperature of 1000°C was chosen for the thermal treatment. Each thermal treatment was for 20 minutes in air with increasing

time intervals up to a limit of 30 days. SBF was not replenished during the experiment and ICP analysis of solutions was taken at 2 hours, 5 hours, 7.5 hours, 1 day, 2 days, 6 days, 12 days, 14 days, 21 days, and 30 days.

Figure 7.5: Graph of ICP data for dissolution products of 58S800 after immersion in SBF at 37°C.



After immersion, samples were washed in acetone and dried overnight in the oven at 60°C, these samples were then used for FTIR analysis to find evidence of an apatite layer. However, from the graph it is seen that concentrations of all species in solution are much higher than in previous experiments using Tris-buffer solution. In each case, the initial values for the concentration of calcium, silica and phosphate ions in solution in SBF are subtracted from the control data, as with the Tris-buffer study. Calcium and silica levels are also higher in solution than the Tris buffer study. This can be explained by the difference in composition between the two solutions. There may be a common ion effect whereby the ions in the solution are also contained in the starting solution itself (with SBF this is more pronounced that in Tris Buffer solution). However, there are still some negative values for the P species in solution, see Appendix 1. This could indicate that these are at times when some of the phosphorus species are involved in activity on the surface of the glass, which is why they are not present in the solution. The characteristic high ratios of phosphate content noted from EDAX measurements are from growths of amorphous hydroxyapatite on most of the surface after immersion. We must also bear in mind that the SBF solution was not replenished throughout the

experiment and the characteristic large evolution of ions into solution from the sol-gel product is observed. This would have an effect on amounts of carbon dioxide in the final solution as well as the likelihood of hydroxycarbonate apatite being formed.

The results from the ICP data given in Figure 7.5 outline the data set for 58S800, (for all other graphs see Appendix 1. In the control group, first data set representing 58S stabilized at 800°C for 24 hours, the calcium species is seen as rising to a maximum at 14 days and at 30 days. The silica release values match this trend showing that the network is released in the same manner as the calcium modifier in this sample. Phosphorus evolution in solution follows a binomial trend with a maximum value at 2 days in SBF. In the second set of data for 58S800, with thermal treatment at 900°C, it is seen that calcium species in solution reach a maximum value at 14 days and at 30 days, similar to the control series. Silica also follows this trend and phosphorus levels reach a maximum at 5 hours then decrease at the 7.5 hours and gradually increase up to 30days. The data for 58S, with thermal treatment at 950°C for 20minutes, gives the most variable data but again we see a change for all species in solution. Initial release is followed by a decrease with each species and calcium reaches a maximum value at 14 days, whereas phosphorus is highest in solution after 1 day.

Calcium and silica liberation follow similar patterns increasing and then decreasing until a stable maximum is achieved at the end of the time period at 30 days. For the final set of data (58S800 with thermal treatment of 1000°C for 20 minutes) we see the most steady pattern for the liberation of calcium and silica into the SBF solution with both species showing second order diffusion characteristics and reaching a maximum concentration at 14 days followed by a small decrease. Phosphorus reaches a maximum value at 7.5 hours in solution and then decreases step wise with respect to time until 30 days. This may indicate that the phosphorus species is more highly bound in the silica network than is the calcium species and requires a liberation of silica before it can be liberated again, in a stepwise manner. The 'step wise' liberation of the phosphorus is seen in all data sets and usually follows that of a silica release whereas high amounts of calcium are parallel to the release of silica. Smoother curves are seen in the data for 58S800, with thermal treatment at 900°C and 1000°C, whereas thermal treatment at 950°C creates a product which has variable dissolution behaviour.

The highest liberation of phosphorus species is seen in the control data set, which indicates that the phosphorus is not as strongly bound in the phase of the material as it is after heat treatments. Calcium levels remain higher than silica levels in all data sets because calcium acts as a modifier in the glass structure with silica acting as the network forming constituent. However, the high levels of silica release into solution indicate that the material is prone to attack when immersed in a liquid medium and could be potentially resorbable. This is in accordance to previous work done by Greenspan et al., [56] where it was found that for both 58S and 77S, 30%wt of silica had been lost in four weeks, which indicated that these sol-gel bioactive glasses were bioresorbable materials. Other authors have also done work on the dissolution of Bioglass® powders in the range 30-710μm with a same high rate of silica dissolution as seen in this study [54]. Monoliths were also used in a dissolution studies focusing on Bioglass® compositions of 60-80mol% SiO_2 [54], which showed concentration in solution relationship more akin to the log versions of the results shown graphically in this work, (see Appendix 1). However, raw data represented in this work reveals a more step-wise behaviour as the network slowly breaks down. One could hypothesize that negative values in the data could suggest that ions are involved in a reaction on the surface. Table 7.5 shows dissolution data from a study by Greenspan et al. [56] using 45S5 melt-derived Bioglass® powder

Table 7.4: Mass in mg obtained for 45S5 Bioglass® after immersion in SBF [56].

Time	Mass in mg Si	Mass in mg Ca	Mass in mg P
7 days	40	-20	-15
14 days	60	-40	-20
28 days	62	-80	-40

The sol-gel derived product has enhanced capabilities as a resorbable material as the network is slowly degraded whilst the network modifiers are easily and rapidly released into the surrounding environment. It is due to the effective release of such ions, that in bone the bioactive affect of the material is increased in such a way that proliferation of cells may occur on the surface followed by the mineralisation of a network and new bone formation. In combination with the evidence, by confocal microscopy, that there is an interconnective pore network, which contributes to the easy release of ions into the surrounding environment. As well as providing pathways allowing attack from the

liquid medium to penetrate the structure. One could hypothesize that this enhances the mechanical properties (Weibull modulus) of the material after implantation.

7.5 Fourier transformed infrared spectroscopy (FTIR) analysis of 58S samples

FTIR is the primary method of identifying apatitic layers on the surface of bioactive materials and previous work done on the 45S5 Bioglass® and 58S-77S Bioglass® systems shows quick layer formation and growth in vitro [10,21,43,54,56,120,123,124,147,149,150]. Some studies report on the effects of surface area to volume ratio on surface reactions of bioactive glass particulates [10,54,149] and others are on glass of different nominal composition i.e. Binary systems and those with MgO additions [42,57,64,129,146,151-153]. Testing criteria for these experiments have also been discussed previously [147] including the standard procedure by which bioactive materials can be tested *in vitro* for peaks indicative of apatite like formation on the surface of the particles. Miyazaki et al., [154] have reported growth of apatite layers on niobium oxide gel in SBF given that certain functional groups are shown to induce apatite growth including. There are many simulated body fluids in use that can be synthesised and used to accommodate these results, they are highly saturated with the ionic make-up required for apatite layer growth on a charged surface. On the surface level, if a material has adequate bonding sites for the attachment of an apatite group then it is easy to prove that it is bioactive to a certain degree. The unique feature of the Bioglass® system is the fact that it elicits this response in very short time and apatite peaks may be found after only 2 hours immersion in solution [147]. This type of experiment is used to confirm bioactivity before cell culture or biological study.

7.5.1 Experimental procedure for FTIR analysis

Quality assurance guidelines from previous studies [147] were observed in all experiments, and care was taken that the samples were washed in reagent grade acetone after immersion to stop any reaction after retrieval. Monolithic fragments were used after immersion in SBF at 37°C for various times using a consistent weight to volume ratio of 0.012g/cm^3 [5]. However, reflective methods were not used in any of the experiments using Method 1 (where sample powder mixed with KBr powder at a ratio of 1:100 was used to press pellets providing accurate results in transmission) as characteristically low adsorption levels were generated when reflectance mode was used

with the Midac M2000. Reflectance methods were used later (see Method 2) but transmission was chosen initially when using the Midac M2000, using a pressed powder pellet and auto gain mode (where the thickness of the pellet was accounted for). In method 2, a Genesis II Mattson, FTIR with Spectronic Unicam was used to obtain data. Sample preparation was easier in this method because this machine had a 'cup' fitting, which allowed sample powder and KBr powder to be simply mixed well in a pestle and then added to the cup for analysis. There is also an abundance of comparative material available when using this method. In addition, transmission spectra, once obtained, can easily be converted to adsorption spectra by use of basic software included in most FTIR equipment.

Initially the reacted surface from monolithic fragments was used to analyse peaks occurring in the main region of 650-400cm^{-1} where phosphate group activity may be visible [54,123,129]. This is the main region of interest when looking for the evidence of an apatite layer where the sample's silicon - oxygen - silicon rocking (475cm^{-1}) peak is diminished after reaction and replaced by hydroxyapatite (600cm^{-1} and 560cm^{-1}) peaks if the sample is bioactive [147]. In the samples prepared by immersion in SBF followed by acetone treatment and drying in air overnight at 60°C, the surface layer was removed with a scalpel and used as the reactant powder to be mixed with KBr powder for analysis. This procedure was also used for samples that had been in immersed in Tris-buffer solution from previous dissolution studies. After thorough mixing of the two powders in the ratio (1:100, reactant to KBr powder), discs were then pressed to 6 tonnes pressure in a die and scanned in transmission mode by FTIR (Midac M2000). These samples were obtained, using a static environment for immersion without replenishment of SBF.

A second method (Method 2) was also used whereby sample powders of a given size were immersed in SBF at 37°C in an orbital shaker at 175rpm [150], to provide a dynamic comparison to the previous static method. A weight to volume ratio of 0.012g/cm^3 was used consistent with previous work by Pereira et al. [54].

Surface area to volume ratios were not used due to the spurious nature of results obtained from samples that had been extensively thermally treated. To be consistent a weight to volume ratio in accordance with Pereira et al. was used. This provided enough SBF to sample ratio for the experiment not to become over saturated with ions

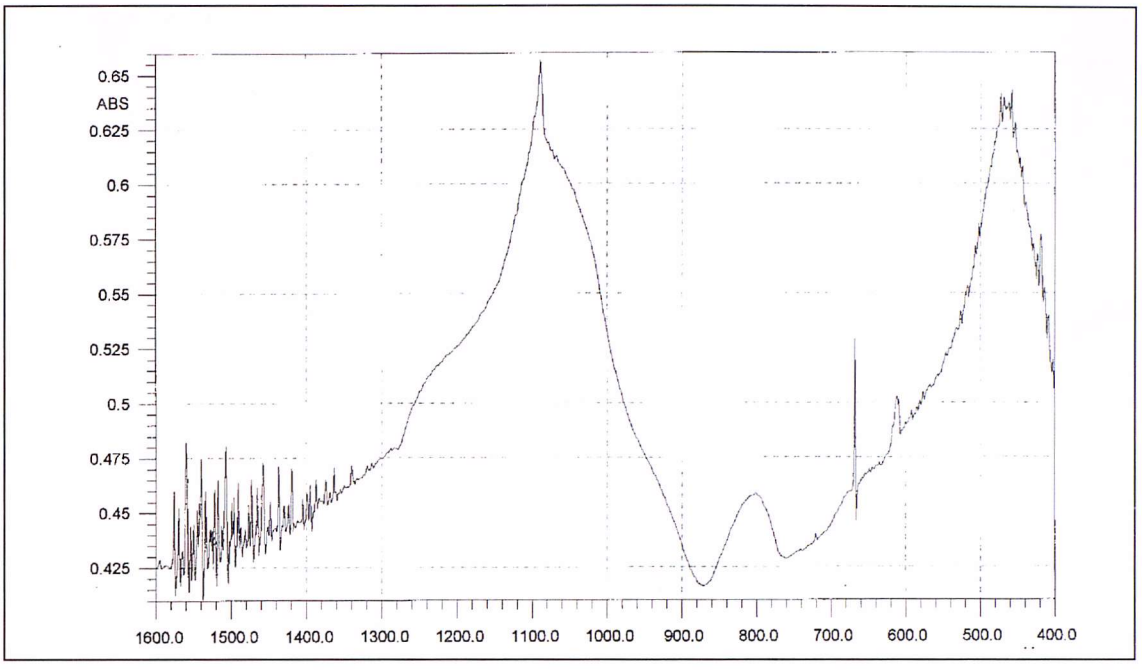
by the end of the time, as shown from dissolution studies which showed no solid matter left in the PE containers throughout testing. After immersion for various times the powders were extracted by filtration and were then washed in reagent grade acetone and dried overnight in air at 60°C. It was found also that drying before mixing with KBr powder was also necessary because both reactant and KBr powders are similarly hydrophilic and should not be exposed to the atmosphere for any length of time. Untreated specimens were initially scanned using FTIR to provide control data. For all scans, an initial KBr pure background scan was firstly recorded. This spectrum was then automatically subtracted from the reacted product spectrum in subsequent runs. A different analytical machine was used in the second method where it was not necessary to press discs to obtain spectra and data were obtained by means of reflectance, by mixing the reactant powder with the pure KBr in the given ratio and then entering this powder into a special 'cup' attachment fitted to the machine. These results remain the most accurate of all data obtained and spectra are shown in Figures 7.8 and 7.9a-c. Results from the initial study are discussed below.

7.5.2 Results using FTIR pellets prepared from thermally treated 58S samples using method 1

In this method a M2000 FTIR by Midac Corporation was used. Method 1 involves scraping the surface layer from the surface of the monolith after retrieval from solution and drying to provide the reactant powder. The reactant powder was then ground and mixed with KBr powder at a ratio of 1:100 to press a pellet required for analysis. Even though the results from this method remain inconclusive, they were very consistent and we attempt here to explain what was achieved.

Samples of 58S from the thermal treatment study were used to obtain data from FTIR by mixing with KBr powder. In none of the spectra, was a peak at $470cm^{-1}$ observed. Considerable activity was observed between $400 < cm^{-1} < 450$. There was no evidence of a peak at $560cm^{-1}$ but there was at $610cm^{-1}$ in all spectra. Activity at the $1090cm^{-1}$ was detected indicating that the glassy phase is still present in the material in agreement with previous authors [42,54,123,129,151]. However, characteristically in each spectrum a definite peak was observed at $800cm^{-1}$, which is assigned to carbonate groups [155].

Figure 7.6: FTIR spectra obtained from untreated 58S800 using Method 1.

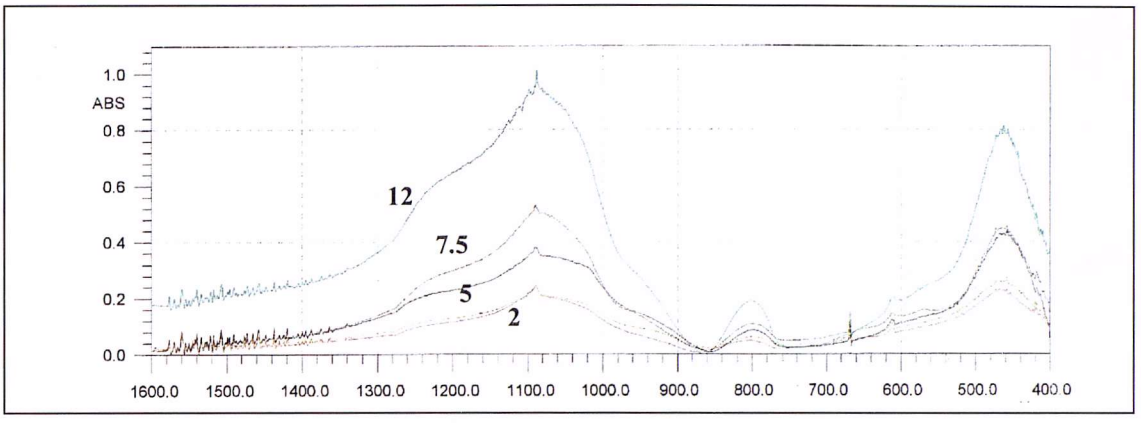


These results remain inconclusive, and do not agree with other authors [54,121]. Reasons for this are discussed further in this chapter. After repetition of analysis by this method the spectra remained unchanged.

7.5.3 Results obtained by method 1 FTIR from samples 58S800 after immersion in Tris buffer solution

Samples of 58S800 were use to generate data by FTIR after use in the dissolution study. First, the samples immersed in Tris-buffer solution. Spectra were obtained using the method 1, involving FTIR of pressed pellets and data were obtained from samples after immersion in Tris-buffer solution for 2, 5, 7.5, 12 and 24 hours. All spectra contained peaks at 800, 610, 470 and 420cm^{-1}. Theses peaks were found to increase in intensity with time but were not consistent with the data from previous authors [54,121] apart from those at 610 and 470cm^{-1}. These were assigned to P-O bending and Si-O-Si stretching respectively. However, no evidence of peaks at 560 was obtained. An example of the spectra obtained from these experiment is shown in Figure 7.6.

Figure 7.7: Spectra obtained by method 1 FTIR analysis of 58S800 after immersion in Tris buffer solution at time periods of 2, 5, 7.5 and 12 hours.



Secondly, we look at the spectra obtained by method 1 of a sample immersed in SBF solution for various time periods. Of a study done with all 58S800 compositions including those made with HF addition the same results as above (the Tris study) were obtained. It was now clear that these results, even if inconsistent with others work were totally reproducible and that the same peaks at 1090, 670, 610 and activity thereafter at $< 470cm^{-1}$ were observed in all spectra. Figure 7.7 shows typical spectra obtained from this study. However, it is now obvious that the characteristic peak at $800cm^{-1}$ is no longer seen. After much experimentation with this method, a different machine was used to generate data.

7.6 Results obtained from FTIR analysis of powder samples after immersion in SBF in an orbital shaker using method 2.

After much trial with method 1, it was realized that more surface area may be needed to provide more convincing evidence of the bioactive properties of this material or that it was possible that the reactant layer was covered by the introduction of amorphous bulk material upon grinding. A method using powders immersed in SBF solution at 37°C in an orbital shaker was used. The same weight to volume ratio as in previous studies [54] was used and sample were immersed for 20 hours in an orbital heated shaker set at 175rpm and 37°C. Samples were extracted and separated from solution by filtration. The reactant powder was dried at 60°C overnight after washing with reagent grade acetone. Data for the 58S800 systems with thermal treatments and those for 58S800 synthesized with different HF additions were obtained. Reacted powder was combined with KBr powder for analysis in a reflectance cup fitting. A background scan was first

recorded for pure KBr powder and subsequently subtracted from all reacted spectra. Spectra obtained from this study are shown below in Figures 7.8 and 7.9a-c.

Figure 7.8: FTIR spectra for 58S800 after immersion in SBF for 20 hours at 37°C.

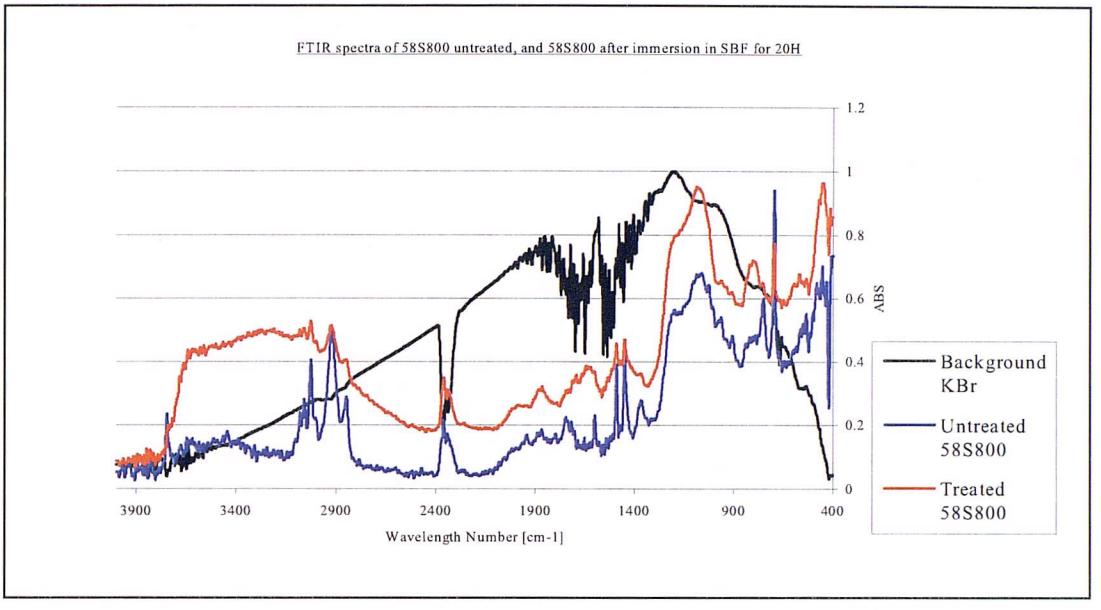


Figure 7.9a: FTIR spectra of 58S800 with thermal treatments after immersion in SBF for 20 hours at 37°C.

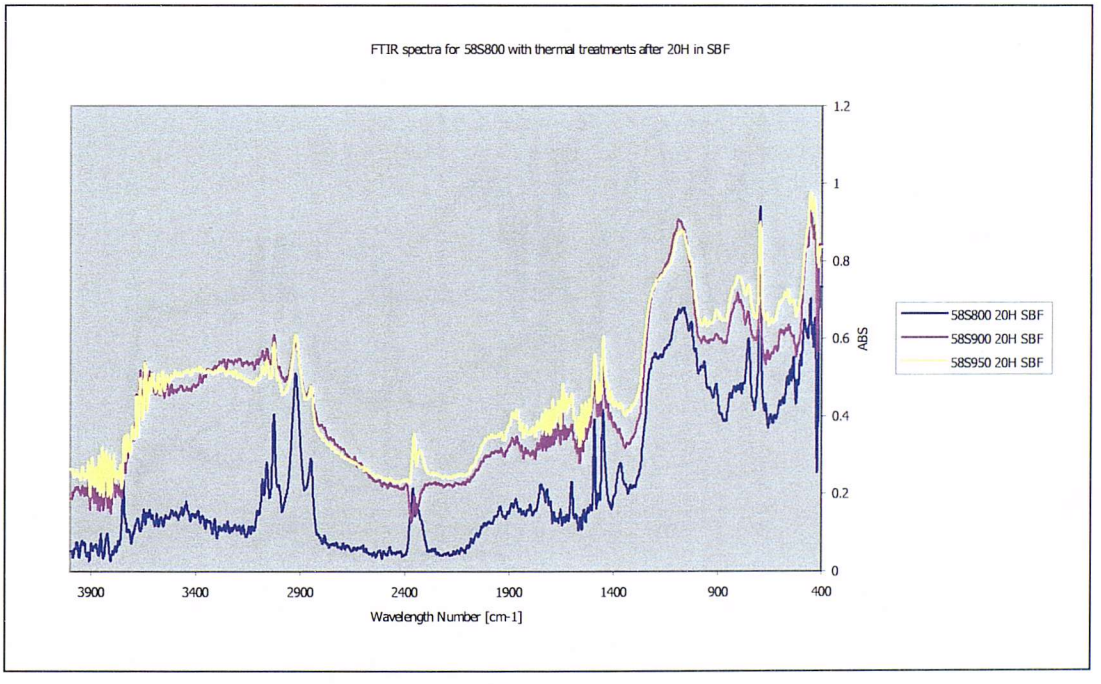


Figure 7.9b: FTIR spectrum for 58S800 treated at 1000°C for 20minutes in air after immersion in SBF for 20 hours at 37°C.

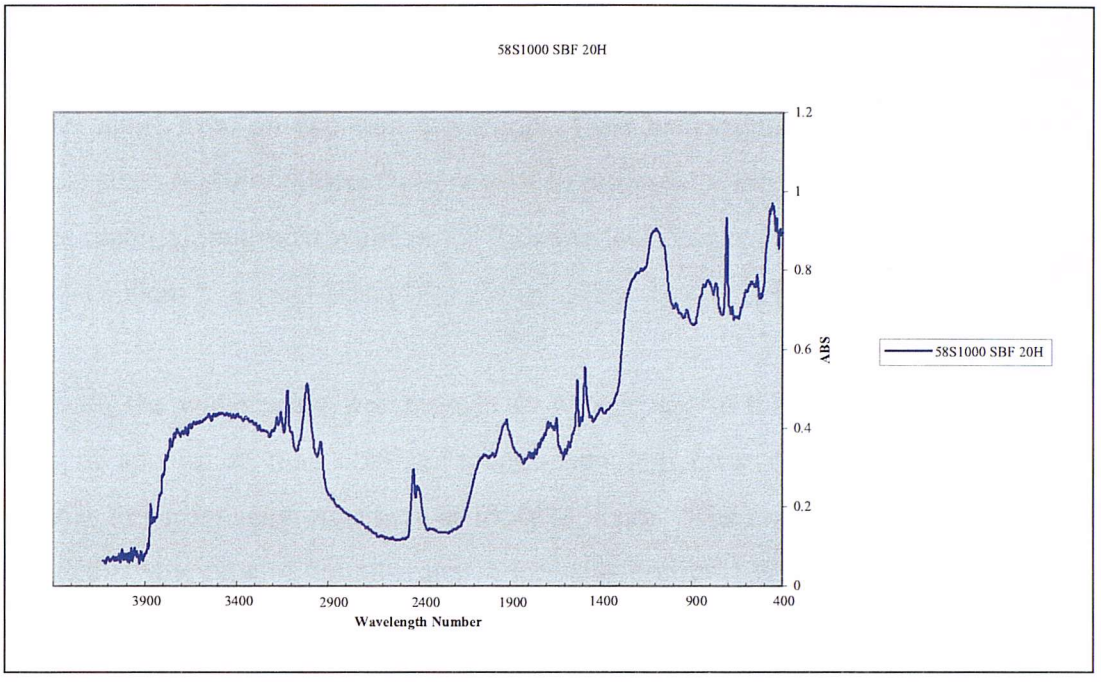
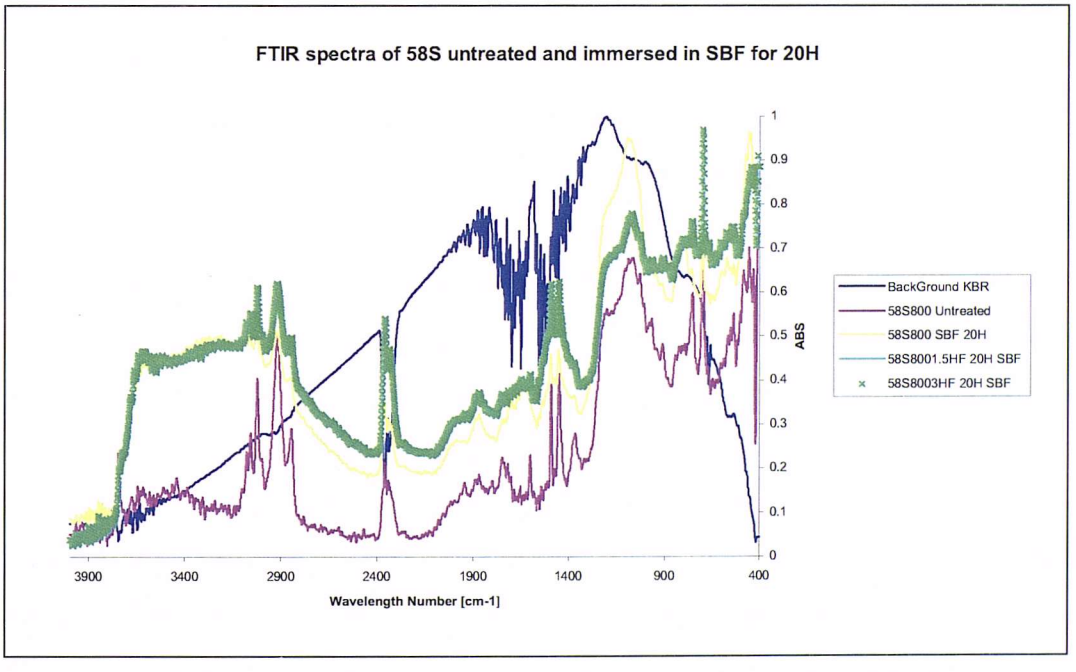


Figure 7.9c: FTIR spectra for 58S800 and 58S800 with HF addition after immersion in SBF for 20 hours at 37°C.



Figures 7.9a-c show the spectra obtained from powder immersion in SBF at 37°C after 20 hours for various different forms of 58S800. In two of the spectra the background spectrum is also included to show any interference with peaks obtained even when subtracted. However, most of the peaks are clearly shown to belong to the reactant powder apart from an apparent reflection of the background at close to 2400cm^{-1}. A spectral scale of 400-4000cm^{-1}was chosen to represent a more comprehensive spectrum for the material, but most work in the biomaterials field is carried out only in the range of 400-1600cm^{-1}.

However, the wider scale was thought to be relevant to this work because secondary peaks of adsorption may confirm species bonding lower down in the spectrum, the presence of carbonate groups seen at 1450-1550 cm^{-1}. The region covered at > 2700cm^{-1} will identify the type of bound water in the structure [54,129,151,155]. Free OH groups are visible at >3600cm^{-1}, with hydrogen bonding shown at regions 3600 < cm^{-1} < 3200, followed by intramolecularly bohund water at 3200 < cm^{-1} < 2700 [54,151,155]. In all spectra obtained there is a detectable amount of this type of water in all 58S800 materials. The unreacted products always contain less than the reacted products, even after using standard drying procedures [147].

From the graph showing the 58S800 untreated versus 58S800 after immersion in SBF for 20 hours, it is evident that the peak at 470cm^{-1} becomes obscured and broadens showing the glassy phase of the silica rich layer being masked by the development of an hydroxycarbonate apatite layer on the surface of the glass particles. This is consistent with previous results [44,54,123,129,149,151] in combination with a peak arising at 580cm^{-1} and the growth of a minor peak on the untreated 58S800 at 602 and 610cm^{-1} which are assigned to P-O bending [10,54,123,129]. At 1100cm^{-1} we see that a minor peak is obscured from the transition of the untreated product to the treated product showing that the glassy phase in the glass is also being obscured [44,149] with activity at 510cm^{-1}, which also represents the glassy phase being masked. Chloride activity seen at 560-830cm^{-1}[155] is also seen to decrease from the untreated product to the 58S800 treated in SBF, were the peak is broadened and no longer defined in the region of 750cm^{-1}. A doublet present at 1410-1450cm^{-1} represents carbonate activity in the sample [141,155]. These peaks are seen in most samples and are seen to become less defined from the unreacted product to the reacted, however, the doublet is observed in both the unreacted and reacted product.

This indicates that the starting material is high in carbonate species as expected from phase evolution and possible crystallization during the process regime involving high carbonate contents also seen in previous work done by Barralet et al. [53] when creating synthetic carbonate hydroxyapatite materials. In addition, the SBF was not replenished and the increase of carbon dioxide in solution is also to be expected in a closed system. Both of these factors may explain the carbonate group activity indicated from all spectra noted. This indicates that the layer formed is more carbonate-rich that phosphate-rich, which is probable considering that this feature is also seen in HCA amorphous layers formed on bioactive materials, which had not had time to crystallize [156]. Activity is also seen in the region 1150-1250cm^{-1} and matching at 2350-2400cm^{-1} outlining P-H stretching and bending modes in the sample [155] present in both untreated and treated spectra for 58S800. After 2700cm^{-1} it is evident that substantial OH bonding activity is visible [151], more obvious in the treated specimen than the untreated. Even though powders were dried after reaction according to procedure [147] there is a considerable amount of intramolecular water still evident, together with freely bound –OH. Activity in peaks outlining Si-O-Ca activity from 800-950cm^{-1} are greater in the treated samples, than in the unreacted sample [10,54,56,123,129].

Looking at the spectra obtained from the 58S800 samples made with HF addition versus the regular recipe, we see that activity in these samples is greater than in comparison to the normal 58S800. Defined peaks given in the unreacted sample at 470cm^{-1} showing the glassy phase are completely masked after immersion. The samples containing 1.5ml and 3ml HF [5%] addition behave almost identically after immersion, they both have the same peaks at 551, 577, 960cm^{-1} indicating phosphate activity. In addition, peaks are seen at 700 and 760cm^{-1} indicating halide activity, these are more intense in the HF addition samples then the regular 58S formula. SEM analysis of these samples indicated the surface formation of CaF_2 crystallites and amorphous HCA growths were also observed [152]. Peaks are also seen in the carbonate region at 1450 and 1493cm^{-1}, for all reacted samples. A doublet in all samples at 2361cm^{-1} represents P-H activity [155]. Bound-water associated peaks [151] appear more strongly after samples have been immersed in SBF solution.

It is also possible that atmospheric water was introduced to the surface of unreacted 58S800 whilst in transition during the process regime and before proper desiccation, creating the appearance of phosphatic activity in the spectrum of the untreated 58S800.

This behaviour indicates the hydrophilic nature of these materials, as with natural silicas [134] the uptake of water can be on very small scale but rapidly bound in the structure. When looking at the spectra of the thermally treated samples of 58S800 and the regular 58S stabilized at 800°C, in both unreacted and reacted forms we see that characteristic peaks for phosphate and carbonate activity are present. At 560cm^{-1} phosphate activity is seen in all treated samples with the peak at 470cm^{-1} representing the glassy phase being completely obscured in the reacted samples. Carbonate activity is seen at 1410 to 1450cm^{-1} and P-H activity is also seen in the region of 2350-2450cm^{-1}, however, this trend is inverted in the sample, which is treated at 950°C. On the end of the spectrum water activity is seen in the region >2700cm^{-1} where consistently more intensity is seen in reacted than unreacted products.

The lack of difference between unreacted and reacted 58S spectra may be due to the fact that a hydroxyapatite layer has already had time to form on the highly reactive surface of the 58S in atmospheric water before desiccation during storage, as the reaction was already started without the need for immersion due to the high surface area of these powders, their hydrophilic nature and the possible hydroxycarbonate apatite phases previously nucleated in the processing regime. However, it is apparent that carbonate peaks in combination with water activity are seen in all spectra, this is evident due to the specific peaks associated with water which are present in all samples, especially those at 700cm^{-1}. Those occurring at >2700cm^{-1} are evident from the spectra [54,141,151].

7.7 Discussion of results from dissolution studies and FTIR data obtained for 58S Bioglass®

From the nature of these sol-gel derived materials, when placed in liquid medium we see that there is a rapid release trend. This is to be expected since high surface areas are involved. For experiments using powders and particulates, there are even higher surface areas increasing this effect. From the nature of the phase evolution produced during processing, we can also suggest what dissolution products may evolve and perhaps deduce the solubility of this material completely. Due to the modifying phase being unresolved and shown as amorphous, we cannot totally predetermine how this phase will behave. The results from FTIR indicate the formation of a carbonate hydroxyapatite, which is calcium deficient. However, peaks outlining strong phosphate

activity are not visible, this can be due to several factors. First, when a nanophase separated material grows crystallites on its surface; these crystallites may be very small, thus making specific identification of phases difficult with normal methods such as XRD or small angle XRD. It was found in the unreacted product, which had been thermally treated at 1050°C, that peaks are visible which show different calcium phosphate phases active in the material and peaks of an apatite phase. However, for very small crystals on the surface these peaks may be shadowed by an amorphous halo background if any of the bulk material is also scanned. The XRD analysis of the 58S800 shows that only two amorphous halos are visible, one being on the slope of the other.

It can be interpreted that this phase is a constituent of the bulk, derived from ground powder samples, and not necessarily from the surface, if the layer is small. The surface phase is the rate determining step in dissolution experiments because care is taken to avoid creating any new surface, which would affect dissolution rates. X-Ray diffraction surface analysis showed non-crystalline behaviour even after the sample was thermally treated to 1200°C, (see Chapter 6). From the peaks which diminish, we can say that this effect is due to the loss of carbonate from the surface at temperatures above 1000°C. However, more sensitive techniques such as AFM may be needed to identify specific sites of crystallites, their nature or silanol surface. It could also be that phase separation in the material causes different areas of specific surface reactivity and hydroxycarbonate apatite formation. Secondly, the hydroxyapatite family can incorporate many substitutional groups within the structure of the general formula ($Ca_{10}(PO_4)_6(OH)_2$) and previous authors have mentioned that often a calcium deficient form of hydroxyapatite is produced in favour to the highly defined and crystalline hydroxyapatite [90]. It has also been suggested that a highly ordered crystalline phase of hydroxyapatite can only be obtained given longer times (24-28 days) [90].

Hydroxyapatite synthesis can also be the result of thermal treatment of a specifically synthesized glass with controlled composition [157]. Amorphous HCA is developed on the surface at short times and is observed in much of the previous work done on bioactive glasses and glass-ceramics [54,158]. In the hydroxyapatite family, upon labelling the PO_4 group as group A and the OH group as group B, we find that there can be many different substitutions of the A and B groups which produce apatites without a Ca:P ratio of 1.67 [158]. Carbonate groups can replace group A or B in hydroxyapatite; however, it is more usual that type A substitution takes precedence. Type B substitution

with carbonate groups is not unheard of but the C axis in this case is larger and less likely. In human bone, we find a mixture of both type A and B substitution for carbonate groups. Non substituted hydroxyapatite may fail by extrusion after implantation [30]. Hydroxyapatite that includes carbonated A and B may be a better material for use in a biological situation.

From previous work, we know that in carbonated hydroxyapatite the Ca:P ratio is 1.78 and carbonate content is 3.8wt% [158]. In contrast to the ratio of 1.67 for pure hydroxyapatite and 1.5 ratio for calcium deficient hydroxyapatite. There are many ratios available from precursor phases, which also have different densities. By taking the average values from the bulk however we can confirm the composition, but cannot identify preferential areas for nucleation, for hydroxycarbonate apatite growth. We can identify surface growths as being calcium deficient hydroxyapatite by compositional ratios given at the specific site on the growth at high magnification using SEM/EDAX, see Chapter 6. FTIR spectra outline an alkali deficient material that cannot be stoichiometric calcium hydroxyapatite but rather carbonate substituted hydroxyapatite. The temperature at which the material is immersed in SBF can also affect the product found in the layer formed on the surface after immersion. At certain pH, this can provide conditions for preferential growth of a more carbonated apatite in preference to another substitution, such as calcium. The presence of this type of carbonated hydroxyapatite is confirmed in the FTIR analysis of all 58S samples.

There is also the "the common ion effect" effect to consider when commenting on the general trends of ICP data, the fact that ions in solution may inhibit those derived from the gel-glass if the solution becomes too saturated. Separate precipitation in the liquid is not observed during the experiment. The saturation of ions in the media is also different i.e. SBF solution is more saturated than the tris-buffer used in these experiments. Previous authors have tried to explain behaviours of different salts in solution and their effect on ion evolution from the substrate material [159]. Some focus on the effect of different temperatures of the physiological solution with respect to layer formation [156] and others on the composition of the physiological solution with respect to adsorption of proteins on the surface [121].

Studies included measurements of the effects of the composition of the aqueous phase on glass dissolution. Two solutes that were found to accelerate glass dissolution

received the bulk of the attention in these studies, namely the hydroxide ion, OH- and hydrofluoric acid, HF. The steric characteristics of the surface occupied by the alkali ion M+ are sensitive to the size of the ion. This accounts for differences in the rate of attack by aqueous solutions containing different alkali ions. Differences in dissolution rates in the presence of different alkali ions have also been ascribed to differences in rates of transport of the attacking medium through the adsorbed cation layer, in the case of the attack of various alkali hydroxides on silica gel [159]. This indicates that the precautions taken in designing the dissolution experiments in the absence of buffers, the high dilution and frequent exchange were effective in suppressing any pH rise that could affect dissolution rates. This conclusion was supported by the results of measurements of leachate pH that showed that the pH did not increase beyond 8.1, this was also found that even in the most saturated salt solutions [159] . The effect of Tris-buffer in preventing pH rise can be attributed to the fact that it is a zwitterionic species, unlike borate and phosphate. The amine functionality of Tris-buffer causes this molecule to resorb on to the glass surface and reduce its susceptibility to hydrolytic attack. The pH did not rise above 8.13 measured in Tris buffer solution experiments in this work, which is consistent with previous results.

An increased content of network modifiers such as Na^{+} and Ca^{+} in a glass composition also weakens the Si-O-Si bond structure and thus gives rise to higher dissolution rates, even though it does not affect the K_i values for the occupancy of the surface sites. The product 58S800 was the most stable of all 58S variations tested in this work and was chosen for dissolution and cell culture studies. 58S800 did not crack during immersion in a liquid medium. Cracking would increase surface area and lead to an uncontrolled evolution of ions from the material. Such a rise may be gradual, indicative of progressive propagation of microcracks or open pores. Such a gradual mode of degradation would be expected to be more important in the cases of high silica glasses. In the cases of such glasses, the Si-O network is more continuous and, therefore, the surface region of the glass can be expected to be less susceptible to other, more abrupt modes of degradation such as catastrophic rupture. It is also reported that for glasses with a higher silica content bioactivity is lowered, for melt-derived compositions the composition is fixed i.e. for compositions with > 60mol% SiO_2 do not form a crystalline HCA layer even after four weeks in SBF [21]. However, for the sol-gel glasses the limit is extended up to 85mol% SiO_2 being the upper most limit for HCA layer formation

[21], so 58S provided a system of known bioactivity which had a controlled dissolution behaviour be able to avoid spallation during immersion in SBF or Tris buffer solution.

According to models in previous work [159] the replacement of H^+ by a metal ion in the surface sites can facilitate the access of the aqueous medium to the Si-O-Si network. This steric effect would speed up the kinetics of both dissolution and re-precipitation and thus the observed solubility would not be affected. Calcium phosphate cements have been the subject of many studies in the last decade because of their biocompatibility and their capacity to fill bone cavities [157]. The dissolution-precipitation chemical reactions at room and body temperature involve crystalline phase transformations. Orthophosphate salts are distinguished from meta- and pyrophosphates in that they contain PO_4^{3-} groups rather than PO_3^- or $P_2O_7^{4-}$, respectively. Previously authors had only been interested in orthophosphate salts because pyro- and metaphosphates hydrolyse in body fluids and because high concentrations of these ions can result in extraosseous calcification. Increasing the calcium to phosphorus ratio (Ca/P) is associated with an increase in the basicity of these salts. According to the solubility diagrams [157] it can be observed that, at 37°C, HA is the least soluble salt at a pH of 4.2; for values lower than this, DCP is the least soluble salt. In addition, it was observed that for pH values lower than 8.5 the most soluble salt is TTCP; for pH values higher than 8.5 the most soluble salt is DCPD. In the system $Ca(OH)_2$-H_3PO_4-H_2O only a limited number of calcium phosphates can be obtained by precipitation in the form of crystalline solids with well-defined stoichiometry, physical and thermodynamic properties [160]. In fact, attention in the biomedical field is generally focused on the monocalcium phosphate (MCPM), dicalcium phosphate dihydrate (DCPD), octocalcium phosphate (OCP) and precipitated hydroxyapatite (PHA) because their respective solubility products are well established.

However, due to the nanophase separation observed in 58S800 we can only speculate as to which phases occur in what quantities, as resolution to provide EDAX proof of these phases to the 2Å level had not been possible. Analysis from XRD and FTIR indicated that a calcium deficient hydroxy-carbonate-apatite layer is formed on the surface of this material, rather than a pure form of HA. Previous authors testing the effect of different temperatures on the apatite layer formation on bioactive materials [156] also found that after using XRD analysis accompanied by FTIR they found pure calcium-deficient hydroxyapatite (CDHAp) $[Ca_{10-x}(HPO_4)_x(PO_4)_{6-x}(OH)_{2-x}]$ was formed. Complete

reaction occurs within 18, 11, and 6.5h at 37, 45 and 56°C respectively. HAp formation was characterized by an initial period of wetting of the α-TCP precursor, an induction period and a growth period during which the transformation to HAp occurs. The HAp produced by a cement-type reaction may exist over a compositional range and can be characterized in terms of its Ca/P ratio of 1.67. Stoichiometric HAp, $Ca_{10}(PO_4)_6(OH)_2$ has a Ca/P ratio of 1.67, while CDHAp, $Ca_{10-x}(HPO_4)_x(PO_4)_{6-x}(OH)_{2-x}$ may have Ca/P ratios extending to 1.5. For fully calcium-deficient HAp, x is equal to unity. Hydrolysis of α-TCP to HAp at low temperature is particularly attractive for several reasons. It utilizes a single precursor and forms fully calcium deficient HAp, which is more soluble than stoichiometric HAp and therefore may incorporated into bone more readily by osteocytes.

A more distinguishable OH- band was the vibrational mode neighbour of the principal PO_4^{3-} adsorption bands at $630cm^{-1}$, as seen in the resultant spectrum of 58S800. In addition, the spectrum of the hydrolysis product possessed the adsorption band arising from HPO_4^{2-}. A flat weak band relative to stoichiometric HAp at $872cm^{-1}$ assigned as P-OH stretch of HPO_4^{2-} group, which is unique to calcium deficient minerals [156]. Thus, the data from FTIR analysis of 58S800 and its family of thermally treated 58S800 and 58S800 with HF additions show the HAp formed to be calcium-deficient.

Rodríguez-Lorenzo and Vallet-Regí reported that temperatures in the range of 25-37°C are necessary to obtain apatites with crystal sizes in the range of adult human bone [161]. They also stated that longer reaction times produced calcium phosphate apatites with increased Ca/P ratios. Carbonate addition is also noticed by these authors who postulated that the aging of precipitated powder could lead to the incorporation of minor quantities of carbonate. From their work [161] it is also reported that it is possible to force the incorporation of carbonate ions into the apatite structure without introducing monovalent cations. The morphology of the apatite produced is considered as a function of reaction conditions (static or dynamic) and time.

Vallet-Regí examines the difference in Ca/P molar ratio in the layer formed when gel-glasses are soaked in SBF in other work [162]. He reports values of 1.6 decreasing to a value close to 1. He found that the chemical composition of the apatite layer formed was very heterogeneous and that there is evidence for the presence of a composition gradient across the layer. Apatite crystals were found to constitute the region close to

the glass substrate, whereas calcium concentration decreased from the inner region to the layer surface. Thusly, Vallet-Regí proposed a continuous recrystallization process of the calcium phosphate with a low Ca/P ratio compared to that of the apatite taking place in the bulk layer and that the apatite front progresses from the interior to the outermost part of the layer. In this same work, [162] the important issue of static versus dynamic SBF test regimes is explored. Ultimately the dynamic regime for SBF testing (where the SBF is continuously renewed) [162] shows that the deficiency in calcium increases if the *in vitro* test is carried out with a continuous renewal of the nutrient SBF solution. This is attributed to the lower pH values of the solution compared to that of the static test.

However, it had also been found [156] that the HA formed at 37°C has smaller crystallite size compared to those formed at 45°C and 56°C and that the extent of hydrolysis in pre-formed pellets was controlled by the penetration of water to the reactant α-TCP sites. However, experiments involving immersion at different temperatures was beyond the scope of this current work, 37°C was used but we expect that the crystallites formed on the surface would initially be rather small and hard to detect by normal XRD analysis with the bulk of the amorphous glass remaining below. It is confirmed in this work with 58S Bioglass® that calcium deficient HA is formed on the surface of the monoliths and powder after immersion in SBF.

CHAPTER 8 CELL CULTURE STUDIES

After confirming bioactivity by FTIR analysis, the next level of testing is in cell culture studies. Only after this step has been successful, can animal implantation be proposed. This chapter deals with the cell culture work done on 58S bioactive gel-glasses made at Imperial College in association with the Cell and tissue engineering group from Chelsea and Westminster Hospital.

8.1 Mimicking of bone materials.

As the primary application of the 58S monoliths produced was for use in hard tissue replacement and cortical bone applications it is important to fully understand the nature of bone in the human body and its' functions. Bone is a supporting connective tissue consisting of cells, called osteoblasts that synthesize and export, extracellular substance, or bone matrix. Bone matrix contains collagen fibers and an amorphous component with a high concentration of sulphated proteoglycans. In addition, bone matrix becomes calcified following secretion, with calcium salts in the form of hydroxyapatite crystals. As osteoblasts become surrounded by secretary product, they develop long, slender extensions, cease the secretion of bone matrix, and become osteocytes [92]. Large multinucleated cells called osteoclasts are able to erode the bone matrix, and are important in remodeling and regulating plasma calcium levels. Osteogenic or osteoprogenator cells derived from embryonic mesenchyme cells persist in certain regions and have the capacity to differentiate into osteoblasts.

8.1.1 Microscopic Organization of bone

Osteoblasts arise from mesenchyme cells and are responsible for bone formation (osteogenesis). The principle tissues that are capable of giving rise to osteoblasts are bone marrow, periosteum, and endosteum. Some agents that stimulate bone formation act by inducing proliferation and differentiation of osteoblasts precursor cells rather than direct stimulation of mature osteoblasts. Bone cell formation and bone deposition appear to include the production of osteoblast-derived growth factors that are involved in autocrine and paracrine regulation. There is some evidence that bone cells can produce growth/proliferating factors and perhaps inhibitory factors as well.

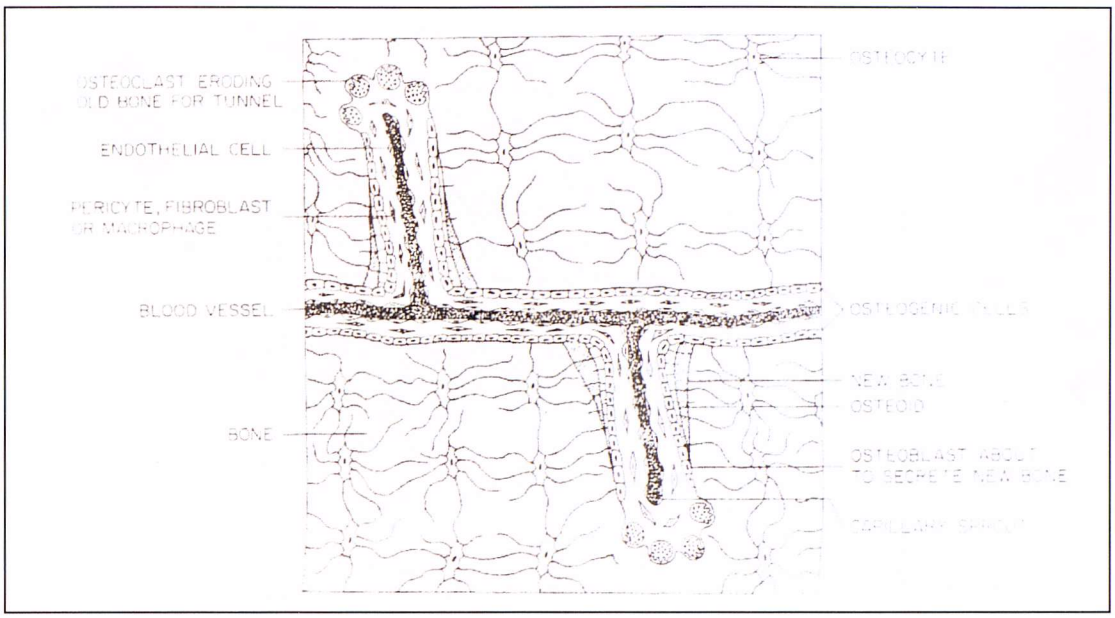


Figure 8.1: Diagram illustrates the formation of haversarian canals in compact bone [92].

Osteoblasts line bone surfaces; they synthesize, package, and export the organic constituents of bone matrix including Type I collagen and sulphated proteoglycans. When active, osteoblasts are usually elongated or columnar, and the nucleus is located in that part of the cell farthest from the bone matrix. The osteoblasts secretes in a polarized fashion. Once bone matrix secretion has been initiated, additional bone matrix is secreted on preexisting bone surfaces. New matrix comes to surround the osteoblasts. The ultimate fate of osteoblasts is to become enclosed within their secretory products as osteocytes.

The osteoblast undergoes a pronounced shape change as it becomes surrounded by bone matrix. Osteoblasts that are inactive in bone matrix secretion tend to be smaller and more flattened or oval than secreting osteoblasts. The microenvironment of bone cells is important to their differentiation. Among the molecules that are suggested to be osteoconductive are fibronectin, collagen, procollagen peptides, and larger proteoglycans. Secretory products of osteoblasts is summarised in Table 8.1.

Table 8.1: Secretory Products of Osteoblasts [92].

Substance	Action/Function or Postulated role
Alkaline phosphatase	Associated with P_i in calcification
Collagen I	Organic component of bone matrix
Hyaluronic acid	Organic constituents of bone matrix
Chrondroitin sulfate	
Keratin sulfate	
Link Protein	
Core protein	
Biglycan	Small gycloprotein; consists of core protein and one or two GAG chains; function unknown; possible role in cell-matrix interaction and control of cell proliferation
Decorin	Small gycloprotein; consists of core proteins and one or two GAG chains; binds type I and II collagen; implicated in regulation of collagen formation
Osteopontin	Present in osteoid at mineralisation front; role in mineralisation process; plays role in anchoring osteoclast to bone surface
Osteonectin	Bonds Ca^{2+} ions, hydroxyapatite, type I collagen, thrombospondin, and other matrix components
Bone scialoprotein	May play role in mineralizing process in bone
Bone morphogenic	Bone inductive activity; normal proteins maintenance of bone; important in the repair processes

Table 8.1, con't: Secretory Products of Osteoblasts [92].

Substance	Action/Function or postulated role
Procollagenase (enzyme)	Collagenase released from procollagenase by plasmin
	Both enzymes play a role in depolymerising osteoid
Plasminogen activator (enzyme)	Converts serum plasminogen to the neural protease plasmin; plasmin releases collagenase from proenzyme procollagenase

8.1.2 Osteocytes

When osteoblasts deposit bone on preexisting surfaces, they eventually become surrounded by bone matrix and are called osteocytes. As osteoblasts become surrounded by intercellular matrix, they extend many long, slender, finger-like extensions or tendrils that contact those of nearby osteocytes. This results in many small channels, called canaliculi that extend throughout the bone matrix and create a circulatory system that provides nourishment for osteocytes. The extensions of each osteocyte touch those extending of nearby osteocytes and gap or communicating junctions are formed.

The canalicular system is not completely satisfactory for the distribution of nutrients, gases, and wastes in bone since it is estimated than an osteocyte cannot survive if more than 0.20mm away from a capillary. If this occurs, then new Haversian systems are required to bring blood vessels into closer proximity to the osteocytes, see Figure 8.1.

8.2 Sample preparation for cell culture studies and experimental procedure.

Due to the highly reactive nature of the sol-gel produced 58S is was known that the glasses produced high concentrations of ions in solution and therefore, samples were soaked before cells were placed on the surface. Because the 58S does not contain sodium, this pre-soaking regime was to ensure that levels of ions were not high enough to kill cells. This method has been used as a 'safe-guard' against cell necrosis before commencing the experiment.

Pre-reaction of discs before cell culture performed by Yannis Xynos from the Chelsea and Westminster group for the initial study done on 58S400 and 58S800 monoliths. Soaking times are optional, as there seems to be no single time agreed. The time was anywhere between 2 hours and 3 days. However, these times can be modified when taking into account the dissolution kinetics of the materials and seeing when ion emissions from the material stabilize. This also seems to be the case when deciding cell densities used for the studies and also the sterilization method used before pre-reaction. The cell culture studies done with colleagues in the Chelsea and Westminster group, used sterilization by UV exposure. Cell densities varied, as did the well sizes in the reaction vessels.

Careful consideration was taken into account whilst processing the monoliths to determine whether the surface was compatible. As seen in the first cell culture studies, the sides of the discs where not uniform (as one side was unexposed during drying, face down on the watchglass). It was apparent that the primary human osteoblasts on the unexposed surface conformed to a flat and squamous state within the same time of immersion as compared to the exposed side. This could be a reflection on the stage of development of the cell line and not necessarily the toxicity of the surface. Nevertheless, dry racks were used to accommodate for any difference in surface created during processing in later cell studies. The conditions used to create a surface giving rise to healthier cell appearance with extended filopodia (the exposed side) were later employed for all monoliths.

In these studies, cells are seen to spread out over the rough surface of the 58S samples and the cell fibrils penetrate pores and can stretch the filopodia back to the surface through a given surface pore system. Care was taken when preparing the cell culture specimens for SEM examination. It was seen that preparations such as 'freeze drying' before analysis shrank cells drastically and broke fibrils of the cells on the surface. In these cases, it is evident that the cell has not suffered necrosis but has been dried out completely before analysis. Giving a less accurate picture of the state of the cell previously. Wet SEM analysis is not yet standard procedure for these types of studies but is highly recommended for analysis of further cell culture studies, see Chapter 9.

There are limitations with respect to glass composition due to a phenomenon called the mixed alkali effect, whereby, pH can build up in a porous structure killing cells. Elaborate surface treatments can be used or pre-treatment regimes to solve this problem [145].

Mixing metal cations gives a reduction of 10^{E5} in conductivity and an increase in corrosion resistance. In a study where several glass compositions were made with missing metal cations but keeping the network connectivity the same [112], it was found that Ca^{2+} ions could have dipole action between non-bridging oxygens. pH change is greatest in distilled water and least with SBF, which is buffered. High Na^{+} content in a bioactive substrate can produce a cytotoxic effect in culture medium, thus pre-reaction with culture medium is used to reduce it. Other studies have examined the effect of texture of the substrate with respect to cell adhesion [145] and showed that a CaP layer was identified on all types of glasses used in the study. It was noted that bone nodules collected on stripes and spots on the patterned surface. Cell morphology was unchanged after 24 hours [145] but cells preferentially adhered to silicon regions and not silica regions. It has been well documented that cells adhere preferentially to rough surfaces and this is to be expected when one considers that, bone has various properties, which are anisotropic, and it provides a myriad of rough and porous regions on which osteoblasts can colonize and proliferate.

8.3 Results of initial cell culture study for 58S400

Primary human osteoblasts were isolated from trabecular bone of femoral heads taken during total hip arthroplasty. All materials tested were sterilized by UV light for one hour and preconditioned with cell culture media for 72h and then were seeded with osteoblasts. After 4 days in culture the substrates were fixed in 2.5% glutaraldehyde in 0.1% phosphate buffer, post-fixed in 1% osmium tetroxide in phosphate buffer and dehydrated in a graded ethanol series. Critical point drying of the samples was followed by gold sputtering. The preparations were examined at 10KV in a Cambridge 360 SEM at Queen Charlotte's Hospital. Micrographs of the results of this study are shown in Figures 8.2a-d, and 8.3a-f. It is evident that the 58S400 is biocompatible however, care was taken to enhance drying methods by incorporation of a drying rack after this study to ensure that both sides were topologically similar and a higher stabilization temperature of 800°C was employed to guard against any toxicity created by residual

nitrates or unreacted chlorine species in the material. However, no cell necrosis was needed after four days in culture regardless of surface used.

8.4 Results of cell culture study using 58S with HF addition

Because 58S catalysed with HF acid at 5%, had not been tested before cell culture experiments were done after production and characterisation of the first batch. Other authors had documented the possibility of enhanced bioactivity by the more highly charged surface when HF was added to the sol. Cell culture studies were done on the material after FTIR analysis had shown the growth of a calcium deficient hydroxyapatite layer after immersion in SBF. The same procedure as used previously (Section 6.2) was employed and micrographs are shown in Figures 8.2c, 8.2d and 8.3a-f. We observe CaF_2 on the surface of these materials, unlike the other batches without HF addition. However, the number of these crystals on the surface is not significantly increased when comparing the 58S batch made with 1.5ml addition [5%] HF and the batch containing 3ml [5%] HF. Both substrates proved biocompatible at the final period of 4 days in culture.

8.5 Discussion

It is also a matter of discussion of which stage the cell may exist on the surface. This is made more obvious when considering genetic analysis as a technique rather than SEM analysis/ visual methods. From visual methods alone, it is hard to tell whether a cell is just resting or whether the cell active on the surface and means to proliferate.

Current research indicates that 58S extract solution can elicit bone stimulating messages without the substrate being present [2]. With upcoming research into such fields of this type using DNA micro-array assays it will be possible to tell what affect composition alone have upon the up and down shifting of genes associated with bone growth and development.

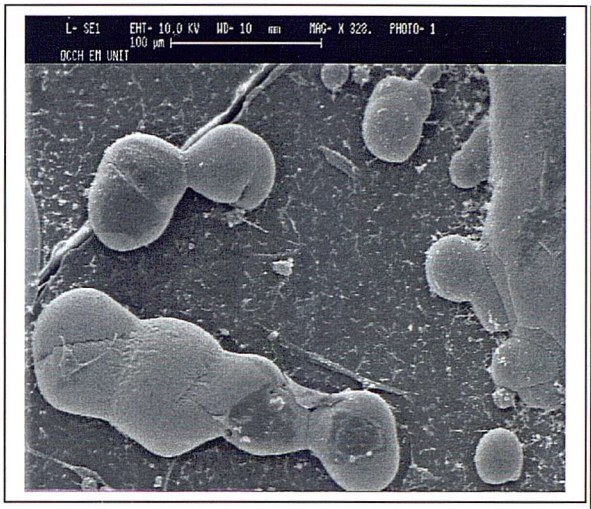


Figure 8.2a: Cell culture colony of primary human osteoblasts after 4 days on the surface of 58S400. Fieldwidth, 358 µm.

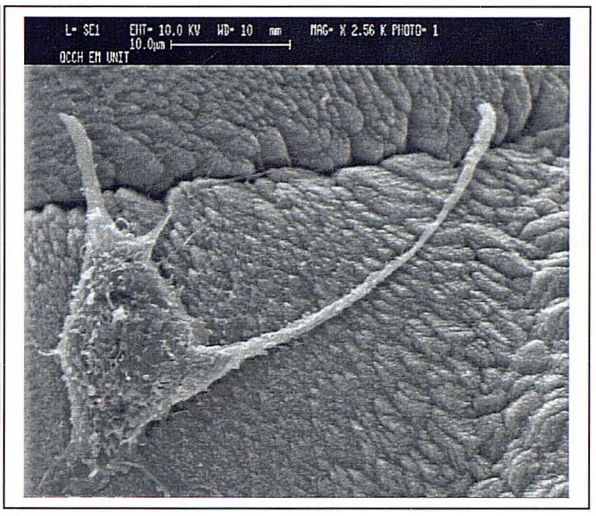


Figure 8.2b: Primary human osteoblast on the surface of 58S400 after 4 days in culture. Fieldwidth, 46 µm.

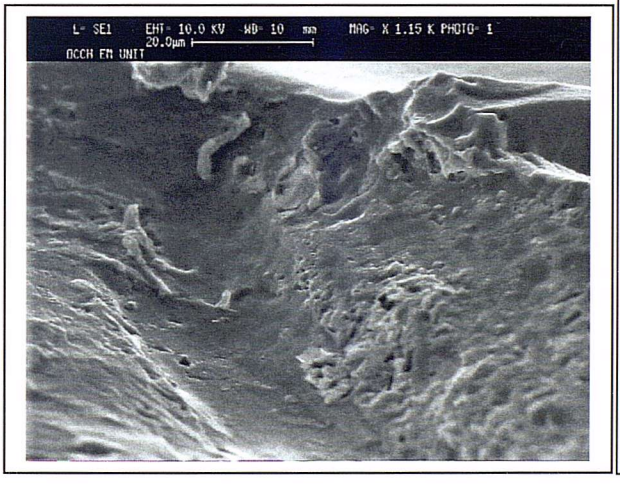


Figure 8.2c: Closer examination of internal porosity of the 58S400 rod surface. Fieldwidth, 91 µm.



Figure 8.2d: Hydrolyzed CaP growths on the surface of 58S400 after immersion in deionised water for two days. Fieldwidth, 55 µm.

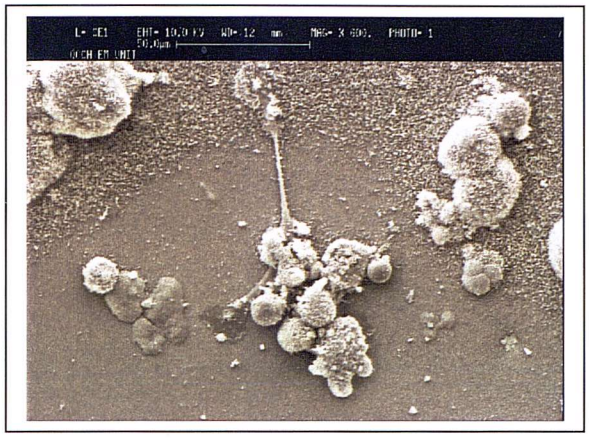


Figure 8.3a: Primary human osteoblast on the surface of 58S800 with 1.5ml HF addition at 5%. Fieldwidth, 233 µm.



Figure 8.3b: CaF_2 crystals on the surface of 58S800 made with 1.5ml HF addition. Fieldwidth, 150 µm.

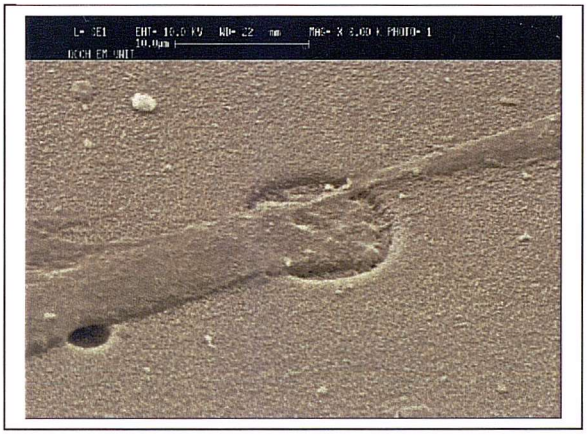


Figure 8.3c: Filopodia from primary human osteoblast penetrates voids which are large enough on the surface of 58S800 with HF addition. Fieldwidth, 40 µm.

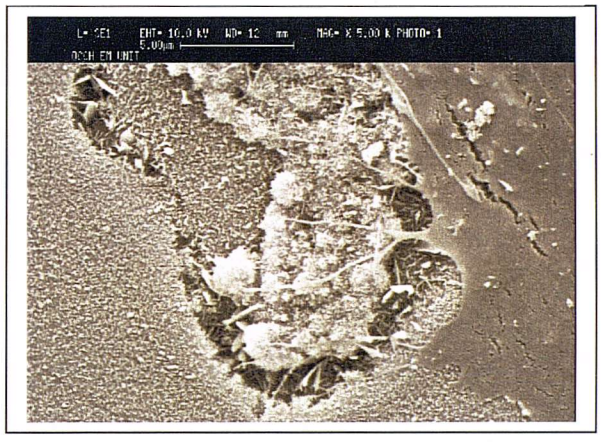


Figure 8.3d: Mineralisation of amorphous growths on the surface of 58S800 with HF addition, osteoblast filopodia is seen extending into growths. Fieldwidth, 24 µm.



Figure 8.3e: General view of cell colony on the surface of 58S800 with 1.5ml HF addition. Fieldwidth, 678 µm.

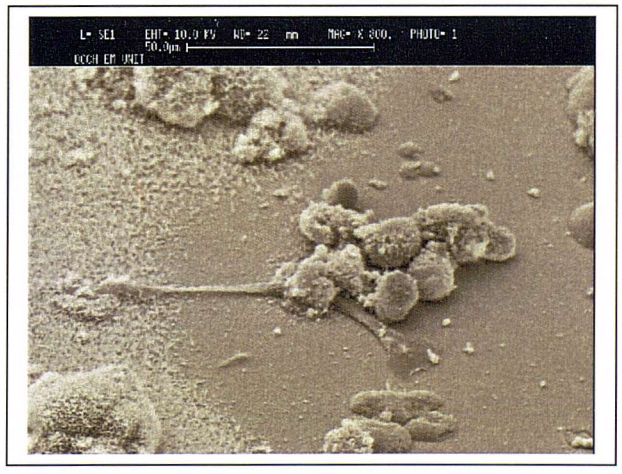


Figure 8.3f: Other view of primary human osteoblast on the surface of 58S800 with 1.5ml HF addition. Fieldwidth, 150 µm.

It is also known than various organs in the body can 'digest' particulates of silica, so long as they remain below a critical size i.e. the kidney has no adverse effects to silica released from an implant at size <18Å. Therefore, it could be postulated that osteoblasts could digest sol-gel phases (tunneling resorption) in a bid to colonize the bone graft material along with the active dissolution once placed in solution exhibited by the material and over time the material could be fully resorbed by the body. It is also true that physiological bone has nanophase size crystal structure and thusly a nanophase type crystal evolution and material scaling would be more biomimetic in these circumstances, enhancing the cell response to the sol-gel derived 58S. In combination with the fact that a carbonate apatite like structure evolves after immersion in SBF which is also more attuned to the physiological condition, rather than a synthetically created HA being used which will in turn be less soluble than any calcium phosphate precursor phase and may fail due to rejection by extrusion.

CHAPTER 9 CONCLUSIONS AND FUTURE WORK

9 Conclusions

In this work, a thorough characterization of the 58S Bioglass® system was achieved. A regime was formulated to produce 58S stable monoliths at a yield of over 90%. Batch making was made possible and samples were characterized and densified in order to more readily control dissolution kinetics, creating a material than had controlled resorption characteristics, which are important for a potential bone graft material. Surface areas and total pore volumes could be modified with thermal treatments in order to create a product with higher skeletal density with controlled resorption characteristics. NMR analysis showed that phosphate existed in a hydroxyapatite environment (~2.3ppm) in the material and a predominantly Q^4 structure for the sol-gel derived 58S, which showed that a highly stable silica network was present. The amorphous nature of this material also showed that ordering of this structure was random. Characteristically high dissolution rates were observed for the gel-glasses made reflecting the effects of their large surface areas and interconnected structure that allows greater mobility inside the monoliths. Dissolution studies confirmed the mobility of calcium from 58S into solution. As a network modifier, it was liberated easily from the structure whilst in solution. Silica dissolution values were also high and calcium phosphate growths were observed on the surface of 58S after immersion in SBF.

Although it is widely accepted as a working description of the general structure of silicate glasses, the random-network theory has been challenged over the details of local structure by alternative "crystallite" and "discrete ion" theories. A summary of the application of various theories to alkali glasses has been made by Mackenzie [137] and more recently by Goodman [137] who proposed a 'strained-mixed-cluster' model. However, conventional techniques for the study of glass structure have been unable to discriminate satisfactorily either between different models or how they describe the change in the local silica structure when increasing amounts of 'modifier' ions. TEM analysis showed the amorphous nature of the material but also nanophase separation, which was previously unrecognized by other optical methods. The samples are easily doped by soaking in liquids, which is an important feature that can be exploited for the use of drug delivery, should such an application be necessary. It was found that features imprinted during the gel stage of the 58S monolith could be carried through to the

stabilized product without catastrophic failure. The mechanical integrity of the material was not tested, but we saw when comparing cutting *in situ* with the 45S5 glass, that 58S sol-gel derived glass behaved less brittle in comparison due to its nanophase structure, which was able to dissipate stress within the structure. These observations show that cutting methods can be used should this be required in the operating theatre before surgery [163]. It was found that the pore structure of the material was created in the gel stage and could not be changed greatly by thermal treatments in different environments. However, the skeletal and bulk densities of the material were affected by different atmospheres, carbon dioxide being the more effective densification medium. Studies also showed that different aging regimes did not drastically affect composition or pore size amongst samples. Nitrogen adsorption in combination with helium pycnometry and mercury porosimetry proved to be accurate tools for examining the surface area, pore size, pore distribution, total pore volume and density of this material.

The 58S produced in the lab at Imperial College proved to be both bioactive (FTIR analysis) and biocompatible (cell culture studies) and can be considered as a good candidate for bone graft material. It is also suggested in this work that HF addition to the sol when processing could increase surface charge and therefore increase bioactivity / cell adhesion for this material, whilst decreasing gellation time. However, manipulation of the sol to draw fibres and produce different forms using non-moulding techniques proved difficult. Procedures such as 'spin-casting' this sol composition required a change in catalyst from acidic to an alkaline one, in combination with a change in water to TEOS ratio and alkoxide chemistry which was beyond the scope of this present study. It is common for an alkaline catalyst to be used when trying to create a linear molecular structure rather than the cluster type structure should be employed and a different water to TEOS ratio to overcome the problems of manipulating the gel before syneresis occurs and the final structure is obtained. Preliminary trials that co-ordinated gel time and using an HF catalyst employed with the original 58S formula to draw fibers, proved unsuccessful in this case.

The main problems with the creation of 3D scaffolds were found in moulding of alkoxide gels. Perhaps a more feasible starting point is the incorporation of "brick' parts that can be fixed together after stabilization to create a larger structure for implantation into larger defect sites. However, sol-gel alkoxide gel compositions are highly corrosive in nature and, normal moulding materials (such as those used for dental applications)

must be avoided, as the gel is likely to either corrode the mould during gelation or absorb and react with constituents from the moulding material during aging. This effect is only enhanced by using a more acidic catalyst or raised temperatures to quicken the aging process of the gel. Most silica moulding materials contain metal ions in the catalyst, making them a potential contaminant and even if such ions were included in the surface of the monolith, they could prove difficult to remove. This is detrimental to the main objective of producing a material that is not toxic in a physiological environment; utmost care should always be taken when choosing the moulding material for biomaterials ultimately for use in humans.

Throughout this work it was also apparent that alkoxide derived materials were particularly fragile before drying and stabilization. In addition, monoliths that survived drying could still fail catastrophically during stabilization upon liberation of certain species such as nitrates or due to internal stresses, caused by unramped cooling. Ideally, Teflon should be used for moulding applications of alkoxide gels to avoid contamination. Skilled mould makers agree that perfect samples come from perfect moulds without rough features from machining. However, PTFE cannot be manipulated in the same manner as other plastics to a finite macroscopic level. PTFE bodies are usually formed by powder sintering, which is expensive regardless of starter material costs. PTFE is not easily machinable from block, as it tends to deform and warps slightly upon cutting, this is also seen when trying to cut sheet PTFE. However, in this work we were able to create a moulding for small rods (maximum diameter 5mm and length 4cm) along with squares and discs. Retrieval from the mould was also difficult if the mould was not fully sealed, as the pore liquor would rapidly evaporate leaving the article stuck to the surface of the mould and, a spatula had to be used to liberate the monolith. This form of retrieval can produce micro cracks, which would later affect the quality and strength of the dried gel, perhaps even leading to catastrophic failure during drying or stabilisation.

Recent work in the field has further pursued the subject of tailored ceramic bodies, which are bioactive. In the work of Rodríguez-Lorenzo et al., [164] the mechanical properties of tailored bioceramic bodies are also explored. However, mechanical testing was beyond the scope of this present work. Current work in the field of novel sol-gel bioactive fibers made in the work of Orefice et al. [165] and Petola et al. [166] show the diversity of sol-gel processing creating different geometries, which are bioactive.

It is suggested that moulding of 3D structure with engineered channels of >100microns is highly feasible given a tightly sealable PTFE mould produced from powder sintering technology. A 2.5-3D scaffold could also be created using reactive ion etching (RIE). This technique is commonly used in the silicon wafer industry to create nanoscale features on the surface of pure silicon and could be adapted to the 58S Bioglass® system. The problems of drying these monoliths was also overcome by using incremental temperature elevations, however the time could not be cut to less than 2 weeks taken to develop a monolith, as this continuously resulted in catastrophic failure. Only one day could be dropped from the aging cycle for small articles of 58S.

XRD analysis showed the possible presence of a secondary (CaP) phase in the material. It is proposed that this may be tricalcium phosphate (β-TCP) as we assume that the phosphorus is present in an orthophosphate environment; a pyrophosphate environment was not confirmed from previous analysis. Even though β-TCP is rapidly soluble in liquid medium, it has been attributed to less spontaneous formation of HA once immersed in a physiological liquid. The other phase being centred around 22.5°2θ being recognized as the silica-rich glass network forming phase, whilst NMR Si MAS experiments revealed a predominantly Q^4 environment for the Si network bonding in 58S. When considering the XRD spectra of the stabilized products, any significant peaks are shadowed by an immense amorphous halo, showing that the structure is still randomly orientated and glass like in nature, even if the cristobalite species predominates owing to the cluster type formation involved in gelation from the acid hydrolysis of TEOS. TEM micrographs indicated that these phases were apparent in the ratio of 60:40 (network to modifying agent). Other areas see are perceived as anomalies such as voids. The two main phases seen in the TEM analysis are indicative of those seen from XRD analysis of the same 58S sample (showing two main amorphous halos).

It became apparent that the opaque nature of these materials was due to both phase separation on the nanometer scale and Rayleigh light scattering effects within the pore system of the structure giving a blue opalescent appearance. No phase difference was found by means of EDAX when examining the transparent rim regions of the monoliths in contrast to the opaque bulk of the sample. Nevertheless, this was to be expected after considering the incremental small areas involved in the regions of phase changes. It is evident from the results in this work that both water and phosphate groups could be acting as nucleating agents in the glass creating a highly reactive surface upon which

calcium phosphate growths are easily created with exposure to atmospheric water. However, concerning the actual 'locality' of the entities within this ternary composition, results obtained by NMR analysis must be treated with caution as many of the major peaks were found to be overlapping in the 45S5 and 58S compositions. However, one can suggest that this gel-glass does conform to well-known theories of glass structure that silica acts as the network-forming species with calcium and phosphate groups as modifiers in the glass structure.

Currently, *in vitro* cell culture studies remain standard protocol for the biocompatibility of biomaterials. Cell culture studies in this work proved that the material was biocompatible but could be further enhanced with gene expression data from these cells on the surface to confirm the actual nature of the cell activity. Incorporation of the investigation of DNA markers that are 'up shifted' at certain time intervals would also indicate a more specified picture as to the cell's behaviour with respect to time on the substrate. However, from this work the addition of HF as a catalyst can create an equally biocompatible environment. The cell colonies on the surface remain unaffected and spread over the CaF_2 square crystallites formed on the surface of this type of 58S. Normally this crystallite feature on the surface would be of concern, raising the toxicity of the surface. Primary human osteoblasts remain healthy after being on the surface of HF addition 58S for four days in culture. Filopodial integration into voids which are large enough and within the matrix of hydroxycarbonate apatite on the surface can indicate a cell that has settled in the environment. No cell necrosis was apparent in any of the studies and prolonged studies with greater time limits were beyond the scope of this work.

An interesting follow up to these types of experiments would test whether cell colonies could grow and proliferate in the 3D scaffold environment of 58S monoliths. The nanophase separation in the 58S material and high surface area properties enhance dissolution kinetics along with the effects of the small crystallites of hydroxycarbonate apatite produced after exposure to moisture and immersion in SBF and Tris buffer solution. This could be more accurately monitored by obtaining specified information on cell activity during the same time line whilst the material is immersed in cell culture.

A simulated study for the dissolution kinetics of corrosion of the implant by blood is also proposed for future work, since blood is the first fluid on the site after implantation.

Animal studies and clinical trials were beyond the scope of this present study. However, initial trials involving 58S and 77S by orthopaedic surgeons in London, Paris and the USA [5,167] have already confirmed the bioactive properties and fast healing times of this material when implanted in rabbit models.

9.1 Further Work

There are many things which must be mentioned about this material to better understand the way in which it works and the full identification of its surface characteristics. Further ideas for analysis include:

1) The identification of surface silanol coverage via chemisorption in combination with mass spectroscopy. A substance such as Tosic acid (which more favourably replaces all –OH sites) could be used to chemisorb on to sites on the surface to show the active silanols on the surface that were displaced, perhaps in combination with AFM identification of similar sites.

2) Drug delivery studies identifying time taken for the drug to reemerge from the glass structure. This is made possible by using a doped specimen of known molecular mass and size (and known luminosity), followed by the measurement of luminosity with respect to time of the same molecule coming out of the doped 58S. Further calculations could be made thereafter using different sizes of different drugs in solution to estimate the delivery time range after implantation.

3) More information gained from cell culture studies by the implementation of micro-array studies in combination with culture time. The use of microarrays could outline the response elicited by substrates for the up and down shifting genes with regard to 'bone making' associated genes. In addition, data could be collected for the secretory products of the osteoblasts to monitor their behaviour on the substrate with respect to time.

4) Krypton and micropore analysis of 58S800, using gas adsorption techniques. This was attempted in this work but not fully pursued.

5) Small angle XRD analysis, with temperature elevation run at the same rate or in combination with DTA analysis to fully understand phase evolution of this material. Scan rate however should be slower than normal to avoid noise in the spectra.

6) SEM EDAX could be employed for identification of nanophase separated regions. Using resolution at the angstrom level, where phases could be fully identified, for composition. Acid etching could be used to remove the orthophosphate fraction of the material to quantify the proportion of silica rich network.

7) Comparative results should be made using an experimental regime, which includes SBF replenishment. This should avoid the build up of ions in solution, whilst keeping the apparatus at the required temperature (37°C), as previously demonstrated by Vallet-Regí et al., [168,169].

8) Weibull Modulus and mechanical property measurements could be made to interpret the material's behaviour after immersion in medium or physiological solutions. This is important to create a situation similar to that of a large size defect with respect to time after immersion. This is proposed rather than dry brittle testing of the material which is less indicative of the situation after implantation.

9) TEM/SEM analysis under vacuum could be used to investigate the fully unreacted product in comparison to that which has reacted during exposure to the atmosphere. In addition, small angle XRD and NMR of the surface layer (reacted product - after exposure to the atmosphere and after immersion in SBF) could be used for specific identification of the hydroxyapatite phase formed.

10) Wet SEM analysis could be employed after cell culture studies, in contrast to regular SEM methods.

Observation of cell secretory products during cell culture would give a clearer picture of the cell stage. In addition, this information can clarify cell responses to as material such as 58S that can elicit bone formation and repair *in vivo*. Genetic repair or drug delivery to certain sites may also be implemented if the carrier scaffold material implanted is impregnated with the drug carrier liquid, issuing the drug to a specific area in the body over a controlled period. With the acceptance of research using blood to provide cell

sources for the patient [170,171], it will also be possible to bypass the possibility of rejection by the body as stem cells remain initially in a state of non-identity. Due to problems encountered in previous neurological research (where embryonic stem cells were introduced into the brains of neurologically diseased patients, which produced side-effects due to problems with cell mortality leading to malignancy), others in this field also support the use of adult stem cells [172]. Even though adult and embryonic stem cell research should be viewed as complementary, the drive to embryonic stem cell research still predominated due to the pluripotent potential of cells, which can provide a 'clean slate' concerning conditions of DNA. Nevertheless, in bone a cell colony using host mesenchyme bone cells sourced from marrow, which would contain the same DNA could be used, when implanted it would be recognized as 'similar/like' to the other cells at the site of implantation. The incorporation of bone marrow cell colonies which had been expanded from those received in host donor bone marrow would perhaps give better results for bone repair than could be achieved using other methods. It has also been noted that adult bone marrow could help repopulate the brain [170,171] after research in mice showed that bone marrow cells from male mice were injected into female mice with no white blood cells of their own. Four months after transplantation, they found significant numbers of neuronal cells in several brain regions – including the cortex, the hypothalamus, and the striatum – that were descendants of the transplanted cells [170,171]. Reddhi et al., [173] have successfully impregnated osteoblasts derived from bone marrow sources back in to the patient with the addition of bone mineral proteins before implantation i.e. BMP-4 and thusly have avoided the embryonic stem cell source.

Due to the clear demand for materials, which can be used in a situation of catastrophic bone loss in emergencies, we are forced to consider materials that can be rapidly available and do not require a donor to obtain more supply. We look towards synthetic means to supply the bone that must be available for such situations and which can induce bone healing and growth. For these purposes, 58S is suggested as a bone replacement material. Being brittle in nature however, this material should be used for void filling applications in small fractures and voids. However, it is uncertain how the material will react mechanically after long-term implantation but animal studies have been successfully carried out without fracture or aseptic loosening of the implant material [167].

For alkoxide sol-gel materials in this work, 3D structures are definitely conceivable. A continuous set-up of interlinking 2D shapes (obtained easily from moulding processes) impregnated with cells and bone morphogenic proteins is a matter for further work. However, previous *in vitro* work done on Bioglass® has been successful without such additives. 58S has excellent potential for those applications which are currently unsatisfied in cases of catastrophic loss or organ failure. The advantages of producing and using this type of material are many. It can be prepared easily for implantation by using UV sterilization followed by soaking in solution before surgery. In addition, this material can also be cut safely from a block after stabilisation. This provides for greater ease of use in operating room situations. Special storage situations are not required for the 58S sol-gel product apart from adequate desiccation. Batch production without excessively high temperatures of 58S800 was achieved in this work, proving also that monoliths could be obtained when using solid calcium nitrate in the sol. It was seen that products of both transparent and opaque nature were produced in this work; the aspect ratios seemed to be the only factor of difference in the two appearances as no difference in phase or composition could be detected by other methods.

Cost effectiveness was also observed showing that a reproducible product could be obtained in 2 weeks and that new levels of moulding could be used to obtain a 3D structure with channels large enough in diameter to support vascularisation. Whether this was initially facilitated by polymer based tubes with osmotic properties or whether the vessel was created by the invasion of bone productive cells, the material displays resorbable characteristics to a certain extent over time. The nanoscale structure may release smaller particles, which in turn could be more easily digested by cells in an invasive colonization process. It is suggested from this work that this material is an excellent candidate for use in bone replacement applications or for use in the production of scaffolds for hard tissue replacement.

List of References

[1] B. Locardi, "Surface reactivity and bioactivity of bulk glass and glass coatings", *Bioceramics and the Human Body*, Editers A.Ravaglioli and A. Krajewski, Elsevier Applied Science, p149, 1992.

[2] I. D. Xynos, A. J. Edgar, L. Buttery, L. Hench and J. Polak, "Ionic products of Bioactive Glass Dissolution Increase Proliferation of Human Osteoblasts and Induce Insulin-like Growth Factor II mRNA Expression and Protein Synthesis", Biochemical and Biophysical Research Communications, 276, pp461-465, 2000.

[3] C.J. Brinker, *Sol-Gel Science:The Physics and Chemistry of sol-gel processing*, Boston, Academic Press, New York, Edited by C.J. Brinker and G.W.Scherer, 1990.

[4] L. Hench and J. West, "Sol-Gel Process", Chem. Rev., vol.90, pp33-72, 1990

[5] D.L. Wheeler, R.G. Hoellrich, S.W. McLoughlin, K.E. Stokes and D.L. Chamberland, "Histological and Mechanical Assessment of Critical-sized Cancellous Defects filled with Sol-gel Bioglass®", Report to US Biomaterials (Preliminary Results) April 29, 1997.

[6] L.L..Hench, F.G. Arauo, .K. West, G.P.LaTorre, "Gel-Silica Optics: Theory and Application", Journal of Sol-gel Science and Technology, 2, pp647-655, 1994.

[7] L. Hench, "Sol-Gel Materials for bioceramic applications", Current Opinion in Solid State and Materials Science, vol.2, pp604-610, 1997.

[8] L. Hench and R. Orefice, "Sol-gel Technology", in *Kirk-Othmer Encyclopaedia of Chemical Technology*, Edited by L. Hench and R. Orefice, Fourth Edition, vol. 22, pp42-68, 1997.

[9] C. Jeffrey Brinker and G.W. Scherer, "Comparison of gel derived and conventional ceramics", in *The Physics and Chemistry of Sol-Gel Processing*, , Ch. 12.1, Academic Press, John Wiley and Sons, , pp746-748, 1990.

[10] M.M. Pereira, A.E. Clark, and L.L. Hench, "Homogeneity of Bioactive Sol-Gel-Derived Glasses in the System CaO-P_2O_5-SiO_2", Journal of Materials Synthesis and Processing, vol.2, no.3, pp189-196, 1994.

[11] P. Calvert, "Examples of Biological Materials", in *Ultrastructure and Processing of Advanced Materials*, Ch.14.2.4, Editers Uhlrich and Uhlmann, New York, Chicester, pp151-154, 1992.

[12] S. Radin, P. Ducheyne, and S. Falaize, "Sol-gel Bioactive Glass with a controlled surface reactivity", p161 in the Proceedings of the 23rd Annual Meeting of the Society for Biomaterials, April 30-May 4 1997, New Orleans, USA.

[13] B. Roy, H. Jain, S. K. Saha and D. Chakervorty, "Phase Separation and Structural Differences between Alkali Silicate Glasses Prepared by the Sol-Gel and Melt Quenched Methods", Journal of American Ceramic Society, vol.81, no.9 pp2360-70, 1998.

[14] R. Roy, "Gel Route to Homogeneous Glass Preparation", J. Am. Ceram. Soc., vol.52, p344, 1969.

[15] G. J. McCarthy and R. Roy, "Gel Route to Homogeneous Glass Preparation: II, Gelling and Desiccation", J. Am. Ceram. Soc., 54, p639, 1971.

[16] W. Vogel, in *The Chemistry of Glass, Classical Theories of Glass Structure*, Translated by N.Kriedl, Licensee Edition for the American Ceramic Society, Inc., Columbus. OH, pp33-36, pp69-72, pp122-123, 1985.

[17] P.F. James, "Nucleation in glass-forming systems – a review", in *Glasses and Glass-Ceramics*, Edited by M.H.Lewis, Chapman and Hall, pp59-83, 1989.

[18] L.L. Hench, "Inorganic-Organic Molecular Bonding in Porous Matrices", Final Report submitted to the Air Force Office of Scientific Research, September 14, 1997.

[19] T. H. Elmer, in *Engineered Materials Handbook®*, Volume 4: Ceramics and Glasses, ASM International, Materials Park, Ohio, p427, 1992.

[20] T. H. Elmer, in *Engineered Materials Handbook®*, Volume 4: Ceramics and Glasses, ASM Handbook International, pp433, 434, 446,449, 1992.

[21] L. L.Hench, D. Wheeler, and D. Greenspan, "Molecular control of Bioactivity in Sol-gel Glasses", Journal of Sol-Gel Science and Technology, Kluwer Academic Publishers, Massachusetts, U.S.A, 1997.

[22] L.L. Hench, "Bioactive Glasses and Glass-Ceramics", *Handbook on Bioactive Ceramics*, vol.1, Edited by T. Yamamuro, L.L. Hench and J. Wilson, CRC Press: Boca Raton, FL. 1990.

[23] L. Hench and J. K. West, "Biological Applications of Bioactive Glasses", Life Chemistry Reports, Vol. 13, pp187-241, 1996.

[24] J. Wilson and S. B. Low, "Bioactive ceramics of periodontal treatment: comparative studies in the Patus monkey", J. Appl. Biomaterials, vol.3, pp123-129, 1992.

[25]L. Hench and O. Andersson, "Bioactive Glasses", Chapter 3, in *An Introduction to Bioceramics*, Edited by Larry L. Hench and June Wilson, Advanced Series in Ceramics – vol.1, World Scientific, pp41-62, 1993.

[26] J. Wilson and D. Nolletti, in *Handbook of Bioactive Ceramics*; Edited by T. Yamamuro, L.L. Hench and J. Wilson., CRC Press: Boca Raton, FL, vol.1, pp283-302, 1990.

[27] P. Revell, *Pathology of Bone*, Springer-Verlag: Berlin, 1986.

[28] R.Cook, E. Fielder, T.Watson, P.Robinson and L.Hench, "Pore Characterisation and Interconnectivity Studies on Bioactive 58S Sol-Gel Glass", Proceedings of Bioceramics 13, Bologna, Key Engineering vols.192-195, pp625-628, 2001.

[29] A.W. Ham, *Histology*, J.B. Lippincott Co.: Philadelphia, PA, 1969.

[30] L.L. Hench, "Bioactive Ceramics: Theory and Clinical Applications", in *Bioceramics 7*; Edited O.H. Andersson, A. Yli-Urop, Butterworth-Heineman Ltd.: Oxford, England, pp3-14, 1994.

[31] L.L. Hench, R. J. Splinter, W. C. Allen and T.K. Greenlee, Journal of Biomedical Materials, Research, vol.2, no.1, pp117-141, 1972.

[32] L.L. Hench and H. A. Paschall, "Histochemical responses at a biomaterial's interface", J.Biomed.Maters.Res., vol.5, no.1, pp49-64, 1974.

[33] C. Y. Kim, A. E. Clark, and L. L. Hench, "Early Stages of Calcium Phosphate Layer Formation in Bioglasses", Journal of Non-Crystalline Solids, vol.113, pp195-202, 1989.

[34] M. Ogino, F. Ohuchi and L.L. Hench, "Compositional dependance of the formation of calcium phosphate films on bioglass", Journal of Biomedical Materials, Research, vol.14, p55-64, 1980.

[35] L.L. Hench, *Fundmental Aspects of Biocompatability,* Edited by D.F. Williams, , CRC Press: Boca Raton, Florida, vol.1, pp.67-85, 1981.

[36] J.P. Zhong, G. P. LaTorre and L.L. Hench, in *Bioceramics 7*, Edited by O.H. Andersson, R. P. Happonen, and A. Yli-Urpo, Butterworth-Heineman Ltd., Oxford, England, p61, 1994.

[37] L.L. Hench and D.E. Clark, "Physical Chemistry of Glass surfaces", Journal of Non-Crystalline Solids, vol.28, no.1, p83-105, 1978.

[38] E. Carlisle, in *Silicon Biochemistry*, Edited by D. Evered and M. O'Connor, Wiley, New York, p123, 1986.

[39] K. Schwarz and D. B. Milne, "Growth-promoting effects of silicon in rats", Nature, vol. 239, p333, 1972.

[40] M. Hott et al.,"Short-term effects of organic silicon on trabecular bone in mature overiectomized rats", Calcif. Tiss.Int., vol.53, p174, 1993.

[41] P.E. Keeting, "Zeolite A increases proliferation, differentiation and transferring growth factor beta production in normal adult osteoblast-like cells *in vitro*", J.of Bone and Min.Res., vol.7, no.11, p1281, 1982.

[42] R. Li, A. E. Clark and L.L. Hench, "An investigation of bioactive glass powders by sol-gel processing", Journal of Applied Biomaterials, vol.2, pp231-239, 1991.

[43] M. M. Pereira and L.L. Hench, "Mechanisms of hydroxyapatite formation on porous gel-silica substrates", in *Biochemical Aspects of Sol-gel Science and Technology,* Edited by D. Avnir and S. Braun, Kluwer, 1996.

[44] L.L. Hench, "Bioceramics : From concept to clinic", J.Am Ceram. Soc., vol. 74 no.7, pp1487-1510, 1991.

[45] F. Kirkbir, H. Murata, D. Meyers, S. Chaudhuri and A. Sarkar, "Drying and Sintering of Sol-Gel Derived Large SiO_2 Monoliths", Journal of sol-gel science and Technology, vol.6, pp203-217, 1996.

[46] R.K. Iler, in *The Chenistry of Silica, Solubility, Polymerization, Colloid and surface properties, and biochemistry*, Chapter 1, The Occurrence, Dissolution and Deposition of Silica, Wiley, New York, pp3-104, 1979.

[47] Ultrastructure Processing of Ceramics, Glasses and Composites in *Ultrastructure Processing of Sol-Gel Silica*, Ch.6, Edited by L.L. Hench and D.R. Ulrich, John Wiley and Sons, pp63-68, 1984.

[48] L. Hench and S. H. Wang, "The Sol-Gel Glass Transformation of Silica", in *Phase Transformations*, vol.24-26, pp785-834, 1990.

[49] L. Hench and G. Orcel and J.L. Nogues, "The Role of Chemical Additives in Sol-gel Processing", in: *Better Ceramics through Chemistry II*, Edited by C.J. Brinker, D.E. Clark., and D. R. Ulrich, vol.73, pp35-47. Materials Research Society, Pittsburgh, PA, 1986.

[50] C. Jeffrey Brinker and G.W. Scherer, in *Sol Gel Science*,The Physics and Chemistry of Sol-Gel Processing, Academic Press, John Wiley and Sons, pp632-675, 1990.

[51] P. Widerhold, "Humidity Measurements", in *Drying of Loose and Particulate Materials*, Edited by Keey, pp1313-1318, 1991.

[52] R.B. Keey, "Moisture in Gases", in *Drying of Loose and Particulate Materials*, Edited by Keey, pp17-152, 1991.

[53] J.E. Barralet, S.M. Best, and W. Bonfield, "Effect of sintering parameters on the density and microstructure of carbonate hydroxyapatite", Journal of Materials Science: Materials in Medicine 11, 719-724 (2000).

[54] M.M. Pereira, A.E. Clark, and L.L. Hench, "Calcium phosphate formation on sol-gel derived bioactive glasses *in vitro*", Journal of Biomedical Materials Research, vol.28, pp693-698, 1994.

[55] M. Jonkinen, H. Rahiala and J. B. Rosenholm, "Relation between aggregation and heterogeneity of obtained structure in sol-gel derived $CaO-P_2O_5-SiO_2$", Journal of Sol-Gel Science and Technology, vol.12, pp159-167,1998.

[56] D.C. Greenspan, J.P. Zhong, G.P. LaTorre and M. Boocher, "The *In-vitro* degradablility of sol-gel Bioglass®", Proceedings of the 23rd Annual Meeting of the Society for Biomaterials, New Orleans, USA, April 30-May 4, p405, 1997.

[57] S. Hayakawa, S. Tsuru, H.Iida, C. Ohtsuki and A. Osaka, "MAS NMR studies of apatite formation on $50CaO.50SiO_2$ glass in simulated body fluid", Phys. Chem. Glasses, vol.37, no.5, pp188-192, 1996.

[58] J. Pérez-Pariente, I. Izquierdo-Barba, J.L. Garcia-Fierro, A.J. Salinas and M. Vallet-Regí, "Structure and surface properties of the apatite growth layer on gel glasses", Bioceramics Volume 12, edited by H. Ohgushi, G. W. Hastings and T. Yoshikawa,World Scientific Publishing Co. Pte. Ltd., Nara, Japan, pp173-176, 1999.

[59] I. Izquierdo-Barba, A. J. Salinas, M. Vallet-Regí, "Effect of the continous solution exchange on the in vitro reactivity of a $CaO-SiO_2$ sol-gel glass", J. Biomedical Materials Research, vol.51, pp191-199, 2000.

[60] I. Izquierdo-Barba, A.J. Salinas and M. Vallet-Regí, "*In vitro* calcium phosphate layer formation on sol-gel glasses in the $CaO-SiO_2$ system", J. Biomedical Materials Research, vol.47, pp243-250, 1999.

[61] A. J. Salinas, M. Vallet-Regí and I. Izquierdo-Barba, "Biomimetic Apatite Deposition on Calcium Silicate Gel Glasses", Journal of Sol-Gel Science Technology vol.21, pp13-25, 2001.

[62] A. Martínez, I. Izquierdo-Barba, and M. Vallet-Regí, "Bioactivity of a $CaO-SiO_2$ Binary Glasses System", Chem. Mater., vol.12, pp3080-3088, 2000.

[63] J.Perez-Pariente, F. Balas, J. Roman, A.J. Salinas and M. Vallet-Regi, "Influence of Composition and Surface Characteristics on the *in vitro* degradability and Bioactivity of SiO_2-CaO-PO_5-MgO Sol-Gel Glasses", J. Biomed. Mater. Res., vol.47, pp170-175, 1999.

[64] Y. Zhang, J.D. Santos, "Microstructural characterisation and *in vitro* apatite formation in $CaO-P_2O_5-TiO_2-MgO-Na_2O$ glass-ceramics", Journal of European Ceramic Society 21, pp169-175, 2001.

[65] R. K.Iler, "Silica in Biology", *The Chemistry of Silica Solubility, Polymerization, Colloid and surface properties, and biochemistry*, J. Wiley and sons.Inc., Interscience, pp754-755, 1979.

[66] J.J. Videau and V.Dupuis, "Phosphates and Biomaterials", Eur.J.Solid State Inorg. Chem. T. vol.28, pp303-07, 1991.

[67] M.Vallet-Regí, I. Izquierdo-Barba, A. J. Salinas, "Influence of P_2O_5 on the crystallinity of the apatite formed in vitro on the surface of bioactive glasses", J. Biomed. Mat. Res., vol.46, pp560-565, 1999.

[68] M. Vallet-Regí, D. Arcos, J. Pérez-Pariente, "Evolution of Porosity during in vitro hydroxycarbonate apatite growth in sol-gel glasses", J. Biomed. Mat. Res., vol.51, pp23-28, 2000.

[69] M. Vallet-Regí and A. Rámila, "New Bioactive Glass and Changes in Porosity during the Growth of a Carbonate Hydroxyapatite Layer on Glass Surfaces", Chem Mater., vol.12, pp961-965, 2000.

[70] M. Vallet-Regí, A.M. Romero, C.V. Ragel, R.Z. LeGeros, "XRD, SEM-EDS, and FTIR studies of *in vitro* growth of an apatite-like layer on sol-gel glasses", Journal of Biomedical Materials Research, vol.44, iss.4, pp416-421, 1999.

[71] T. Peltola, M. Jonkinen, H. Rahiala, E. Levänen, J. B. Rosenholm, I. Kangasniemi, A. Yli-Urpo, "Calcium phosphate formation on porous sol-gel derived SiO_2 and CaO-P_2O_5-SiO_2 substrates *in vitro*", Journal of Biomedical Materials Research, vol.44, iss.1, pp12-21, 1999.

[72] A.J. Salinas, J. Roman, M. Vallet-Regí, J. M. Oliveira, R. N. Correia, M.H. Fernandes, "In vitro bioactivity of glass and glasscermics of the $3CaO \cdot P_2O_5$-$CaO \cdot SiO_2$-$CaO \cdot MgO \cdot 2SiO_2$ system", Biomaterials 21, pp251-257, 2000.

[73] M. Vallet-Regí, A. J. Salinas, J. Román and M. Gil, "Effect of magnesium content on the *in vitro* bioactivity of CaO-MgO-SiO_2-P_2O_5 sol-gel glasses", Journal of Materials Chemistry, vol.9, pp515-518, 1999.

[74] J. Pérez-Pariente, F. Balas, and M. Vallet-Regí, "Surface and Chemical Study of $SiO_2 \cdot P_2O_5 \cdot CaO \cdot (MgO)$ Bioactive Glasses", Chem. Mater., vol.12, pp750-755, 2000.

[75] C.V. Ragel and M. Vallet-Regí, "*In vitro* bioactivity and gentamicin release from glass-polymer-antibiotic composties", Journal of Biomedical Materials Researchl, vol.51, no.3, pp424-429, 2000.

[76] M. Bosetti, L. Hench, M. Cannas, "Interaction of bioactive glasses with peritoneal macrophages and monocytes *in vitro*", J. Biomed. Mater. Res., vol.6, pp79-85, 2002.

[77] R. Siever, "Establishment of equilibrium between clays and sea water", Earth and Planetary Science letters, vol.5, no.2, pp106-110, Oct 1968.

[78] R.K. Iler, in Chapter 1 "The Occurrence, Dissolution and Deposition of Silica", in *The Chemistry of Silica Solubility, Polymerization, Colloid and surface properties, and biochemistry*, J. Wiley and sons.Inc., Interscience, p13, 1979.

[79] F.T. Mackenzie and R.M. Garrels, "Silicates: Reactivity with sea water", Science, 150, 57, pp57-8, 1965.

[80] R.K. Iler, in Chapter 1 "The Occurrence, Dissolution and Deposition of Silica", in *The Chemistry of Silica Solubility, Polymerization, Colloid and surface properties, and biochemistry*, J. Wiley and sons.Inc., Interscience, p14, 1979.

[81] E.S. Tyler and S.A. Barghoorn, "Microoorganisms from the gun flint chert", Science , 147, 463, pp563-577, 1965.

[82] J.H. Oehler and J.W. Schopf, "Artificial microfossils: Experimental studies of permineralisation of blue-green algae in Silica", Science, 174, 1229, pp1229-1231, 1971.

[83] R.K. Iler, "The Occurrence, Dissolution and Deposition of Silica",*The Chemistry of Silica Solubility, Polymerization, Colloid and surface properties, and biochemistry*, J. Wiley and sons.Inc., Interscience, p15, 1979.

[84] G. Gamow, *Biography of the Earth*, New America Library of the World Literature, New York, 1941.

[85] A.I. Oparin, *The origin of life*, translated by Sergins Margulis, Second edition, Dover, New York, 1953.

[86] J.D. Bernal, *The physical basis of life*, Routledge and Kegan Paul, London, 1952.

[87] S.H. Miller, R.L. Degourin and J.C. Hoak, "Ultrastructural features of the early proliferating cells involved in hemopoietic colony formation", Science, vol.117, p3045, 1953.

[88] Ralph K.Iler, "Silica in Biology", *The Chemistry of Silica Solubility, Polymerization, Colloid and surface properties, and biochemistry*, J. Wiley and sons.Inc., Interscience, p731, 1979..

[89] R. Calvert, in *Diatomaceous Earth*, Chemical Catalog. Co. New York, 1930.

[90] J.J. Videau and V.Dupuis, "Phosphates and Biomaterials", Eur.J.Solid State Inorg. Chem. T. 28, pp307-320, 1991.

[91] M. Scheon, in *The problem of fermentation: the facts and the hypostheses*, Chapman and Hall, 1928.

[92] G. Skofronick, "Physics of the skeleton", Chapter 3 in *Medical Physics*, p39ff, p43 Bone mineral, Connective Tissue: Bone and Bone formation, Chapter 7, John Wiley and sons, Edited by John R.Cameron and James, 1978.

[93] K.Powers, *The Development and Characterisation of sol-gel substrates for chemical and optical applications*, PhD thesis, University of Florida, USA, 1998.

[94] C. Fernandez-Lorenzo, J. Martin, L.M. Esquivias, and E. Blanco, "Raman Spectroscopy of Phosphorous-Doped Silica Gels", pp215-219 in *Chemical Processing of Advanced Materials*, Edited by Larry L. Hench and Jon West, John Wiley and Sons, Inc.,1992.

[95] R.K. Iler, in *Science of Ceramic Chemical Processing,* Edited by L.L. Hench and D.R. Ulrich, Wiley, New York, p3, 1986.

[96] J. K. Bailey, "Solvent Quality Effects in Sol-Gel Processing", in *Better Ceramics Through Chemistry V*, Materials Res. Soc Symposium Proceedings Volume 271, Edited by Mark J. Hampden-Smith, Walter G.Klemperer, and C. Jeffrey Brinker, San Francisco, USA, April 27-May 1, pp219-224, 1992.

[97] A.C. Pierre, "The Gelation of Colloidal Gels and The Derajaguin-Landau-Verwey-Overbeek (DVLO) Theory", in *Ultrastructure and Processing of Advanced Materials*, Edited by J.D. Mackenzie and D. R. Ulrich, Wiley, New York, p103, 1992.

[98] J.D. Barrie, and K.A. Aitchison, "A Raman Spectroscopic Study of the Initial Stages of Hydrolysis of TEOS", in *Better Ceramics Through Chemistry V*, Materials Res. Soc Symposium Proceedings, Volume 271, Edited by Mark J. Hampden-Smith, Walter G.Klemperer, and C. Jeffrey Brinker, San Francisco, USA, April 27-May 1, pp225-230, 1992.

[99] D. Hua and D. Smith, "Pore Size and Texture Modification of Silica via Trialkylsilylation", in *Better Ceramics Through Chemistry V*, Materials Res. Soc Symposium Proceedings, Edited by M. J. Hampden-Smith, W. G. Klemperer, and C. Jeffrey Brinker, San Francisco, USA, April 27-May 1, vol.271, p547, pp551-552, 1992.

[100] M. J. R. Wilson, *Drying Kinetics of Pure Silica Aerogels*, Masters Thesis, University of Florida, Gainsville, FL,1989.

[101] S. Wallace, *Structure of Silica Gel Monoliths and Water*, PhD dissertation, University of Florida, Gainesville, FL, 1990.

[102] M.J.R. Wilson, and L.L. Hench, "Real Time Monitoring of Silica Gel Drying Behaviour", in *Ultrastructure Processing of Advanced Materials,* Edited by D. R. Uhlmann and D. R. Ulrich, John Wiley and Sons, New York, , p247, 1992.

[103] T. M. Shaw in *Better Ceramics Through Chemistry II*, Edited by C.J. Brinker, D. E. Clark and D. R. Ulrich, Materials Research Society, vol.73, p215, Pittsburgh, P.A., 1986.

[104] W. Vasconcelos, *Topological Analysis of Densification of Silica Gels*, PhD dissertation, University of Florida, Gainsville, FL,1989.

[105] W.L. Vasconcelos, R.T. DeHoff, and L.L. Hench, "Structural Evolution During Sintering of Optical Sol-Gel Silica", Journal of Non-Crystalline Solids vol.121, pp124-127, 1990.

[106] G.W. Scherer, "Sintering of Low Density Glasses I: Theory", J. Am. Ceram. Soc., 60:236, 1977.

[107] F.G. Araujo, G.P. LaTorre, and L.L. Hench, "Structural Evolution of Porous Type VI Sol-Gel Silica Glass", J. Non-Cryst. Solids, vol.185, pp41-48, 1995.

[108] T.King, "Lasers and Ultrastructure Processing", Chapter 90 in *Chemical Processing of Advanced Materials*, Edited by L. Hench and J. West, John Wiley and Sons, pp997-999, 1992.

[109] M. Nogami and Y. Moriya, "Glass Formation through hydrolysis of $Si(OC_2H_5)_4$ with NH_4OH and HCl solution", Journal of Non-Crystalline Solids, vol.37, p191, 1980.

[110] S.H. Wang, "Sol-Gel Derived Silica Optics", PhD dissertation, University of Florida, Gainsville, FL, 1988.

[111] S.H. Wang, C. Campbell and L. Hench, "Optical Properties of Silica Gel-Glasses", in *Ultrastructure Processing of Advanced Materials,* Edited by D. R. Uhlmann and D. R. Ulrich, John Wiley and Sons, New York, pp145-147, 1988.

[112] E. Claxton, "Effect of Sodium Silicate on bioactive glass-ceramic", PhD Thesis, Department of Materials, Imperial College, London, UK, pp28-32,34,pp44-55,pp57-59,128,pp134-138,162, 1996,

[113] J.X.Lu, B.Flautre, K.Anselme, P.Hardouin, A.Gallur, M.Deschamps, B.Thierry, "Role of interconnections in porous bioceramics on bone recolonisation *in vitro* and *in vivo*", Journal of Material Science: Materials in Medicine 10, pp111-120, 1999.

[114] E.White and E.C. Shores, "Biomaterials aspects of Interpore-200 porous hydroxyapatite", Dent.Clin.N.Amer., 30, p49, 1986.

[115] A. Uchida, S.M.L.Nade, E.R.McCartney and W.Ching, "The use of cermics in bone replacement. A comparative study of three porous ceramics", J.Bone Joint Surg 66B, p269, 1984.

[116] J.J.Klawitter and S.F. Hulbert, "Application of porous cermics for the attachment of load bearing internal orthopedic applications", J.Biomed.Mater.Res.Smyp.2, p161, 1971.

[117] N.S. Adreev, *Phase Separation in Glass*, Edited by O.V. Mazurin and E.A. Porai-Koshits, authorised translation by D.D. Petrova, Netherlands, p100,p298, 1984.

[118] T. Allen, "Surface Area and Pore Size Determination", in *Particle Size Measurement*, 2, Fifth Edition, Chapman and Hall. Editors Brian Scarlett and Genji Jimbo, p39,40,78,79,96,137,136,200, 1997.

[119] F.A.L. Dullien, "Structure of Porous Materials", *Porous Media, Fluid Transport and Pore Structure*, Second Edition, pp1-91, 1992.

[120] O. Peitl, G. P. LaTorre, and L. Hench, "Effect of crystallisation on apatite layer formation of Bioactive Glass 45S5", Journal of Biomechanical Materials Research, vol.30, iss.4, pp509-514, April 1996.

[121] K.D. Lobel and L.L. Hench, "*In-Vitro* Protein Interactions with Bioactive Gel-glass, Journal of Sol-Gel Science and Technology 7, pp69-76, 1996.

[122] K. Tsuru, C. Ohtsuki, A. Osaka, T. Iwamoto and J.D. Mackenzie, "Bioactivity of sol-gel derived organically modified silicates, Part 1: *In vitro* examination", Journal of Materials Science: Materials in Medicine 8, pp157-161, 1997.

[123] R. Li, A. Clark and L. Hench, "Effects of structure and surface area on bioactive powders by sol-gel process", *Chemical Processing of Advanced Materials*, Edited by Larry L. Hench and Jon West, John Wiley and Sons, Inc., pp627-633, 1992.

[124] L.L. Hench and J.K. West, "Biological Applications of Bioactive Glasses", in Life Chemistry Reports, vol.13, pp187-241, 1996.

[125] C. A.Leon y Leon, "New perspectives in mercury porosimetry", Advances in Colloid and Interface Science, vol.76-77, pp341-372, 1998.

[126] T. Allen, "Limitations of mercury porosimetry", in *Surface Area and Pore Size Determination*, Fifth Edition, Chapman and Hall, Edited by Brian Scarlett and Genji Jimbo, p157, 1997.

[127] K. S. TenHuisen and P. W. Brown, "Phase evolution during the formation of α-Tricalcium Phosphate", J. Am Ceram. Soc., 82 [10] 2813-18, 1999.

[128] Private communication:- Dr. Robert Hill – "Phase separation detection in XRD of glasses".

[129] F. Brands, R. Fresa, A. Constantini and A. Buri, "Bioactivity of 1.25CaO-SiO_2 glass: an FTIR and X-ray study on powdered samples", Biomaterials 17, p2247-2251, 1996.

[130] Personal email communication, Katherine Wallace, University of Limerick, 13th March 2000.

[131] A.F. Wells, *Structural Inorganic Chemistry*, Third Edition, Oxford Press, p160, pp651-810, 1962.

[132] N. Rangavittal, A.R. Landa-Cánovas. J. M. González-Calbet, M. Vallet-Regí, "Structural study and stability of hydroxyapatite and β-tricalcium phosphate: Two important bioceramics", J. Biomed. Mater. Res. 51/4, pp660-668, 2000.

[133] *Adsorption on and Surface Chemistry of Hydroxyapatite*, Edited by Dwarika N. Misra, Plenum Press, New York, p19, p24, 1984.

[134] S. Mann, C. Perry, R.Williams, C. Fyfe, G. Gobbi, and G. Kennedy, "The characterisation of the Nature of Silica in Biological Systems", J. Chem. Soc., Chem. Commun., nos.1-12, 1983.

[135] J. Bailey and M. McCartney, "Characterization of structural development in sol-gel systems by cryogenic transmission electron microscopy", *Ultrastructure Processing of Ceramics, Glasses and Composites*, John Wiley and Sons, Edited by L.Hench and D.R. Ulrich, pp57-69, 1984.

[136] H. Zhang and B. Mitchell, "A method for determining crystallisation kinetic parameters from one isothermal calorimetric experiment", J. Mater. Res., 15, [4], April 2000.

[137] R.Dupree and D.Holland, "MAS NMR: a spectroscopic technique for structure determination in glasses and ceramics", *Glasses and Glass-Ceramics*, Edited by M.H.Lewis, Chapman and Hall, pp1-38, 1989.

[138] P.G. Galliano, J.M. Porto Lopez, E.L. Varetti, I. Sobrados, and J. Sanz, "Analysis by nuclear magnetic resonance and Raman spectroscopies of the structure of Bioactive Alkaline-Earth Silicon phosphate glasses", Materials Research Bulletin, vol.29, no.12, pp1297-1306, 1994.

[139] N. Ford and R. Todhunter, "Applications of microporous glasses", *Glasses and Glass-Ceramics*, Edited by M.H.Lewis, Chapman and Hall, pp203-223, 1989.

[140] M. Bruan, P Hartmann and C. Jana, "^{19}F and ^{31}P NMR spectroscopy of calcium apatites", Journal of Materials Science: Materials in Medicine 6, pp150-154, 1995.

[141] D. Eisenberg and W. Kauzmann, "The Structure and Properties of Water", and "Refractive Index at Infra-red frequencies" in *The Structure and Properties of Water*, p58,62,64,68,199, 200, Oxford at the Clarendon Press, 1969.

[142] T.F.Watson, "Fact and Artefact in Confocal Microscopy", Adv. Dent Res., vol.11, no.4, pp433-441, November 1997.

[143] S.J. Glass and D.J. Green, "Permeability and infiltration of partially sintered ceramics", J. Am Ceram Soc., vol.82, pp2745-2752, 1999.

[144] *Water Chemistry*, Edited by Vernon L. Snoeyink and David Jenkins, John Wiley and Sons, p24, 60, 90, 91, 146, 156, 243-246, 251, 252, 282, p298, 1980.

[145] Seminar proceedings of The UK Society for Biomaterials at the University of Nottingham, School of Biomedical Science, Speakers - Dr. Rob Hill on "The common ion effect" (Imperial College), and S. Anderson on "The osteoblastic response to silica and silicon patterned surfaces" (University of Nottingham), September 2000.

[146] K. Tsuru, C. Ohtsuki, A. Osaka, T. Iwamoto and J.D. Mackenzie, "Bioactivity of sol-gel derived organically modified silicates, Part 1: *In vitro* examination", Journal of Materials Science: Materials in Medicine 8, pp157-161, 1997.

[147] L. Warren, A. Clark, and L. Hench, "An investigation of Bioglass powders: Quality assurance test procedure and test criteria", J. Biomed. Res. Applied Biomaterials, vol.23, no.A2, pp201-209, 1989.

[148] K. Wallace, "Influence of sodium oxide content on bioactive glass properties, Journal of Materials Science, Materials in Medicine, vol.10, iss.12, pp697-701, 1999.

[149] D.C. Greenspan, J.P. Zhong and G.P. LaTorre, "Effect of Surface Area to Volume ratio on the *In Vitro* Surface reactions of Bioactive Glass Particulates", Proceedings of the 7th International Symposium on Ceramics in Medicine. Turku, Finland, in *Bioceramics 7*, Edited by O.H. Andersson and A. Yli-Urpo, 1994.

[150] D.C. Greenspan, J.P. Zhong, X.F. Chen, and G. P. LaTorre, "The evaluation of degradability of melt and sol-gel derived Bioglass *in-vitro*", Presented at the proceedings of *Bioceramics 10*, 1997.

[151] D. P. Zarubin, "Infrared spectra of hydrogen bonded hydroxyl groups in silicate glasses. A re-interpretation", Phys.Chem.Glasses, vol.40, no.4, pp184-192, 1999.

[152] P. Li, K. Nakanshi, T. Kokubo and K. de Groot, "Induction and morphology of hydroxyapatite, precipitated from metastable simulated body fluids on sol-gel prepared silica", Biomaterials, vol.14, no.4, pp963-967, 1993.

[153] J. Clement, J.M. Manero, J. A. Planell, G. Avila and S. Martinez, "Analysis of the structural changes of a phosphate glass during dissolution in simulated body fluid", Journal of Materials Science: Materials in Medicine, vol.10, pp729-732, 1999.

[154] T. Miyazaki, H.M. Kim, T. Kokubo, H. Kato, N. Nakamuro, and C. Ohisuki, "Bonelike Apatite formation on Niobium Oxide Gel in Simulated Body Fluid", Key Engineering Materials Volumes. vol.192-195, pp43-46. Proceedings of Bioceramics 13, Bologna, November 13-20th, 2000.

[155] M. Hesse, H. Meier, B. Zeeh, "Spektroskopische Methoden in der organischen Chemie" , 4., uberarbeitete Auflage, 243 Abbildungen, 96 Tabellan, Georg Thieme Verlag Stuttgart, New York, 1991.

[156] C. Durucan and P.W. Brown, "α-Tricalcium phosphate hydrolysis to hydroxyapatite at and near physiological temperature", Journal of Materials Science: Materials in Medicine 11, pp365-371, 2000.

[157] E.Fernandez, F.J. Gil, M.P. Ginebra, F.C. M. Driessens, J.A.Planell and S.M.Best, "Calcium Phosphate bone cements for clinical applications, Part 1: Solution chemistry", Journal of Materials Science : Materials in Medicine 10, pp169-176, 1999.

[158] N. Patel, S. M. Best, I. R. Gibson., S. King and W. Bonfield, "Preparation and Characterization of Hydroxyapatite and Carbonate substituted Hydroxyapatite Granules", Proceedings of Bioceramics 13, Bologna, Italy, 22-26 November 2000, Key Engineering Materials Volumes, pp7-10, 2001.

[159] C.L. Wickert, A.E. Vieira, J.A. Dehne, X. Wang, D.M. Wilder and A. Barkatt, "Effects of salts on silicate glass dissolution in water: kinetics and mechanisms of dissolution and surface cracking", Phys. Chem. Glasses, vol.40, no.3, pp157-70, 1999.

[160] E.Fernandez, F.J. Gil, M.P. Ginebra, F.C. M. Driessens, J.A.Planell and S.M.Best, "Calcium Phosphate bone cements for clinical applications, Part II: Precipitate formation during setting reactions", Journal of Materials Science: Materials in Medicine 10, pp177-183, 1999.

[161] L.M. Rodríguez-Lorenzo and M. Vallet-Regí, "Controlled Crystallization of Calcium Phosphate Apatites", Chem. Mater., vol.12, pp2460-2465, 2000.

[162] M. Vallet-Regí, J. Pérez-Pariente, I. Izquierdo-Barba, and A. J. Salinas, "Compositional Variations in the Calcium Phosphate Layer Growth on Gel Glasses Soaked in a Simulated Body Fluid", Chem. Mater., vol.12, pp3770-3775, 2000.

[163] Private communication/Video 'The Mechanical cutting of 45S5 and 58S with dental saw, c/o Richard Cook, Guy's Hospital. Video of practical experiment.

[164] L.M. Rodríguez-Lorenzo, M. Vallet-Regí, J.M. Ferreira, M.P. Ginebra, C. Aparicio, J. A. Planell, "Hydroxyapatite cermic bodies with tailored mechanical properties for diferent applications", J. Biomed. Mater. Res. vol.60, pp159-166, 2002.

[165] R. Orefice, L. Hench, A. Clark, A. Brennan, "Novel sol-gel bioactive fibers", J. Biomed. Mater. Res., vol.55, pp460-467, 2001.

[166] T. Petola, M. Jokinen, S. Veittola, J. Simola, A. Yli-Urpo, "*In vitro* bioactivity and strctural features of mildy heat-treated sol-gel derived silica fibers", J. Biomed. Mater. Res., vol.54, pp579-590, 2001.

[167] M. Hamadouche, A. Meunier, D.C. Greenspan, C. Blanchat, J. Zhong, G.P. LaTorre, L. Sedel, "*In Vivo* Absorbability of Bulk Sol-Gel Bioactive Glasses", Transactions of the Sixth World Biomaterials Congress, p1388, Kamuela, Hawaii, USA, May 15-20, 2000.

[168] M. Vallet-Regí, J. Pérez-Pariente, I. Izquierdo-Barba, and A. J. Salinas, "Compositional Variations in the Calcium Phosphate Layer Growth on Gel Glasses Soaked in a Simulated Body Fluid", Chem. Mater., vol.12, pp3770-3775, 2000.

[169] A. Rámila, M. Vallet-Regí, "Static and dynamic *in vitro* study of a sol-gel glass bioactivity", *Biomaterials 22*, pp2301-2306, 2001.

[170] E. Mezey, K.J. Chandross et al., "Turning Blood into Brain: Cells Bearing Neuronal Antigens Generated *In Vivo* from Bone Marrow", Science, vol.290, pp1779-1782, 2000.

[171] T.R. Brazelton, F.M.V. Rossi et al., "From Marrow to Brain: Expression of Neuronal Phenotypes in Adult Mice from Adult Bone Marrow-Derived Cells", Science, vol.290, pp1775-1779, 2000.

[172] Electronic reference, "UF scientists explore adult stem cell potential", University of Florida, UF News, April 16, 2001. [http://www.uf.edu.us]

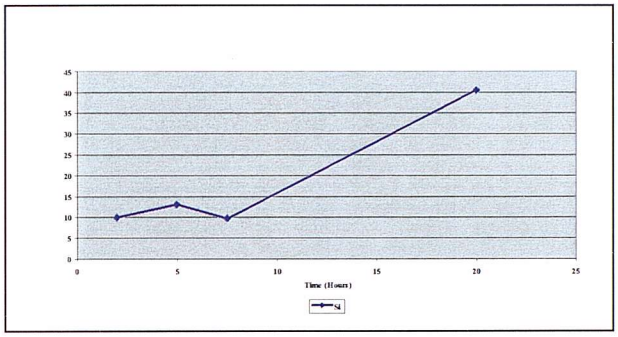
[173] A.H. Reddhi, "New Biomaterials, Stem Cells and Morphogens for Tissue Engineering", Proceedings of Bioceramics 13, Key Engineering Vols.192-195, pp459-462, 2001.

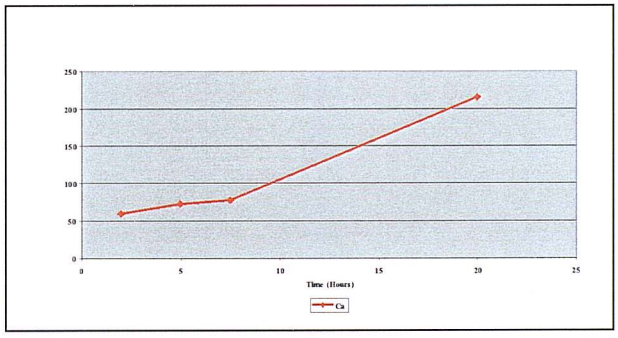
APPENDIX 1

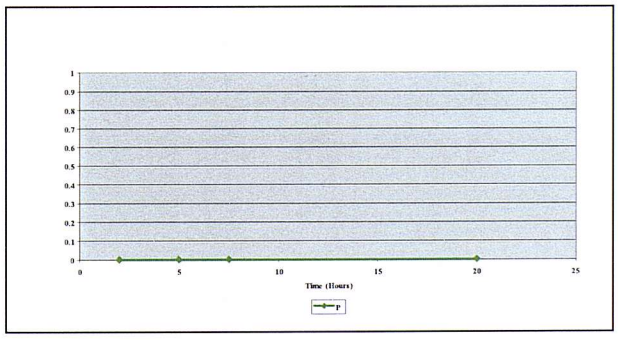
Sample description	page
Dissolution profile for 58S400 treated at 850°C after immersion in Tris buffer solution at 37°C	207
Dissolution profile for 58S400 treated at 950°C after immersion in Tris buffer solution at 37°C	208
Dissolution profile for 58S400 treated at 1050°C after immersion in Tris buffer solution at 37°C	209
Dissolution profile for 58S400 treated at 1100°C after immersion in Tris buffer solution at 37°C	210
Dissolution profile for 58S600 treated at 850°C after immersion in Tris buffer solution at 37°C	211
Dissolution profile for 58S600 treated at 950°C after immersion in Tris buffer solution at 37°C	212
Dissolution profile for 58S800 after immersion in SBF solution at 37°C	213
Dissolution profile for 58S800 after immersion in Tris buffer solution at 37°C	214
Dissolution profile for 58S800 treated at 950°C after immersion in Tris buffer solution at 37°C	215

Graphs for dissolution products of 58S400 with thermal treatment at 850°C, after immersion in Tris buffer solution at 37°C

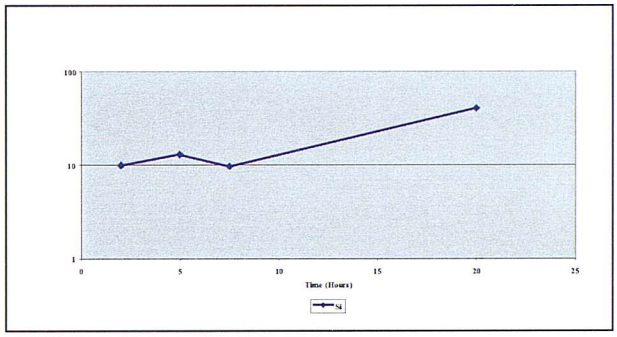
Graphs showing conc. of element in solution (Micrograms per ml)

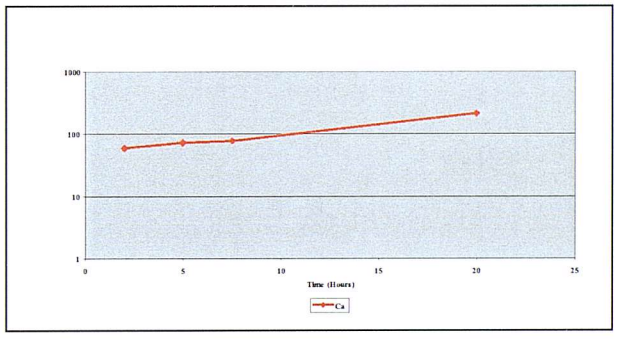






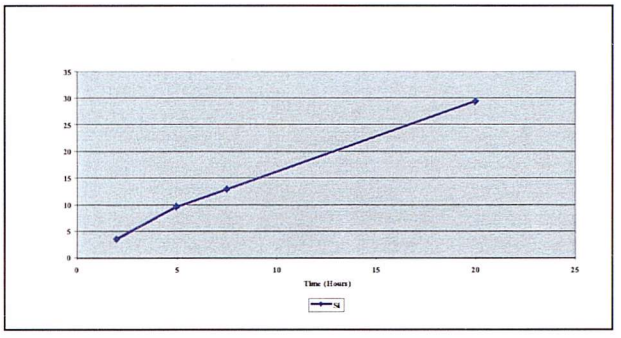
Graphs showing Log conc. of element in solution (Micrograms per ml)

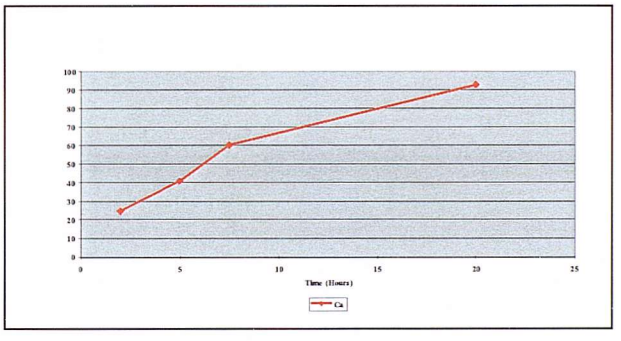


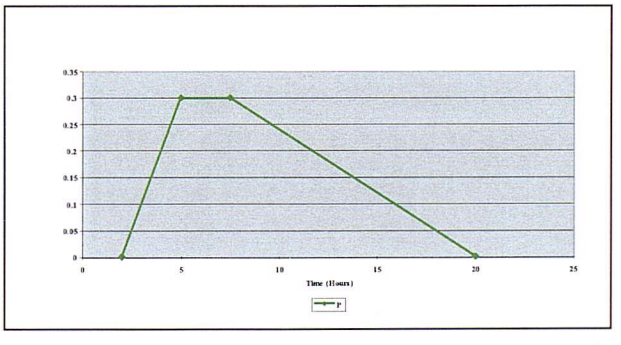


Graphs for dissolution products of 58S400 with thermal treatment at 950°C, after immersion in Tris buffer solution at 37°C

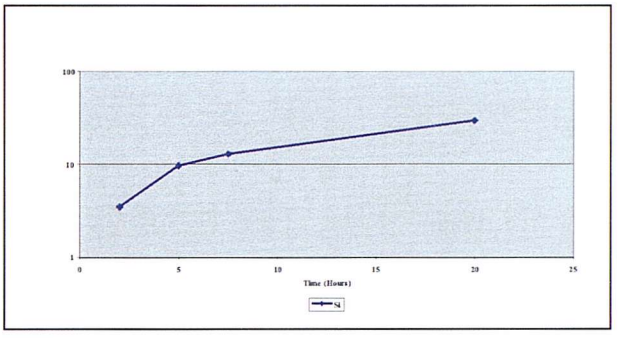
Graphs showing conc. of element in solution (Micrograms per ml)

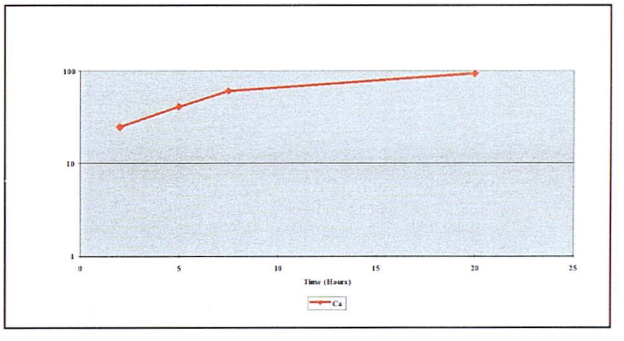






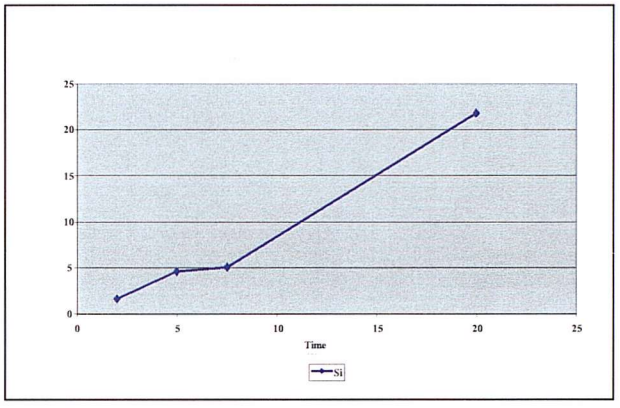
Graphs showing Log conc. of element in solution (Micrograms per ml)

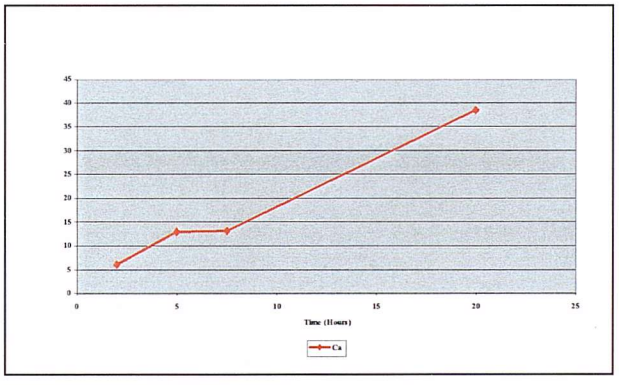


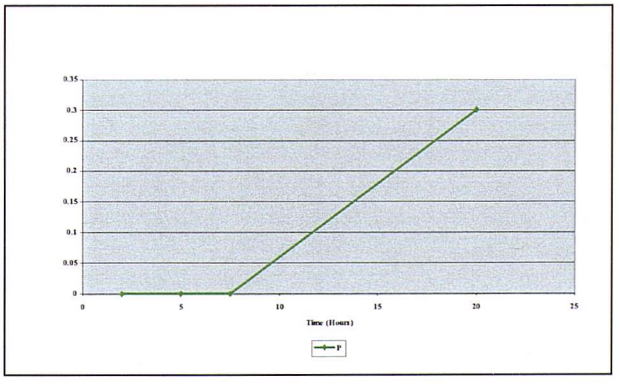


Graphs for dissolution products of 58S400 with thermal treatment at 1050°C, after immersion in Tris buffer solution at 37°C

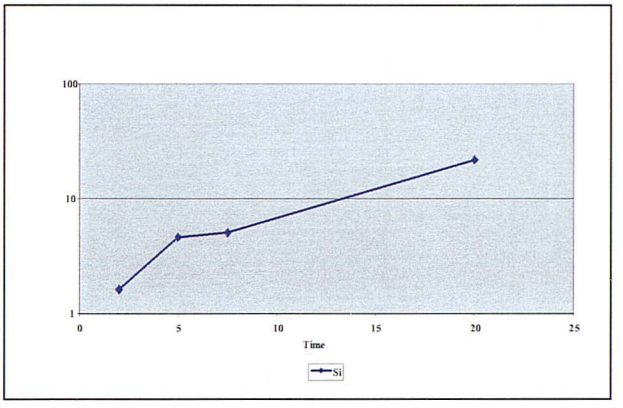
Graphs showing conc. of element in solution (Micrograms per ml)

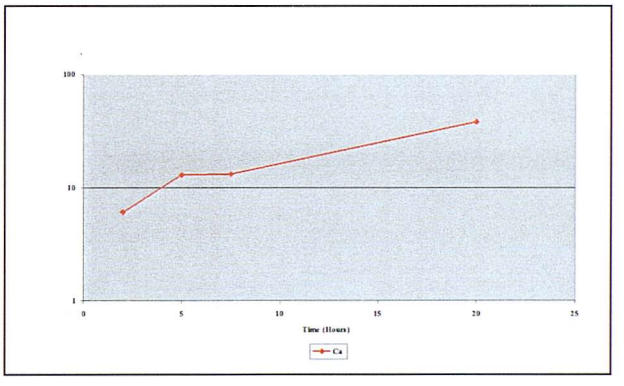






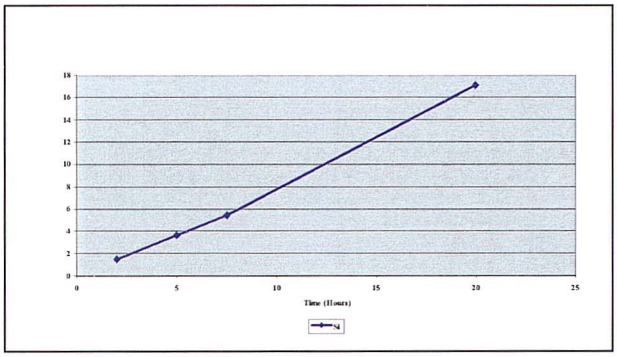
Graphs showing Log conc. of element in solution (Micrograms per ml)

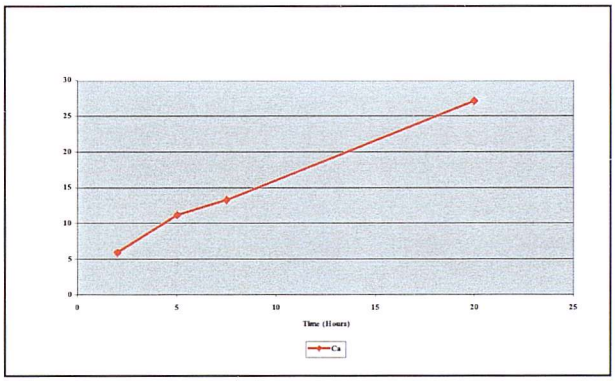


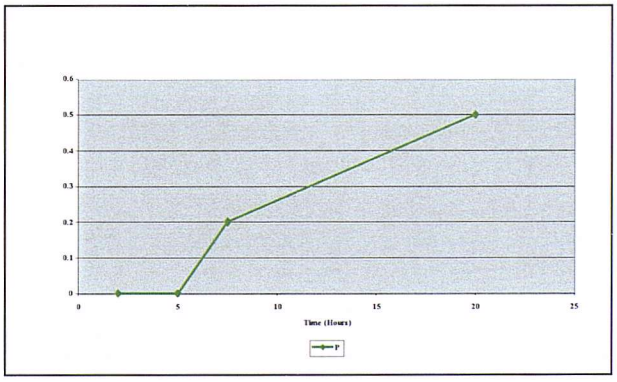


Graphs for dissolution products of 58S400 with thermal treatment at 1100°C, after immersion in Tris buffer solution at 37°C

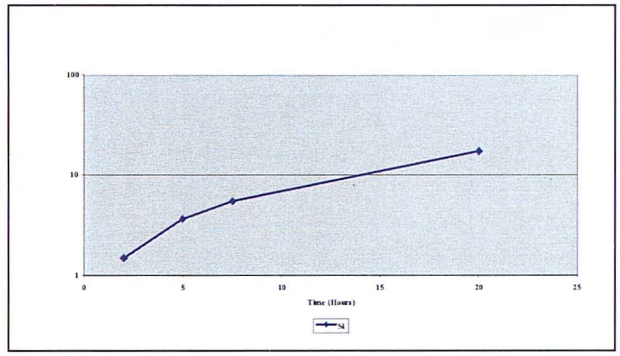
Graphs showing conc. of element in solution (Micrograms per ml)

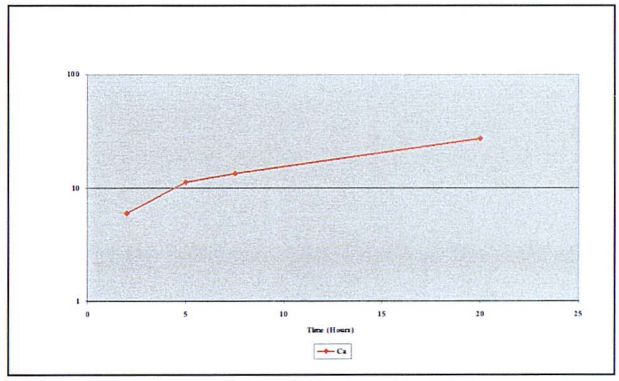






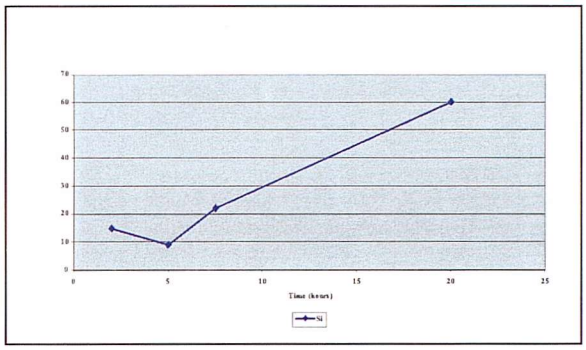
Graphs showing Log conc. of element in solution (Micrograms per ml)

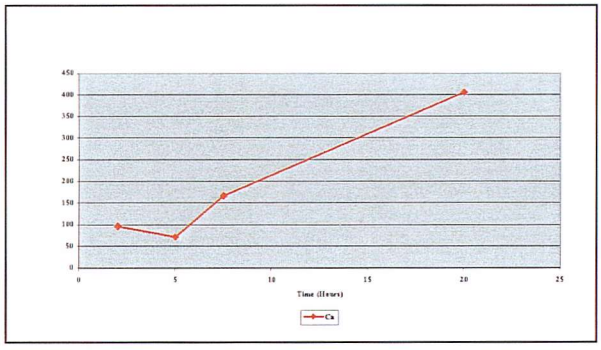


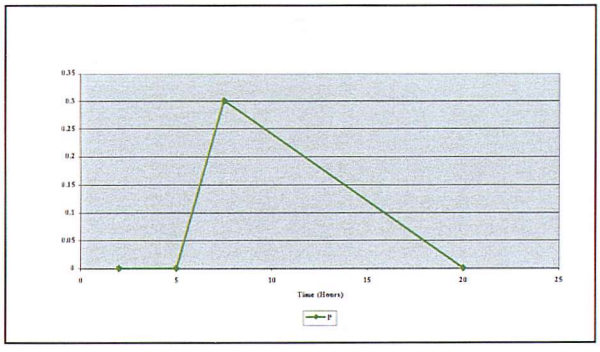


Graphs for dissolution products of
58S600 with thermal treatment at 850°C, after immersion in Tris buffer solution at 37°C

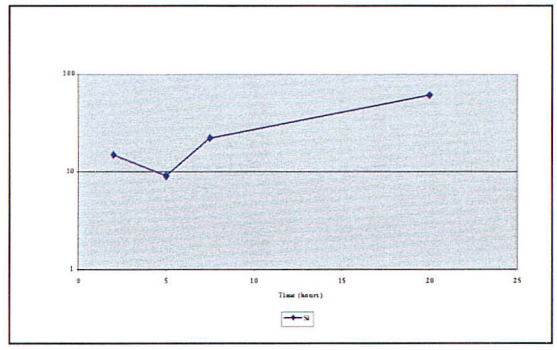
Graphs showing conc. of element in solution (Micrograms per ml)

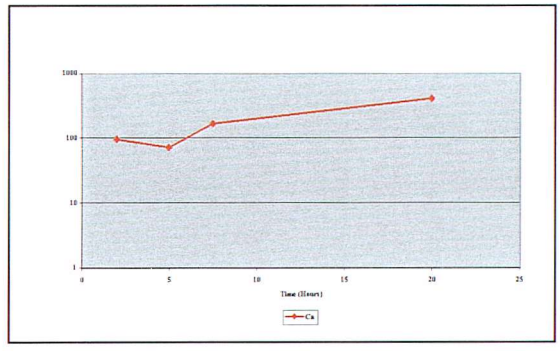






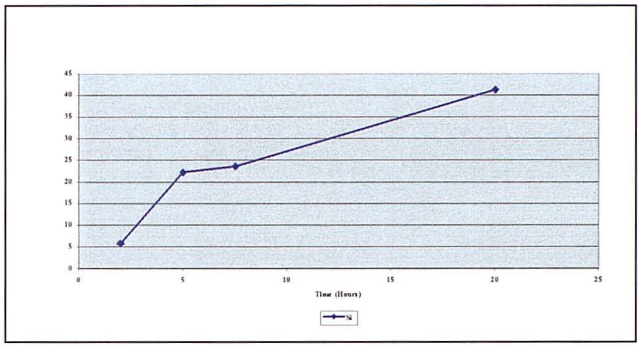
Graphs showing Log conc. of element in solution (Micrograms per ml)



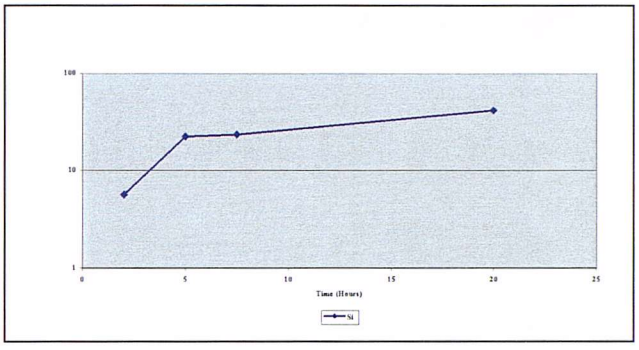


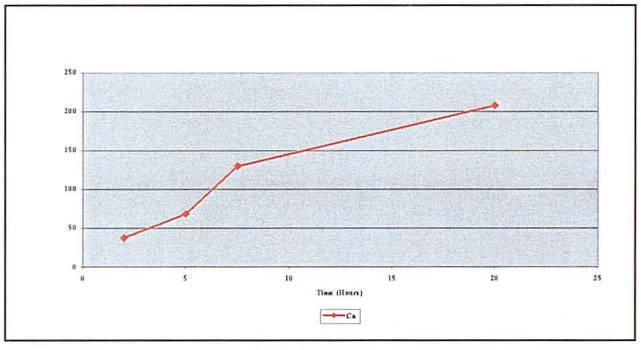
Graphs for dissolution products of
58S600 with thermal treatment at 950°C, after immersion in Tris buffer solution at 37°C

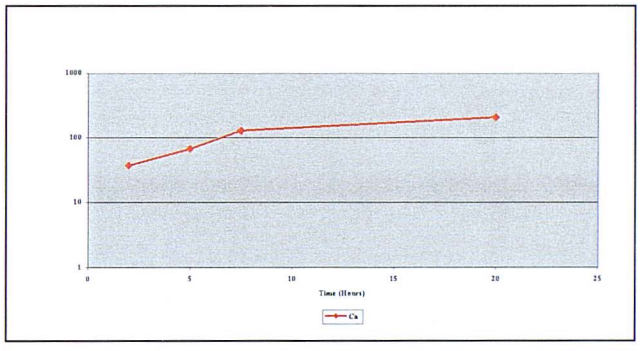
Graphs showing conc. of element in solution (Micrograms per ml)

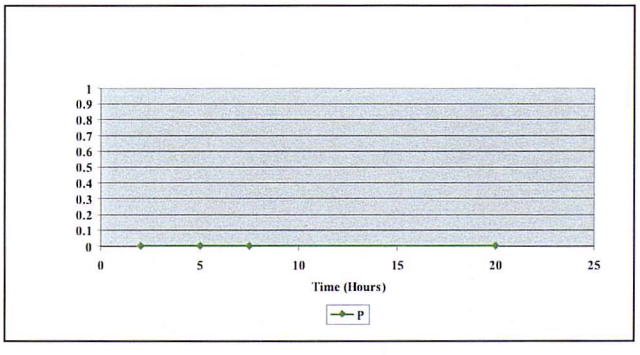


Graphs showing Log conc. of element in solution (Micrograms per ml)



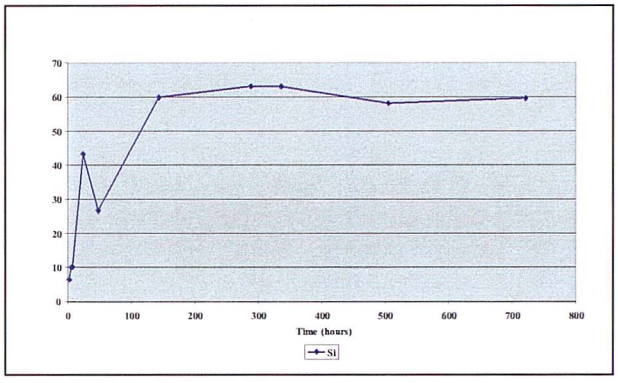


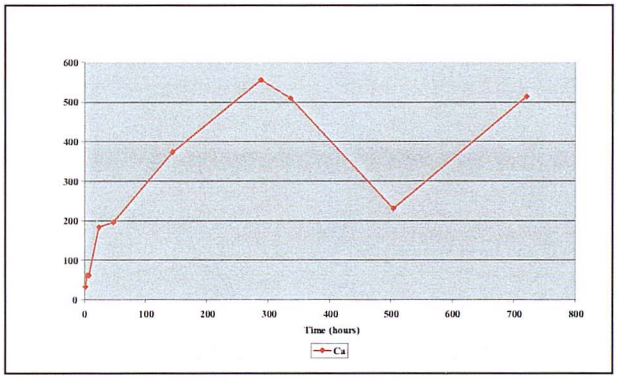


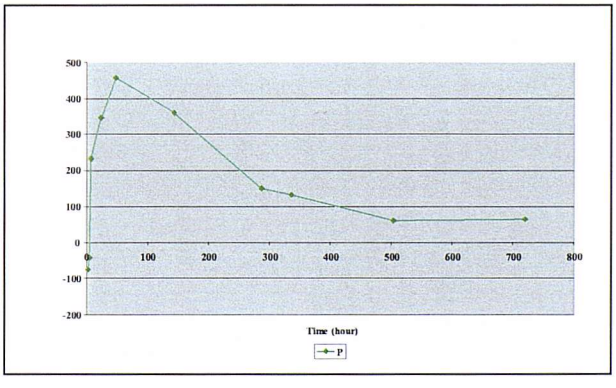


Graphs of dissolution product for 58S800 after immersion in SBF at 37°C

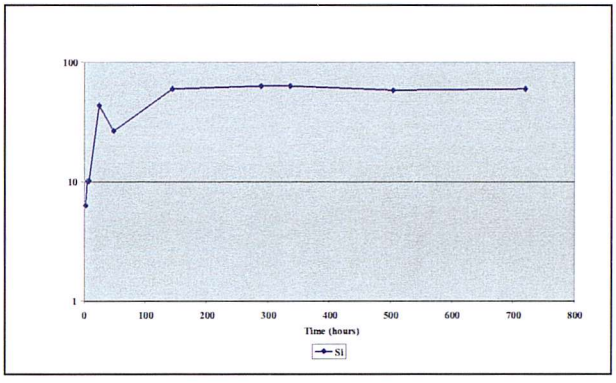
Graphs showing conc. of element in solution (Micrograms per ml)

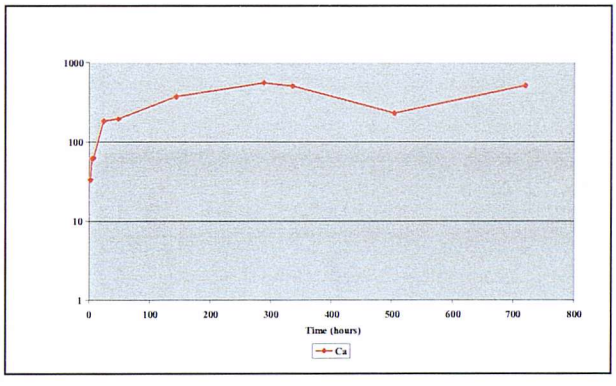






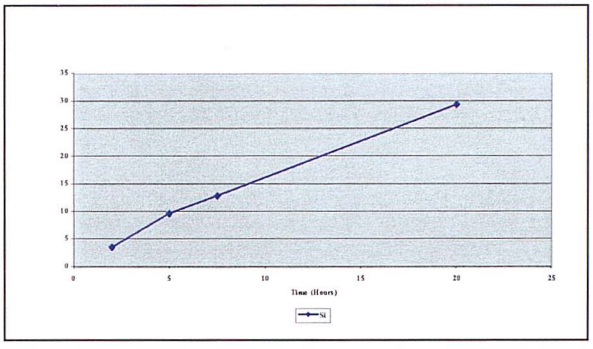
Graphs showing Log conc. of element in solution (Micrograms per ml)

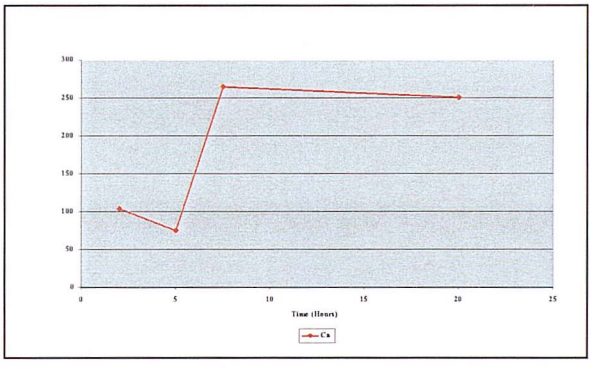


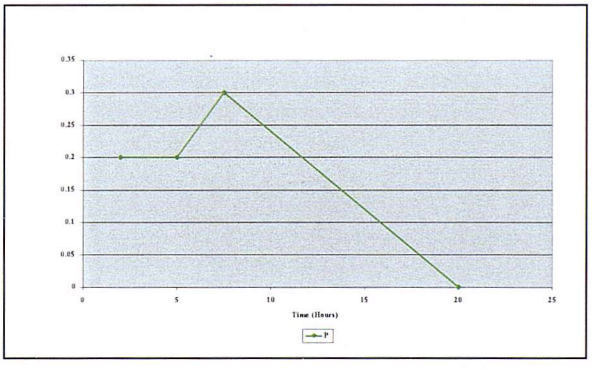


Graphs for dissolution products of
58S800 after immersion in Tris buffer solution at 37°C

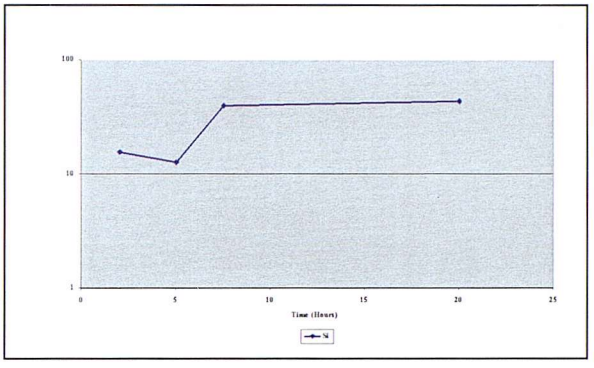
Graphs showing conc. of element in solution (Micrograms per ml)

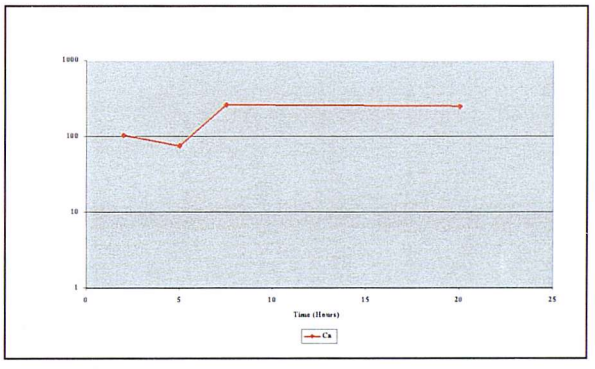






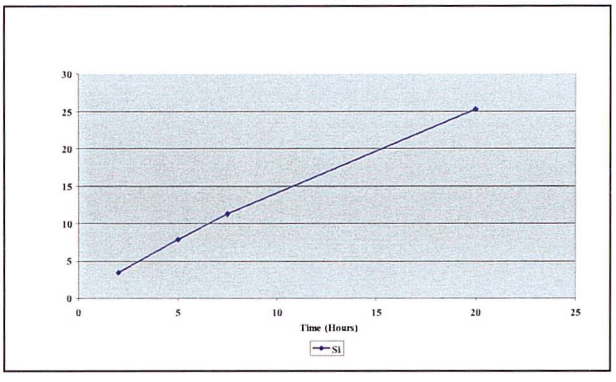
Graphs showing Log conc. of element in solution (Micrograms per ml)

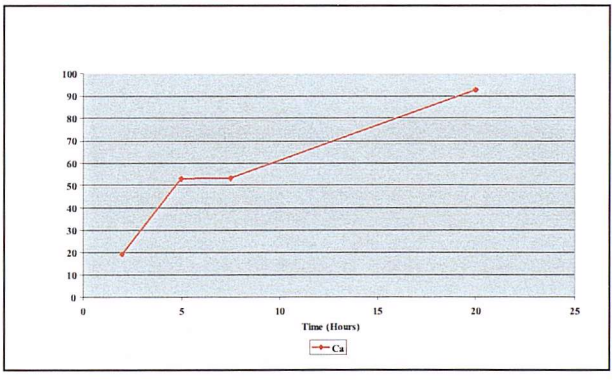


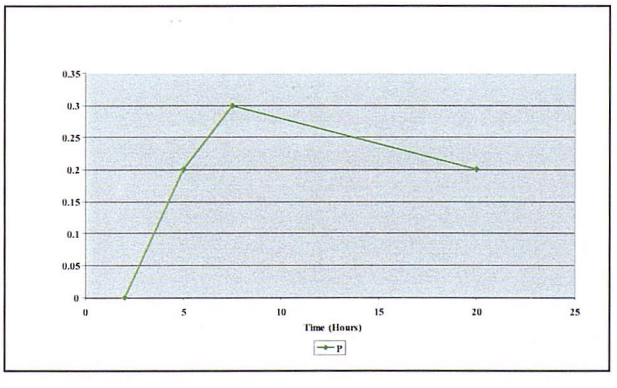


Graphs for dissolution products of 58S800 with thermal treatment at 950°C, after immersion in Tris buffer solution at 37°C

Graphs showing conc. of element in solution (Micrograms per ml)







Graphs showing Log conc. of element in solution (Micrograms per ml)

